Report of Investigations 2013-3

TSUNAMI INUNDATION MAPS OF SITKA, ALASKA

by
Elena N. Suleimani, Dmitry J. Nicolsky, and Rich D. Koehler

View from the southwest of downtown Sitka. Photo by Wells Williams.

Published by

STATE OF ALASKA
DEPARTMENT OF NATURAL RESOURCES

DIVISION OF GEOLOGICAL & GEOPHYSICAL SURVEYS

2013

Report of Investigations 2013-3

TSUNAMI INUNDATION MAPS OF SITKA, ALASKA

by
Elena N. Suleimani, Dmitry J. Nicolsky, and Rich D. Koehler

2013

STATE OF ALASKA
Sean Parnell, *Governor*

DEPARTMENT OF NATURAL RESOURCES
Joe Balash, *Acting Commissioner*

DIVISION OF GEOLOGICAL & GEOPHYSICAL SURVEYS
Robert F. Swenson, *State Geologist and Director*

Publications produced by the Division of Geological & Geophysical Surveys (DGGS) are available for free download from the DGGS website (**www.dggs.alaska.gov**). Publications on hard-copy or digital media can be examined or purchased in the Fairbanks office:

Alaska Division of Geological & Geophysical Surveys
3354 College Rd., Fairbanks, Alaska 99709-3707
Phone: (907) 451-5020 Fax (907) 451-5050
dggspubs@alaska.gov
www.dggs.alaska.gov

Alaska State Library
State Office Building, 8th Floor
333 Willoughby Avenue
Juneau, Alaska 99811-0571

Alaska Resource Library & Information Services (ARLIS)
3150 C Street, Suite 100
Anchorage, Alaska 99503-3982

Elmer E. Rasmuson Library
University of Alaska Fairbanks
Fairbanks, Alaska 99775-1005

University of Alaska Anchorage Library
3211 Providence Drive
Anchorage, Alaska 99508-4614

CONTENTS

FIGURES

TABLES

APPENDIX

TSUNAMI INUNDATION MAPS OF SITKA, ALASKA

by
E.N. Suleimani[1], D.J. Nicolsky[1], and R.D. Koehler[2]

Abstract

The purpose of this study is to evaluate potential tsunami hazards for the community of Sitka. We numerically model the extent of inundation from tsunami waves generated by near- and far-field tectonic sources. We performed numerical modeling of historic events at Sitka, such as the tsunami triggered by the 1964 Great Alaska Earthquake, and the tsunami waves generated by the recent 2011 Tohoku and 2012 Haida Gwaii earthquakes. Hypothetical tsunami scenarios include variations of the extended 1964 rupture, megathrust earthquakes in the Alaska Peninsula region and in the Cascadia subduction zone, and a thrust earthquake in the region of the Queen Charlotte–Fairweather fault zone. Results of numerical modeling combined with historical observations in the region are intended to provide guidance to local emergency management in tsunami hazard assessment, evacuation planning, and public education for the reduction of future tsunami risk.

INTRODUCTION

Subduction of the Pacific plate under the North American plate has caused numerous great earthquakes and still has the greatest potential to generate tsunamis in Alaska. The Aleutian megathrust, where the Pacific plate is being subducted, is the most seismically active tsunamigenic fault zone in the United States (fig. 1). Several historic tsunamis generated by earthquakes on the Alaska–Aleutian subduction zone have resulted in widespread damage and loss of life after traveling for hours across the Pacific and impacting exposed coastal locations. However, tsunamis originating in the vicinity of the Alaska Peninsula, Aleutian Islands, and the Gulf of Alaska are considered to be a near-field hazard for Alaska, and can reach Alaska's coastal communities within minutes of the earthquake. Saving lives and property depends on how well a

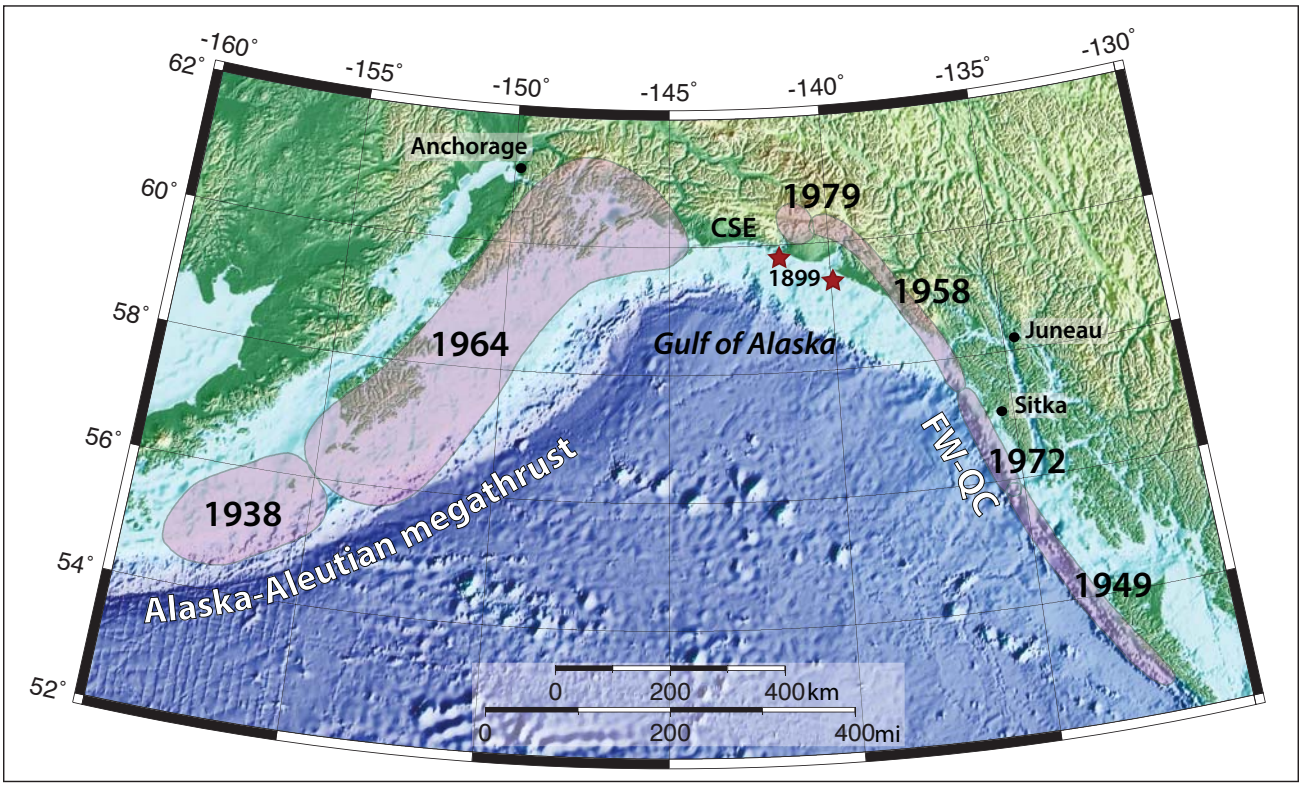

Figure 1. Map of south-central and southeastern Alaska, with rupture areas of the major historical earthquakes shaded in lavender. Red stars indicate epicenters of two September 1899 earthquakes. CSE=Chugach–St. Elias fold and thrust belt; FW–QC=Fairweather–Queen Charlotte fault system.

[1]Alaska Earthquake Information Center, Geophysical Institute, University of Alaska, P.O. Box 757320, Fairbanks, AK 99775-7320; elena@gi.alaska.edu; djnicolsky@alaska.edu
[2]Alaska Division of Geological & Geophysical Surveys, 3354 College Rd., Fairbanks, AK 99709-3707; richard.koehler@alaska.gov

community is prepared, which makes it essential to estimate the potential flooding of the coastal zone in the event of a local or distant tsunami.

On March 27, 1964, the largest earthquake ever recorded in North America struck south-central Alaska. This M_W9.2 megathrust earthquake generated the most destructive tsunami in Alaska history and, farther south, impacted the west coasts of the United States and Canada. In addition to the major tectonic tsunami, which was generated by an ocean floor displacement between the trench and the coastline, more than 20 local tsunamis were generated by landslides in coastal Alaska. They arrived almost immediately after shaking was felt, leaving no time for warning or evacuation. Of the 131 fatalities associated with this earthquake, 122 were caused by tsunami waves (Lander, 1996). Local tsunamis caused most of the damage and accounted for 76 percent of tsunami fatalities in Alaska. The city of Sitka on Baranof Island (fig. 2) was the only port in southeastern Alaska that suffered significant damage from tsunami waves.

The production of tsunami evacuation maps for a community consists of several stages. First, we develop credible hypothetical tsunami scenarios on the basis of relevant local and distant sources and tsunami generation mechanisms. We characterize tsunami sources using the level of detail that is necessary to describe the essential characteristics of the wave, with local tsunami sources having more detailed characterization. Next, we perform model simulations for each of these scenarios. The results are then compared with historical tsunami observations, if such data exist. Finally, we develop a "worst case" inundation line that encompasses the maximum extent of flooding based on model simulation of all source scenarios and historical observations. The "worst case" inundation line becomes a basis for local tsunami hazard planning and for developing evacuation maps.

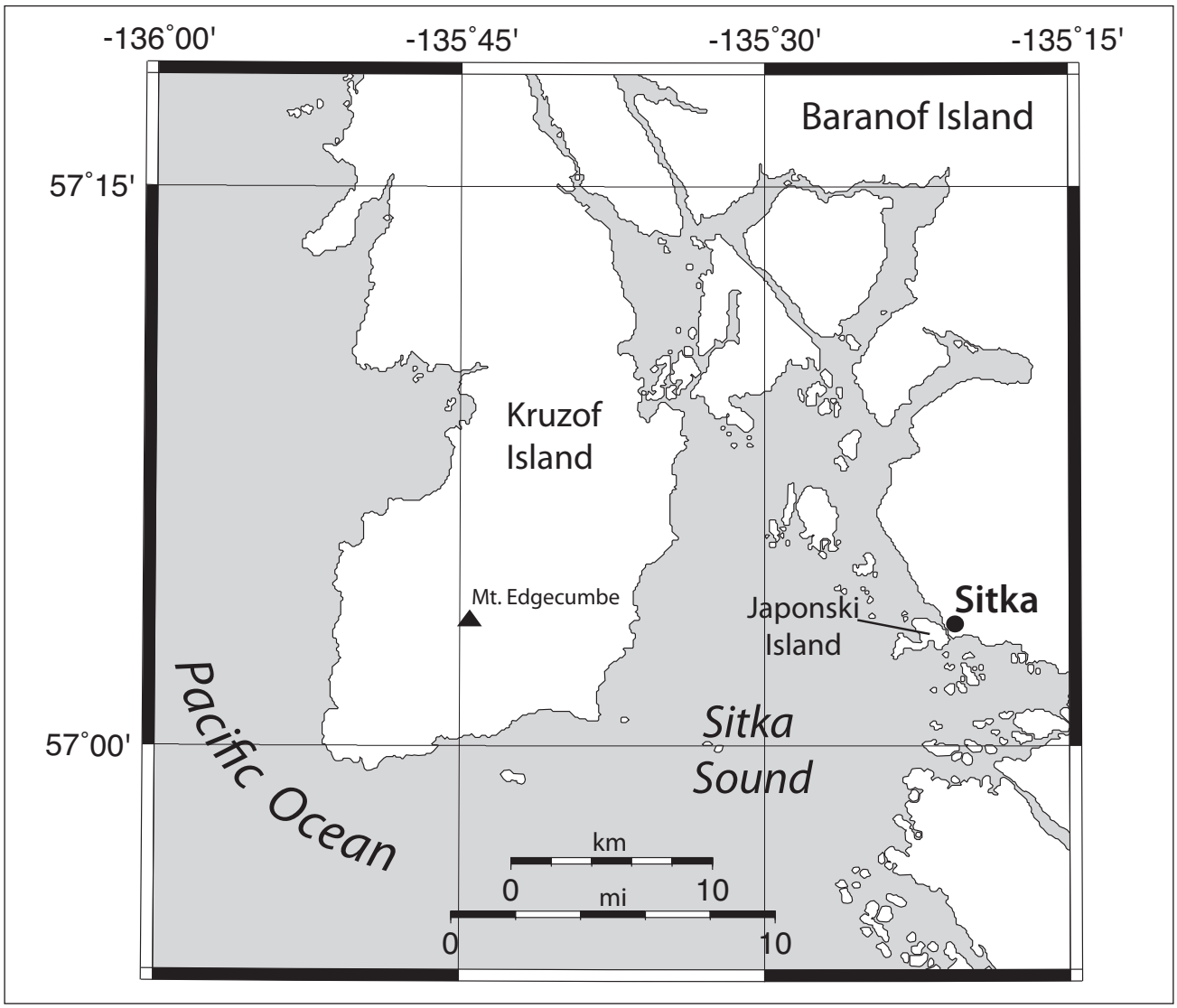

Figure 2. Location of Sitka in Sitka Sound, on Baranof Island.

The tsunami inundation maps of Sitka described in this report represent the results of the continuous effort between state and federal agencies[3] to produce inundation maps for many Alaska coastal communities. In this report, we generally provide both metric and imperial units of measure. If it is necessary to quote some existing data, we state the data in the original and metric units of measure. Recall that one inch (1 in) is approximately 2.54 centimeters (2.54 cm), one foot (1 ft) is approximately 0.305 meters (0.305 m), and one mile (1 mi) is approximately 1.609 kilometers (1.609 km).

PROJECT BACKGROUND: REGIONAL AND HISTORICAL CONTEXT

Setting

The community of Sitka, the former capital of Russian Alaska, is in southeastern Alaska, on the west coast of Baranof Island, facing the Pacific Ocean (fig. 2). It is about 950 km (590 mi) east–southeast of Anchorage and 150 km (95 mi) southwest of Juneau at approximately 57°3' North latitude and 135°20' West longitude, and it is only accessible by boat or plane. When the United States purchased Alaska from Russia in 1867, Sitka became the first capital of the Alaska Territory and remained so until the capital was moved to Juneau in 1906. The population of Sitka in 2011 was 9,000, with approximately 3,500 households. By population, it is the fourth largest city in the State of Alaska. The U.S. Coast Guard Air Station Sitka and the Rocky Gutierrez Sitka Airport are both on Japonski Island in Sitka Sound. According to the Alaska Division of Community Advocacy (2011) database, the Borough of Sitka is known historically for resource extraction including fishing, mining, and lumber. A large fishing fleet is based in Sitka Harbor and specializes in salmon, halibut, and sablefish. Sitka is the sixth largest port in the United States by the value of seafood harvest. Recently, the economy has been diversified into accommodating summer cruise ships and eco-tourists. Cruise ships bring more than 120,000 people to Sitka annually (Sitka, 2012–2013). Figure 3 shows an aerial view of Sitka Sound.

Due to its remote location, low-lying population center, and high influx of seasonal tourists, the potential impact of a tsunami event on the economy and infrastructure of Sitka is high. To manage this risk, we have developed tsunami inundation maps for Sitka in the scope of the National Tsunami

Figure 3. Aerial view of Sitka, looking from southeast.

[3]To help mitigate the hazard that earthquakes and tsunamis pose to Alaska coastal communities, the Alaska Tsunami Mapping Team (ATMT) was created. It consists of personnel from the Geophysical Institute at the University of Alaska Fairbanks and from the State of Alaska Division of Geological & Geophysical Surveys. The ATMT participates in the National Tsunami Hazard Mitigation Program by evaluating and mapping potential inundation of selected parts of the Alaska coastline using numerical tsunami modeling.

Hazard Mitigation Program. Sitka, as a high-priority region for tsunami inundation mapping, will benefit from tsunami hazard maps that summarize potential tsunami impact on the population and infrastructure.

Regional seismotectonics

The primary tectonic elements of the Pacific/North American plate boundary in southern Alaska are the Alaska–Aleutian megathrust, Chugach St. Elias (CSE) fold and thrust belt, and the >1,000-km-long (>620-mi-long) Fairweather–Queen Charlotte (FW–QC) fault system (fig. 1). In the Sitka area, plate motion is accommodated along the Fairweather fault, a transform fault that extends primarily offshore along the entire southeastern Alaska coastline, becoming the Queen Charlotte fault to the south in British Columbia (fig. 4). Fletcher and Freymueller (2003) estimate a slip rate of ~44.6 ± 2.0 mm/yr (~1.8 ± 0.08 in/yr) for the northern Fairweather fault, one of the highest rates observed across any strike-slip fault in the world. Figure 4 shows rupture areas of large historic earthquakes and seismic activity in southeastern Alaska with locations determined by the Alaska Earthquake Information Center (AEIC) at the University of Alaska Fairbanks. Prior to initiation of a regional seismic network in Alaska in the early 1970s, only larger events with $M_W \geq 6$ could be located. Since the installation of the network, events of smaller size can be detected.

The entire Fairweather–Queen Charlotte fault system has ruptured in large strike-slip earthquakes over the last century: 1927 (M_S7.1), 1949 (M_S8.1,), 1958 (M_S7.9), and 1972 (M_S7.6) (Sykes, 1971; Page, 1973; Tocher, 1960). The 1958 event, known as the "Lituya Bay earthquake", triggered a large landslide into Lituya Bay that generated a 530-m-high (1,740-ft-high) wave (Miller, 1960). These events indicate that seismic slip along the FW–QC fault system is parallel to the direction of motion between the North American and the Pacific plates (Doser and Lomas, 2000). Most of the modern seismic events along the Fairweather fault in this area are larger magnitude aftershocks of these historic sequences. Fletcher and Freymueller (2003) estimate that only 75 years is required to build up slip equivalent to the M_S7.9 1958 earthquake along the northern Fairweather fault, and Nishenko and Jacob (1990) have estimated a recurrence interval of 120 to 130 years for earthquakes similar to the 1972 M_S7.6 Sitka and 1949 M_S8.1 Queen Charlotte earthquakes, respectively.

In the vicinity of Haida Gwaii (formerly known as the Queen Charlotte Islands), relative plate motion is also mainly transform, and accommodated by oblique strike-slip deformation. A M_S7.5 earthquake north of Haida Gwaii occurred on January 5, 2013, as a result of shallow strike-slip faulting along the plate boundary, rupturing a 140-km-long (87-mi-long) segment of the fault (AEIC event page). The epicenter of this event was 326 km (203 mi) south of Juneau (fig. 4) and straddles the rupture areas of the 1972 and 1949 events. This event could possibly be related to the October 28, 2012, M_W7.8 earthquake that occurred to the south in Haida Gwaii along the same plate boundary system. The velocity of the relative plate motion in the area is about 49 mm (2 in) per year (DeMets and Dixon, 1999). Mazzotti and others (2003) used GPS data to constrain a change in the relative plate motion from mainly transform to oblique strike-slip from north to south along the plate boundary, respectively. Their results indicate that convergence rates change from about 8 mm (0.3 in) per year to about 15 mm (0.6 in) per year from northern to southern Haida Gwaii (fig. 4). Plate motion models indicate about 20° of current oblique convergence that started about 5 Ma (DeMets and others, 1990; DeMets and Dixon, 1999). Two models exist to explain the accommodation of convergence off Haida Gwaii: Internal shortening (for example, Rohr and others, 2000) versus underthrusting of the Pacific plate (for example, Smith and others, 2003). Mazzotti and others (2003) concluded that the GPS data cannot discriminate between the two models, showing that while 6–7 mm (0.23–0.27 in) per year of convergence is accommodated by internal shortening, the remaining 6–10 mm (0.23–0.39 in) per year of convergence cannot be unambiguously assigned to any of the two proposed mechanisms. Recent studies of oblique convergence across the Queen Charlotte fault (Smith and others, 2003; Bustin and others, 2007) compiled different geophysical data and demonstrated strong evidence for an underthrusting model that was also supported by a detailed teleseismic receiver function analysis. The studies concluded that the 10-km-thick (6.2-mi-thick) low-velocity zone dipping to the east at 28° defines the underthrusting oceanic crust located beneath a thin continental crust (Bustin and others, 2007). The mechanism of the recent M_W7.8 Haida Gwaii earthquake (fig. 4) was mostly shallow thrust on the eastward-dipping fault plane, with a dip of 18.5° and strike of 317.1° corresponding to that of the plate boundary (Lay and others, 2013), supporting the proposed underthrusting model.

METHODOLOGY AND DATA

Grid development and data sources

One of the problems in tsunami modeling is that the governing equations for water dynamics are continuous. In this work, we discretize the shallow-water equations in spherical coordinates on Arakawa C-grid (Arakawa and Lamb, 1981) using a finite difference method. To resolve a wave, the grid must be fine enough, with at least four points per wavelength (Titov and Synolakis, 1995); more points than that are often necessary to achieve satisfactory accuracy (for example, Titov and Synolakis, 1997). To compute a detailed map of potential tsunami inundation triggered by local and distant earthquakes, we employ a series of nested computational grids. A nested grid allows for higher resolution in areas where it is needed, without expending computer resources in areas where it is not. The bathymetric and topographic relief in each nested grid is based on digital elevation models (DEMs) developed at the National Geophysical Data Center (NGDC) of the National Oceanic & Atmospheric Administration (NOAA), in Boulder, Colorado. The extent of each grid used for Sitka mapping is listed in table 1. The coarsest grid spans the central and northern Pacific Ocean and has a resolution of 2 arc-minutes (≈ 2 km), while the highest resolution grid is localized near the town of Sitka. The spatial resolution of the high-resolution grid, 15×16 m (49×52 ft), satisfies NOAA minimum recommended requirements for

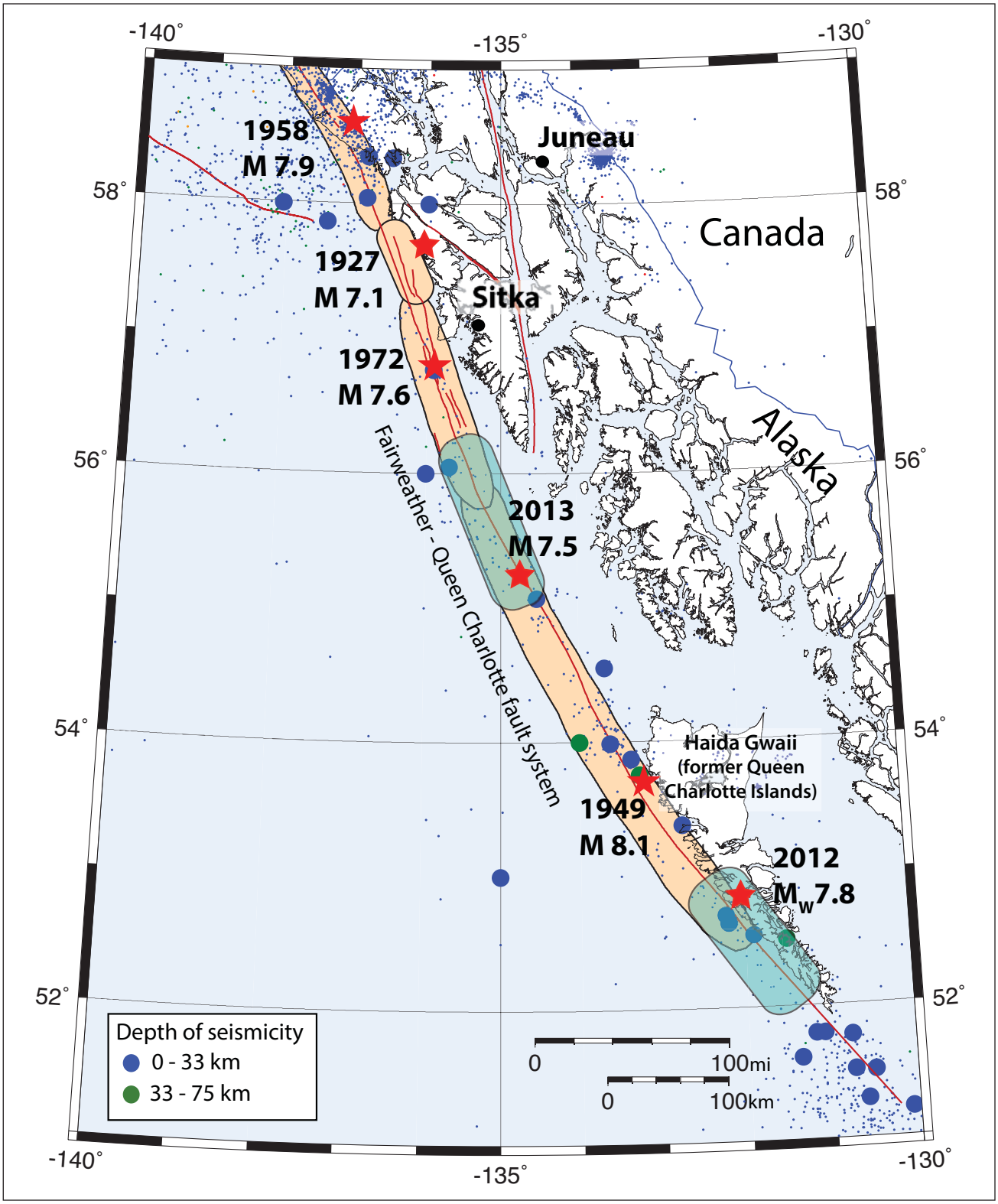

Figure 4. Earthquakes in southeastern Alaska, from the Alaska Earthquake Information Center catalog. Small dots correspond to earthquakes with magnitude less than 5. Large circles show significant earthquakes of magnitude 5 and greater, and are color-coded according to depth. Red stars mark epicenters of large earthquakes. Peach-shaded areas indicate rupture zones of historic earthquakes, and the turquoise-shaded areas show rupture zones of the two most recent earthquakes along the FW–QC fault system.

Table 1. Nested grids used to compute propagation of tsunami waves to the city of Sitka. The high-resolution grid is used to compute the inundation. Note that the grid resolution in meters is not uniform and is used to illustrate grid fineness near Sitka. The first dimension is the longitudinal grid resolution, while the second is the latitudinal one.

Grid name	Resolution		West – East boundaries	North – South boundaries
	Arc-seconds	Meters (near Sitka)		
Northern Pacific, *Level 0*	120 × 120	1,850 × 3,700	120°00'E – 100°00'W	10°00'N – 65°00'N
Southeastern Alaska, *Level 1*	24 × 24	402 × 740	130°00'W – 141°00'W	54°00'N – 60°00'N
Juneau West, *Level 2*	8 × 8	132 × 246	133°15'W – 137°15'W	55°45'N – 59°36'N
Chatham Strait, *Level 3*	2.67 × 2.67	44 × 82	133°17'W – 135°41'W	56°45'N – 58°00'N
Sitka, *high resolution grid*	0.89 × 0.53	15 × 16	135°12'45"W – 135°31'06"W	57°01'14"N – 57°08'50"N

computation of tsunami inundation (National Tsunami Hazard Mapping Program [NTHMP], 2010).

The bathymetry data for the 2-arc-minute resolution grid shown in figure 5 is extracted from the ETOPO2 data set (NOAA, National Geophysical Data Center). To develop 15-meter, 2.67-, 8- and 24- arc-second resolution grids, shoreline, bathymetric, and topographic digital datasets were obtained from several U.S. federal and academic agencies, including: NOAA's National Ocean Service, Office of Coast Survey, and NGDC; the U.S. Fish & Wildlife Service (FWS); the U.S. Geological Survey (USGS); and the U.S. Army Corps of Engineers (USACE). All data were shifted to World Geodetic System 1984 (WGS 84) horizontal and Mean Higher High Water (MHHW) vertical datums. The data sources and methodology used to create the 24-, 8-, and 2.67- arc-second DEMs are described in greater detail in Caldwell and others (2012) and Lim and others (2011). The development of the high-resolution grid for Sitka, which was used to calculate the extent of inundation and flow depths, is described in Hickman and others (2012). The horizontal datum for this grid is WGS84, and the vertical datum is MHHW.

Numerical model of tsunami wave propagation and runup

NOAA recently published a technical memorandum outlining major requirements for numerical models used in inundation mapping and tsunami forecasting, and describes a procedure for model evaluation (National Tsunami Hazard Mapping Program [NTHMP], 2010). There are two major components to this process. The first is model validation, which ensures that the model correctly solves appropriate equations of motion by comparing model results with known solutions. This is achieved through analytical and laboratory benchmarking. The second component is model verification, which is testing the model, using observations of real events through field data benchmarking. The numerical model currently used by the AEIC for tsunami inundation mapping has been validated through a set of analytical benchmarks, and tested against laboratory and field data (Nicolsky and others, 2011; Nicolsky, 2012). The model solves nonlinear shallow-water equations using a finite-difference method on a staggered grid. For any coarse–fine pair of computational grids, we apply a time-explicit numerical scheme as follows. First, we compute the water flux within a coarse-resolution grid. These values of computed flux are used to define the water flux on a boundary of the fine-resolution grid. Consequently, the water level and then the water flux are calculated over the fine-resolution grid. Finally, the water level computed in the fine-resolution grid is used to define the water level within the area of the coarse-resolution grid that coincides with the fine grid. Despite the fact that developed nested grids decrease the total number of grid cells needed to preserve computational accuracy within certain regions of interest, actual simulations are still prohibitive if parallel computing is not implemented. Here, we use the Portable Extensible Toolkit for Scientific computation (PETSc), which provides sets of tools for the parallel numerical solution of shallow-water equations. In particular, each computational grid listed in table 1 can be subdivided among an arbitrary number of processors. The above-mentioned passing of information between the water flux and level is implemented efficiently using PETSc subroutines.

We assess tsunami hazard in Sitka Sound by performing model simulations for each tsunami source scenario. To simulate tsunami dynamics caused by a seafloor deformation from an earthquake, we assume some simplifications. First, an initial displacement of the ocean surface is equal to the vertical displacement of the ocean floor induced by the earthquake rupture process. Second, we do not account for the finite speed of the rupture propagation along the fault and consider the ocean bottom displacement to be instantaneous.

At the end of a tsunami simulation, each of the grid points has either a value of 0 if no inundation occurs or 1 if seawater reaches the grid point at any time. The inundation line approximately follows the 0.5 contour between these 0- and 1-point values but was adjusted visually to accommodate obstacles or local variations in topography not represented by the DEM. Although the developed algorithm has passed through the rigorous benchmarking procedures (Nicolsky and others, 2011; Nicolsky, 2012), uncertainties in the location of the inundation line are still present. This uncertainty

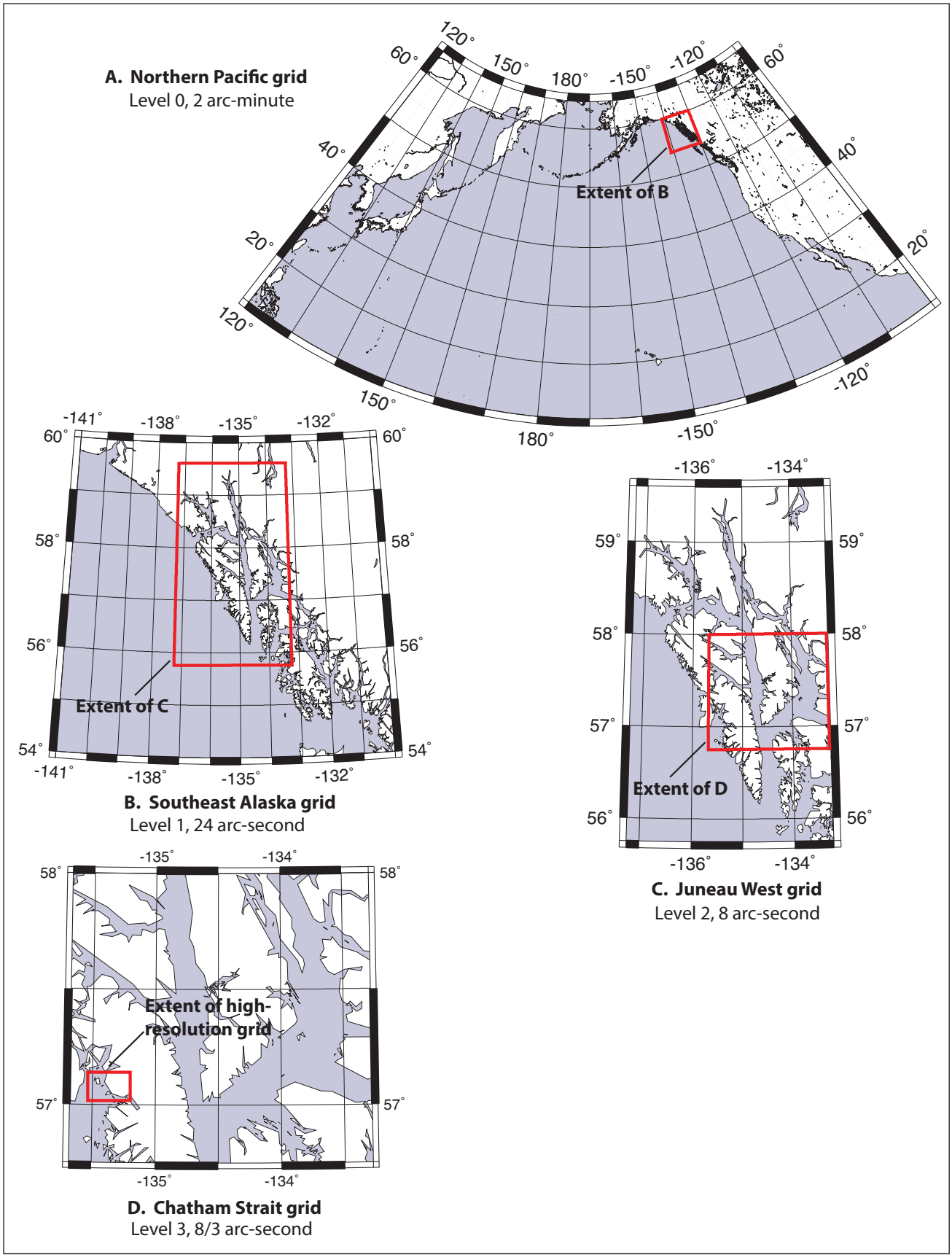

Figure 5. Telescoping embedded bathymetry/topography grids for numerical modeling of tsunami propagation and runup. The lowest resolution grid, Level 0, covers the central and northern Pacific Ocean. Location of each embedded grid is marked by a red rectangle. Refer to table 1 for grid parameters.

is difficult to quantify due to complexities in the modeling process. Many factors can affect the accuracy of the inundation line, including suitability of the earthquake source model, accuracy of the bathymetric and topographic data, and the adequacy of the numerical model in representing the generation, propagation, and run-up of tsunami waves. In this report, we do not attempt to adjust the modeled inundation limits to account for these uncertainty factors.

One of the limitations of the model is that it does not take into account the periodic change of sea level due to tides. We conducted all model runs using bathymetric data that correspond to MHHW. As a result, the elevation of the inundation line could be lower or slightly higher than that given in this report, depending on the tides at the time of a tsunami.

Historic tsunamis in Sitka

Sitka's location on the Pacific coast exposes it to tsunami waves coming from multiple directions. Table 2 summarizes the tsunami effects at Sitka from the most significant earthquakes of the last century. We have also analyzed the Sitka tidal gauge records of the most recent trans-Pacific and local tsunamis and compared them with the 1964 record (table 3).

In the following section we describe results of numerical modeling of the three historic tsunamis that affected Sitka: (a) Alaska 1964; (b) Tohoku 2011; and (c) Haida Gwaii 2012. We modeled these events for the purpose of the site-specific model verification, and to evaluate their coseismic deformation models for future use in the development of hypothetical tsunami sources. We chose the 1964 Alaska tsunami because it generated the highest recorded wave at Sitka, while the Tohoku 2011 and the Haida Gwaii 2012 events represent the far- and near-field tsunami sources, respectively, with different directional properties.

(a) Tsunami of the Great Alaska Earthquake of March 28, 1964

The analysis of recorded tsunami data shows that the only tsunami event that produced significant wave amplitudes and runup at Sitka was the tsunami of the 1964 Great Alaska Earthquake. Sitka was the only port in southeastern

Table 2. Tsunami effects at Sitka as summarized by Lander (1996).

Date	Magnitude (M_S)[a]	Origin	Max. runup (m)	Comments
11/10/1938	8.3	Alaska Peninsula	< 0.1	
04/01/1946	7.3	Eastern Aleutian Islands	0.4	
08/22/1949	8.1	British Columbia	< 0.1	
03/04/1952	8.1	Hokkaido, Japan	< 0.1	
11/04/1952	8.2	Kamchatka Peninsula	0.2	
03/09/1957	8.3	Central Aleutian Islands	0.4	
07/10/1958	7.9	Southeastern Alaska	< 0.1	
05/22/1960	8.6	Chile	0.5	
03/28/1964	8.5	Gulf of Alaska	2.4	Dock collapsed
02/04/1965	8.2	Western Aleutian Islands	< 0.1	
10/17/1966	8.0	Peru	< 0.1	
05/16/1968	7.9	Honshu, Japan	< 0.1	
07/30/1972	7.6	Southeastern Alaska	< 0.1	
02/28/1979	7.1	Gulf of Alaska	0.1	
11/30/1987	7.6	Gulf of Alaska	0.1	
07/30/1995	7.8	Chile	<0.1	

[a]M_S is lower than M_W for very large events because the M_S scale saturates at high magnitudes.

Table 3. Observed peak tsunami amplitudes at Sitka taken from the West Coast/Alaska Tsunami Warning Center catalog of recent tsunamis.

Date	Magnitude (M_w)	Origin	Peak amplitude (above state of tide in m)
03/28/1964	9.2	Gulf of Alaska	2.0
11/15/2006	8.1	Kuril Islands	0.125
01/13/2007	8.2	Kuril Islands	0.08
02/27/2010	8.8	Chile	0.21
03/11/2011	9.0	Honshu, Japan (Tohoku)	0.42
10/28/2012	7.8	Haida Gwaii, Canada	0.1
01/05/2013	7.5	Southeastern Alaska	0.07

Alaska that reported significant damage. The vessels at sea were undamaged, and most of the boats lost were tied up at docks and in small boat harbors. The total damage to docks and other harbor structures by tsunami waves was estimated at about $1 million[4]. The 1964 tsunami affected numerous communities along the Pacific Northwest coast, Hawaii, and Alaska and was studied in depth by several investigators (e.g., Plafker, 1967; Wilson and Tørum, 1968; Plafker and others, 1969). In this study, we use two coseismic deformation models of the 1964 earthquake, namely the Johnson and others (1996) and the Suleimani (2011) models, to generate the vertical displacements of the sea floor during the earthquake. We hereafter reference Johnson and others (1996) as the Johnson deformation model (JDM) and Suleimani (2011) as the Suleimani deformation model (SDM).

Simulation of the 1964 event: Source function based on coseismic deformation model by Johnson and others (1996) (JDM).

A detailed analysis of the 1964 rupture zone was presented by Johnson and others (1996) through joint inversion of tsunami and geodetic data. To derive a slip distribution, they inverted far-field tsunami waveforms from 23 tidal stations in the Pacific Ocean, and geodetic data in the form of vertical and horizontal displacements. The fault model consisted of eight subfaults representing the Kodiak Island (KI) asperity, nine subfaults in the Prince William Sound (PWS) asperity, and one subfault representing the Patton Bay fault, one of the two megathrust splay faults that ruptured during the earthquake (Plafker, 1967). The contribution of the Patton Bay fault to the far-field tsunami waveform was negligible. The inversion results indicated two regions of high slip corresponding to areas of high moment release derived by Christensen and Beck (1994) from long-period P-wave seismograms: the Prince William Sound asperity with an average slip of 18 m (59 ft), and the Kodiak asperity with an average slip of 10 m (33 ft). The fault parameters required to compute sea floor deformation are the epicenter location, rupture area, dip, rake, strike, and amount of slip on the fault. We use the equations of Okada (1985) to calculate the distribution of coseismic uplift and subsidence resulting from this slip distribution. This source function was previously applied to calculation of the 1964 tsunami inundation in Kodiak and Kachemak Bay communities. The results are described in Suleimani and others (2002, 2003, 2005). The coseismic vertical deformation resulting from the JDM is shown in figure 6a.

Simulation of the 1964 event: Source function based on coseismic deformation model by Suleimani (2011) (SDM).

This newly revised coseismic slip distribution of the 1964 rupture is based on a model of Suito and Freymueller (2009), which was developed as a 3-D viscoelastic model in combination with an afterslip model, using realistic geometry with a shallow-dipping elastic slab to describe the postseismic deformation that followed the 1964 earthquake. The authors used the inversion-based model by Johnson and others (1996) as a basis for their coseismic slip model, adjusting it to the new geometry and critically reinterpreting the coseismic data. Suleimani (2011) used results of the near-field modeling of the 1964 tsunami to constrain the amount of slip placed on intraplate splay faults, and to evaluate the extent of the Patton Bay fault. The revised model included contribution of coseismic horizontal displacements into the initial tsunami wave field through the component of the ocean surface uplift due to horizontal motion of the steep ocean bottom slopes. The tsunami simulations revealed that including deformation due to horizontal displacements in the source function resulted in an increase of far-field tsunami amplitudes. The coseismic vertical deformation resulting from the SDM is shown in figure 6(b).

Figure 7 shows a comparison of the tsunami wave recorded by the Sitka tidal station on March 28, 1964, with the predictions of the AEIC tsunami model (see page 6) (Nicolsky and others, 2011; Nicolsky, 2012) that employs the two source functions of the 1964 earthquake described above, the JDM and the SDM. Despite differences in the coseismic deformation pattern (fig. 6), both models provide good agreement with the observed wave phase for up to 8 hours of wave propagation, and also a good fit to the wave amplitudes recorded by the Sitka tidal station.

(b) The Tohoku tsunami of March 11, 2011

The catastrophic Tohoku tsunami of March 11, 2011, produced a small wave in Sitka, with the maximum recorded wave amplitude of 42 cm (16.5 in). The tsunami source function that represents the slip distribution of the 2011 Tohoku earthquake was provided by Shengji Wei of Caltech Tectonic Observatory (http://www.tectonics.caltech.edu/). We calculated vertical coseismic deformation resulting from the given slip model using the equations of Okada (1985). The resulting tsunami source function is shown in figure 8. Figure 9 shows a comparison between the observed wave history at Sitka as recorded by the Sitka tidal station, and the calculated time series at the same location. The plot illustrates that the far-field Tohoku tsunami did not produce a significant wave at Sitka due to directivity of the tsunami source (waves directed primarily to the northwest and southeast) and the resulting energy propagation patterns (Tang and others, 2012).

(c) The Haida Gwaii tsunami of October 28, 2012

The Haida Gwaii earthquake of October 28, 2012, generated a tsunami that was recorded at the Sitka tide gauge as well as at a number of tide stations along the west coast of the U.S. The tsunami produced significant local runup (> 7 m in places) along the west coast of Haida Gwaii (James and others, 2013). We obtained three source models of this

[4]$1 in 1964 had about the same buying power as $7.49 in 2013.

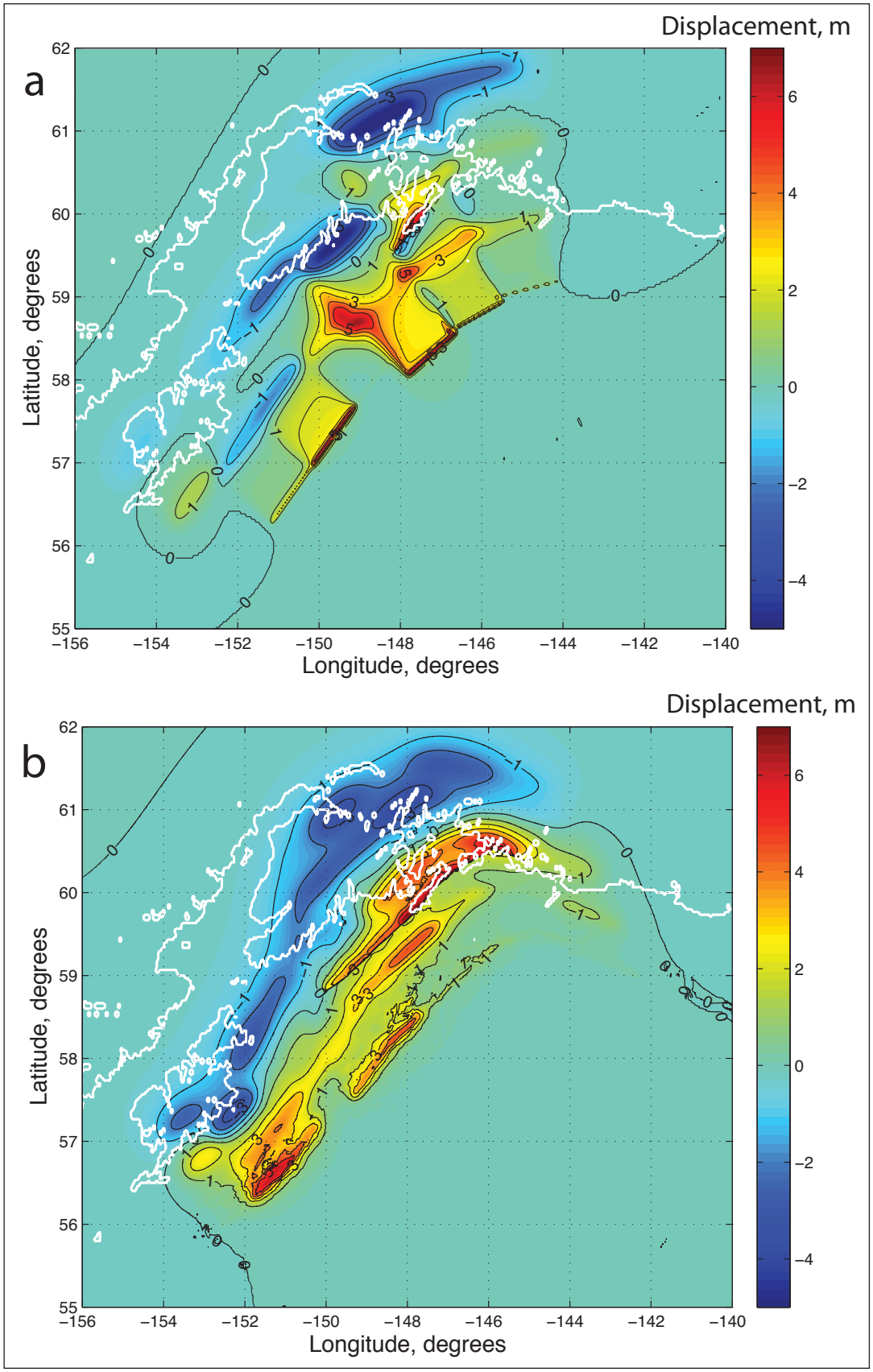

Figure 6. Vertical coseismic deformation for (a) Johnson and (b) Suleimani deformation models.

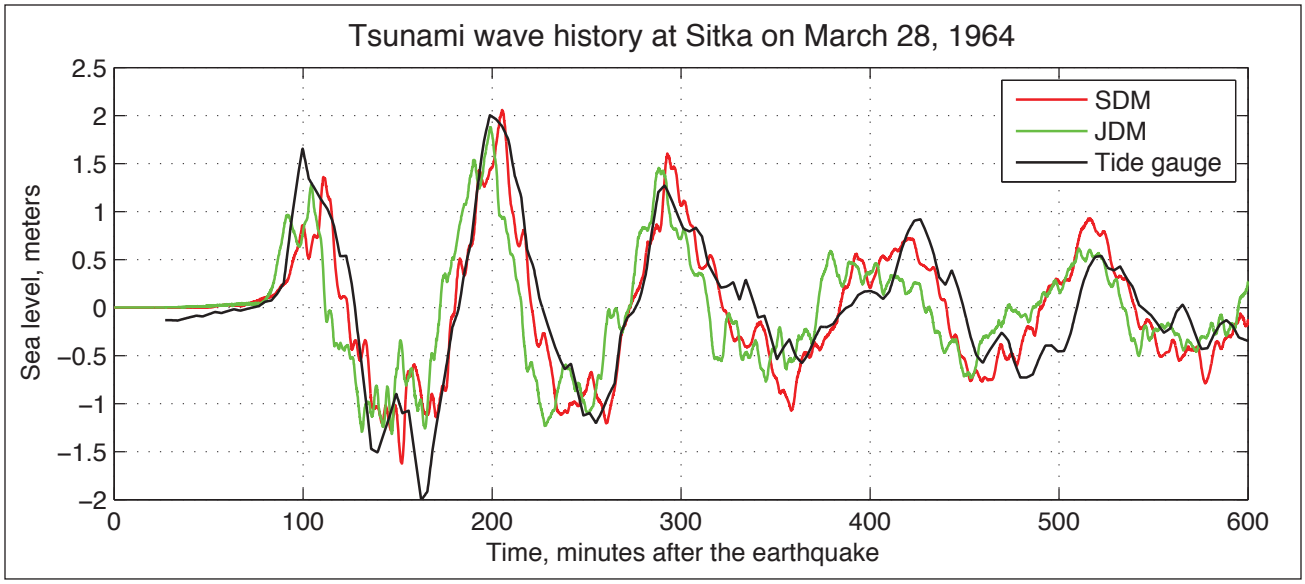

Figure 7. Recorded sea level at Sitka during tsunami generated by the 1964 Great Alaska Earthquake, and the calculated time series for two different source functions of the 1964 tsunami, Johnson Deformation Model (JDM) and Suleimani Deformation Model (SDM).

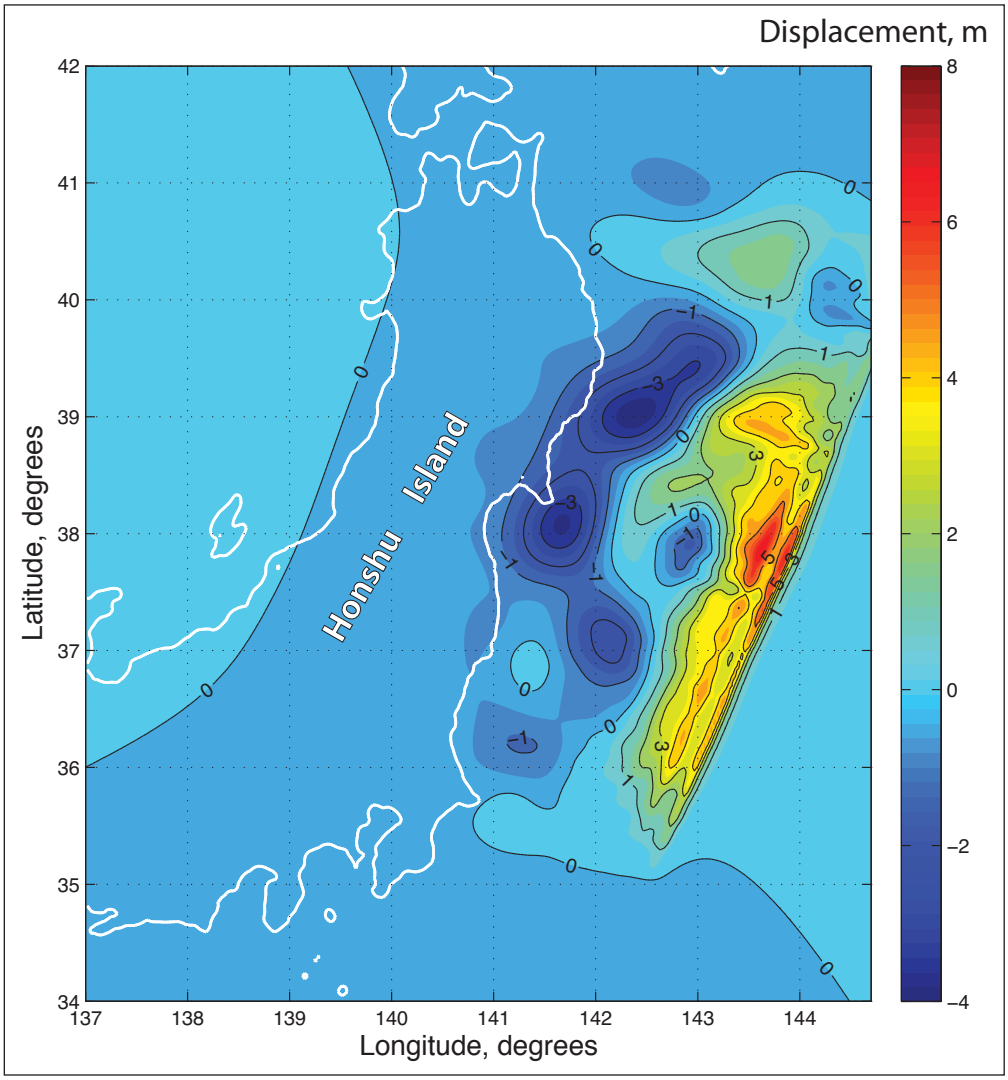

Figure 8. Vertical co-seismic deformation for the source model of the 2011 Tohoku tsunami.

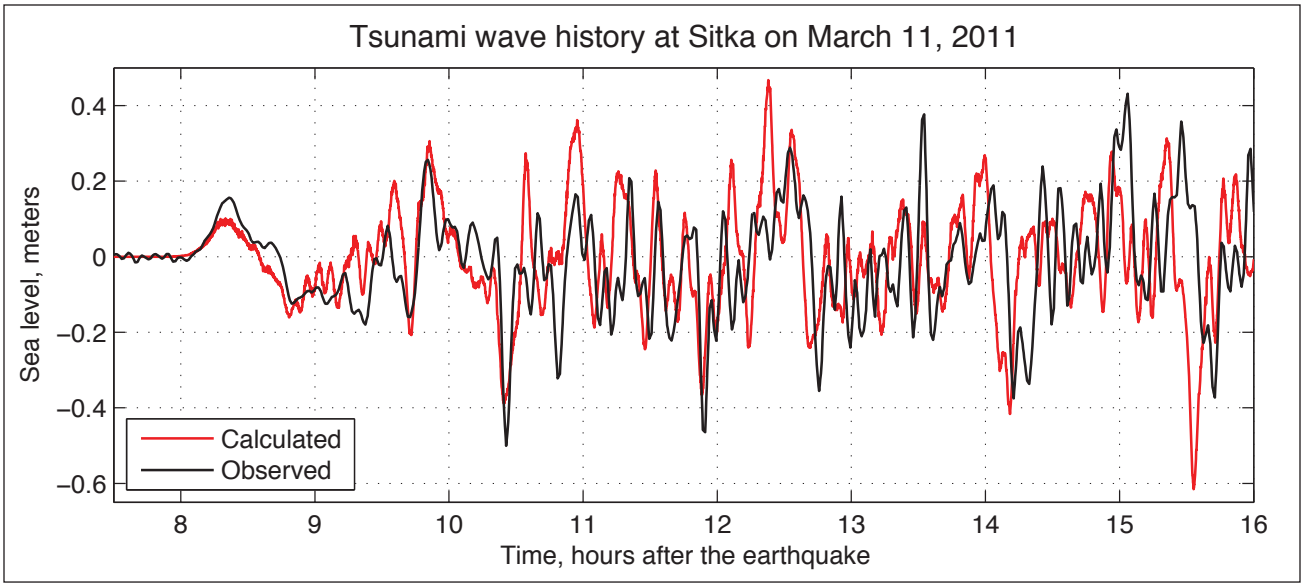

Figure 9. Recorded sea level at Sitka during the 2011 Tohoku tsunami, compared with the time series calculated for the source function shown in figure 8.

event that were based on seismic waveform inversion of the slip distribution: the Caltech source (http://www.tectonics.caltech.edu/), the USGS source (http://earthquake.usgs.gov/), and the source function by Chen Ji (http://www.geol.ucsb.edu/faculty/ji/big_earthquakes/2012/10/canada.html). These three source functions are shown in figures 10, a–c, respectively. We simulated the tsunami wave history at the point that corresponds to the location of the Sitka tidal station using our validated tsunami model (Nicolsky and others, 2011; Nicolsky, 2012). Figure 11 demonstrates a comparison between the recorded wave and the simulated time history corresponding to the three source functions. The time series point was located in the Sitka numerical grid of 15-m resolution. The simulated time series demonstrates that the model by Chen Ji provides the best fit to the amplitudes of the recorded wave at Sitka for up to 2.5 hours after the arrival of the first wave. All three models provide a good fit to the wave phases of oscillations recorded by the Sitka tidal station (fig. A-1a) for the first 2 hours. We use the source mechanism of the Haida Gwaii earthquake as a basis for the hypothetical near-field tsunami source in the area of Haida Gwaii (scenario 9).

Numerical modeling of three historic tsunamis at Sitka demonstrates that the employed numerical model of tsunami propagation and runup generates tsunami waveforms that are in good agreement with the observed arrival times and wave phases. The model also provides a good fit to the recorded tsunami amplitudes at Sitka, which indicates that the proposed coseismic deformation models for the three historic earthquakes adequately describe the coseismic slip distribution.

Hypothetical tectonic tsunami sources

Based on the analysis of historic tsunamis that affected Sitka, we consider several tectonic tsunami sources for the construction of the tsunami hazard map for the Sitka area. Taking into account the directional properties of a tsunami source and previous studies of the far-field effects of the 1964 tsunami (Myers and Baptista, 2001; Suleimani, 2011), we conclude that the section of the Aleutian megathrust that includes the Alaska Peninsula, Kodiak Island, and Prince William Sound (fig. 12) is the area best positioned to generate a tsunami wave that will significantly affect Sitka.

Table 2 shows that tsunami effects at Sitka due to long-distance historic events are minor. Tang and others (2012) performed a detailed study of the energy distribution during the 2011 Tohoku tsunami and concluded that the propagated energy and the location of the tsunami source are the most important source parameters for predicting tsunami impacts. The energy flux is redirected by the seafloor topography, resulting in tsunami impacts of very different levels of severity along a relatively short section of the coastline, compared with the distance from the tsunami source. For example, neither the 2006 Kuril Islands tsunami, nor the devastating 2011 Tohoku tsunami generated any wave damage at Sitka, while both events resulted in significant damage, high wave amplitudes, and strong currents in the harbor at Crescent City, California (Dengler and others, 2009; Wilson and others, 2011). To assess a potential tsunami impact on Sitka from a far-field tectonic scenario, we considered multiple segments of subduction zones around the Pacific Ocean that could potentially generate a trans-oceanic tsunami with an impact on Sitka. The tsunami sources included segments of the Kuril–Kamchatka and the Yap–Marianas–Izu Bonin subduction zones (Gica and others, 2008) that have the appropriate directional properties with respect to the coast of southeastern Alaska. Numerical experiments demonstrated that none of these hypothetical far-field tsunami sources resulted in a sizable wave at Sitka, therefore we did not include these sources in the final list of scenarios (table 4).

To construct regional tsunami scenarios for Sitka, we analyzed historic events along the Fairweather–Queen Charlotte

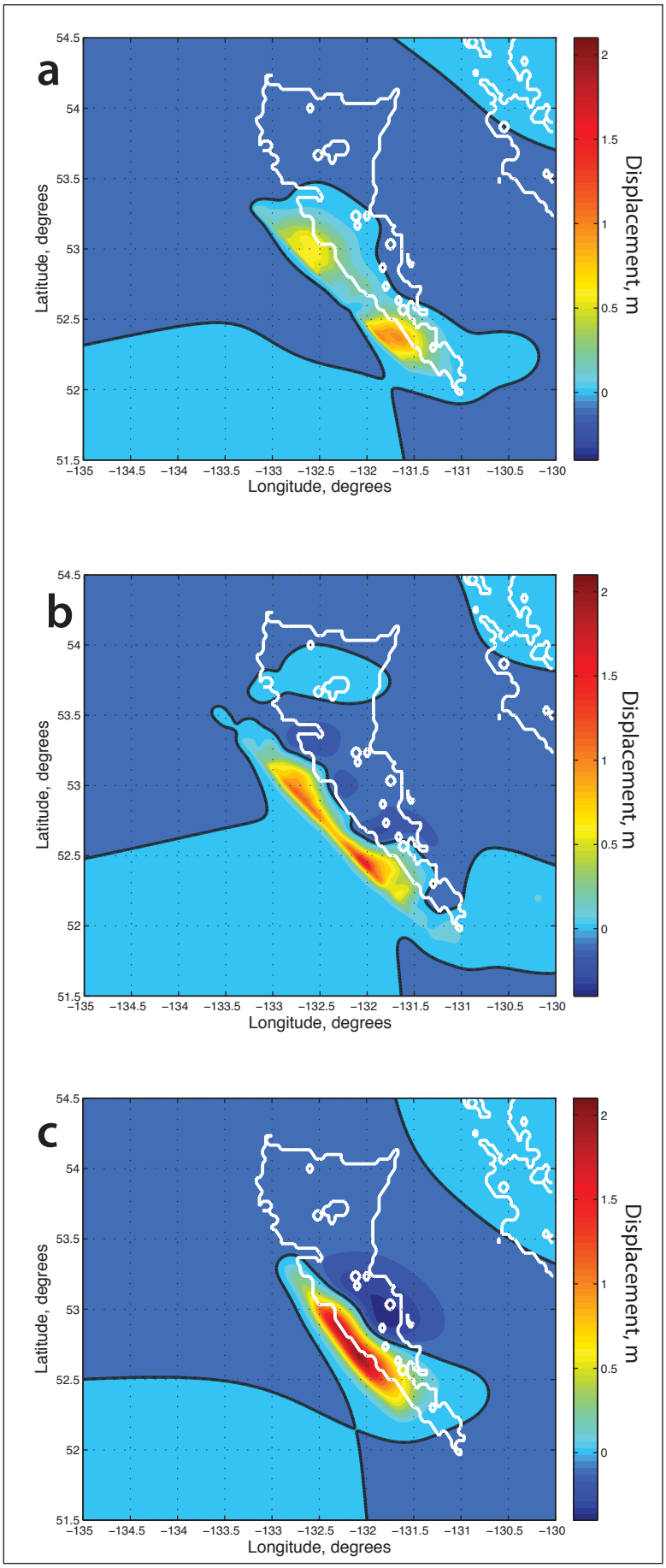

Figure 10. Vertical coseismic deformation patterns corresponding to three different slip models of the October 28, 2012, Haida Gwaii earthquake.

a. 10/28/12 Haida Gwaii deformation model by Caltech.

b. 10/28/12 Haida Gwaii deformation model by U.S. Geological Survey.

c. 10/28/12 Haida Gwaii deformation model by Chen Ji.

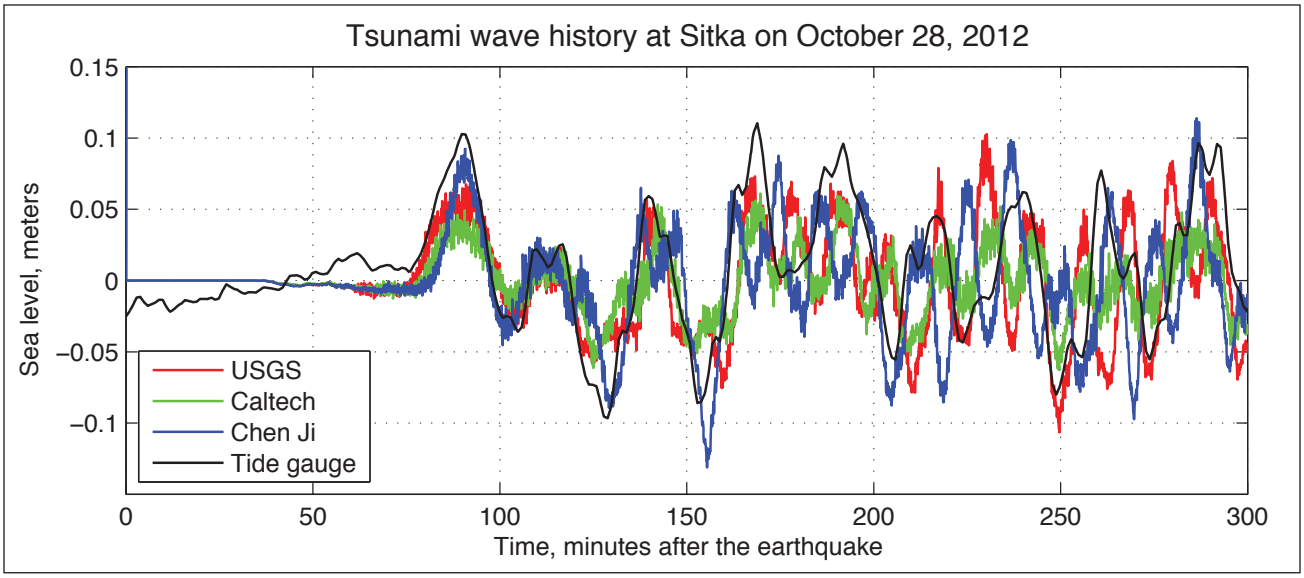

Figure 11. Recorded sea level at Sitka during the 2012 Haida Gwaii tsunami, compared with the time series calculated for three source functions shown in figure 10.

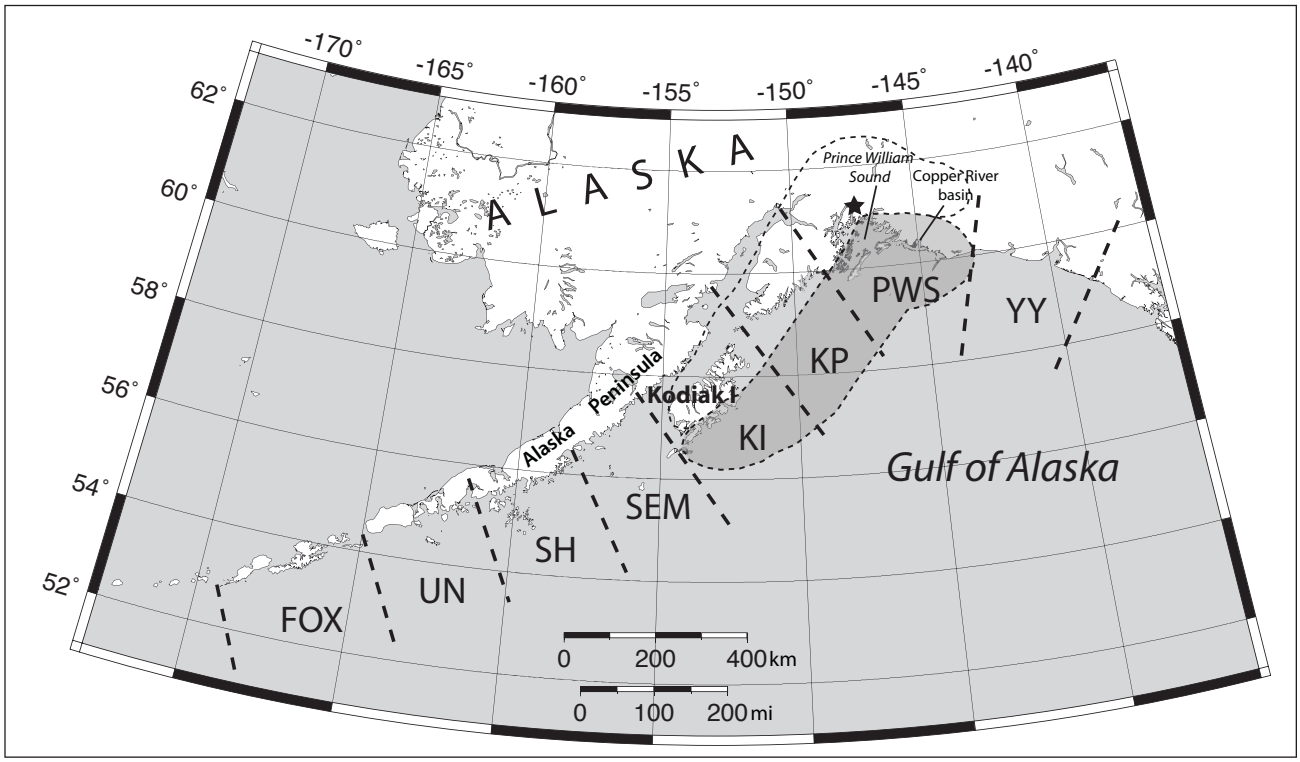

Figure 12. Map of Alaska with rupture zone of the 1964 Great Alaska Earthquake and segments of the Alaska–Aleutian megathrust: the Yakataga–Yakutat (YY), Prince William Sound (PWS), Kenai Peninsula (KP), Kodiak Island (KI), Semidi Islands (SEM), Shumagin Islands (SH), Unimak Island (UN), and the Fox Islands (FOX) segments. The star indicates the epicenter of the 1964 earthquake. The dashed contour delineates regions of coseismic uplift (shaded) and subsidence above the 1964 rupture area (Plafker, 1969).

Table 4. All hypothetical scenarios used to model tsunami runup in Sitka.

Scenario 1	*Multi-Segment event based on the JDM (PWS, KP, KI, and YY segments)*
Scenario 2	*Multi-Segment event based on the SDM (PWS, KP, KI, and YY segments)*
Scenario 3	*Modified multi-segment event: rupture of the PWS, KP, and YY segments of the JDM*
Scenario 4	*Modified multi-segment event: rupture of the PWS, KP, and YY segments of the SDM*
Scenario 5	*Multi-Segment event: the Tohoku-type rupture of the PWS, KP and KI segments*
Scenario 6	*The SAFRR tsunami scenario (SEM and SH segments)*
Scenario 7	*Rupture in the Eastern Aleutians, from Semidi Islands to Fox Islands (SEM, SH, UN and FOX segments)*
Scenario 8	*Rupture on the Cascadia subduction zone*
Scenario 9	*M_w8.2 thrust earthquake in the Haida Gwaii area*

fault system (fig. 4). Another hypothetical tsunamigenic earthquake worth considering is rupture of the Cascadia subduction zone, involving subduction of the Juan de Fuca plate beneath the North America plate along the Pacific Northwest coast (from Vancouver Island, British Columbia, to California).

In modeling the considered tsunami sources, we assume that the initial displacement of the ocean surface is equal to the vertical displacement of the ocean floor induced by the earthquake rupture process. We do not account for the finite speed of the rupture propagation along the fault and consider the ocean bottom displacement to be instantaneous.

For the purpose of constructing tsunami source scenarios that span from south-central Alaska to the eastern Aleutians, we follow the notations of Nishenko and Jacob (1990) for the segments of the megathrust that have been repeatedly ruptured by large and great earthquakes, or for gaps between the rupture segments: Yakataga–Yakutat (YY), Prince William Sound (PWS), Kenai Peninsula (KP), Kodiak Island (KI), Semidi Islands (SEM), Shumagin Islands (SH), Unimak Island (UN), and Fox Island (FOX) segments (fig. 12).

We describe below all tectonic tsunami sources that were used to calculate propagation and runup of tsunami waves at Sitka and then included in calculation of the composite extent of inundation and the composite distribution of flow depths. The coseismic deformation pattern for each scenario is shown in figure 13, and table 4 provides a summary of all scenarios.

(a) Models of a hypothetical earthquake in the rupture area of the 1964 Great Alaska Earthquake

The rupture area of the 1964 earthquake is at the eastern end of the Aleutian megathrust (fig. 12). Although the PWS, KP, and KI segments ruptured together during the 1964 earthquake, they have different earthquake histories. As summarized by Nishenko and Jacob (1990) and Carver and Plafker (2008), the KI segment has produced large and great earthquakes independently of the PWS and KP segments, with the recurrence interval for the Kodiak asperity estimated as low as 60 years, while that for the PWS–KP asperity appears to be several hundred to 900 years.

The YY segment, at the eastern end of the megathrust, represents a complex collision zone where the Yakutat microplate moves northwest toward central Alaska at 48 mm (1.9 in) per year (Carver and Plafker, 2008). This segment lies within a transition from predominantly strike-slip motion to the east and southeast to shallow-dipping subduction to the west (Nishenko and Jacob, 1990). The interaction between the Yakutat block and the Pacific and North American plates is complex and not well characterized.

Shennan and others (2009) tested the hypothesis that in some seismic cycles megathrust segments can combine, as proposed in the segmentation model by Nishenko and Jacob (1990), and produce earthquakes larger than historical earthquakes. The authors present paleoseismic evidence that earthquakes 900 and 1,500 years B.P. ruptured three segments of the Aleutian megathrust (the PWS, KP, and KI segments) in addition to an eastward extension of the PWS segment that involved the western margin of the Yakutat microplate. Shennan and others (2009) suggested that an increase in seismic moment is less significant in terms of tsunami hazard than an increase in tsunami generation area of this multi-segment rupture, due to coseismic uplift over a large segment of the shallow continental shelf off the Yakataga coast. To model inundation at Sitka from this potential event, we applied the following constraints based on the hypothetical earthquake model of Shennan and others (2009). The extended source function includes four segments of the Aleutian megathrust: the PWS, KP, KI, and YY segments. The total seismic moment is about 15 percent greater than that of the 1964 earthquake. The new source function produces coseismic vertical uplifts along the Gulf of Alaska coastline segment between the Copper River basin and Yakataga area, in order to match the coseismic deformation pattern with the paleoseismic data (Shennan and others, 2009).

To construct a rupture model for the YY segment, we assume four subfaults whose parameters are listed in table 5. We calculate coseismic deformations produced by this segment using the Okada algorithm (Okada, 1985), and then combine them with the 1964 coseismic deformations produced either by the JDM (scenario 1) or by the SDM (scenario 2).

Scenario 1. *Multi-Segment JDM event: Source function based on extension of the JDM.*

The JDM (segments KI, KP, and PWS) is extended by including coseismic deformation for the YY segment.

Scenario 2. *Multi-Segment SDM event: Source function based on extension of the SDM.*

The SDM (segments KI, KP, and PWS) is extended by including coseismic deformation for the YY segment.

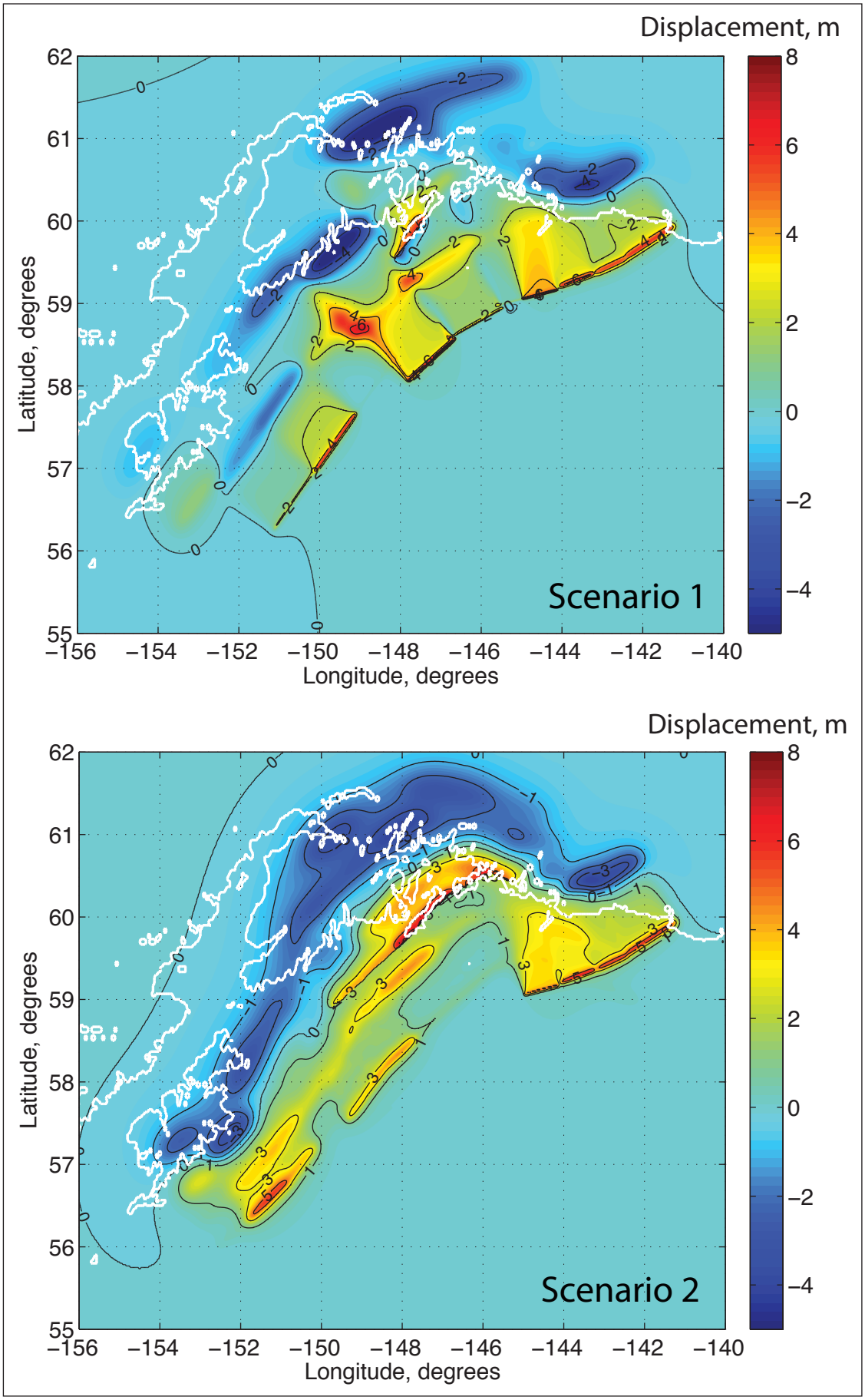

Figure 13. Vertical coseismic deformations corresponding to scenarios 1–9.

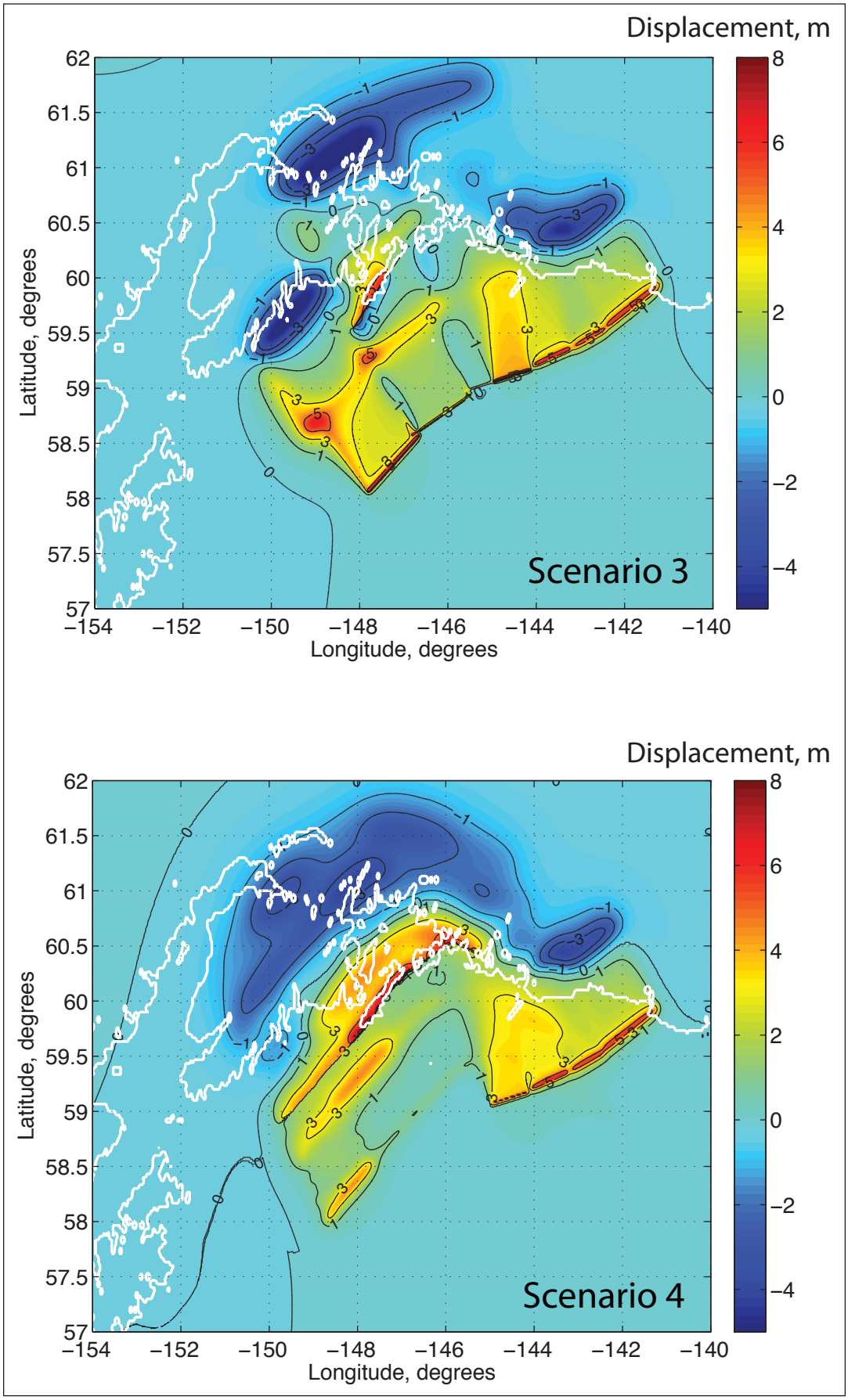

Figure 13 (cont'd). Vertical coseismic deformations corresponding to scenarios 1–9.

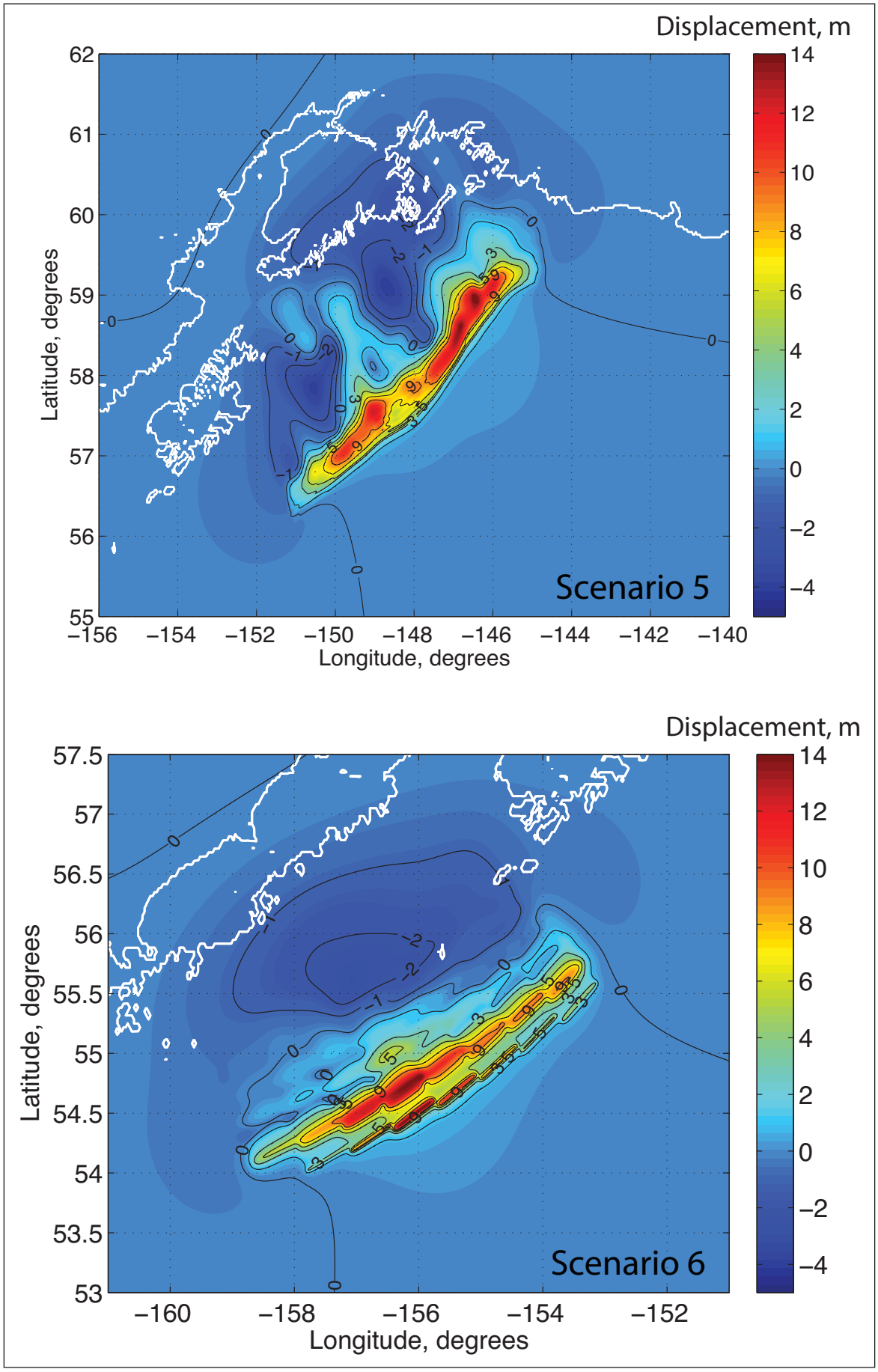

Figure 13 (cont'd). Vertical coseismic deformations corresponding to scenarios 1–9.

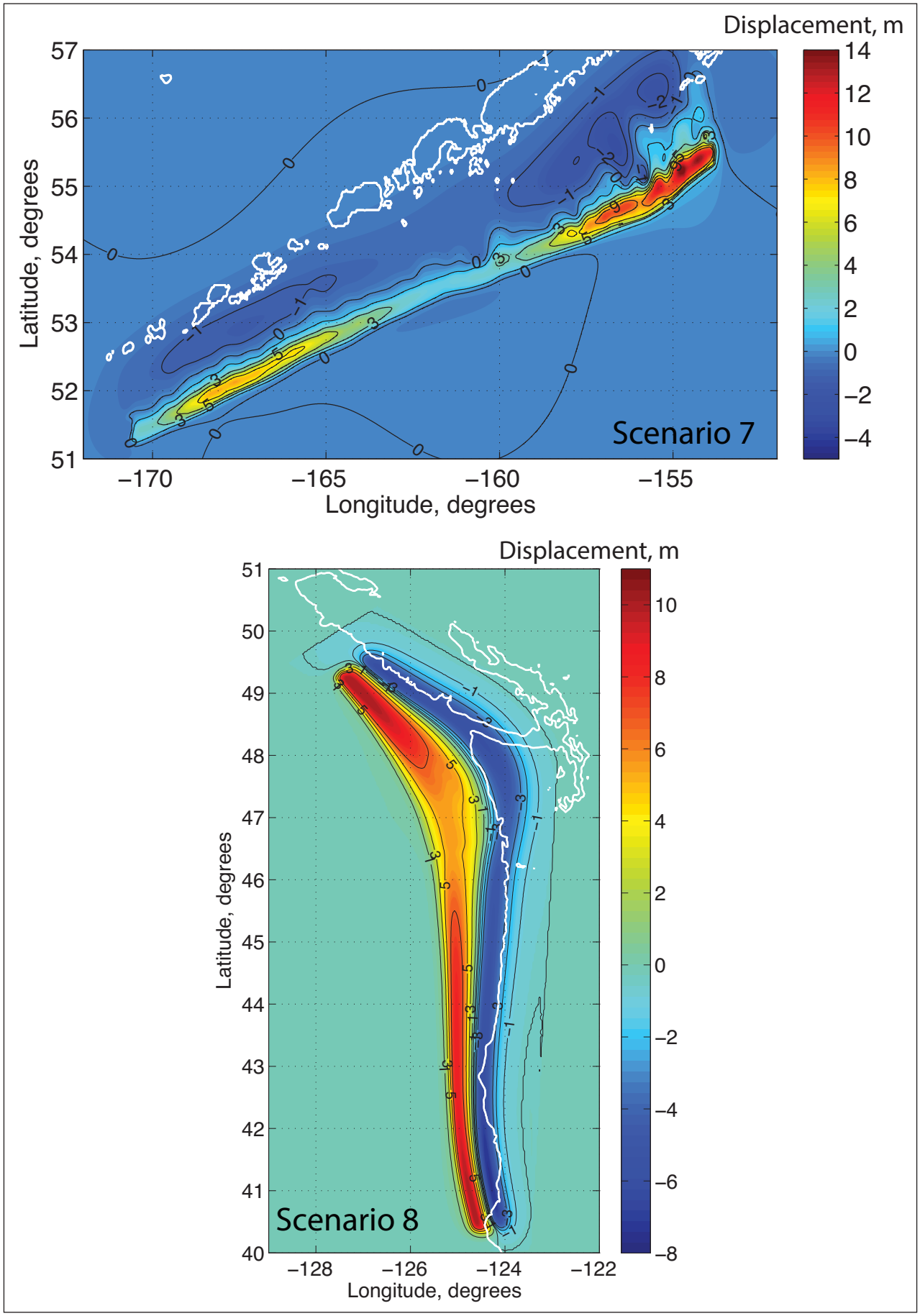

Figure 13 (cont'd). Vertical coseismic deformations corresponding to scenarios 1–9.

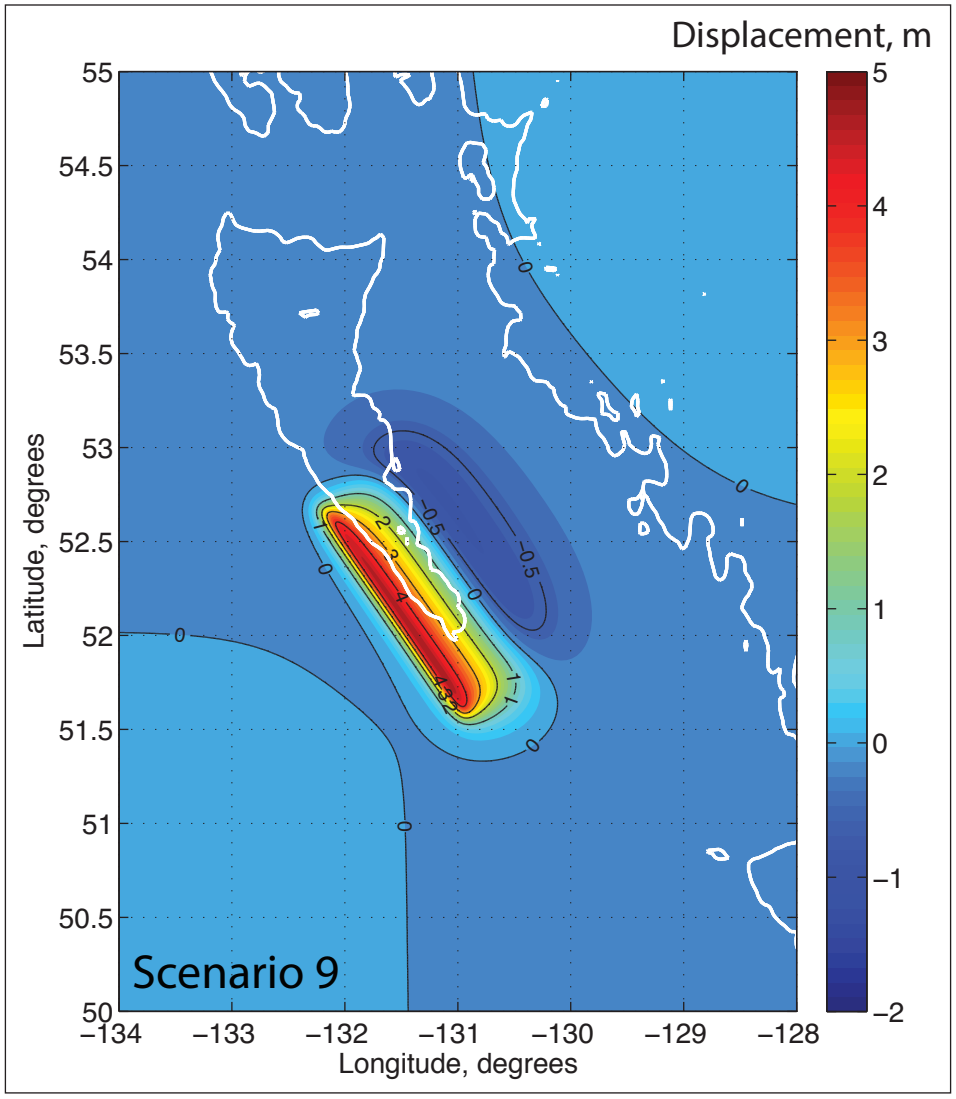

Figure 13 (cont'd). Vertical coseismic deformations corresponding to scenarios 1–9.

Scenario 3. *Multi-Segment JDM event: The PWS and KP segments of the 1964 rupture, and the YY segment.*
The model includes the coseismic deformations in the PWS and KP segments of the 1964 rupture as defined in the JDM, and deformations in the YY segment.

Scenario 4. *Multi-Segment SDM event: The PWS and KP segments of the 1964 rupture, and the YY segment.*
The model includes the coseismic deformations in the PWS and KP segments of the 1964 rupture as defined in the SDM, and deformations in the YY segment.

Scenario 5. *Multi-Segment event: The PWS, KP and KI segments with Tohoku-type slip distribution in the down-dip direction.*

We used a recently published model of global subduction zone geometries, called Slab 1.0 (Hayes and others, 2012), to construct hypothetical tsunami sources along the eastern end of the Aleutian megathrust (fig. 12). In the Slab 1.0 model, the plate interface is defined by the slab surface isodepth contours with a contour interval of about 2 km. We discretized the interface into subfaults with the down-dip dimension equal to the contour interval, and with the along-strike dimension ranging from about 4 to 6 km (~2.5 to ~3.7 mi). We chose to discretize the interface with rectangular subfaults, since coseismic deformations are calculated using Okada's formulas (Okada, 1985) that require rectangular fault geometry. The resulting high-resolution mosaic allows for prescribing fine variations of slip in both down-dip and along-strike directions. We constructed four hypothetical tsunami sources using the discretized interface for the section of the megathrust between the PWS and SH segments (fig. 12). The four sources included the following segments: (a) PWS–KP–KI, (b) KP–KI, (c) KP–KI–SEM, and (d) KI–SEM–SH. Figure 14 shows sections of the discretized interface overlaid with the slip distribution pattern, which is identical for all four sources. The slip is distributed almost uniformly along the strike,

Table 5. Fault parameters for the Yakataga–Yakutat segment

Lat [deg. N]	Lon [deg. W]	Depth[a] [km]	Length [km]	Width [km]	Strike [deg.]	Dip [deg.]	Rake [deg.]	Slip [m]
59.17	144.12	1	50.1	190	256	12	90	15
59.36	143.23	3	51.1	141	250.4	10	90	15
59.54	142.42	5	47.8	114.8	245.8	6	90	15
59.94	141.21	5	79.7	99.6	237.8	8	90	15

[a]Depth is to the top of the subfault plane.

except for the edges of the ruptures, where slip tapers. As for the down-dip direction, we assume the concentration of higher slip closer to the shallow part of the rupture, similar to that in the Tohoku 2011 earthquake. During that event, unexpectedly large displacements were recorded up-dip of the epicenter of the main shock, based on seafloor GPS and seafloor pressure gauge observations, suggesting up to 80 m (262 ft) of coseismic slip beneath the frontal wedge on the plate boundary (Ito and others, 2011).

We conducted a numerical experiment to select the hypothetical source that produces the highest tsunami amplitudes and runup values at Sitka. All sources had the same seismic moment that corresponds to a M_W9.2 rupture. Using the Okada algorithm, we calculated vertical coseismic displacements for each source, and modeled tsunami wave propagation and runup at Sitka. The simulated maximum wave amplitudes at the Sitka Harbor for the sources described above (a-d) are 2.8 m, 2.4 m, 2.3 m and 1.9 m, respectively. The PWS-KP-KI source generated the largest tsunami effects at Sitka and was chosen as scenario 5.

(b) Source models of hypothetical tsunamigenic earthquakes in the Alaska Peninsula segment of the Alaska-Aleutian subduction zone.

Scenario 6. *The SAFRR Tsunami Scenario: Segments SH and SEM.*

The USGS Science Application for Risk Reduction (SAFRR) project, in collaboration with NOAA and State of California agencies, has developed a plausible hypothetical tsunami scenario to describe the impacts of a tsunami generated by an earthquake in the Alaska Peninsula region (Ross and others, 2012). The USGS Tsunami Source Working Group defined the scenario source as a M9.0 earthquake similar to the Tohoku 2011 event, but located between the Shumagin Islands and Kodiak Island, in the SH and SEM segments of the megathrust (fig. 12). The rupture area, represented by 56 subfaults, is about 350×200 km (217×124 mi), with an average slip of 15.7 m (51.5 ft) and a maximum slip of 75 m (246 ft). The concentration of higher slip closer to the trench was adopted for the SAFRR scenario following the derived slip distributions for the Tohoku earthquake.

Scenario 7. *Multi-Segment event: SEM, SH, UN, and FOX segments.*

This scenario is based on the slip model of a hypothetical earthquake that incorporates the entire rupture areas of the 1788, 1938, and 1946 events as well as the eastern end of the 1957 rupture zone (Ryan and others, 2010). The authors proposed a great earthquake of M_W~9.0 that ruptures most of the eastern Aleutian megathrust, noting that in order to generate an earthquake of this magnitude in the eastern Aleutians, it is necessary to rupture through multiple segments of the megathrust, including sections that may be weakly coupled. The authors also chose these particular sections of the megathrust because of the absence of any tectonic features that might work as barriers to the rupture. Figure 15 shows the discretized Slab 1.0 interface (Hayes and others, 2012) in the area of the proposed source, overlaid with the slip distribution pattern. The largest amount of slip is placed at the eastern end, which is a nearly fully locked segment of the megathrust beneath the Semidi Islands, based on the GPS studies by Freymueller and others (2008). We assign a much smaller amount of slip to the middle part of the rupture, where coupling of the plate interface changes from about 30 percent locked at the Shumagin Islands to freely slipping west of the Shumagins (Fournier and Freymueller, 2007). The amount of slip increases again at the western end of the rupture, where little moment was released in 1957. This scenario is similar to the 1957 event that ruptured a long section of the megathrust with highly variable slip along strike (Johnson and others, 1994). The moment magnitude for this hypothetical event is 9.2.

(c) Model of the Cascadia Subduction Zone Earthquake

Paleoseismic records reveal that great tsunamigenic earthquakes repeatedly occur on the Cascadia subduction zone with irregular intervals averaging about 500 years (Atwater and others, 2004). The latest trans-Pacific tsunami generated by an earthquake at Cascadia occurred in January 1700 (Satake and others, 1996; Atwater and others, 2005). The impact of this tsunami on Alaska coastal communities was not documented, likely due to low population density along the Alaska coast at that time. Multiple models of Cascadia subduction zone ruptures are presented by Satake and others (2003) and Priest and others (2009), and by references therein. These models describe hypothetical coseismic displacement fields with various levels of detail. Because a Cascadia subduction zone earthquake is considered to be a medium-field tsunami source to the southeastern Alaska coast, a relatively simple "worst-case credible" rupture of the Cascadia subduction zone is used in this report.

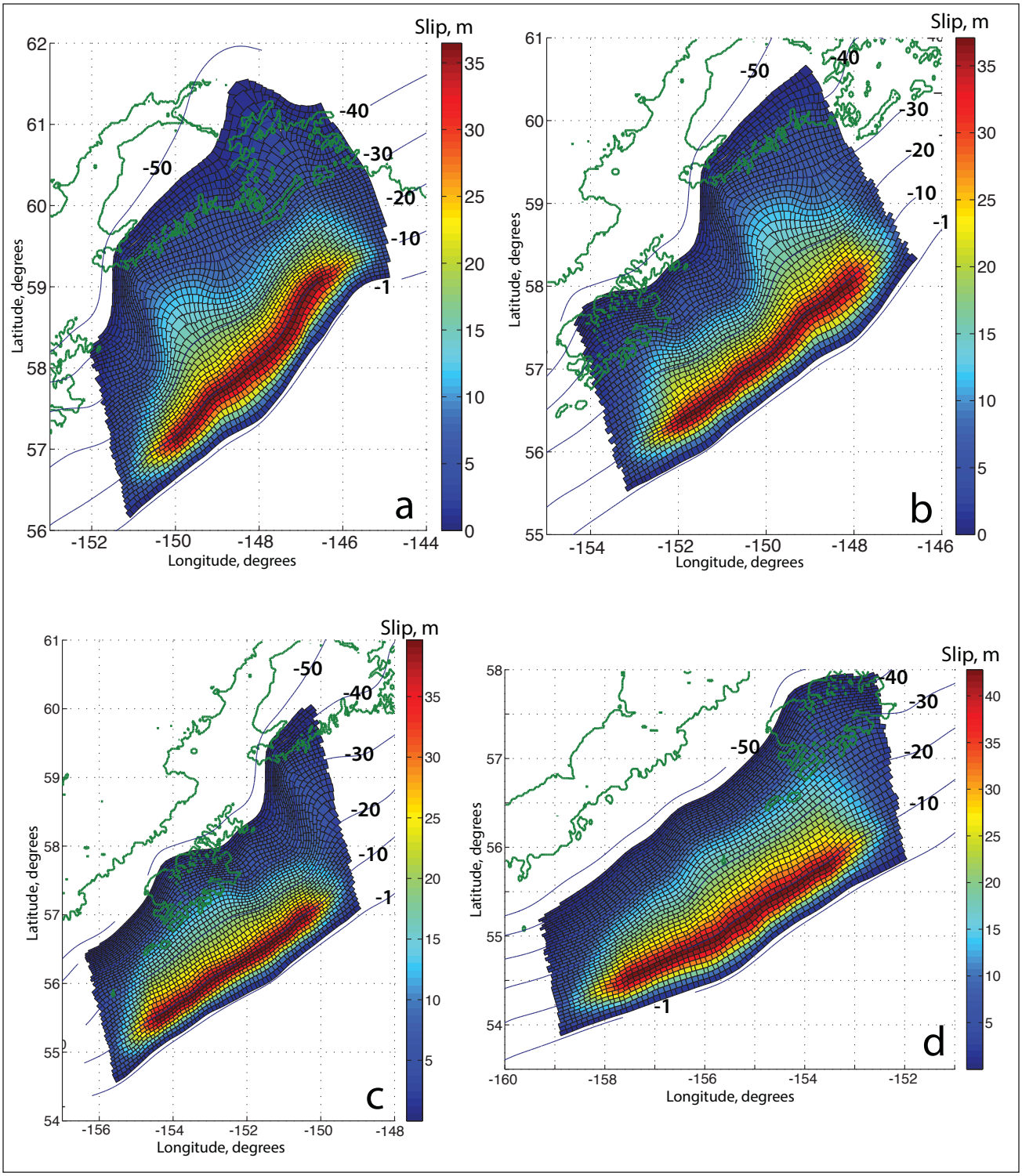

Figure 14. Sections of the eastern Aleutian megathrust interface discretized using the Slab 1.0 model. The four sources correspond to the following combinations of segments shown in figure 12: (a) PWS–KP–KI, (b) KP–KI, (c) KP–KI–SEM, and (d) KI–SEM–SH. The interface mosaic is overlaid with the slip distribution patterns. Green contour is the shoreline, and blue labeled contours show depth in km to the plate interface.

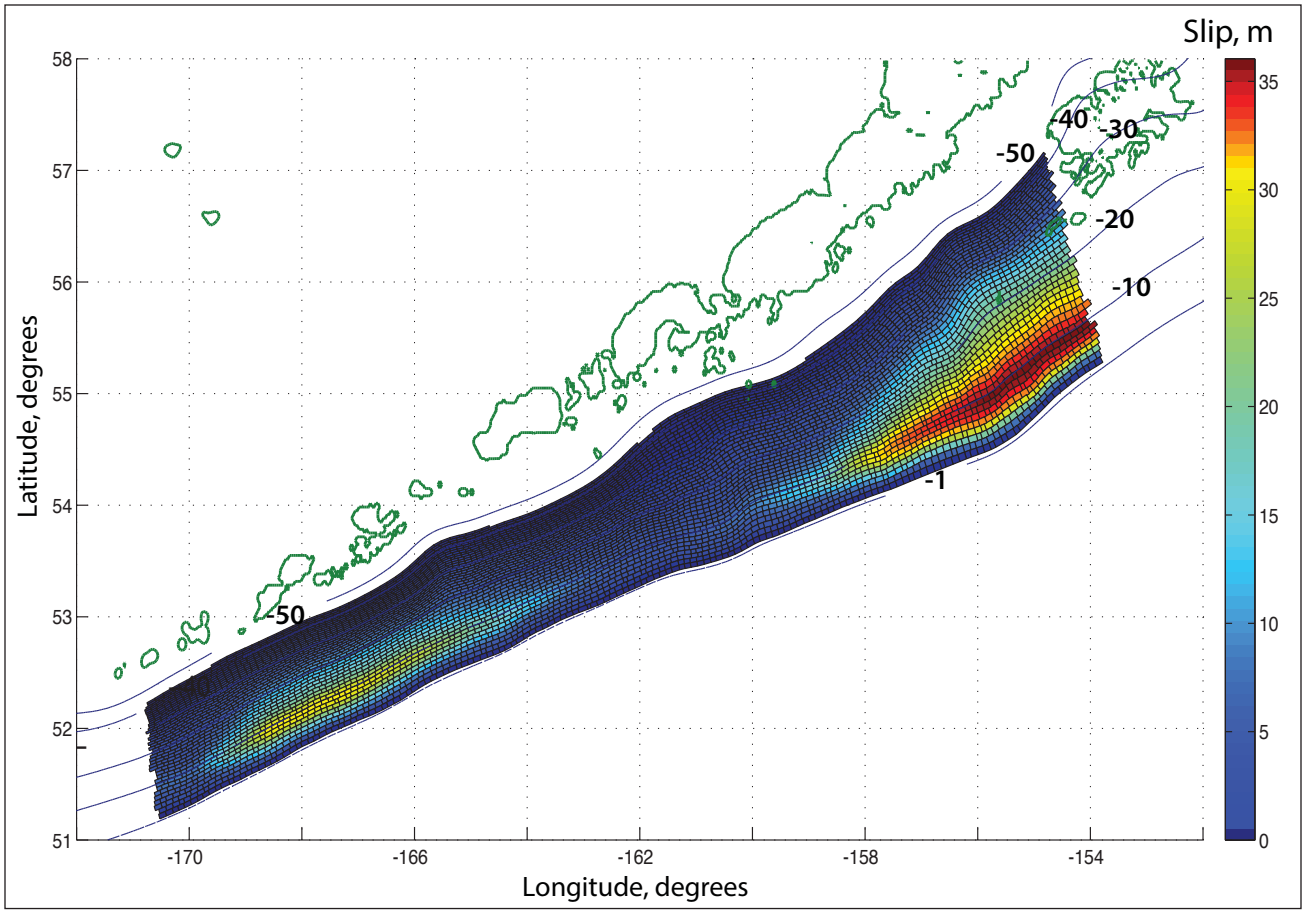

Figure 15. Segment of the Aleutian megathrust interface between Kodiak Island and Yunaska Island, discretized using the Slab 1.0 model. The interface mosaic is overlaid with the slip distribution pattern. Green contour is the shoreline, and blue labeled contours show depth in km to the plate interface.

Scenario 8. *Rupture of the Cascadia subduction zone, including portions of the margin along the British Columbia, Washington, Oregon, and northern California shore.*

Wang and others (2003) concluded that the down-dip limit of the rupture in the 1700 Cascadia earthquake could not be constrained using the tsunami heights in Japanese historical records. The authors suggested a conservative approach for Cascadia coseismic deformation assuming that full coseismic rupture takes place over the entire locked zone and that slip decreases linearly down-dip to zero halfway into the present effective transition zone. The most recently updated and probably more reasonable model assumes that the slip distribution in the down-dip direction is bell-shaped (Witter and others, 2011). In this report, the assumed M_W9 rupture (fig. 13) recovers 1,200 years' worth of plate convergence with about 36 m (118 ft) of maximum slip (Witter and others, 2011).

d) Source model of a hypothetical tsunamigenic earthquake in the Haida Gwaii area

Scenario 9. *A hypothetical earthquake in the Haida Gwaii area.*

Following the proposed underthrusting model of the oblique convergence across the Queen Charlotte fault (Bustin and others, 2007), and the source mechanism of the recent M_W7.8 Haida Gwaii earthquake of October 28, 2012, we assume a hypothetical rupture in the southern part of the Haida Gwaii on a 150-km-long (93-mi-long) subduction fault plane dipping at 28°, with a strike equal to that of the Queen Charlotte fault (table 6; fig. 13). The moment magnitude for this event is 8.2, assuming a value of 2.75×10^{11} Pa for shear modulus. Leonard and others (2012) estimated a recurrence interval of events of similar magnitude in the Haida Gwaii

Table 6. Fault parameters for the hypothetical Haida Gwaii earthquake.

Lat [deg. N]	Lon [deg. W]	Depth[a] [km]	Length [km]	Width [km]	Strike [deg.]	Dip [deg.]	Rake [deg.]	Slip [m]
51.5736	130.9405	7	150	60	325	28	110	10

[a]Depth is to the top of the fault plane.

area at about 800 years, under the assumption that there is no significant deformation of the Pacific plate. The authors note that accommodating even 2 mm (0.08 in) per year of convergence by internal shortening of the Pacific plate would increase this interval by about 30 percent. Even though a similar event further north along the Queen Charlotte fault would generate a larger wave at Sitka, we do not consider such an event a credible scenario, because the relative plate motion north of Haida Gwaii is transform, and all recorded earthquakes there had strike-slip mechanism.

Landslide tsunami hazard potential

Tsunamis caused by underwater slope failures are a significant hazard in the fjords of coastal Alaska and other high-latitude fjord coastlines (Lee and others, 2006). Kulikov and others (1998) analyzed tsunami catalog data for the North Pacific coast and showed that this region has a long record of tsunami waves generated by submarine and subaerial landslides, avalanches, and rock falls. For example, as a result of the 1964 earthquake, about 20 local submarine and subaerial landslide tsunamis were generated in Alaska (Lander, 1996), which accounted for 76 percent of the tsunami fatalities.

The coast of southeastern Alaska has numerous fjords. In a fjord setting, glacial rivers and streams form a delta at the head of a fjord and deposit sediment that easily loses strength during an earthquake. A primary cause of submarine landslides in fjords is the accumulation of sediments on steep underwater slopes. Masson and others (2006) divide all factors that contribute to initiation of submarine landslides into two groups: factors related to geologic properties of landslide material (such as overpressure due to rapid deposition), and those associated with external events (such as earthquakes or sea level change), noting that usually more than one factor contributes to a single landslide event. Hampton and others (2002) note that in a fjord environment, where the deltaic sediment is deposited rapidly, the sediment builds up pore-water pressures and could liquefy under extreme low tide conditions or ground shaking during an earthquake, due to low static shear strength. While ground shaking is one of the most common triggering mechanisms for submarine slope failures, a close relationship has been demonstrated between coastal landslides and extreme low tides (Thomson and others, 2001; Kulikov and others, 1998). On November 3, 1994, a massive submarine landslide destroyed a timber dock on the east shore of Skagway harbor. A resultant wave killed one worker, and damaged and destroyed boats and docks in the harbor, causing about $2 million in repairs. A numerical modeling study by Thomson and others (2001) demonstrated that the primary cause of the 1994 Skagway slide was the critical overloading of the slope materials at a time of extreme low tide. Human activities can also trigger submarine landslides (Masson and others, 2006; Bornhold and others, 2001). Because of these diverse mechanisms, assessment of landslide-generated tsunami hazard is a challenging task.

Fjords in southeastern Alaska are also prone to tsunami waves generated by subaerial rockfalls caused by fractures in the bedrock along fjord sidewalls. Evans and Clague (1994) described the process of glacier debuttressing as an important mechanism that generates instability of the rock slopes due to relaxation of internal stress after deglaciation. Southeastern Alaska is a tectonically active area, and rock-slope failures in such environments are often triggered by earthquakes. Although it is hard to separate the contribution of a seismic event into the triggering of a rockfall, Cossart and others (2008) found that glacial unloading and associated stress release play an important role in triggering rock-slope failures. The largest known historic tsunami wave generated by a subaerial rock-slope failure followed an estimated 30 million m^3 (1,050 million ft^3) landslide in Lituya Bay, Alaska, on June 9, 1958. The slope failure was triggered by a M7.9 earthquake on the nearby Fairweather fault (fig. 4). When the landslide entered the water, it produced tsunami runup up to 530 m (1,740 ft) high on the opposite shore of the bay (Miller, 1960). A comprehensive study of an unstable rock slump, which was identified on the northern shore of Tidal Inlet in Glacier Bay National Park, concluded that a rapid failure of the landslide would result in significant hazard to park visitors (Wieczorek and others, 2007). Results of numerical modeling indicate that landslide-generated waves of extremely high amplitude can be expected in Tidal Inlet, and waves up to 10 m (33 ft) high outside of the inlet, with significant wave activity lasting for several hours.

The recent tsunami hazard assessment study by Leonard and others (2012) was the first attempt to quantify tsunami hazard for the entire Canadian coast. The study provided, in particular, an overview of potential tsunami sources along the Pacific coast of Canada, including both tectonic and landslide sources. This tsunami-hazard assessment report includes the description of several historic landslide tsunamis that occurred in fjords along the Pacific coast of North America. It was concluded, however, that the current knowledge of landslide tsunami sources in the fjords of the Pacific coast of Canada is not sufficient to perform probabilistic tsunami modeling of potential failures in the area. The analysis of submarine continental slope landslides has led to the conclusion that this hazard is negligible compared to other Pacific tsunami sources (Leonard and others, 2012).

While we acknowledge that communities in southeastern Alaska are considered at risk from locally generated waves because of their proximity to landslide-prone fjords in the seismically active zone, we do not quantify this category of landslide tsunami hazard for Sitka in the current report due to poor constraints on the parameters of potential slides, such as locations, volumes, and geotechnical properties. A record of tsunami waves generated by slides off the continental slope in southeastern Alaska does not exist, and the authors are not aware of any geotechnical investigations in the area for the evidence of underwater slides. Because of the limited evidence for past tsunamigenic landslide events off the continental slope along the southeastern Alaska coast, and the absence of any slope stability analysis for the area, it is not possible to develop a credible landslide tsunami scenario for Sitka.

MODELING RESULTS

Results of hypothetical tsunami scenarios

We performed numerical calculations for all scenarios described above. In every case, we modeled the water dynamics in each grid listed in table 1, and computed the extent of inundation and flow depths only in the highest-resolution grid. Figure 16 shows calculated inundation limits for those scenarios that resulted in measurable inundation zones in Sitka, namely scenarios 2, 5, 6, and 8. Since none of the tsunami sources that correspond to the scenarios in figure 16 are near-field events, they do not produce any tectonic land changes in Sitka, and therefore the inundation zones have the same reference level of the MHHW shoreline. Scenario 5, the Tohoku-type event that ruptures the PWS, KP, and KI segments of the megathrust, produces the largest inundation zone in Sitka. A large section of Sitka downtown adjacent to the City Harbor gets flooded, as well as the area around the harbor on Japonski Island, and the buildings for University of Alaska Southeast and Mt. Edgecumbe High School. Scenarios 6 and 8, the SAFRR tsunami source and the Cascadia subduction zone rupture, respectively, result in very similar inundation zones, which are significantly smaller than the extent of inundation from scenario 5. This is explained by the directional properties of the tsunami sources: the rupture in the Cascadia subduction zone will generate a wave that has the maximum energy flux perpendicular to the source area in the near field (that is, to the west and east), and later during the trans-Pacific propagation the energy will be redistributed and directed toward the coast of the Philippines. Similarly, the SAFRR tsunami source will produce the maximum energy flux perpendicular to the trench in the near field, and the propagated energy is directed mostly to the coast of Southern California and Mexico. Scenario 2, which simulates the extended 1964 rupture, produces a slightly larger inundation zone compared to that of scenarios 6 and 8.

Map sheet 1 shows the maximum composite calculated extent of inundation for all scenarios, and the maximum composite flow depths over dry land. The tsunami flow depth is an important indicator of potential damage, and must be differentiated from runup height (Synolakis and Bernard, 2006). For easier visual reference, we indicate the values of 0.3 m (1 ft), which approximately corresponds to shin height, and 1.8 m (6 ft), which is just above the average person's body height.

In the northern part of the town, noticeable inundation occurs in the area along Halibut Point Road between its north end, which is close to the delta of Starrigavan Creek, and Kuhnle Drive in the south. The section of the road between the dock and the road's dead end is flooded with flow depths up to 4 m (13 ft).

In the central part of the town, which includes downtown, harbors, and Japonski Island, the entire coastline is inundated, according to the composite worst-case scenario. The maximum flow depths are expected along the shores of the northern harbor and in the channel that separates Japonski Island from the mainland.

In the southeastern part of the town, the area between Sawmill Creek Road and the shoreline next to the Sitka southeast subdivision is completely inundated. Sawmill Creek Road, which follows the shoreline, is flooded in several places, as does the Industrial Park in Sawmill Cove. The maximum flow depths in both areas reach 5 m (16 ft).

Time series and other numerical results

To provide a more accurate assessment of tsunami hazards in Sitka, we have supplemented the inundation maps with the time series of the modeled water level and velocity dynamics at certain locations around the town and in Sitka Sound. The time of arrival of the first wave, the maximum wave amplitude, and the duration of wave action are important factors that should be considered by emergency managers during evacuation planning. The appendix contains plots of sea level and velocity time series for selected scenarios at critical locations in Sitka Sound. For each location shown by a number in figures A-1a, A-1b, and A-1c, we plot the sea level and water velocity in figures A-2 and A-3 for scenarios 2–5 and 6–9, respectively. The zero time corresponds to the epicenter origin time, and elevations correspond to the post-earthquake MHHW datum. Velocity magnitude is calculated as water flux divided by water depth, thus the velocity value can have large uncertainties if the water depth is small. In the plots shown, the velocity is computed only where the water depth is greater than 0.3 m (1 ft).

Sources of errors and uncertainties

The hydrodynamic model used to calculate tsunami propagation and runup is a nonlinear, flux-formulated, shallow-water model (Nicolsky and others, 2011; Nicolsky, 2012). The model passed the verification and validation tests required for numerical codes used in production of tsunami inundation maps (Synolakis and others, 2007; NTHMP, 2012).

The source mechanism remains the biggest unknown in the problem of tsunami modeling. Since the initial condition for the modeling is determined by the displacement of the ocean bottom, the largest source of errors is the earthquake model. When the tsunami is generated in the vicinity of the coast, the direction of the incoming waves, their amplitudes and times of arrival are determined by the initial displacements of the ocean surface in the source area because the distance to the shore is too small for the waves to disperse. Therefore, the near-field inundation modeling results are especially sensitive to the fine structure of the tsunami source. The modeling process is highly sensitive to errors when the complexity of the source function is combined with its proximity to the coastal zone. Finally we mention that the horizontal resolution of the grid used for inundation modeling is 15 m. This scale is limited by the resolution of the topographic and bathymetric data used for the grid construction. The 15 m resolution is high enough to describe major relief features, but the existing model cannot accurately resolve small topographic features, buildings, and other facilities.

SUMMARY

We present the results of numerical modeling of earthquake-generated tsunami waves for the town of Sitka in southeastern Alaska. The presented maps have been completed using the best information available and are believed to be accurate; however, their preparation required many assumptions. We have considered several tsunami scenarios and have provided an estimate of maximum credible tsunami inundation. Actual conditions during a tsunami event may vary from those considered, so the accuracy cannot be guaranteed. Landslide tsunami sources are not included in the current study due to unknown potential impact of such events on Sitka. The limits of inundation shown should only be used as a guideline for emergency planning and response action. Actual areas inundated will depend on specifics of earth deformations, on-land construction, and tide level, and may differ from areas shown on the map. The information on this map is intended to permit state and local agencies to plan emergency evacuation and tsunami response actions in the event of a major tsunamigenic earthquake. These results are not intended for land-use regulation.

ACKNOWLEDGMENTS

This project was supported by the National Oceanic and Atmospheric Administration grants 27-014d and 06-028a through the Cooperative Institute for Arctic Research. Numerical calculations for this work were supported by a grant of High Performance Computing (HPC) resources from the Arctic Region Supercomputing Center (ARSC) at the University of Alaska Fairbanks as part of the US Department of Defense HPC Modernization Program. We thank Dr. Lucinda Leonard and an anonymous reviewer for their thoughtful reviews of the draft manuscript and maps.

REFERENCES

Alaska Division of Community Advocacy, 2011, Sitka Community Overview, http://www.commerce.state.ak.us/dca/commdb/CF_BLOCK.cfm, Community Database Online.

AEIC event page, http://www.aeic.alaska.edu/quakes/queen_charlotte_20130105.html

Arakawa, Akio, and Lamb, V.R., 1981, A potential enstrophy and energy conserving scheme for the shallow water equations: Monthly Weather Review, v. 109, p. 18–36.

Atwater, B.F., Tuttle, P.F., Schweig, E.S., Rubin, C.M., Yamaguchi, D.K., and Hemphill-Haley, Eileen, 2004, Earthquake recurrence inferred from paleoseismology, *in* Gillespie A.R., Porter, S.C., and Atwater, B.F., eds., The Quaternary Period in the United States: New York, Elsevier Science, p. 331–350.

Atwater, B.F., Musumi-Rokkaku, Satoku, Satake, Kenji, Tsuji, Yoshinobu, Ueda, Kazue, and Yamaguchi, D.K., 2005, The orphan tsunami of 1700—Japanese clues to a parent earthquake in North America: U.S. Geological Survey Professional Paper 1707 (prepared in cooperation with the Geological Survey of Japan, the University of Tokyo, and the University of Washington, and published in association with University of Washington Press), 133 p.

Bornhold, B.D., Thomson, R.E., Rabinovich, A.B., Kulikov, E.A., and Fine, I.V., 2001, Risk of landslide-generated tsunamis for the coast of British Columbia and Alaska, *in* Mahmoud, M., van Everdingen, R., and Carss, J., eds., An earth odyssey—Proceedings of the 54th Canadian Geotechnical Society Conference: Richmond, B.C., Bitech Publishers, Ltd., p. 1,450–1,454.

Bustin, A.M.M., Hyndman, R.D., Kao, H., and Cassidy, J.F., 2007, Evidence for underthrusting beneath the Queen Charlotte margin, from teleseismic receiver function analysis: Geophysical Journal International, v. 171, no. 3, p. 1,198–1,211, doi:10.1111/j.1365-246X.2007.03583.x.

Caldwell, R.J., Taylor, L.A., Eakins, B.W., Carignan, K.S., and Collins, S.V., 2012, Digital elevation models of Juneau and Southeast Alaska—Procedures, data sources and analysis: National Geophysical Data Center, NOAA Technical Memorandum NESDIS NGDC-53, 66 p.

Carver, G.A., and Plafker, George, 2008, Paleoseismicity and neotectonics of the Aleutian subduction zone—An overview, *in* Freymueller, J.T., Haeussler, P.J., Wesson, R.L., and Ekström, G., eds., Active tectonics and seismic potential of Alaska: American Geophysical Union Geophysical Monograph 179, p. 43–63.

Christensen, D.H., and Beck, S.L., 1994, The rupture process and tectonic implications of the Great 1964 Prince William Sound Earthquake: Pure and Applied Geophysics, v. 142, no. 1, p. 29–53.

Cossart, Etienne, Braucher, R., Fort, M., Bourlès, D.L., and Carcaillet, Julien, 2008, Slope instability in relation to glacial debuttressing in Alpine areas (upper Durance Catchment, southeastern France)—Evidence from field data and ^{10}Be cosmic ray exposure ages: Geomorphology, v. 95, no. 1-2, p. 3–26.

DeMets, Charles, and Dixon, T.H., 1999, New kinematic model for the Pacific–North America motion from 3 Ma to present, I, Evidence for steady motion and biases in the NUVEL-1A model: Geophysical Research Letters, v. 26, p. 921–924.

DeMets, Charles, Gordon, R.C., Argus, D.F., and Stein, Seth, 1990, Current plate motions: Geophysical Journal International, v. 101, no. 2, p. 425–478.

Dengler, L.A., Uslu, Burak, Barberopoulou, Aggeliki, Yim, S.C., and Kelly, Annabel, 2009, The November 15, 2006 Kuril Islands generated tsunami in Crescent City, California: Pure and Applied Geophysics, v. 166, p. 37–53.

Doser, D.I., and Lomas, R., 2000, The transition from strike-slip to oblique subduction in southeastern Alaska from seismological studies: Tectonophysics, v. 316, p. 45–65.

Eckel, E.B., 1967, Effects of the earthquake of March 27, 1964, on air and water transport, communications, and utilities systems in south-central Alaska: U.S. Geological Survey Professional Paper 545-B, p. B1–B27.

Evans, S.G., and Clague, J.J., 1994, Recent climatic change and catastrophic geomorphic processes in mountain environments: Geomorphology, v. 10, p. 107–128.

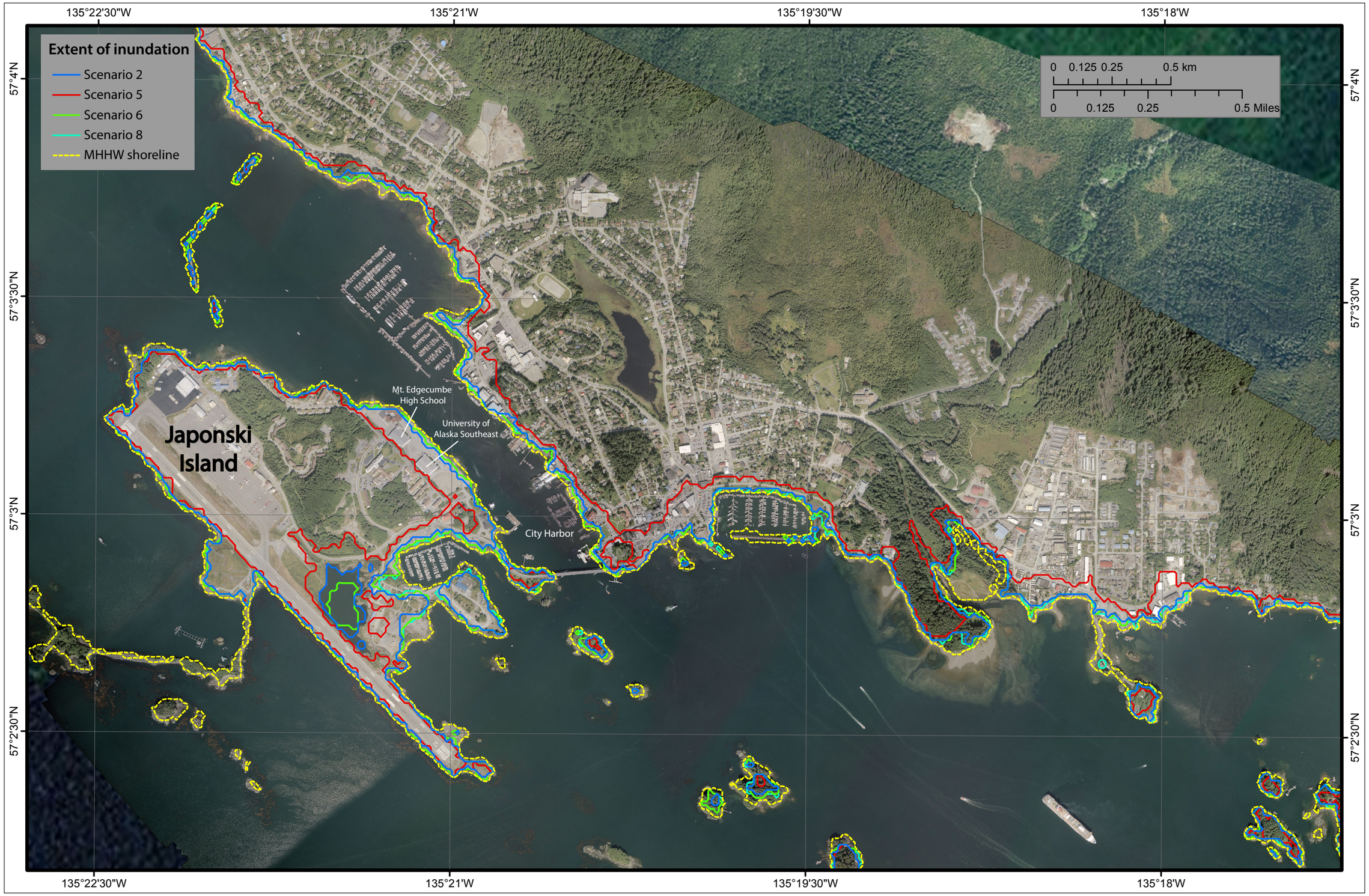

Figure 16. Calculated potential inundation in Sitka for Scenarios 2, 5, 6, and 8 with respect to the MHHW shoreline.

Fletcher, H.J., and Freymueller, J.T., 2003, New constraints on the motion of the Fairweather fault, Alaska, from GPS observations: Geophysical Research Letters, v. 30, p. 1139, doi:10.1029/2002GL016476.

Fournier, T.J., and Freymueller, J.T., 2007, Transition from locked to creeping subduction in the Shumagin region, Alaska: Geophysical Research Letters, v. 34, p. 6, DOI:10.1029/2006GL029073.

Freymueller, J.T., Woodard, H., Cohen, S., Cross, R., Elliott, J., Larsen, C., Hreinsdottir, S., and Zweck, C., 2008, Active deformation processes in Alaska, based on 15 years of GPS measurements, *in* Freymueller, J.T., Haeussler, P.J., Wesson, R., and Ekström, G., eds., Active Tectonics and Seismic Potential of Alaska: Washington, D.C., American Geophysical Union Geophysical Monograph, 179, p. 1–42., doi:10.1029/179GM02.

Gica, Edison, Spillane, M.C., Titov, V.V., Chamberlin, C.D., and Newman, J.C., 2008, Development of the forecast propagation database for NOAA's Short-term Inundation Forecast for Tsunamis (SIFT): NOAA Technical Memorandum OAR PMEL-139, 89 p.

Hampton, M.A., Lemke, R.W., and Coulter, H.W., 2002, Submarine landslides that had a significant impact on man and his activities, Seward and Valdez, Alaska, *in* Schwab, W.C., Lee, H.J., and Twichell, D.C., eds., Submarine Landslides—Selected Studies in the U.S. Exclusive Economic Zone: U.S. Geological Survey Bulletin 2002, p. 123–134.

Hayes, G.P., Wald, D.J., and Johnson, R.L., 2012, Slab1.0—A three-dimensional model of global subduction zone geometries: Journal of Geophysical Research, v. 117, no. B1, doi:10.1029/2011JB008524.

Hickman, P.J., Suleimani, E.N., and Nicolsky, D.J., 2012, Digital elevation model of Sitka Harbor and the city of Sitka, Alaska—Procedures, data sources, and quality assessment: Alaska Division of Geological & Geophysical Surveys Miscellaneous Publication 144, 38 p.

Ito, Yoshihiro, Tsuji, Takeshi, Osada, Yukihito, Kido, Motoyuki, Inazu, Daisuke, Hayashi, Yutaka, Tsushima, Hiroaki, Hino, Ryota, and Fujimoto, Hiromi, 2011, Frontal wedge deformation near the source region of the 2011 Tohoku–Oki earthquake: Geophysical Research Letters, v. 38, no. 15, L00G05, doi:10.1029/2011GL048355.

James, Thomas, Rogers, Garry, Cassidy, John, Dragert, Herb, Hyndman, Roy, Leonard, Lucinda, Nykolaishen, Lisa, Riedel, Michael, Schmidt, Michael, and Wang, Kelin, 2013, Field studies target 2012 Haida Gwaii Earthquake: EOS v. 94, no. 22, p. 197–198.

Johnson, J.M., Tanioka, Yuichiro, Ruff, L.J., Satake, Kenji, Kanamori, Hiroo, and Sykes, L.R., 1994, The 1957 Great Aleutian Earthquake: Pure and Applied Geophysics, v. 142, no. 1, p. 3−28.

Johnson, J.M., Satake, Kenji, Holdahl, S.R., and Sauber, Jeanne, 1996, The 1964 Prince William Sound earthquake—Joint inversion of tsunami waveforms and geodetic data: Journal of Geophysical Research, v. 101, no. B1, p. 523–532.

Kulikov, E.A., Rabinovich, A.B., Fine, I.V., Bornhold, B.D., and Thomson, R.E., 1998, Tsunami generation by landslides at the Pacific coast of North America and the role of tides: Oceanology, v. 38, no. 3, p. 323–328.

Lander, J.F., 1996, Tsunamis affecting Alaska, 1737–1996: Boulder, Colorado, National Geophysical Data Center (NGDC), NOAA, Key to Geophysical Research Documentation, v. 31, 195 p.

Lay, Thorne, Ye, Lingling, Kanamori, Hiroo, Yamazaki, Yoshiki, Cheung, Kwok Fai, Kwong, Kevin, and Koper, K., 2013, The October 28, 2012 M_W7.8 Haida Gwaii underthrusting earthquake and tsunami—Slip partitioning along the Queen Charlotte fault transpressional plate boundary: Earth and Planetary Science Letters, Available online 11 June 2013, ISSN 0012-821X, http://dx.doi.org/10.1016/j.epsl.2013.05.005 (http://www.sciencedirect.com/science/article/pii/S0012821X13002434).

Lee, H.J., Ryan, H., Kayen, R.E., Haeussler, P.J., Dartnell, P., and Hampton, M.A., 2006, Varieties of submarine failure morphologies of seismically-induced landslides in Alaskan fjords: Norwegian Journal of Geology, v. 86, no. 3, p. 221–230.

Leonard, L.J., Rogers, G.C., and Mazzotti, Stephane, 2012, A preliminary tsunami hazard assessment of the Canadian coastline: Geological Survey of Canada, Open File 7201, 126 p., doi:10.4095/292067.

Lim, E., Eakins, B.W., and Wigley, R., 2011, Coastal relief model of southern Alaska—Procedures, data sources and analysis: NOAA Technical Memorandum NESDIS NGDC-43, 22 p.

Masson, D.G., Harbitz, C.B., Wynn, R.B., Pedersen, G., and Løvholt, F., 2006, Submarine landslides—Processes, triggers and hazard prediction: Philosophical Transactions of the Royal Society A, v. 364, p. 2,009–2,039, doi:10.1098/rsta.2006.1810.

Mazzotti, Stephane, Hyndman, R.D., Flueck, Paul, Smith, A.J., and Schmidt, Michael, 2003, Distribution of the Pacific/North America motion in the Queen Charlotte Islands—S. Alaska plate boundary zone: Geophysical Research Letters, v. 30, no. 14, doi:10.1029/2003GL017586.

Miller, D.J., 1960, The Alaska Earthquake of July 10, 1958—Giant wave in Lituya Bay: Bulletin of the Seismological Society of America, v. 50, no. 2, p. 253–266.

Myers, E.P., and Baptista, A.M., 2001, Analysis of factors influencing simulations of the 1993 Hokkaido Nansei-Oki and 1964 Alaska tsunamis: Natural Hazards, v. 23, no. 1, p. 1–28.

National Tsunami Hazard Mapping Program (NTHMP), 2010, Guidelines and best practices for tsunami inundation modeling for evacuation planning: NTHMP Mapping & Modeling Subcommittee, NOAA.

———2012, Proceedings and Results of The 2011 NTHMP Model Benchmarking Workshop, Boulder: U.S. Department of Commerce/NOAA/NTHMP, (NOAA Special Report). 436 p. (Available at http://nthmp.tsunami.gov)

Nicolsky, D.J., Suleimani, E.N., and Hansen, R.A., 2011, Validation and verification of a numerical model for tsunami

propagation and runup: Pure and Applied Geophysics, v. 168, p. 1,199–1,222, http://dx.doi.org/10.1007/s00024-010-0231-9.

Nicolsky, D.J., 2012, Alaska tsunami model, *in* Proceedings and Results of the 2011 NTHMP Model Benchmarking Workshop: Boulder, CO, U.S. Department of Commerce/NOAA/NTHMP, NOAA Special Report, p. 55–87 (available at http://nthmp.tsunami.gov).

Nishenko, S.P., and Jacob, K.H., 1990, Seismic potential of the Queen Charlotte–Alaska–Aleutian seismic zone: Journal of Geophysical Research, v. 95, no. B3, p. 2,511–2,532.

Okada, Yoshimitsu, 1985, Surface deformation due to shear and tensile faults in a half-space: Bulletin of the Seismological Society of America, v. 75, no. 4, p. 1,135–1,154.

Page, R.A., 1973, The Sitka, Alaska earthquake of 1972: Earthquake Information Bulletin, v. 5, p. 4–9.

Plafker, George, 1967, Surface faults on Montague Island associated with the 1964 Alaska earthquake: U.S. Geological Survey Professional Paper 543-G, p. G1–G42.

———1969, Tectonics: U.S. Geological Survey Professional Paper 543-I, p. G1–G74.

Plafker, George, Kachadoorian, Reuben, Eckel, E.B., and Mayo, L.R., 1969, Effects of the earthquake of March 27, 1964, on various communities: U.S. Geological Survey Professional Paper 542-G, 50 p.

Priest, G.R., Goldfinger, Chris, Wang, Kelin, Witter, R.C., Zhang, Yinglong, and Baptista, A.M., 2009, Confidence levels for tsunami-inundation limits in northern Oregon inferred from a 10,000-year history of great earthquakes at the Cascadia subduction zone: Natural Hazards, v. 54, no. 1, doi10.1007/s11069-009-9453-5.

Rohr, K.M.M., Scheidhauer, Maren, and Trehu, A.M., 2000, Transpression between two warm mafic plates—The Queen Charlotte fault revisited: Journal of Geophysical Research, v. 105, no. B4, p. 8,147–8,172, doi:10.1029/1999JB900403.

Ross, S.L., Jones, L.M., Wilson, R.I., Bahng, B., Borrero, J.C., Brosnan, D.M., Bwarie, J.T., Geist, E.L., Johnson, L.A., Hansen, R.A., Kirby, S.H., Knight, E., Knight, W.R., Long, K., Lynett, P.J., Miller, K.M., Mortensen, C.E., Nicolsky, D.J.., Oglesby, D.D., Perry, S.C., Porter, K.A., Real, C.R., Ryan, K.J., Suleimani, E.N., Thio, H.K., Titov, V.V., Wein, A.M., Whitmore, P., and Wood, N.J., 2012, USGS SAFRR tsunami scenario—Potential impacts to the U.S. west coast from a plausible M9 earthquake near the Alaska Peninsula [abs.]: American Geophysical Union Fall Meeting, San Francisco, Calif., December 3–7, 2012.

Ryan, H.F., Blakely, R.J., Kirby, S.H., Scholl, D.W., von Huene, R., 2010, USGS multi-hazard demonstration project tsunami scenario—Selecting a scientifically defensible Aleutian megathrust earthquake source [abs.]: American Geophysical Union Fall Meeting, San Francisco, Calif., December 3–7, 2012.

Satake, Kenji, Shimazaki, Kunihiko, Tsuji, Yoshinobu, and Ueda, Kazue, 1996, Time and size of a giant earthquake in Cascadia inferred from Japanese tsunami records of January 1700: Nature, v. 379, no. 6562, p. 246–249.

Satake, Kenji, Wang, Kelin, and Atwater, B.F., 2003, Fault slip and seismic moment of the 1700 Cascadia earthquake inferred from Japanese tsunami descriptions: Journal of Geophysical Research, v. 108, no. B11, p. 2,535–2,551, doi:10.1029/2003JB002521.

Shennan, Ian, Bruhn, Ronald, and Plafker, George, 2009, Multi-segment earthquakes and tsunami potential of the Aleutian megathrust: Quaternary Science Reviews, v. 28, no. 1–2, p. 7–13.

Sitka, Alaska: 2012–2013 Community profile, http://www.sitka.net.

Smith, A.J., Hyndman, R.D., Cassidy, J.F., and Wang, Kelin, 2003, Structure, seismicity, and thermal regime of the Queen Charlotte transform margin: Journal of Geophysical Research, v. 108, no. B11, p. 2,539, doi:10.1029/2002JB002247.

Suito, Hisashi, and Freymueller, J.T., 2009, A viscoelastic and afterslip postseismic deformation model for the 1964 Alaska earthquake: Journal of Geophysical Research, v. 114, no. B11, p. 404–426, doi:10.1029/2008JB005954.

Suleimani, E.N., 2011, Numerical studies of tectonic and landslide-generated tsunamis caused by the 1964 Great Alaska Earthquake: Fairbanks, Alaska, University of Alaska Fairbanks, Ph.D. dissertation, 181 p.

Suleimani, E.N., Combellick, R.A., Marriott, D.A., Hansen, R.A., Venturato, A.J., and Newman, J.C., 2005, Tsunami hazard maps of the Homer and Seldovia areas, Alaska: Alaska Division of Geological & Geophysical Surveys Report of Investigation 2005-2, 28 p., 2 sheets, scale 1:12,500.

Suleimani, E.N., Hansen, R.A., and Kowalik, Zygmunt, 2003, Inundation modeling of the 1964 tsunami in Kodiak Island, Alaska, *in* Yalciner, A.C., Pelinovsky, E.N., Okal, Emile, and Synolakis, C.E., eds., Submarine Landslides and Tsunamis: NATO Science Series, Series IV, Earth and Environmental Sciences, v. 21, p. 191–201.

Suleimani, E.N., Hansen, R.A., Combellick, R.A., Carver, G.A., Kamphaus, R.A., Newman, J.C., and Venturato, A.J., 2002, Tsunami hazard maps of the Kodiak area, Alaska: Alaska Division of Geological & Geophysical Surveys Report of Investigation 2002-1, 16 p., 4 sheets, scale 1:12,500.

Sykes, L.R., 1971, Aftershock zones of great earthquakes, seismicity gaps, and earthquake prediction for Alaska and the Aleutians: Journal of Geophysical Research, v. 75, p. 8,021–8,041.

Synolakis, C.E., and Bernard, E.N., 2006, Tsunami science before and beyond Boxing Day 2004, *in* Thompson, J.M.T., Heppert, H.E., and Sparks, R.S.J., eds., Extreme Natural Hazards: Philosophical Transactions of the Royal Society, Mathematical, Physical, and Engineering Sciences, v. 364, no. 1845, p. 2,231–2,265.

Synolakis, C.E., Bernard, E.N., Titov, V.V., Kânoğlu, U., and González, F.I., 2007, Standards, criteria, and procedures for NOAA evaluation of tsunami numerical models: Seattle, Washington, NOAA/Pacific Marine Environmental Laboratory, Technical Memorandum OAR PMEL-135, 55 p.

Tang, Liujuan, Titov, V.V., Bernard, E.N., Wei, Yong, Chamberlin, C.D., Newman, J.C., Mofjeld, H.O., Arcas, Diego, Eble, M.C., Moore, Christopher, Uslu, Burak, Pells, Clint, Spillane, Michael, Wright, Lindsey, and Gica, Edison, 2012, Direct energy estimation of the 2011 Japan tsunami using deep-ocean pressure measurements: Journal of Geophysical Research, v. 117, no. C8, doi:10.1029/2011JC007635.

Thomson, R.E., Rabinovich, A.B., Kulikov, E.A., Fine, I.V., and Bornhold, B.D., 2001, On numerical simulation of the landslide-generated tsunami of November 3, 1994, in Skagway Harbor, Alaska, *in* Hebenstreit, G.T., ed., Tsunami research at the end of a critical decade: Kluwer, p. 243–282.

Titov, V.V., and Synolakis, C.E., 1995, Evolution and runup of breaking and nonbreaking waves using VTSC-2: Journal of Waterway, Port, Coastal and Ocean Engineering, v. 121, no. 6, p. 308–316.

———1997, Extreme inundation flows during the Hokkaido–Nansei–Oki Tsunami. Geophysical Research Letters, v. 24, no. 11, p, 1,315–1,318.

Tocher, D., 1960, The Alaska earthquake of July 10, 1958: Movement on the Fairweather fault and field investigation of southern epicentral region: Bulletin of the Seismological Society of America, v. 50, no. 2, p. 267–292.

Wang, Kelin, Wells, R.E., Mazzotti, Stephane, Hyndman, R.D., and Sagiya, Takeshi, 2003, A revised dislocation model of interseismic deformation of the Cascadia subduction zone: Journal of Geophysical Research, v. 108, no. B1, p. 2,026–2,038, doi:10.1029/2001JB001227, http://www.agu.org/pubs/crossref/2003/2001JB001227.shtml.

Wieczorek, G.F., Geist, E.L., Motyka, R.J., and Jakob, M., 2007, Hazard assessment of the Tidal Inlet landslide and potential subsequent tsunami, Glacier Bay National Park, Alaska: Landslides, v. 4, p. 205–215.

Wilson, B.W., and Tørum, A., 1968, The tsunami of the Alaskan Earthquake, 1964: Engineering evaluation: U.S. Army Corps of Engineers, Technical memorandum No. 25, 401 p.

Wilson, Rick, Dengler, Lori, Borrero, J.C., Synolakis, C.E., Jaffe, B., Barberopoulou, A., Ewing, L., Legg, M.R., Ritchie, A., Lynett, P., Admire, A., McCrink, T., Falls, J., Rosinski, A., Treiman, J., Manson, M., Silva, M., Davenport, C., Lancaster, J., Olson, B., Pridmore, C., Real, C.R., Miller, K., and Goltz, J., 2011, The effects of the 2011 Tohoku tsunami on the California coastline**:** Seismological Research Letters, v. 82, no. 3, p. 459–460.

Witter, R.C., Zhang, Y., Wang, K., Priest, G.R., Goldfinger, C., Stimely, L.L., English, J.T., and Ferro, P.A., 2011, Simulating tsunami inundation at Bandon, Coos County, Oregon, using hypothetical Cascadia and Alaska earthquake scenarios: Oregon Department of Geology and Mineral Industries Special Paper 43, 57 p.

APPENDIX A-1
MAPS SHOWING LOCATIONS OF TIME SERIES POINTS

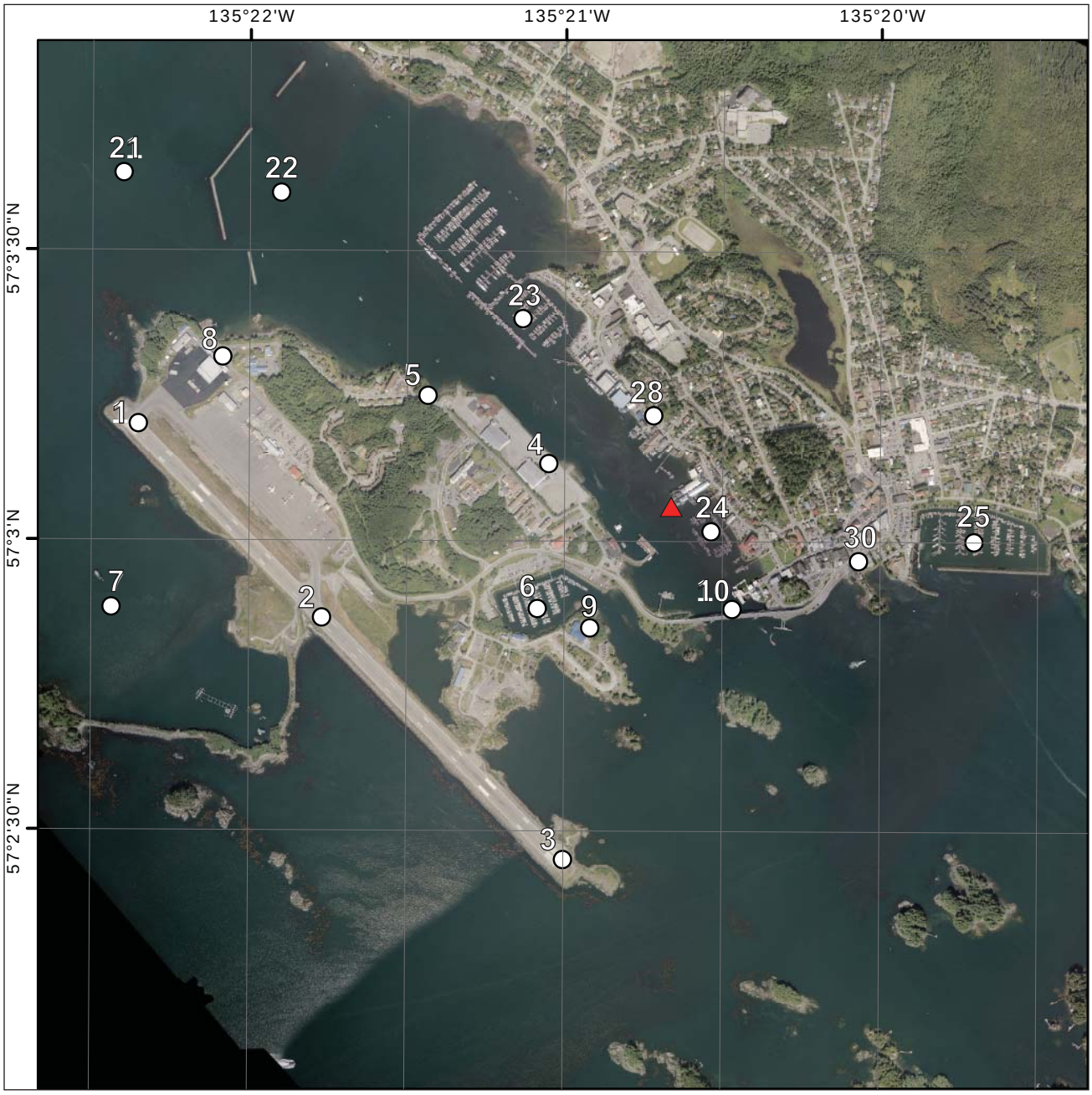

Figure A-1a. Map showing locations of time series points. The red triangle indicates the location of the Sitka tidal station.

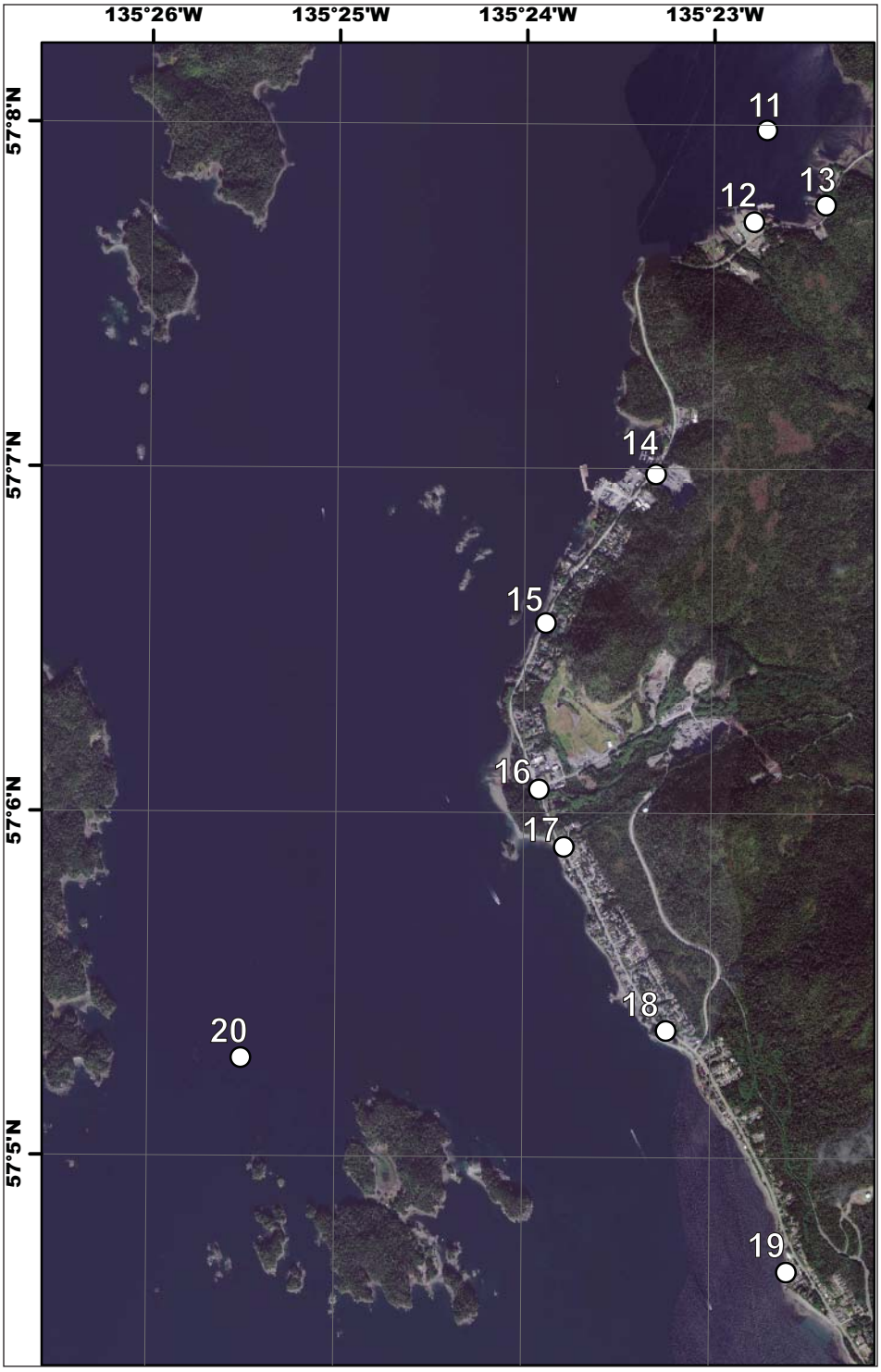

Figure A-1b. Map showing locations of time series points.

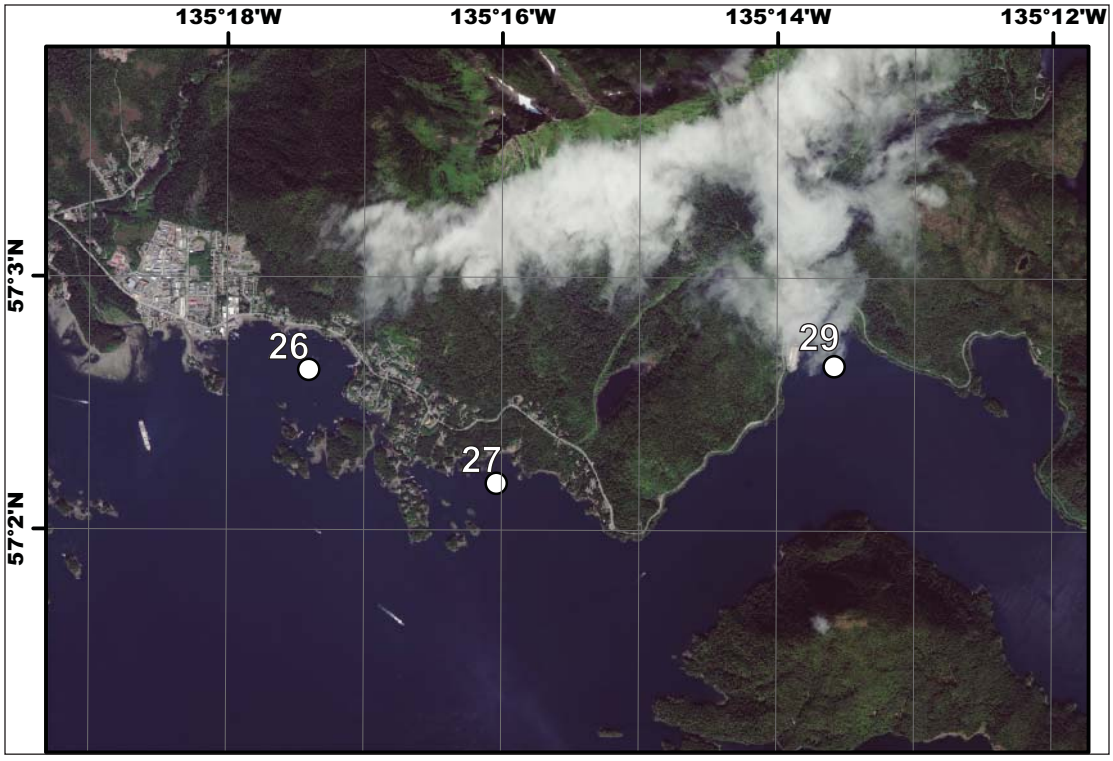

Figure A-1c. Map showing locations of time series points.

APPENDIX A-2
TIME-SERIES PLOTS OF WATER LEVEL AND VELOCITY AT SELECTED LOCATIONS FOR SCENARIOS 2–5

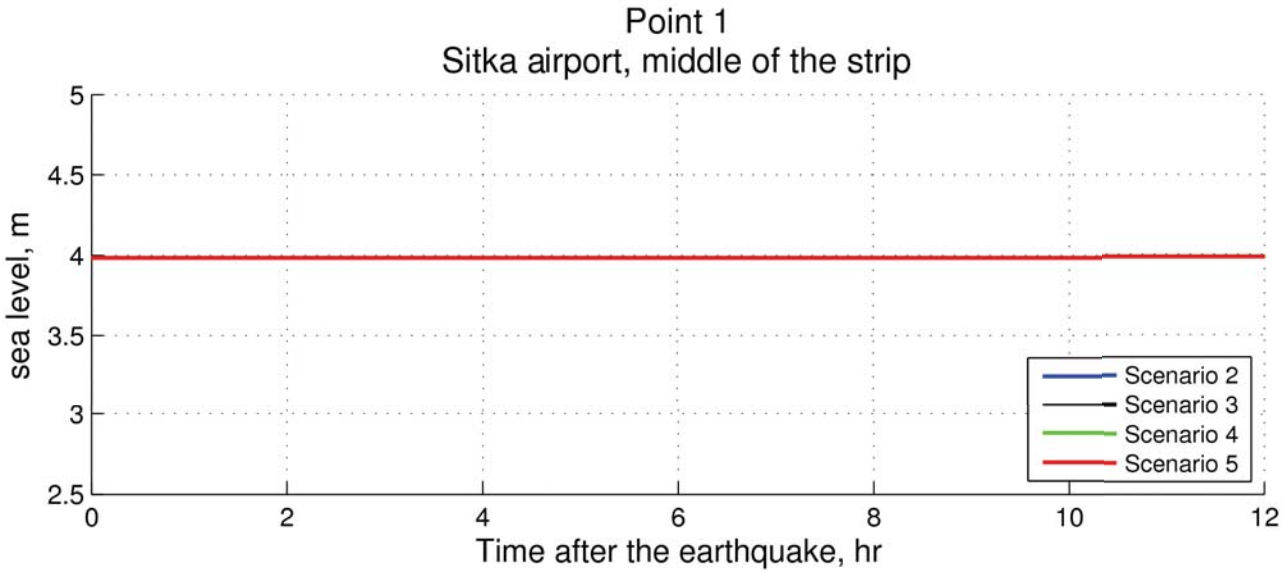

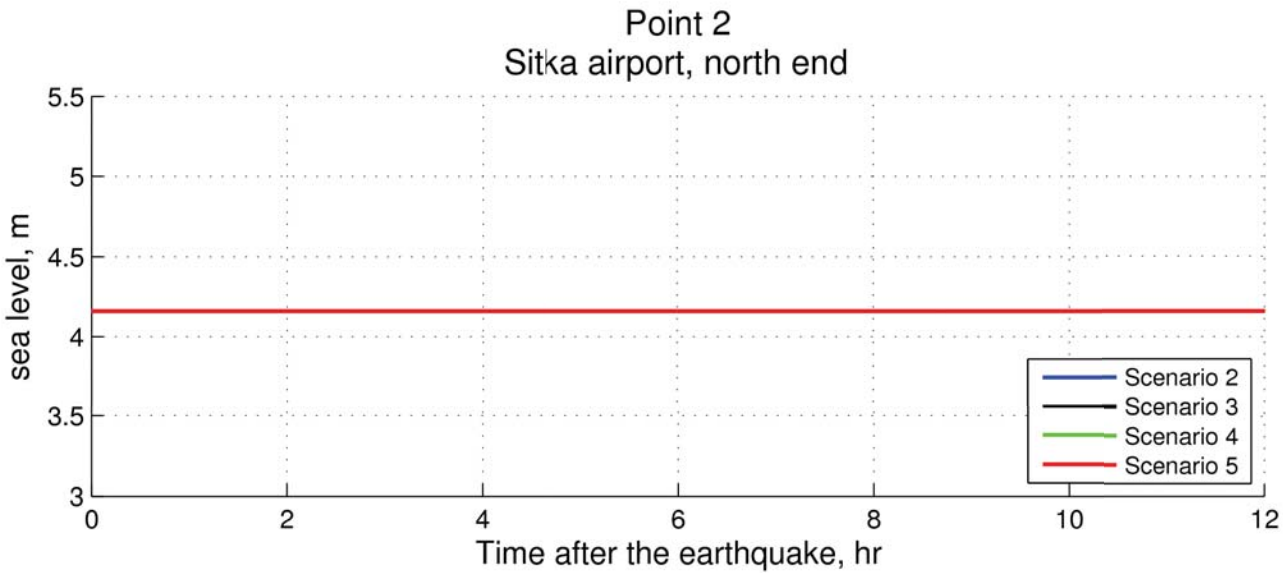

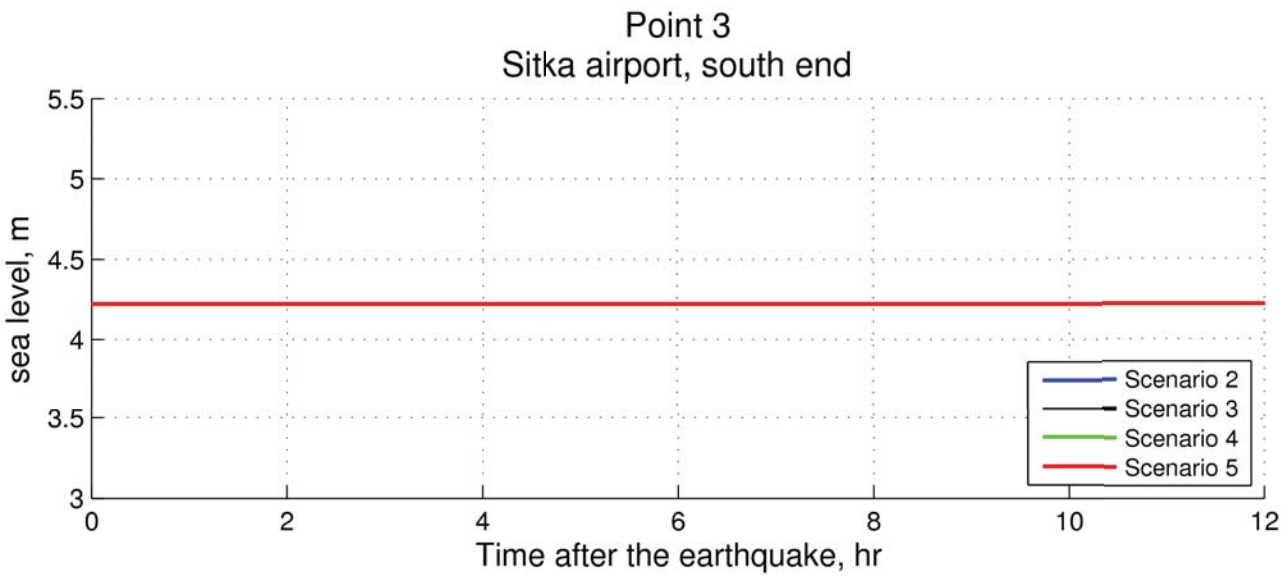

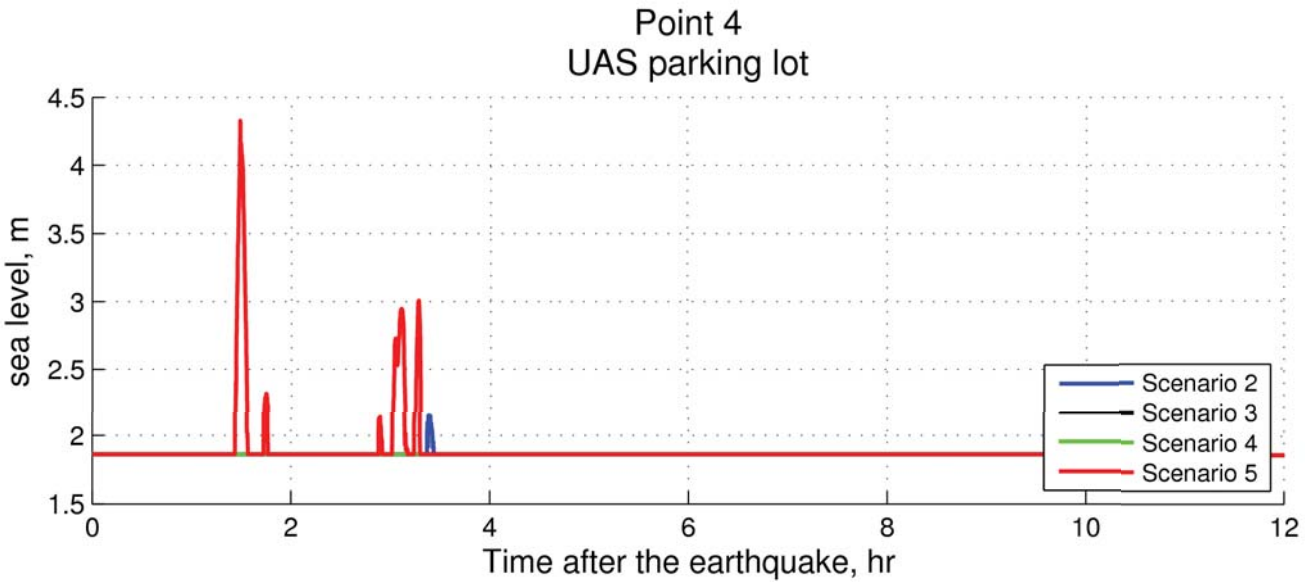
Point 4
UAS parking lot
sea level, m
Time after the earthquake, hr
Scenario 2
Scenario 3
Scenario 4
Scenario 5

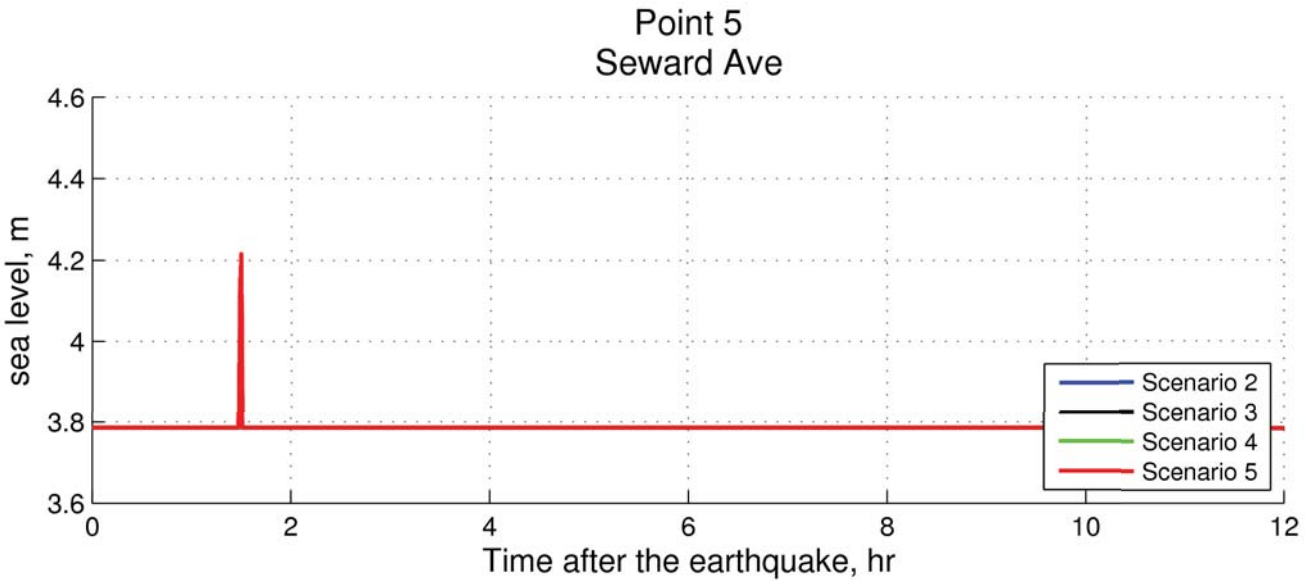
Point 5
Seward Ave
sea level, m
Time after the earthquake, hr
Scenario 2
Scenario 3
Scenario 4
Scenario 5

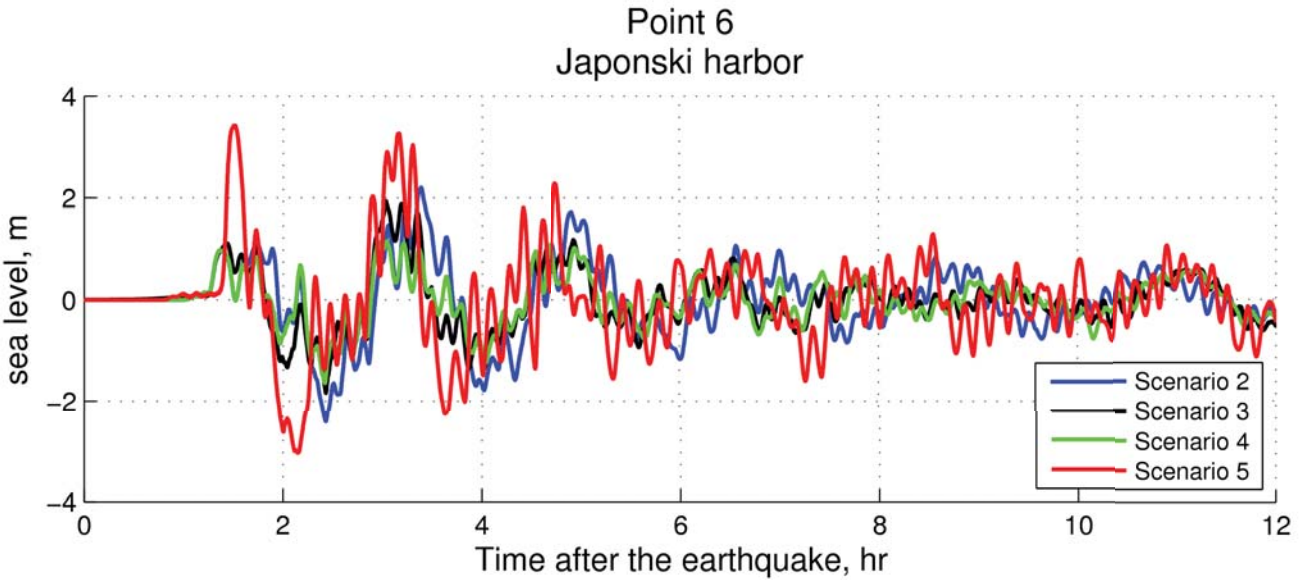
Point 6
Japonski harbor
sea level, m
Time after the earthquake, hr
Scenario 2
Scenario 3
Scenario 4
Scenario 5

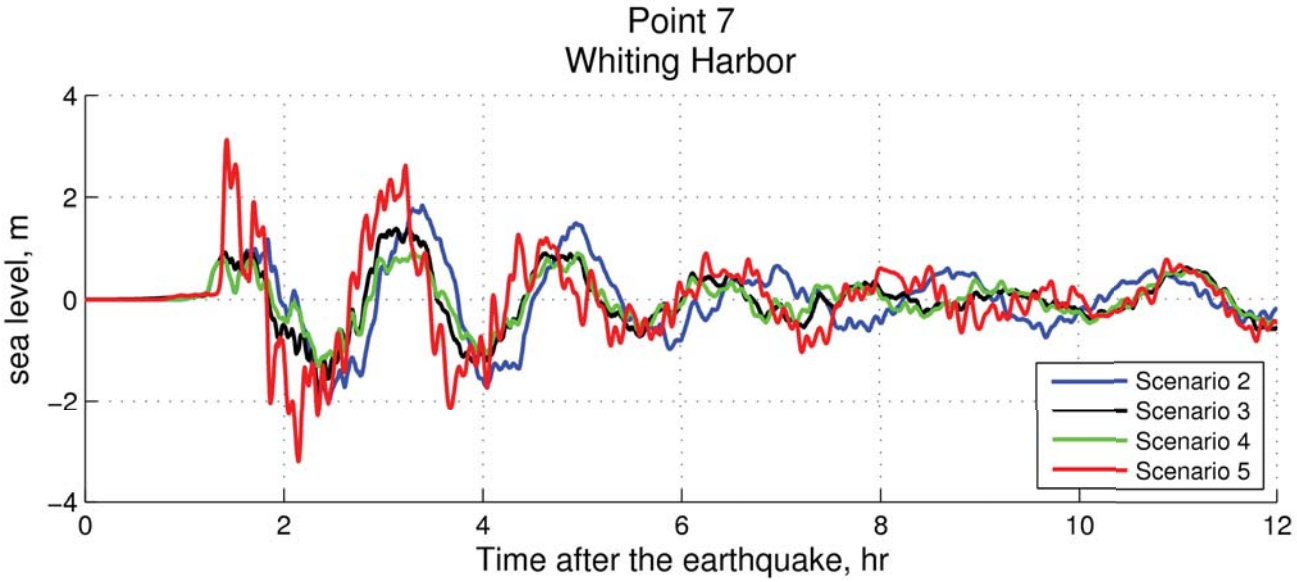
Point 7
Whiting Harbor
sea level, m
Time after the earthquake, hr
Scenario 2
Scenario 3
Scenario 4
Scenario 5

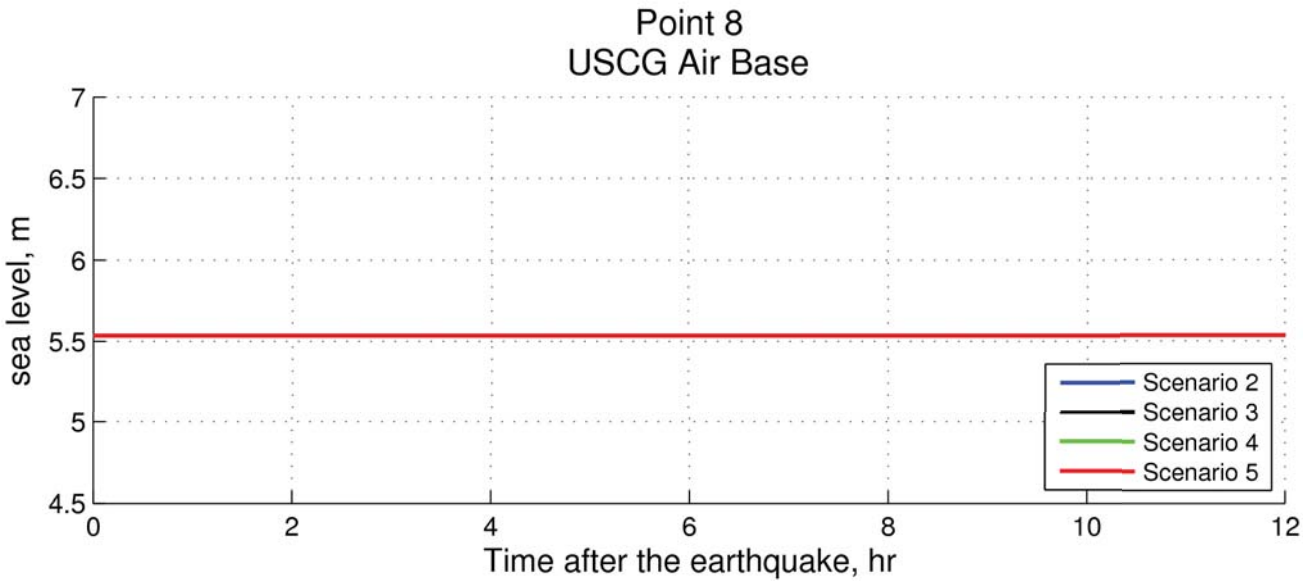
Point 8
USCG Air Base
sea level, m
Time after the earthquake, hr
Scenario 2
Scenario 3
Scenario 4
Scenario 5

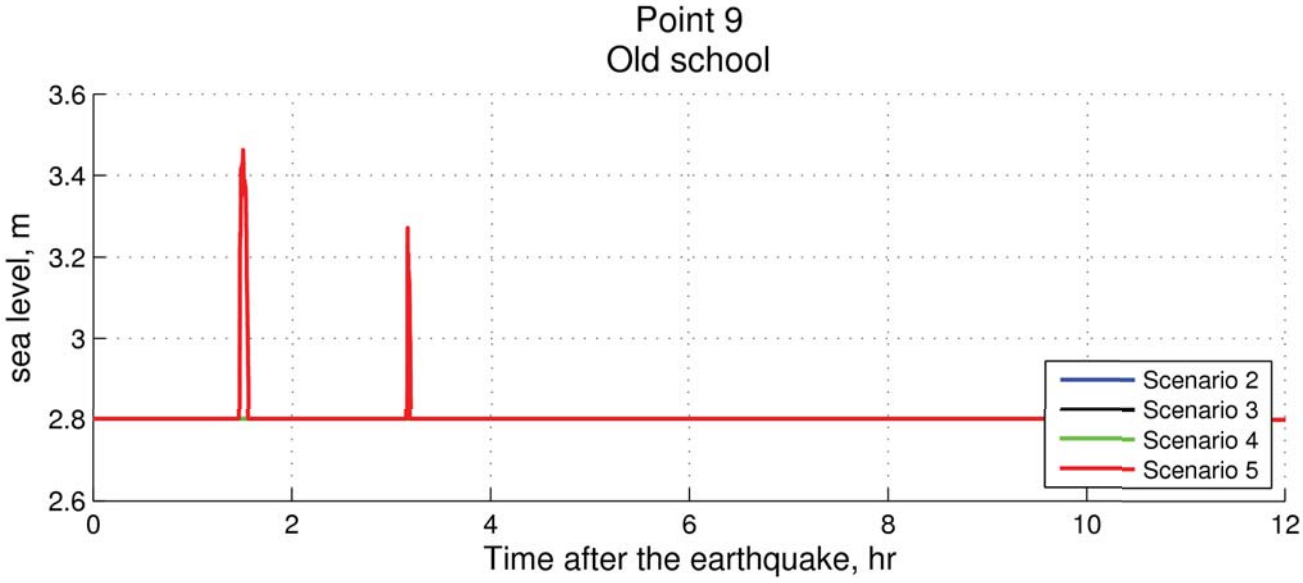
Point 9
Old school
sea level, m
Time after the earthquake, hr
Scenario 2
Scenario 3
Scenario 4
Scenario 5

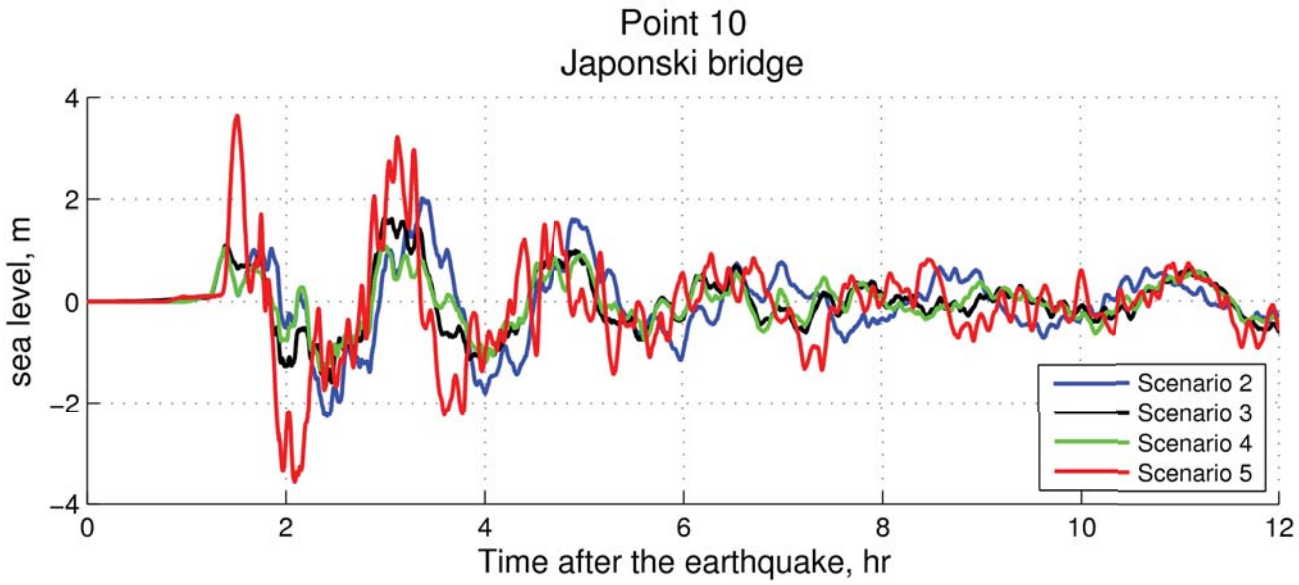
Point 10
Japonski bridge
sea level, m
Time after the earthquake, hr
Scenario 2
Scenario 3
Scenario 4
Scenario 5

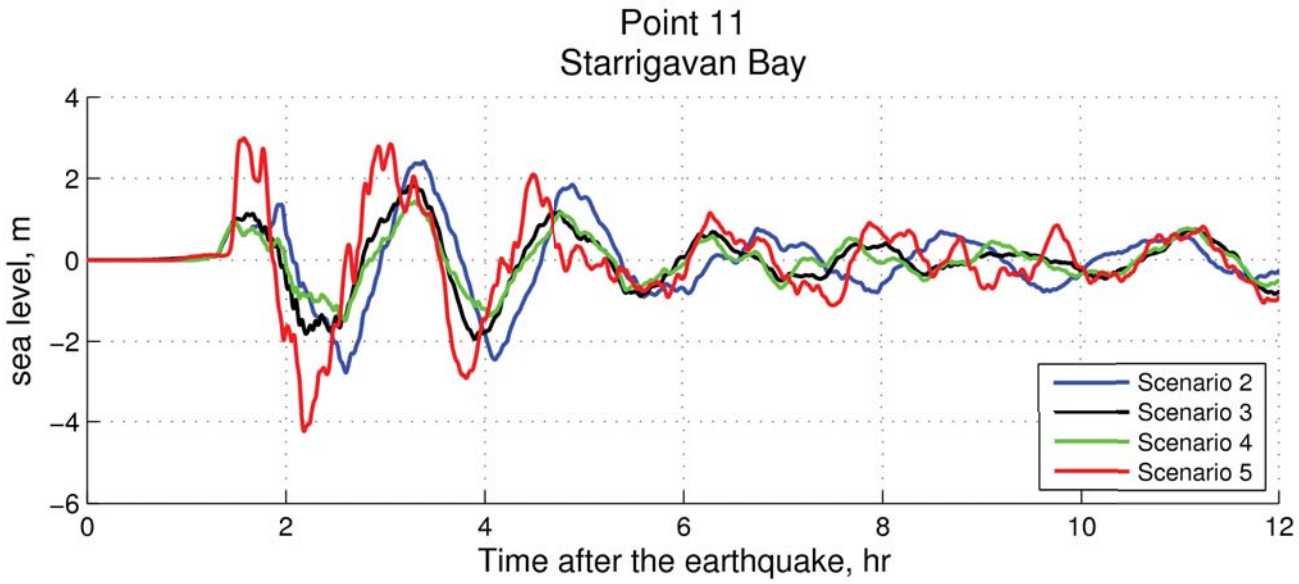
Point 11
Starrigavan Bay
sea level, m
Time after the earthquake, hr
Scenario 2
Scenario 3
Scenario 4
Scenario 5

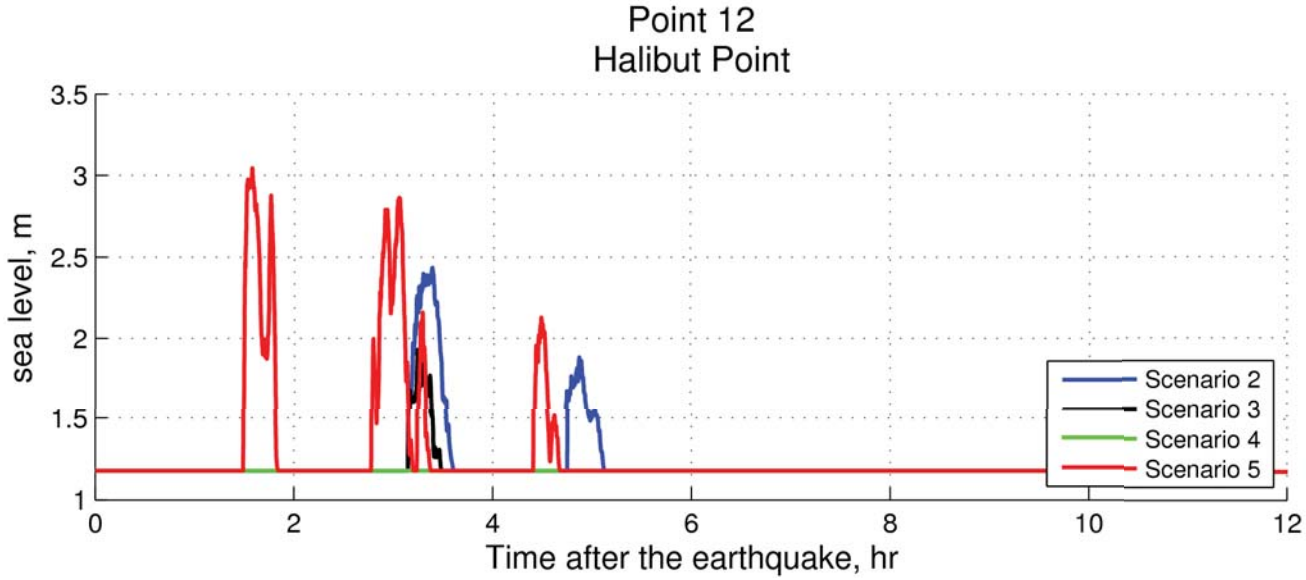
Point 12
Halibut Point
sea level, m
Time after the earthquake, hr
Scenario 2
Scenario 3
Scenario 4
Scenario 5

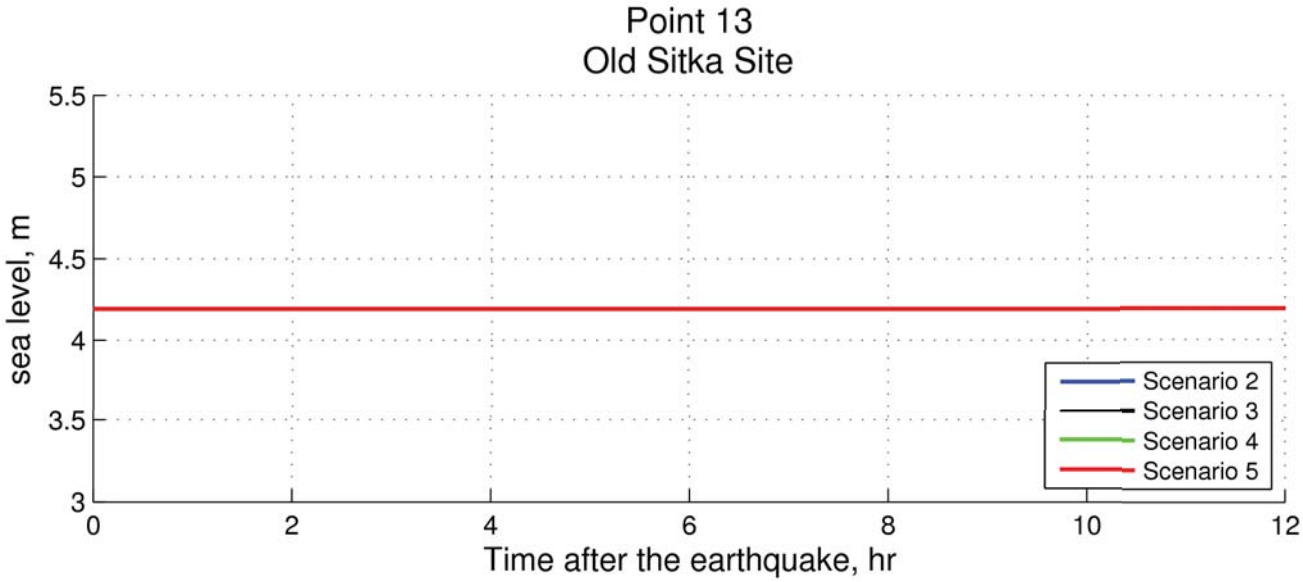
Point 13
Old Sitka Site
sea level, m
5.5
5
4.5
4
3.5
3
0
2
4
6
8
10
12
Time after the earthquake, hr
Scenario 2
Scenario 3
Scenario 4
Scenario 5

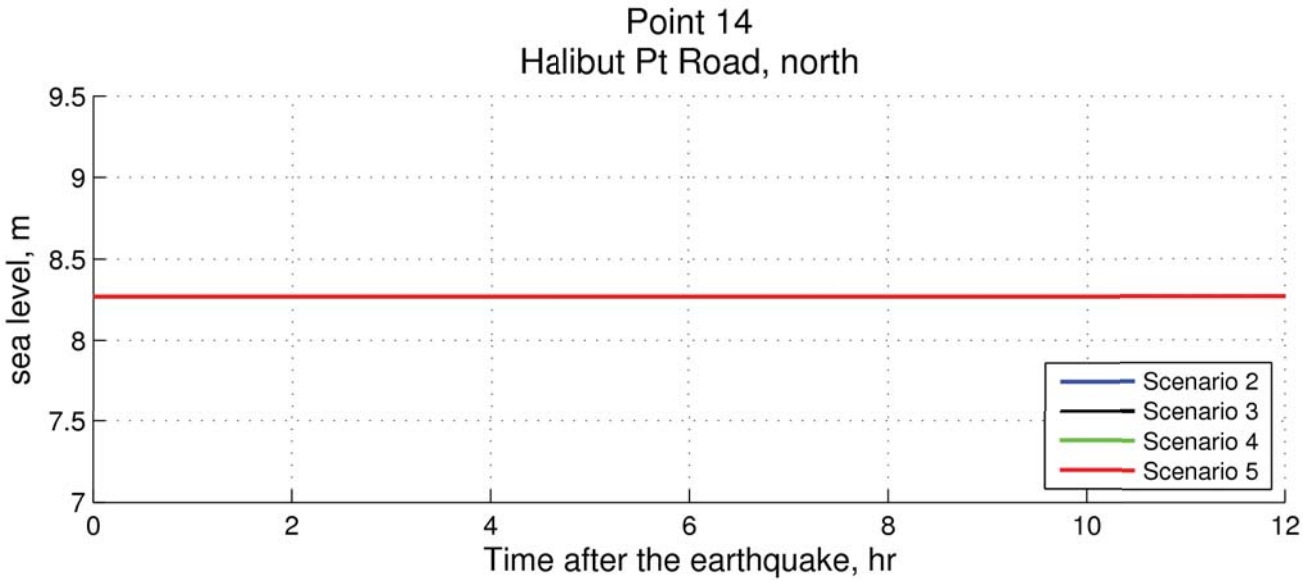
Point 14
Halibut Pt Road, north
sea level, m
9.5
9
8.5
8
7.5
7
0
2
4
6
8
10
12
Time after the earthquake, hr
Scenario 2
Scenario 3
Scenario 4
Scenario 5

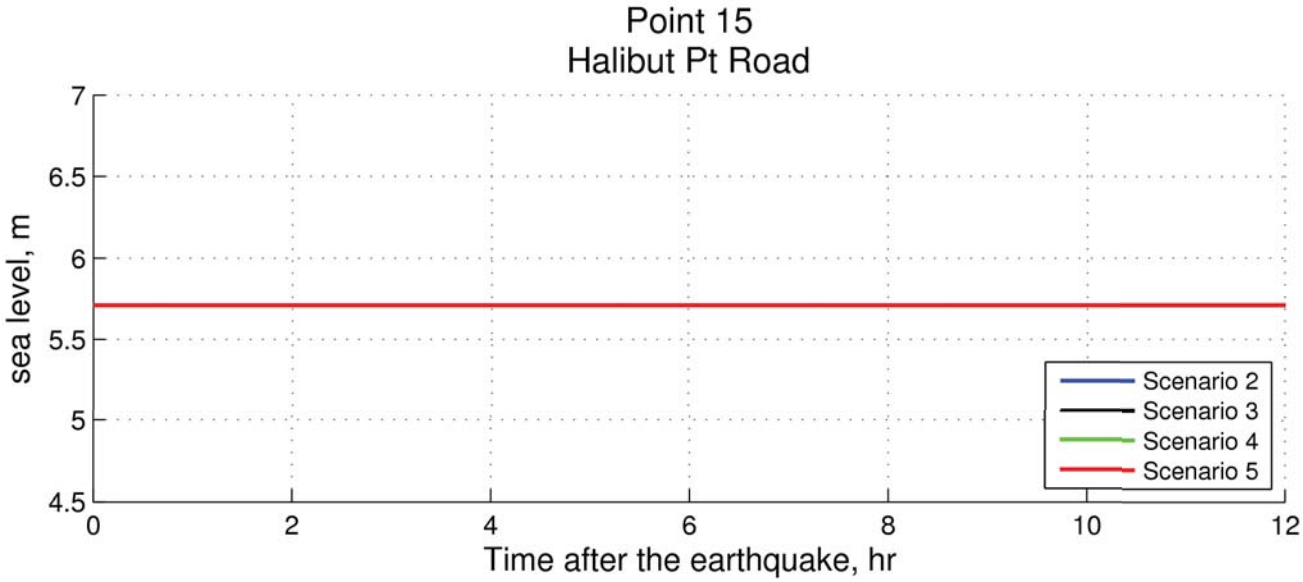
Point 15
Halibut Pt Road
sea level, m
7
6.5
6
5.5
5
4.5
0
2
4
6
8
10
12
Time after the earthquake, hr
Scenario 2
Scenario 3
Scenario 4
Scenario 5

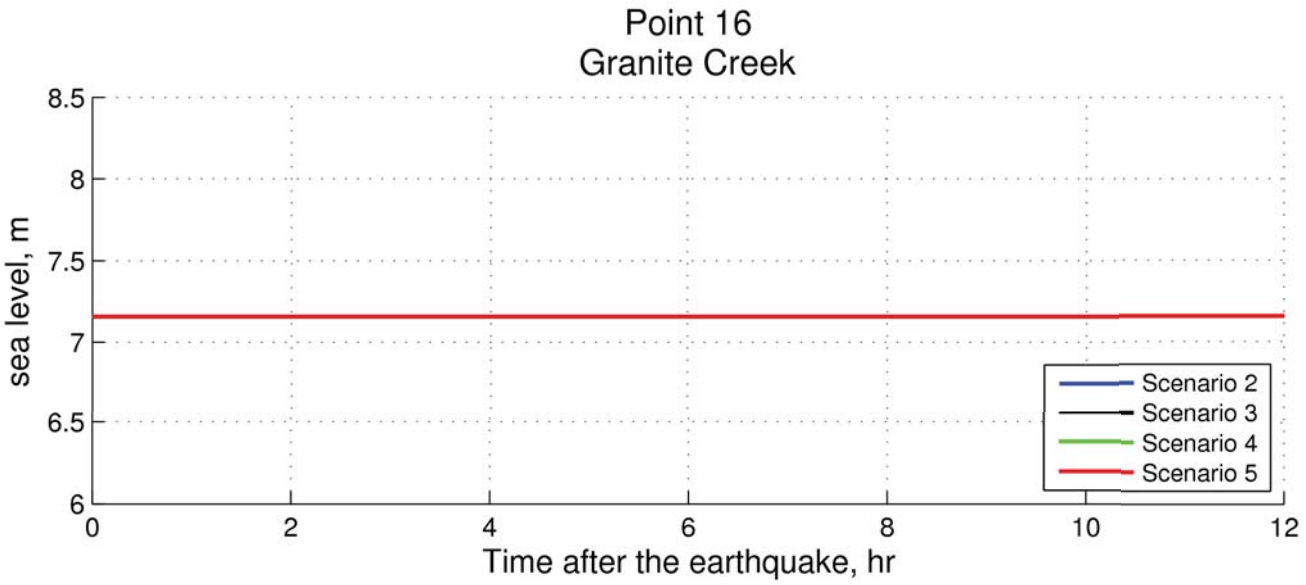
Point 16
Granite Creek
sea level, m
8.5
8
7.5
7
6.5
6
0
2
4
6
8
10
12
Time after the earthquake, hr
Scenario 2
Scenario 3
Scenario 4
Scenario 5

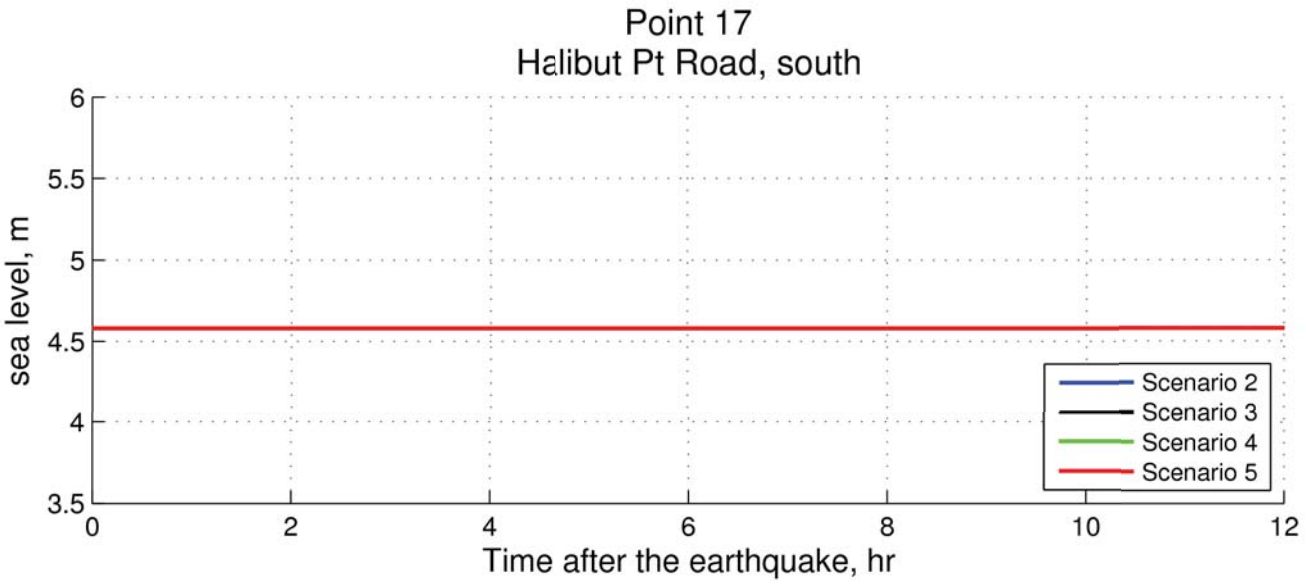
Point 17
Halibut Pt Road, south
sea level, m
6
5.5
5
4.5
4
3.5
0
2
4
6
8
10
12
Time after the earthquake, hr
Scenario 2
Scenario 3
Scenario 4
Scenario 5

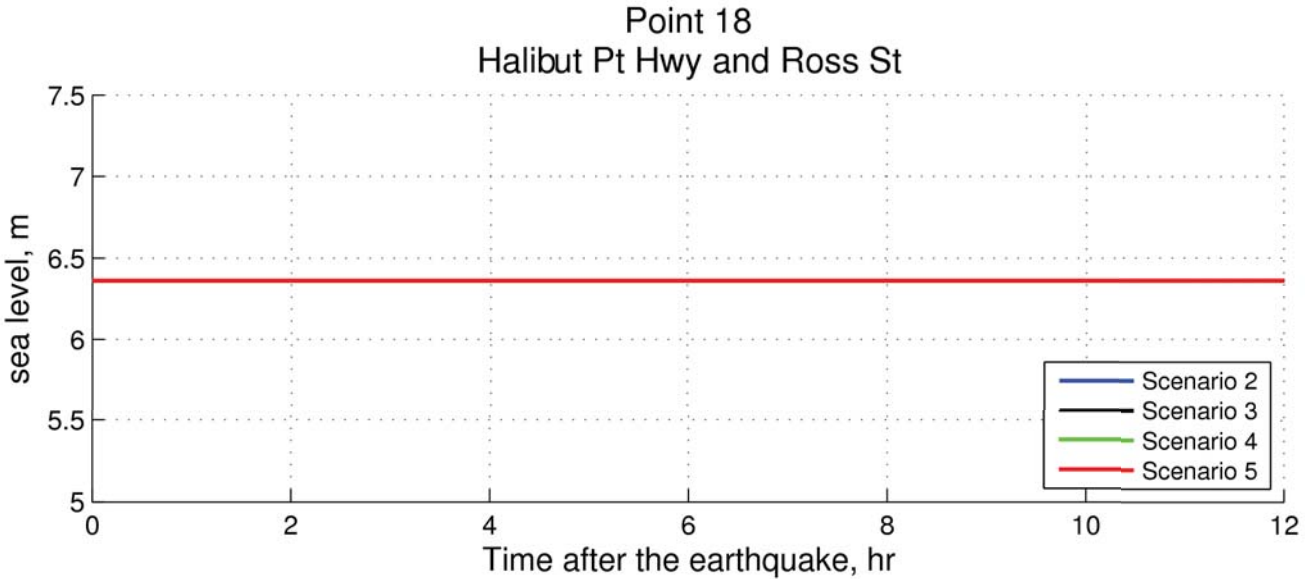
Point 18
Halibut Pt Hwy and Ross St
sea level, m
7.5
7
6.5
6
5.5
5
0
2
4
6
8
10
12
Time after the earthquake, hr
Scenario 2
Scenario 3
Scenario 4
Scenario 5

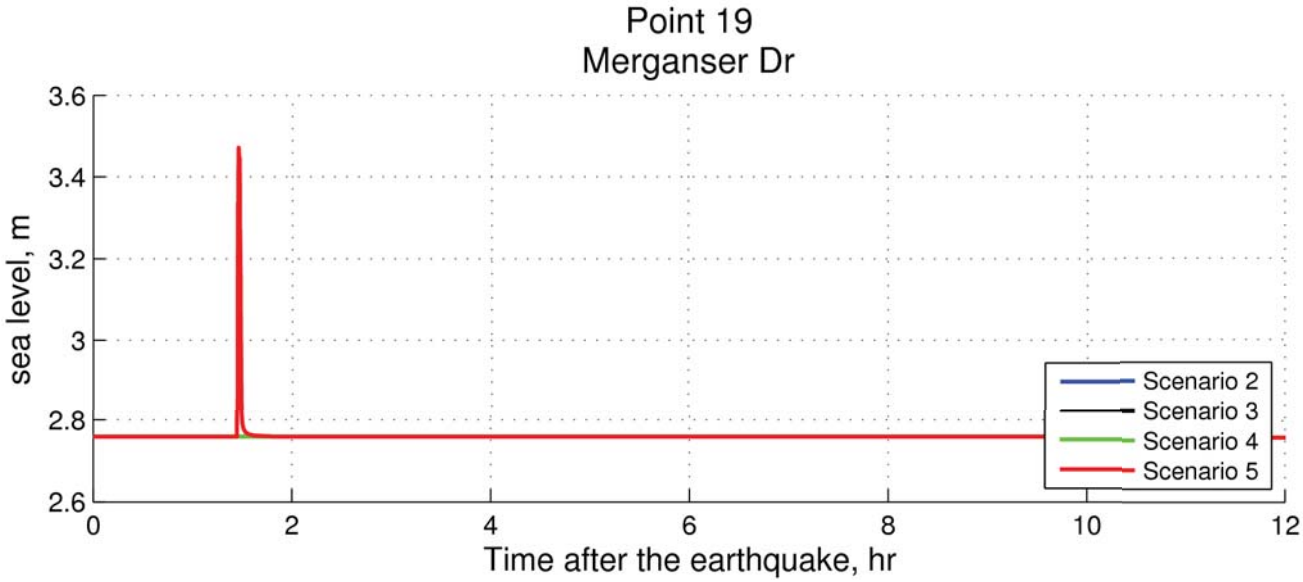
Point 19
Merganser Dr
sea level, m
Time after the earthquake, hr
Scenario 2
Scenario 3
Scenario 4
Scenario 5

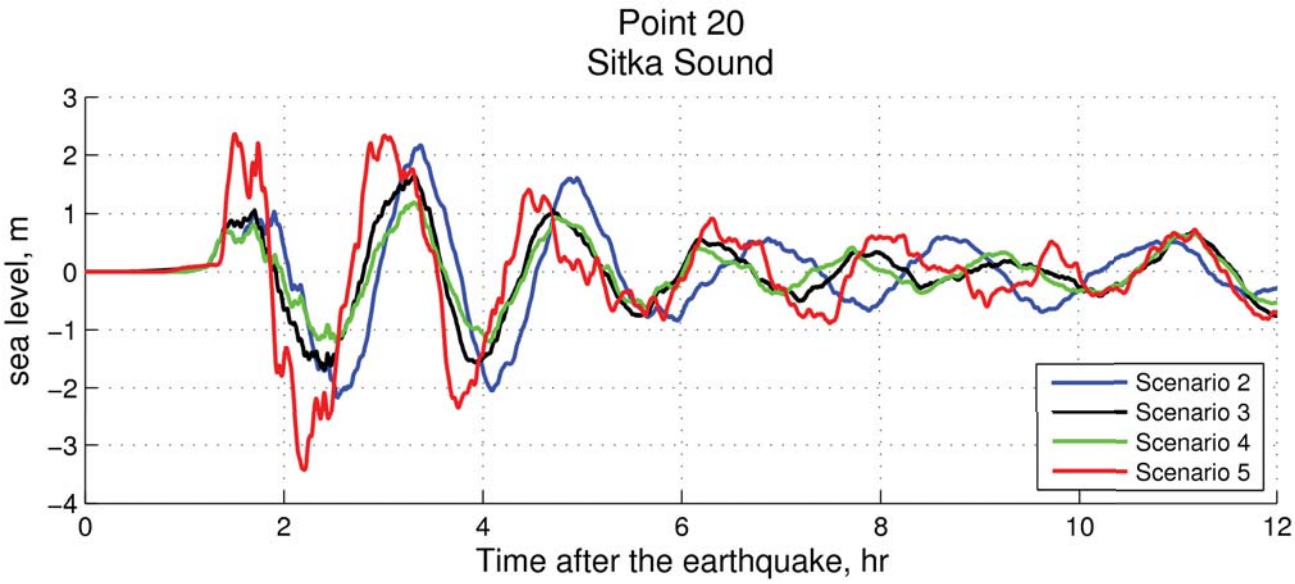
Point 20
Sitka Sound
sea level, m
Time after the earthquake, hr
Scenario 2
Scenario 3
Scenario 4
Scenario 5

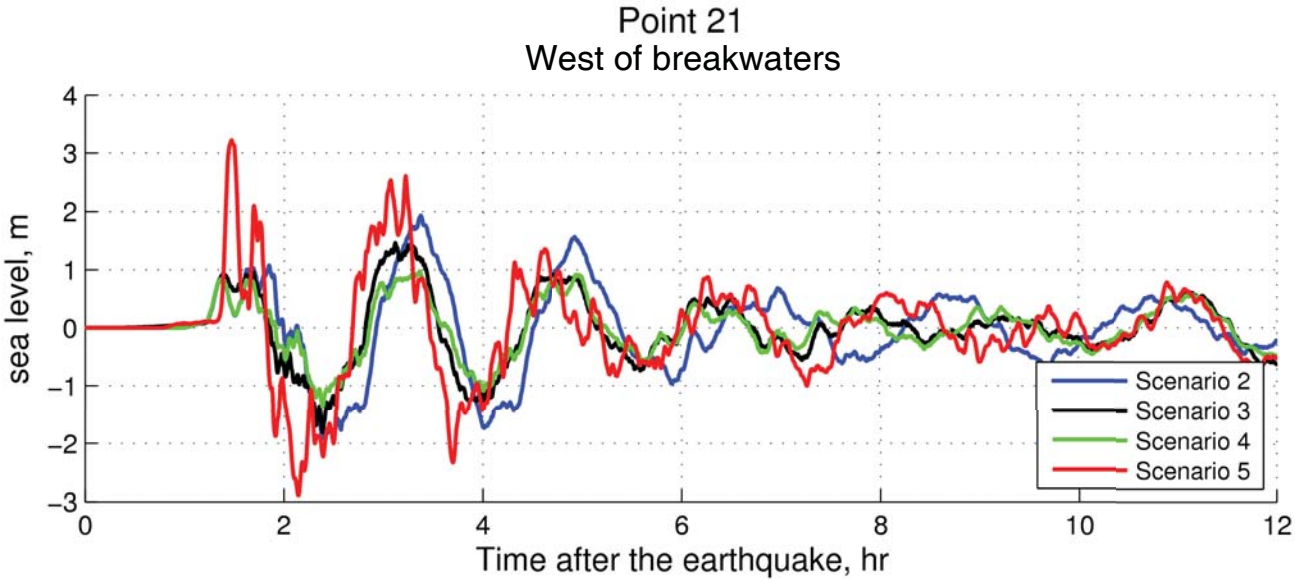
Point 21
West of breakwaters
sea level, m
Time after the earthquake, hr
Scenario 2
Scenario 3
Scenario 4
Scenario 5

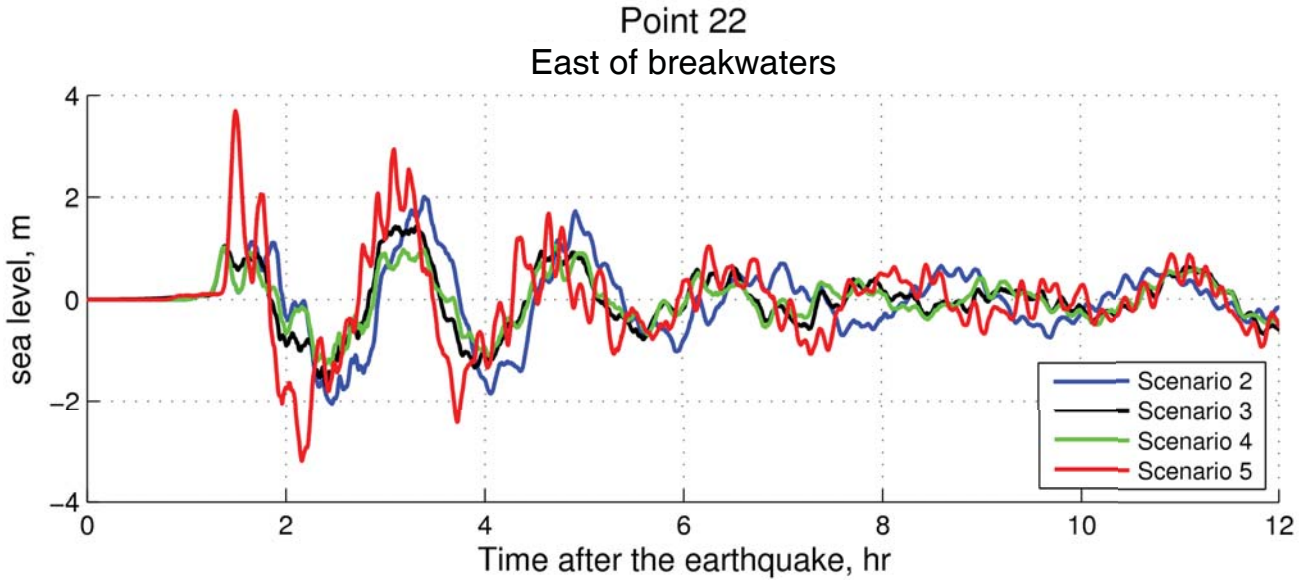
Point 22
East of breakwaters
sea level, m
Time after the earthquake, hr
Scenario 2
Scenario 3
Scenario 4
Scenario 5

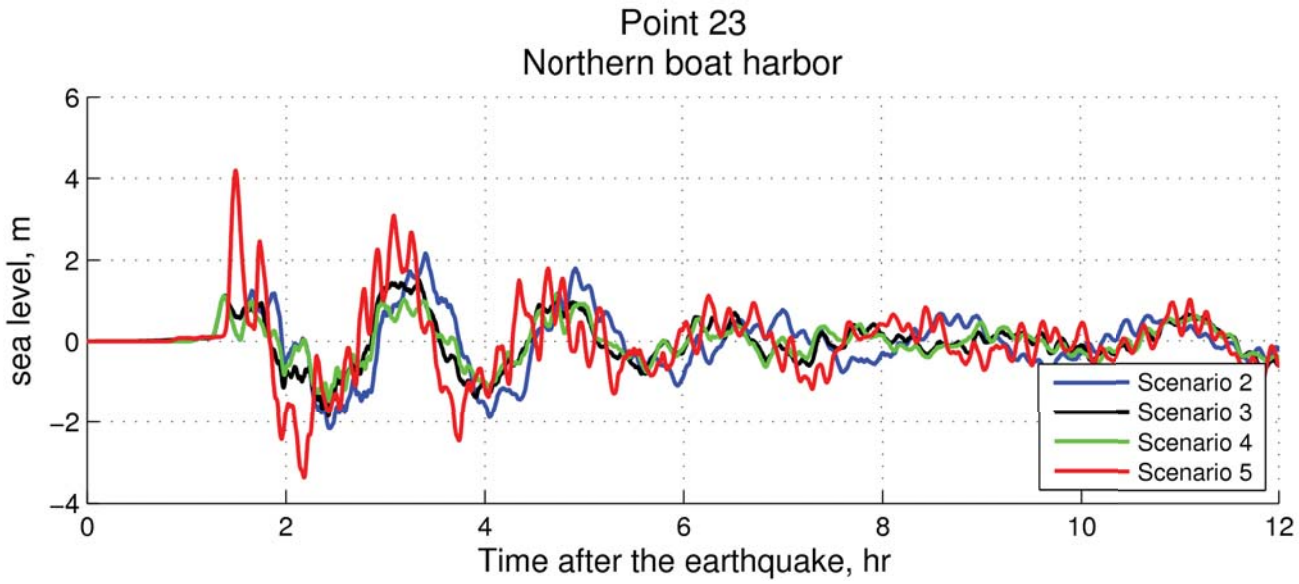
Point 23
Northern boat harbor
sea level, m
Time after the earthquake, hr
Scenario 2
Scenario 3
Scenario 4
Scenario 5

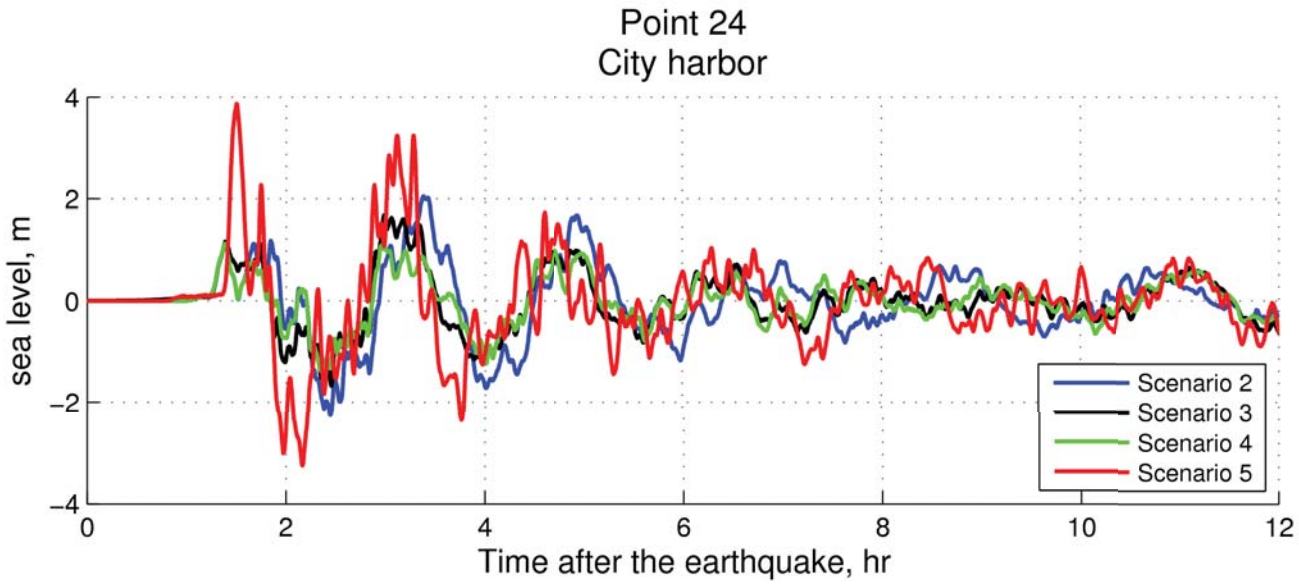
Point 24
City harbor
sea level, m
Time after the earthquake, hr
Scenario 2
Scenario 3
Scenario 4
Scenario 5

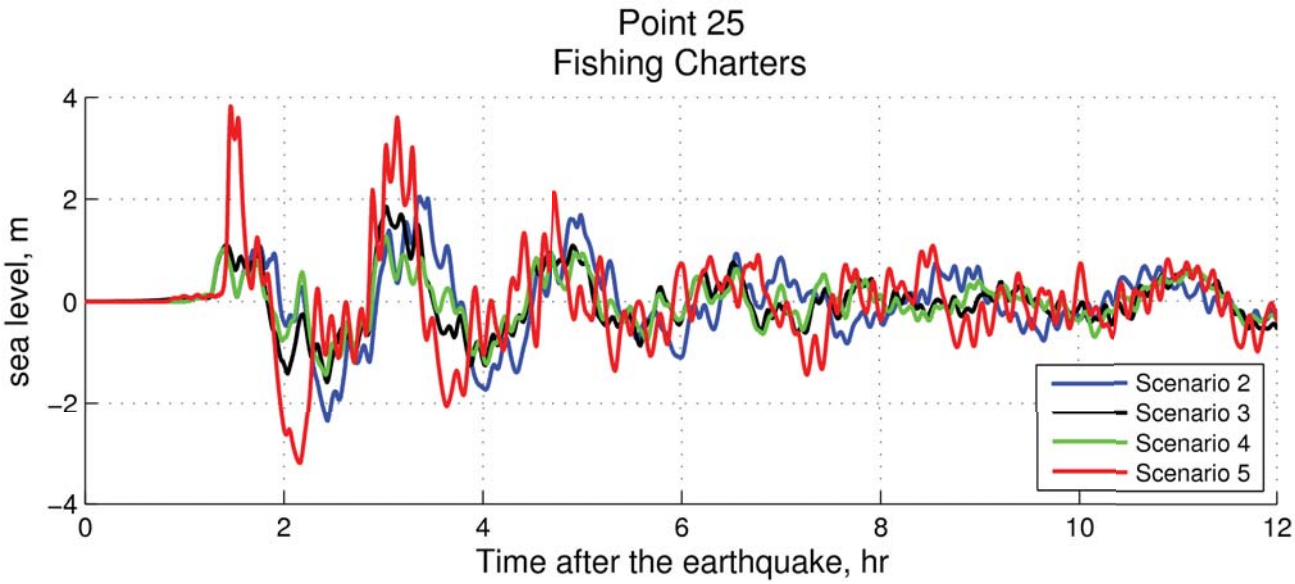
Point 25
Fishing Charters
sea level, m
Time after the earthquake, hr
Scenario 2
Scenario 3
Scenario 4
Scenario 5

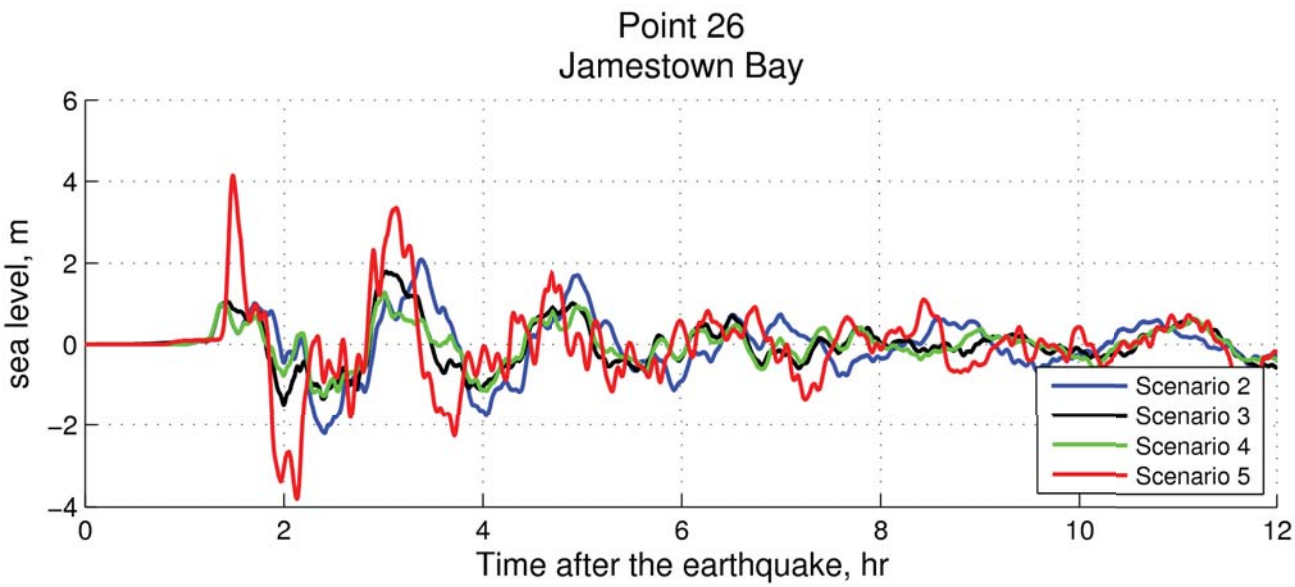
Point 26
Jamestown Bay
sea level, m
Time after the earthquake, hr
Scenario 2
Scenario 3
Scenario 4
Scenario 5

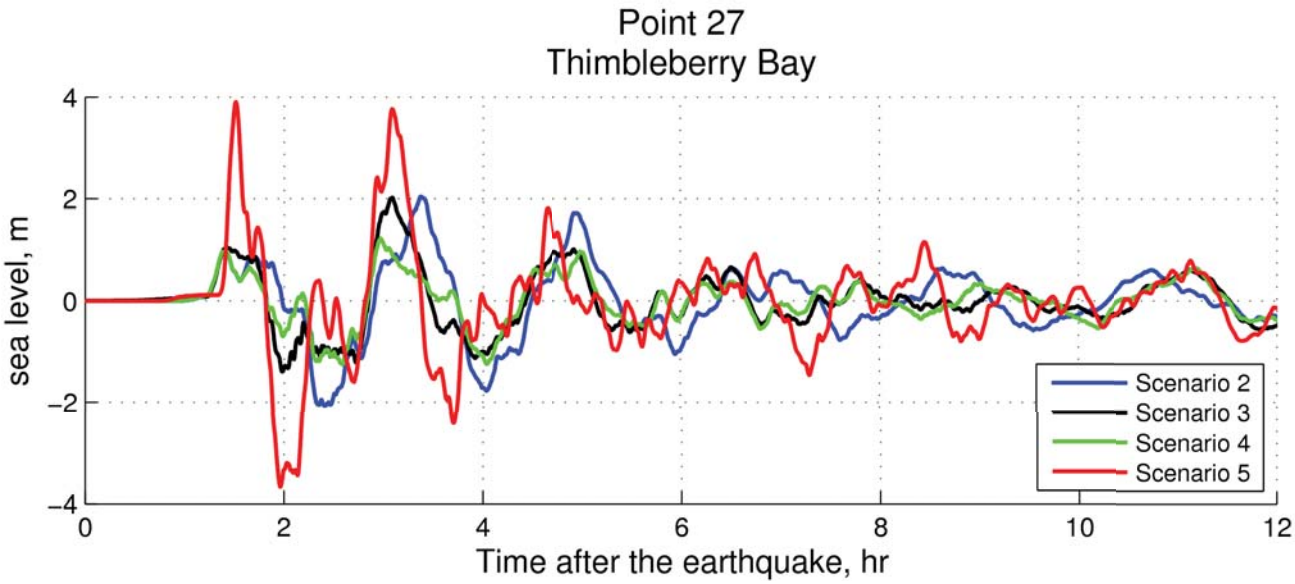
Point 27
Thimbleberry Bay
sea level, m
Time after the earthquake, hr
Scenario 2
Scenario 3
Scenario 4
Scenario 5

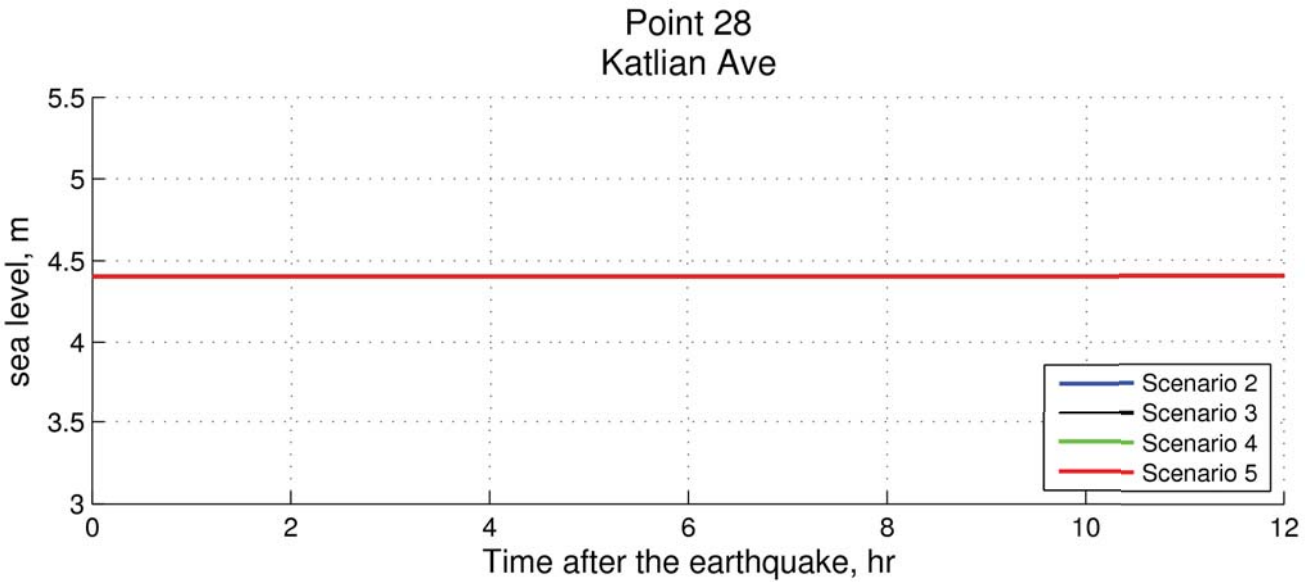
Point 28
Katlian Ave
sea level, m
Time after the earthquake, hr
Scenario 2
Scenario 3
Scenario 4
Scenario 5

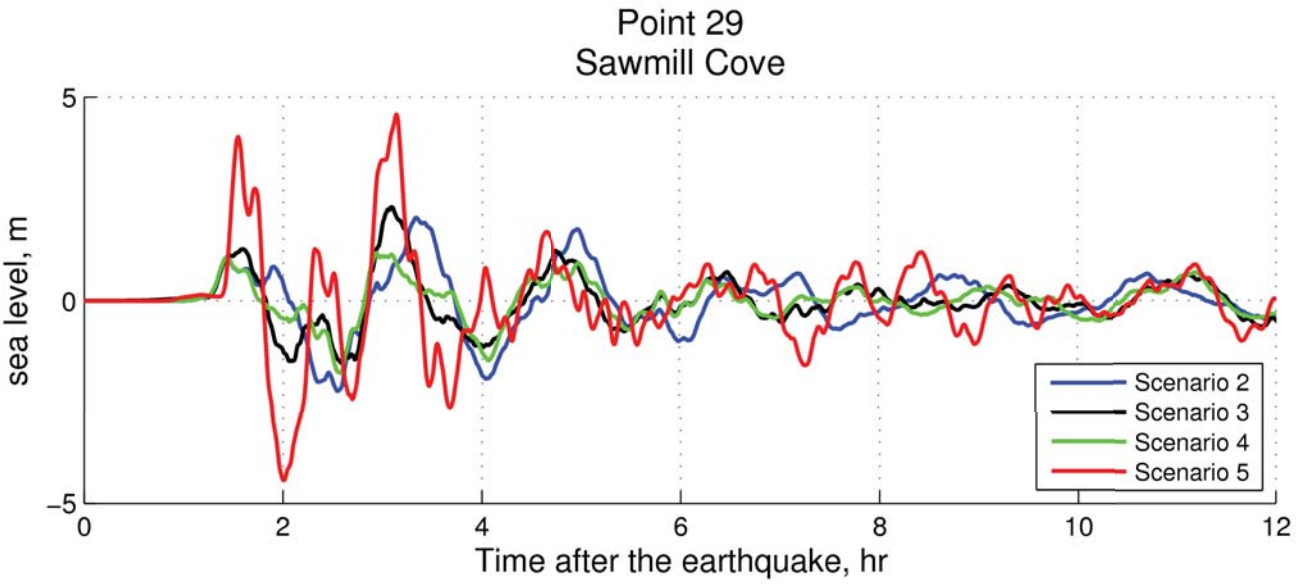
Point 29
Sawmill Cove
sea level, m
Time after the earthquake, hr
Scenario 2
Scenario 3
Scenario 4
Scenario 5

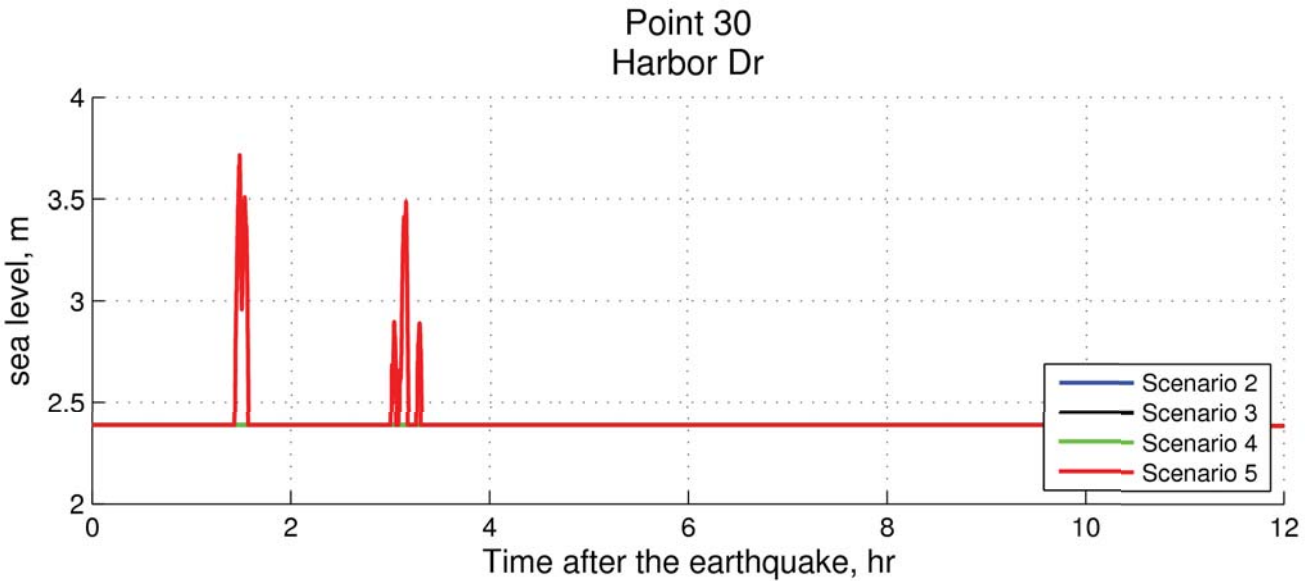
Point 30
Harbor Dr
sea level, m
Time after the earthquake, hr
Scenario 2
Scenario 3
Scenario 4
Scenario 5

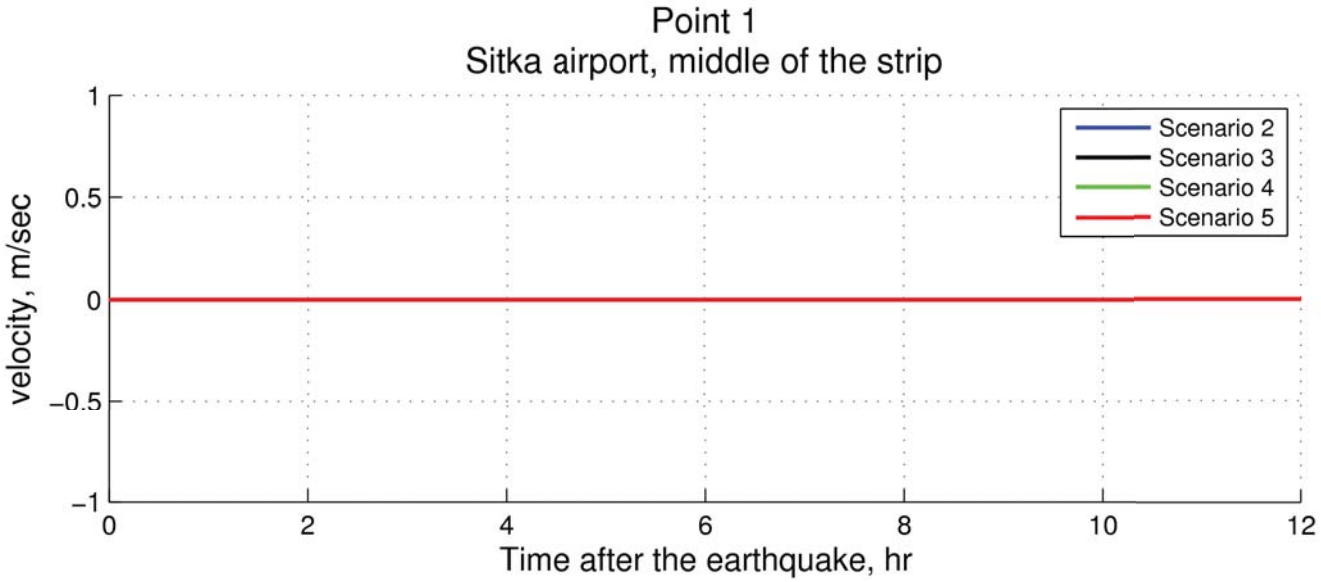
Point 1
Sitka airport, middle of the strip
velocity, m/sec
Time after the earthquake, hr
Scenario 2
Scenario 3
Scenario 4
Scenario 5
1
0.5
0
−0.5
−1
0
2
4
6
8
10
12

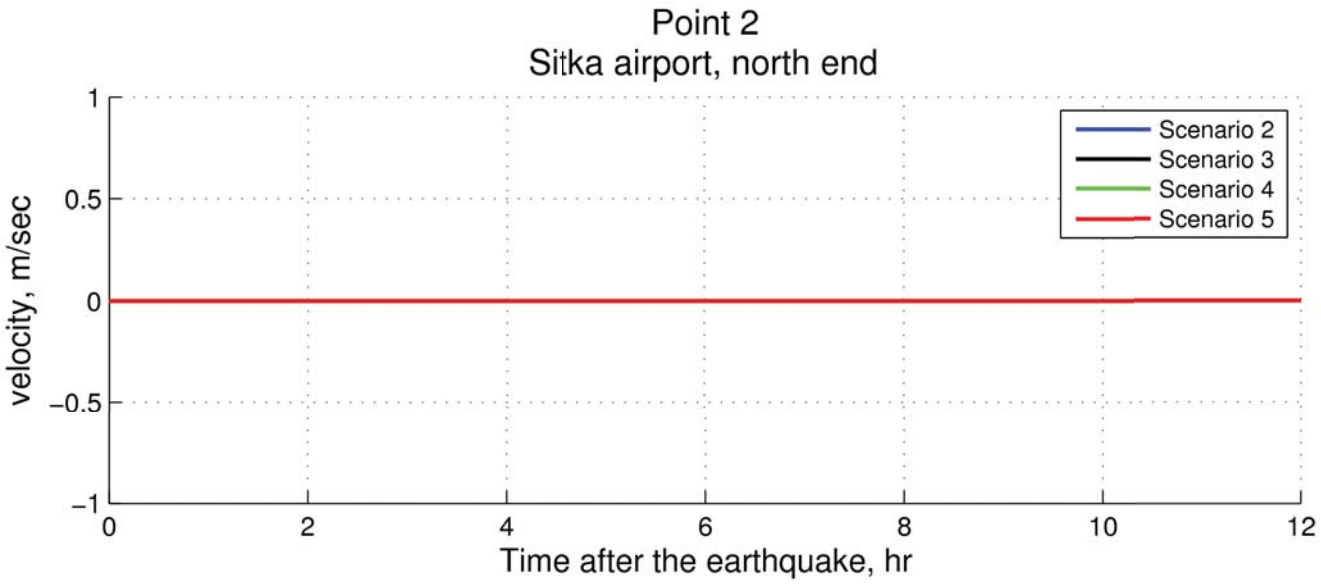
Point 2
Sitka airport, north end
velocity, m/sec
Time after the earthquake, hr
Scenario 2
Scenario 3
Scenario 4
Scenario 5
1
0.5
0
−0.5
−1
0
2
4
6
8
10
12

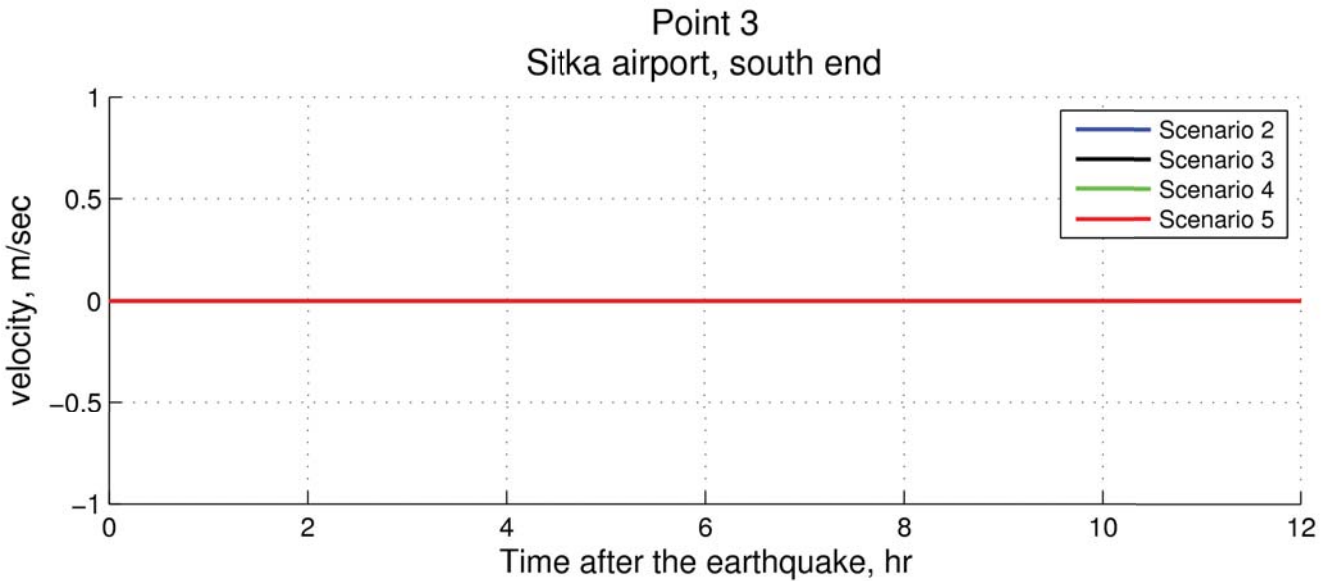
Point 3
Sitka airport, south end
velocity, m/sec
Time after the earthquake, hr
Scenario 2
Scenario 3
Scenario 4
Scenario 5
1
0.5
0
−0.5
−1
0
2
4
6
8
10
12

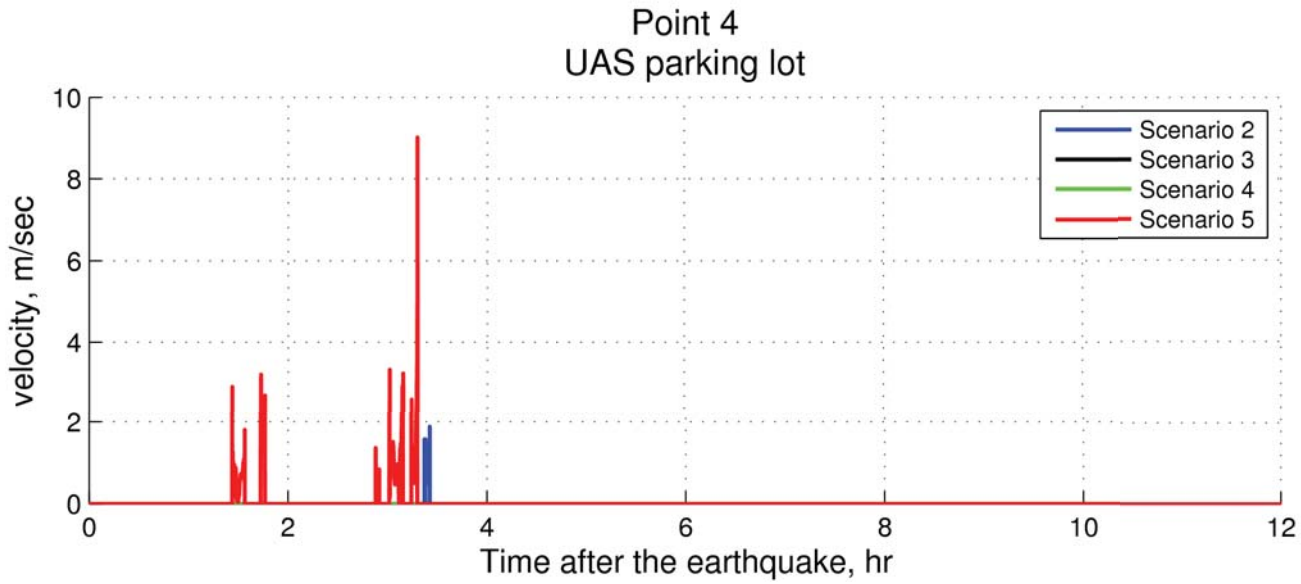
Point 4
UAS parking lot
velocity, m/sec
Time after the earthquake, hr
Scenario 2
Scenario 3
Scenario 4
Scenario 5

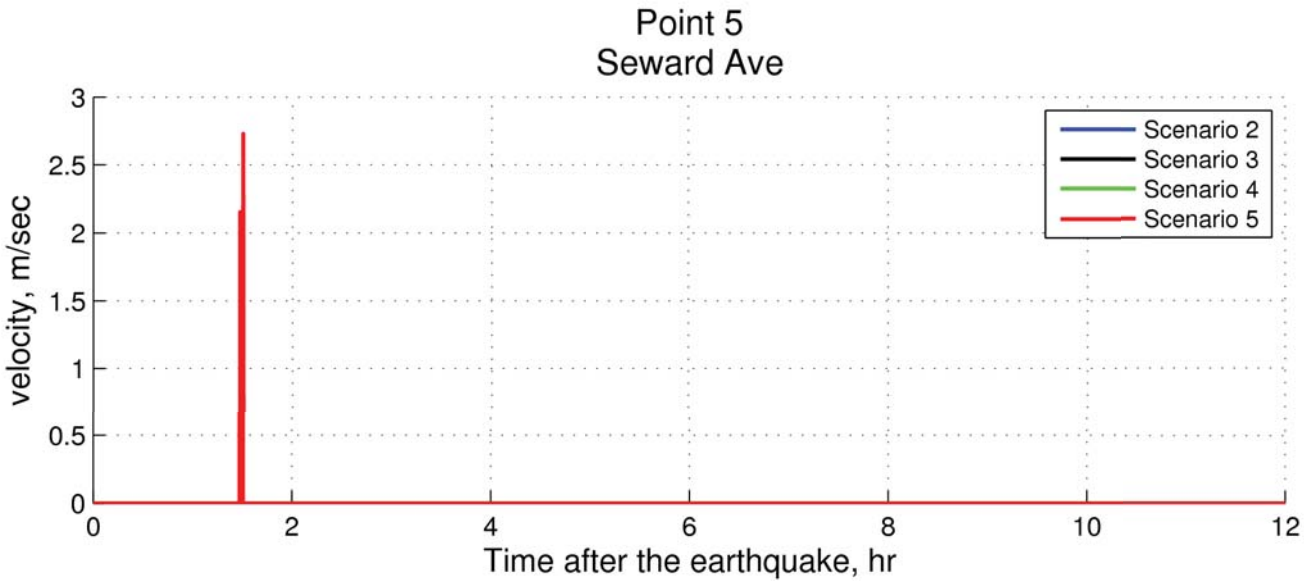
Point 5
Seward Ave
velocity, m/sec
Time after the earthquake, hr
Scenario 2
Scenario 3
Scenario 4
Scenario 5

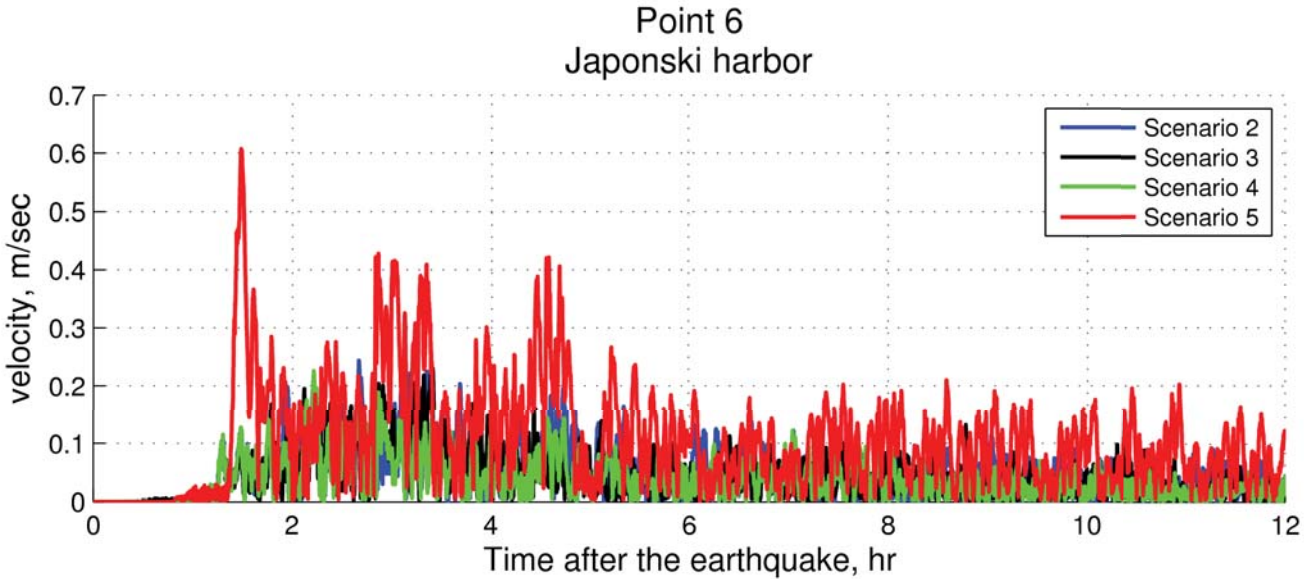
Point 6
Japonski harbor
velocity, m/sec
Time after the earthquake, hr
Scenario 2
Scenario 3
Scenario 4
Scenario 5

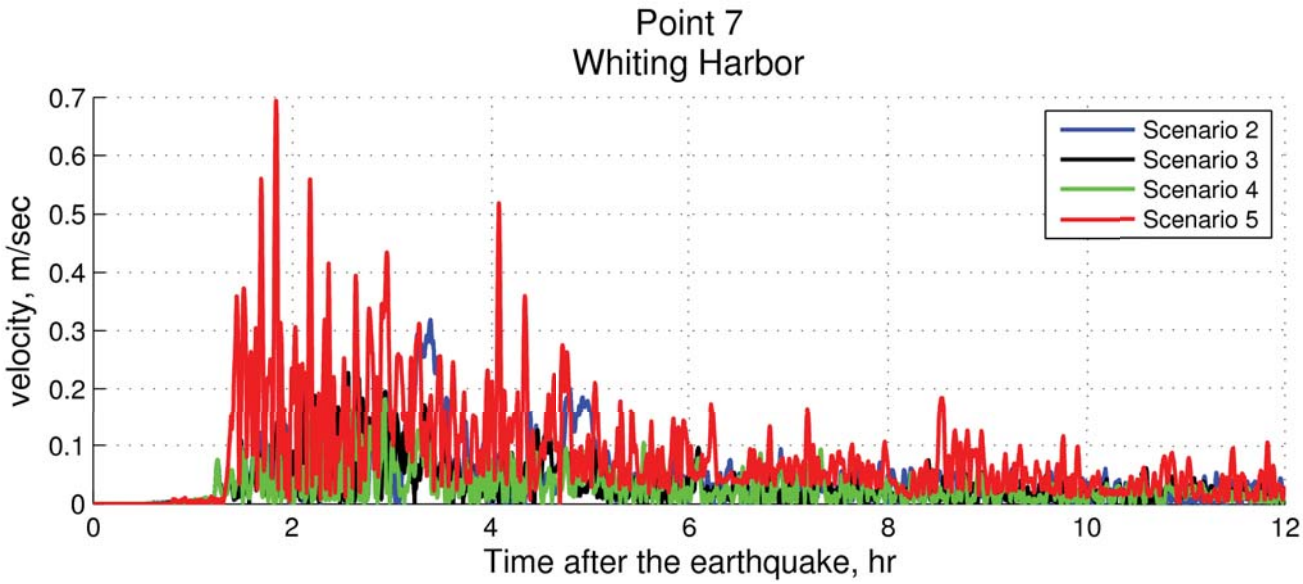
Point 7
Whiting Harbor
velocity, m/sec
Time after the earthquake, hr
Scenario 2
Scenario 3
Scenario 4
Scenario 5

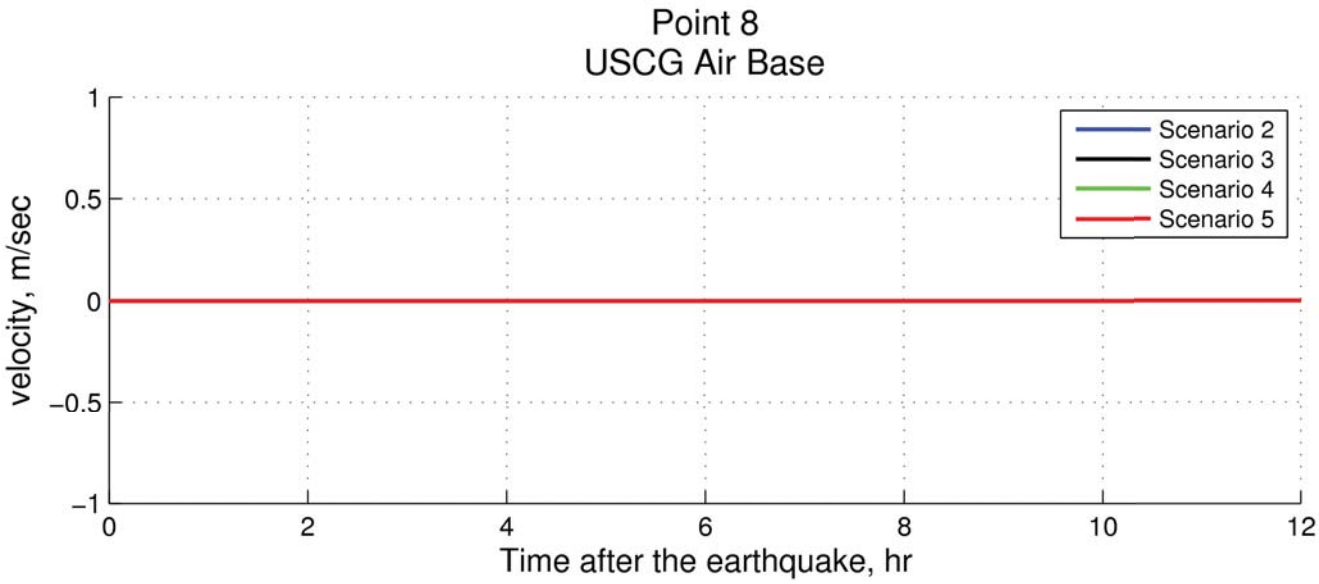
Point 8
USCG Air Base
velocity, m/sec
Time after the earthquake, hr
Scenario 2
Scenario 3
Scenario 4
Scenario 5

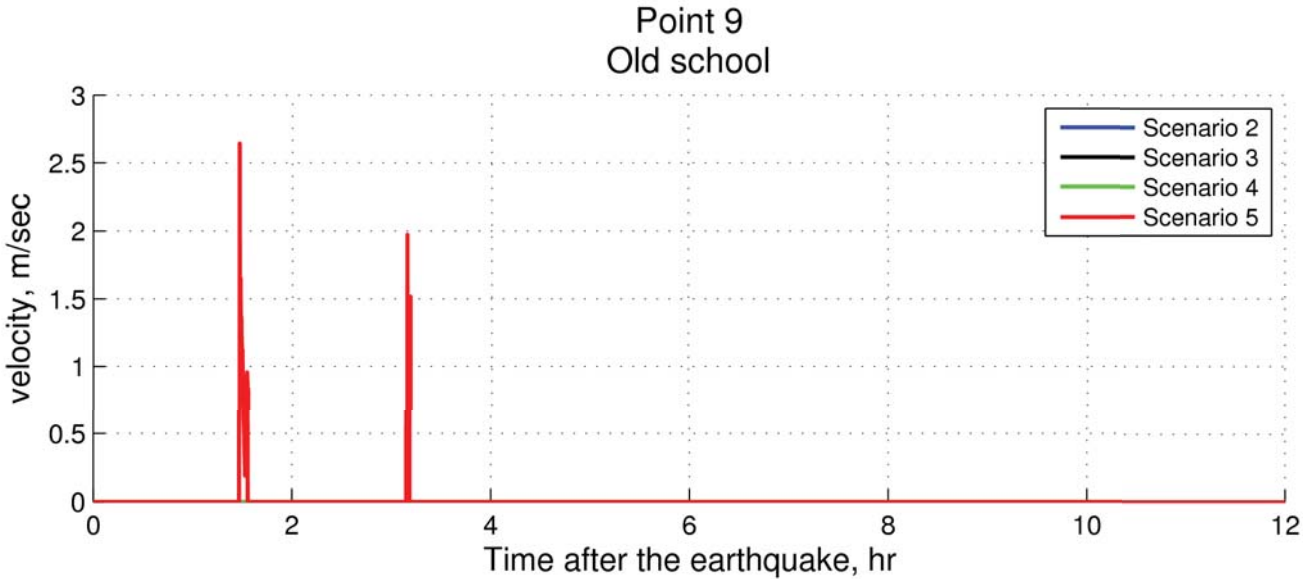
Point 9
Old school
velocity, m/sec
Time after the earthquake, hr
Scenario 2
Scenario 3
Scenario 4
Scenario 5

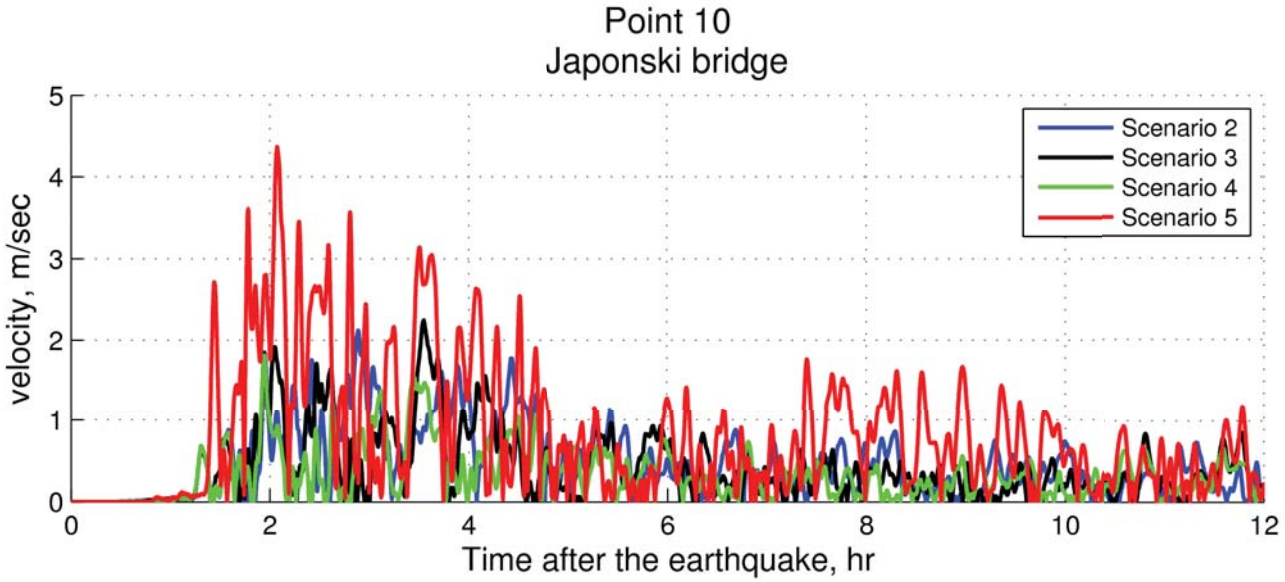
Point 10
Japonski bridge
velocity, m/sec
Time after the earthquake, hr
Scenario 2
Scenario 3
Scenario 4
Scenario 5

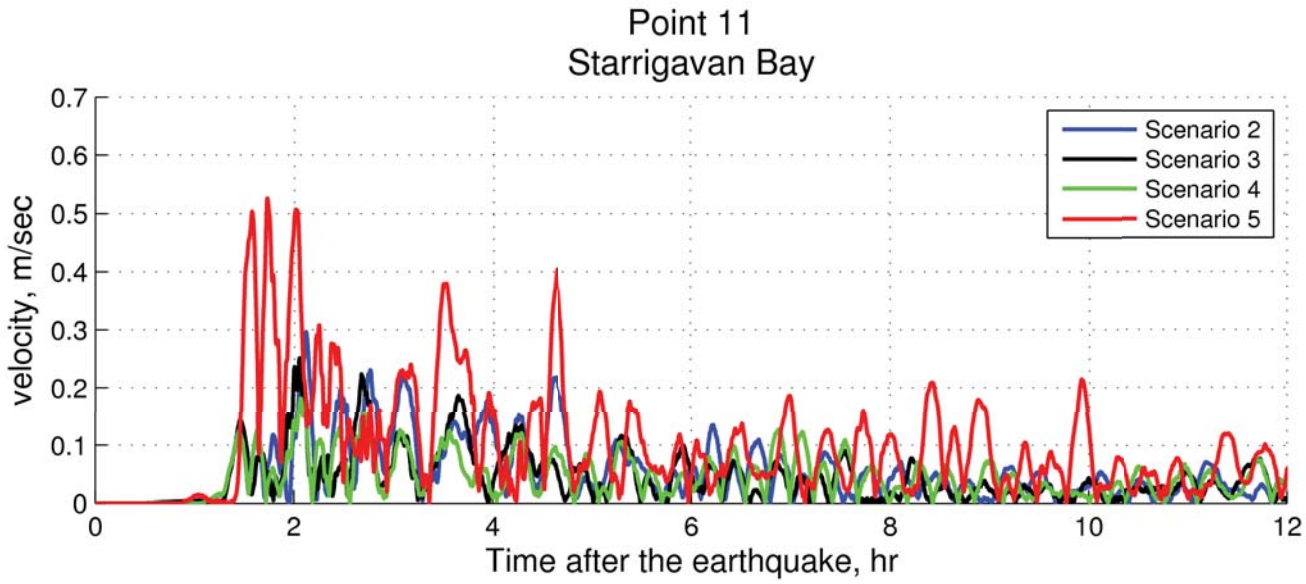
Point 11
Starrigavan Bay
velocity, m/sec
Time after the earthquake, hr
Scenario 2
Scenario 3
Scenario 4
Scenario 5

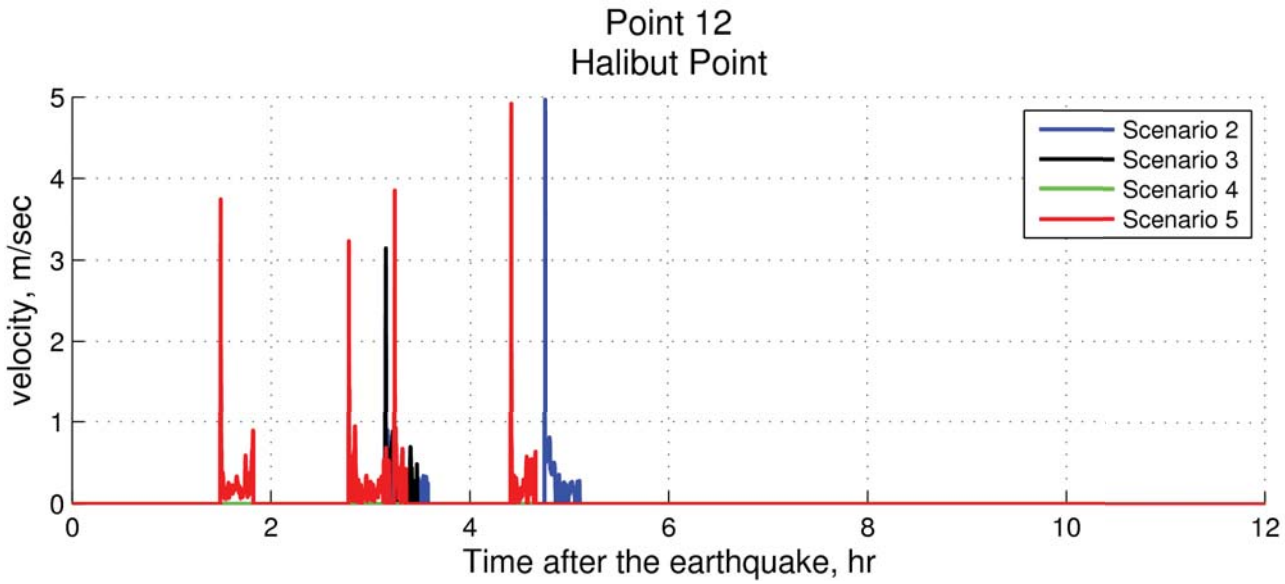
Point 12
Halibut Point
velocity, m/sec
Time after the earthquake, hr
Scenario 2
Scenario 3
Scenario 4
Scenario 5

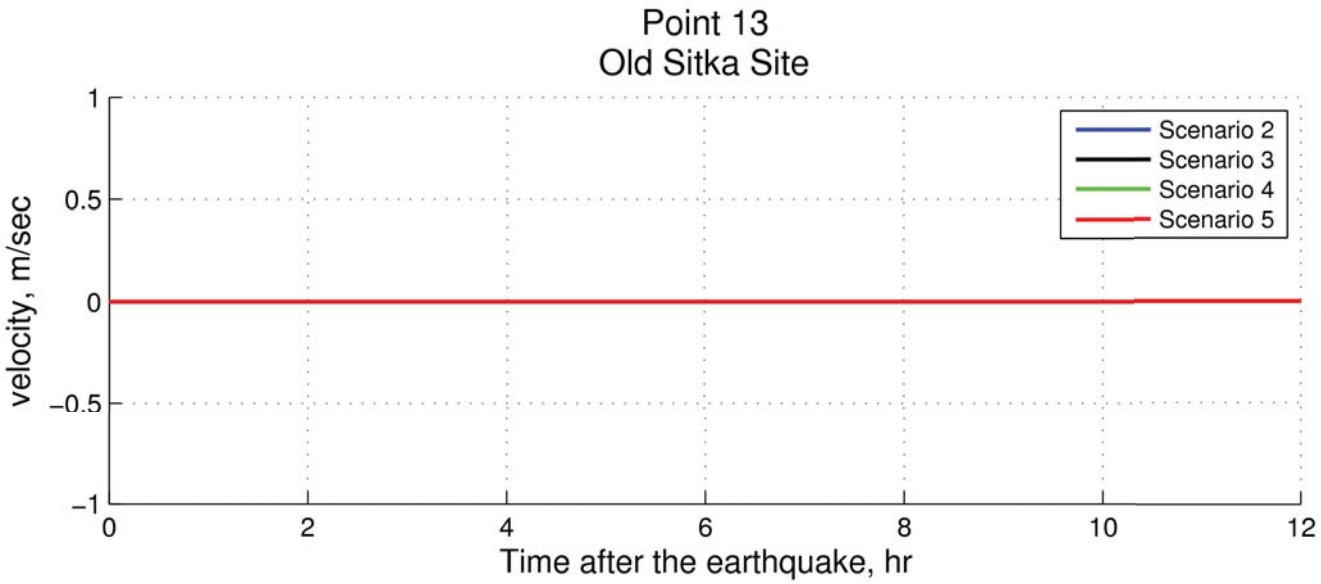
Point 13
Old Sitka Site
velocity, m/sec
Time after the earthquake, hr
Scenario 2
Scenario 3
Scenario 4
Scenario 5
1
0.5
0
−0.5
−1
0
2
4
6
8
10
12

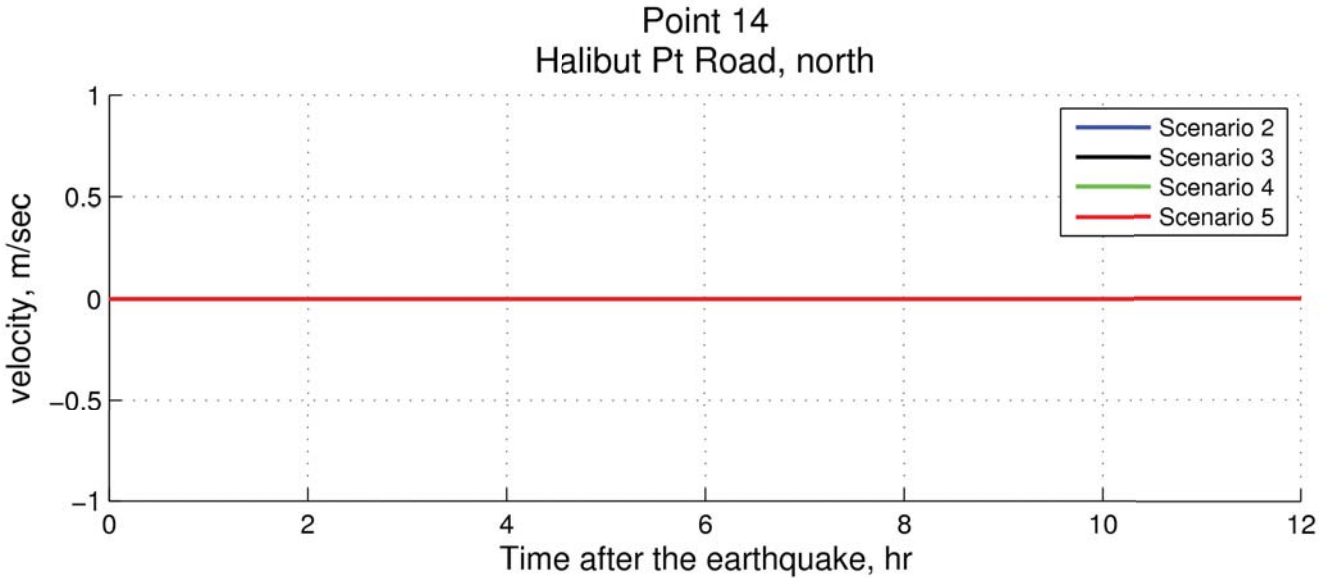
Point 14
Halibut Pt Road, north
velocity, m/sec
Time after the earthquake, hr
Scenario 2
Scenario 3
Scenario 4
Scenario 5
1
0.5
0
−0.5
−1
0
2
4
6
8
10
12

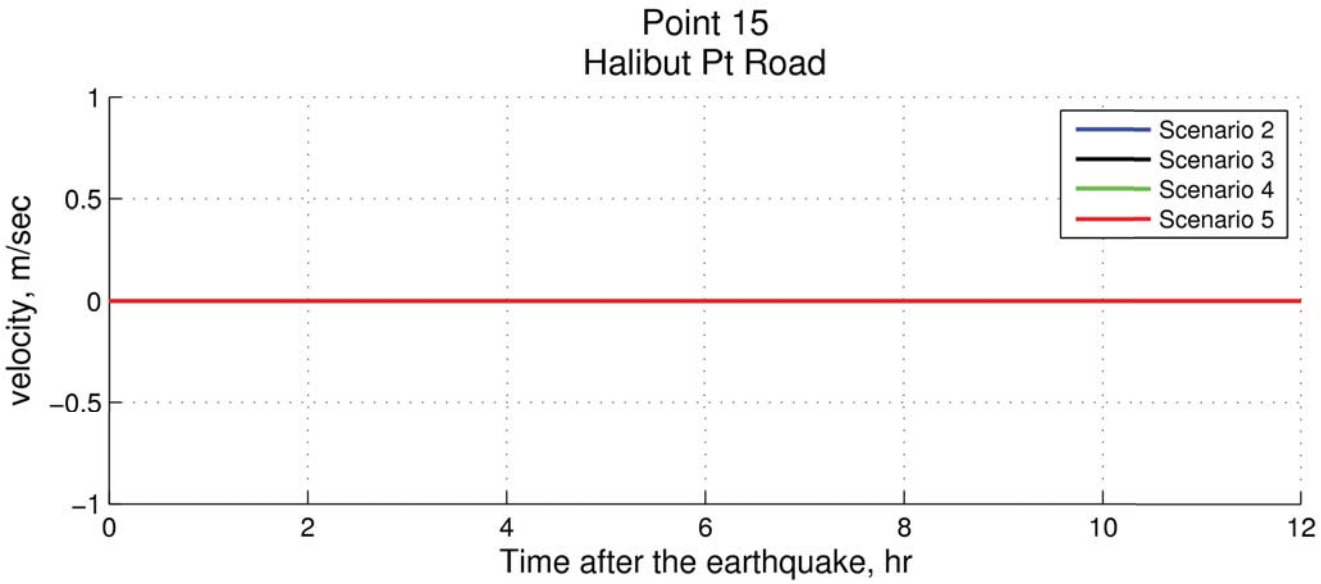
Point 15
Halibut Pt Road
velocity, m/sec
Time after the earthquake, hr
Scenario 2
Scenario 3
Scenario 4
Scenario 5
1
0.5
0
−0.5
−1
0
2
4
6
8
10
12

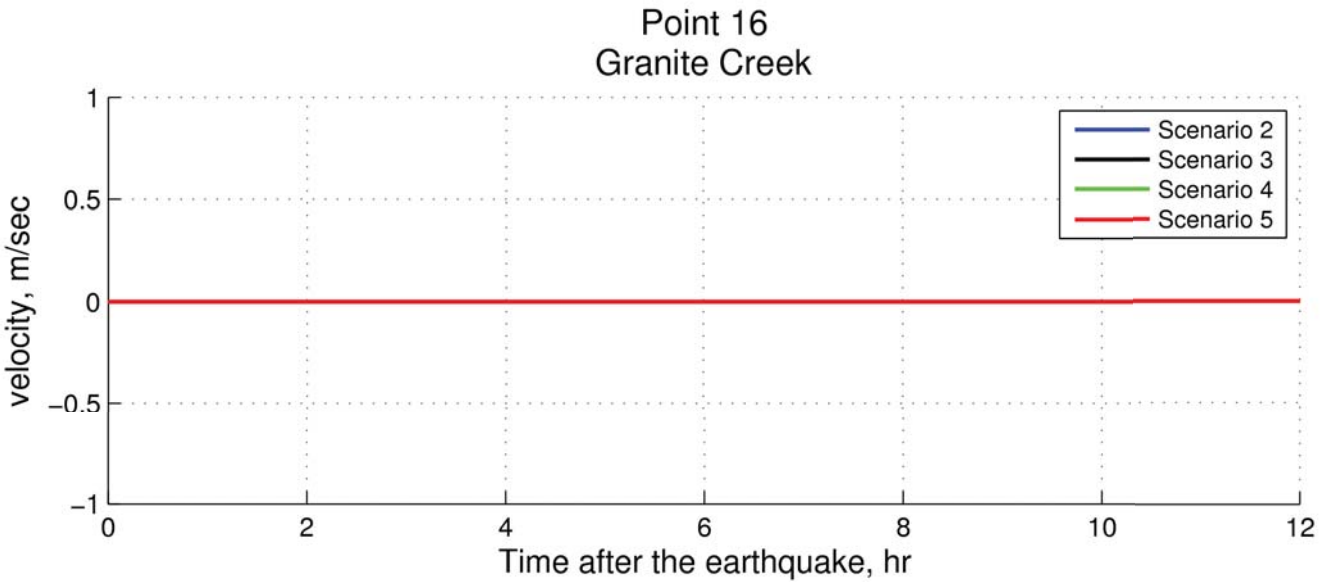
Point 16
Granite Creek
Scenario 2
Scenario 3
Scenario 4
Scenario 5
velocity, m/sec
1
0.5
0
−0.5
−1
0
2
4
6
8
10
12
Time after the earthquake, hr

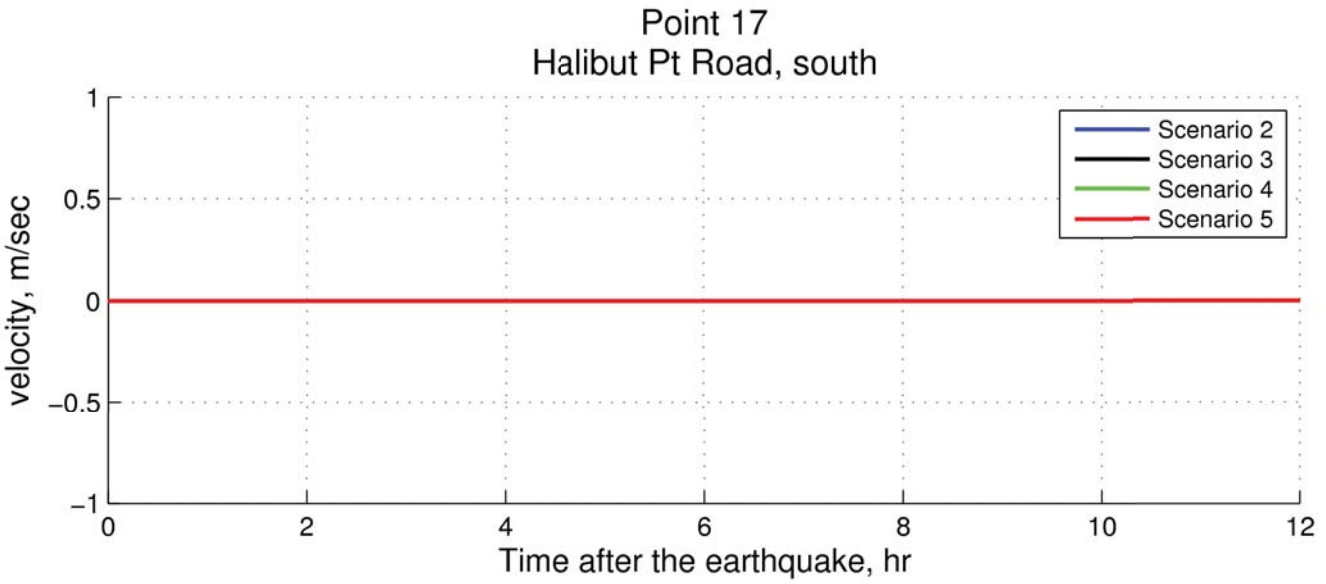
Point 17
Halibut Pt Road, south
Scenario 2
Scenario 3
Scenario 4
Scenario 5
velocity, m/sec
1
0.5
0
−0.5
−1
0
2
4
6
8
10
12
Time after the earthquake, hr

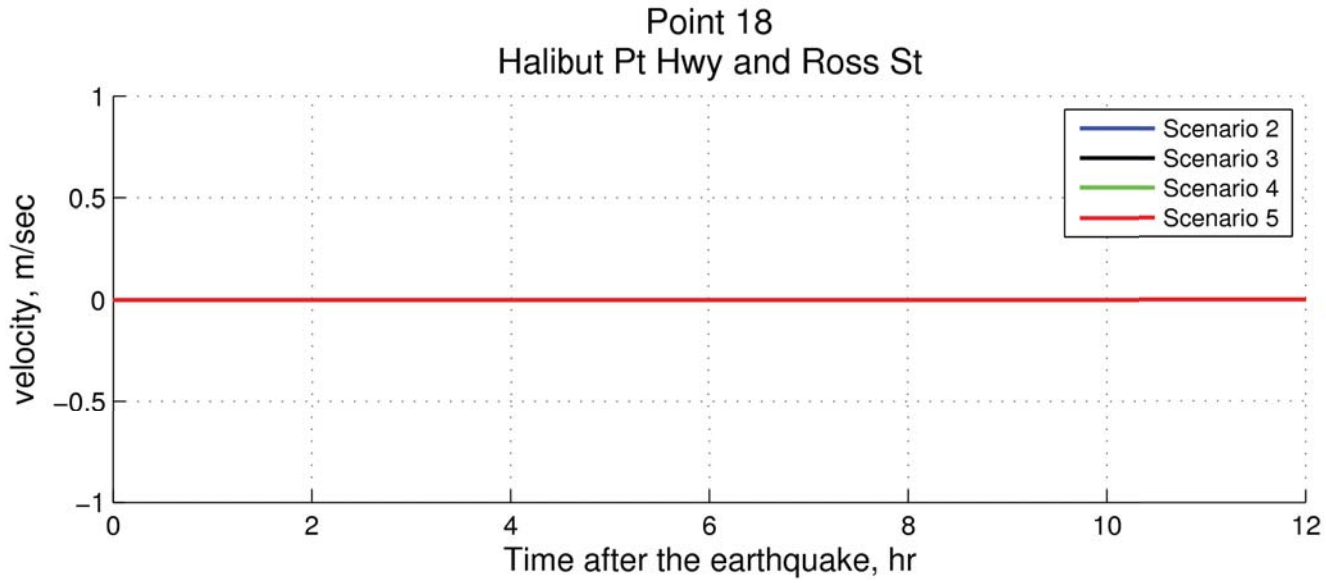
Point 18
Halibut Pt Hwy and Ross St
Scenario 2
Scenario 3
Scenario 4
Scenario 5
velocity, m/sec
1
0.5
0
−0.5
−1
0
2
4
6
8
10
12
Time after the earthquake, hr

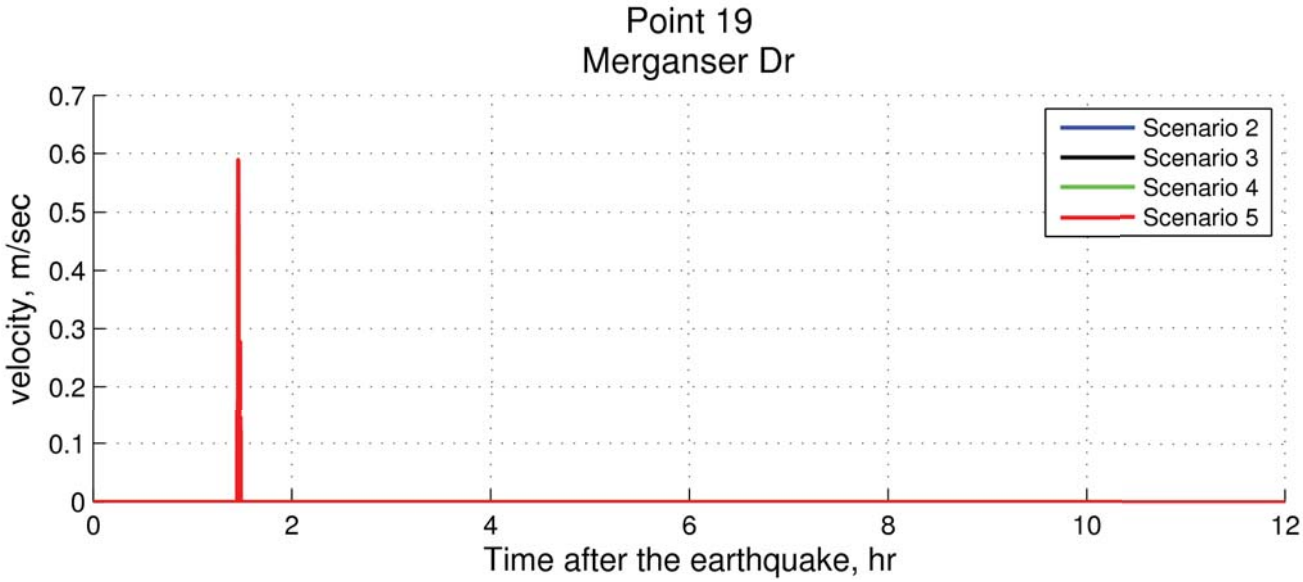
Point 19
Merganser Dr
velocity, m/sec
Time after the earthquake, hr
Scenario 2
Scenario 3
Scenario 4
Scenario 5

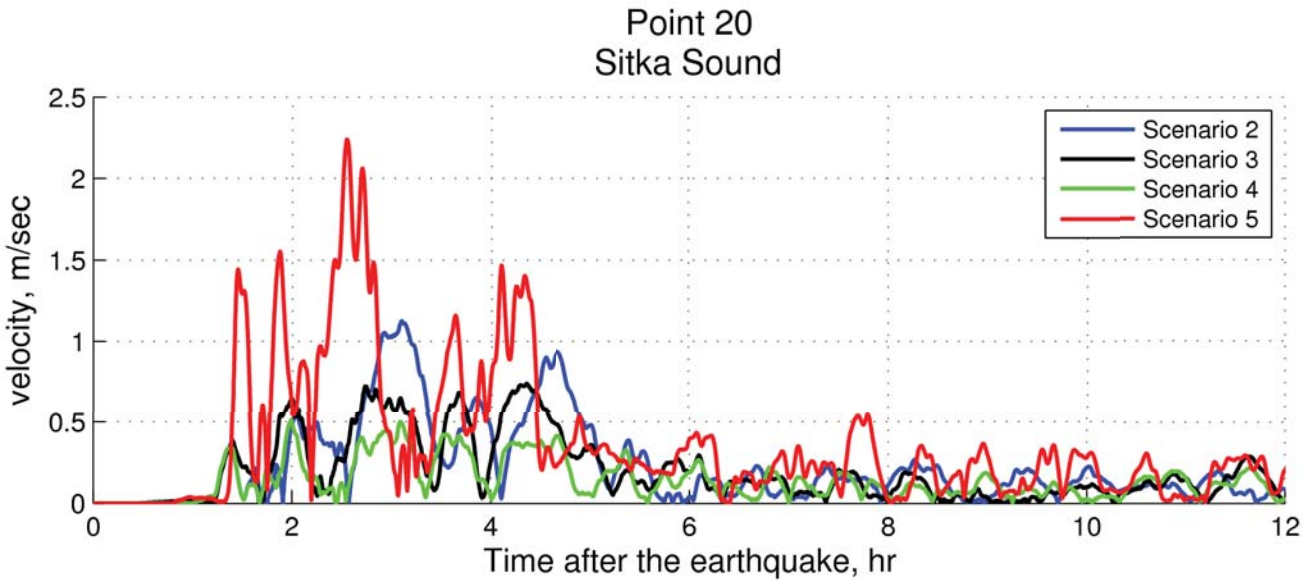
Point 20
Sitka Sound
velocity, m/sec
Time after the earthquake, hr
Scenario 2
Scenario 3
Scenario 4
Scenario 5

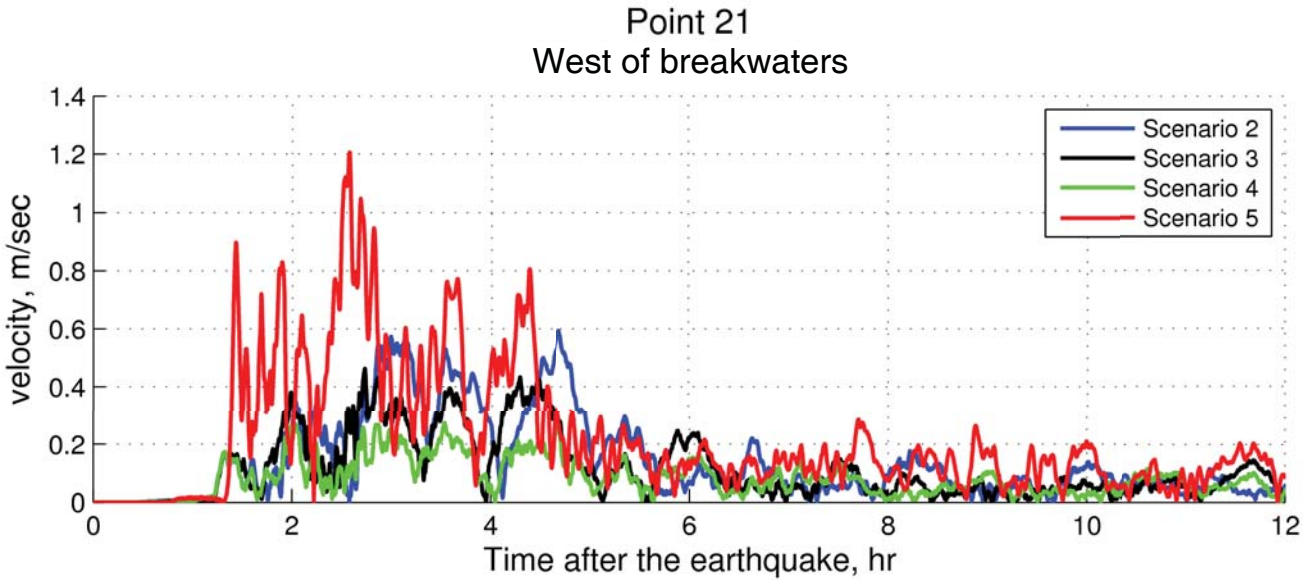
Point 21
West of breakwaters
velocity, m/sec
Time after the earthquake, hr
Scenario 2
Scenario 3
Scenario 4
Scenario 5

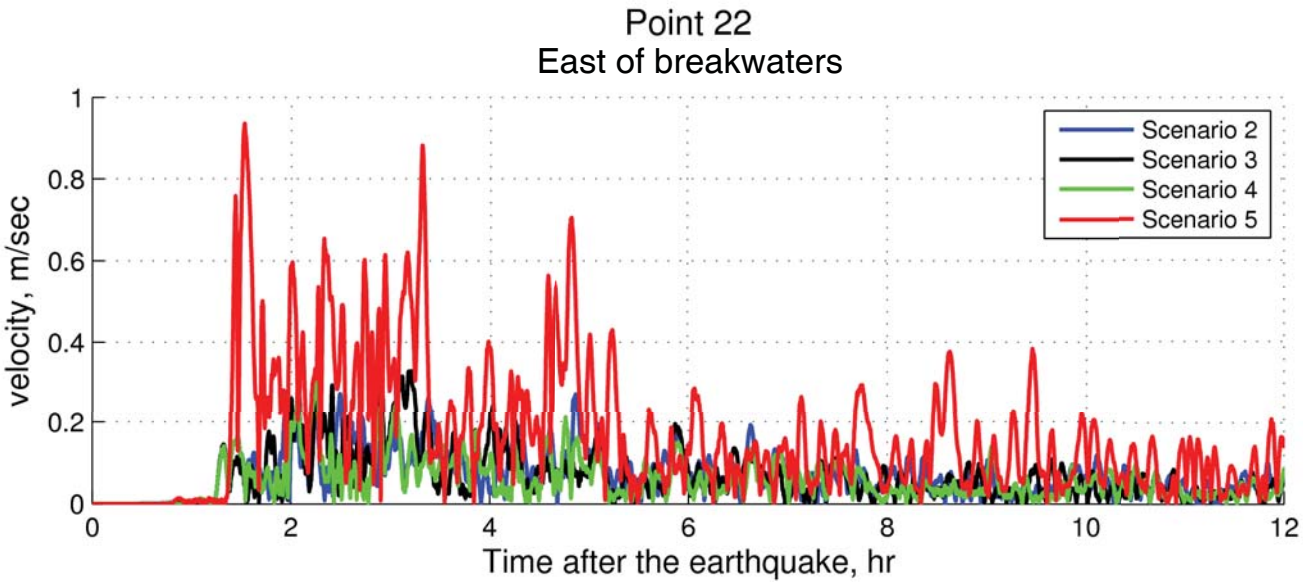
Point 22
East of breakwaters
velocity, m/sec
Time after the earthquake, hr
Scenario 2
Scenario 3
Scenario 4
Scenario 5

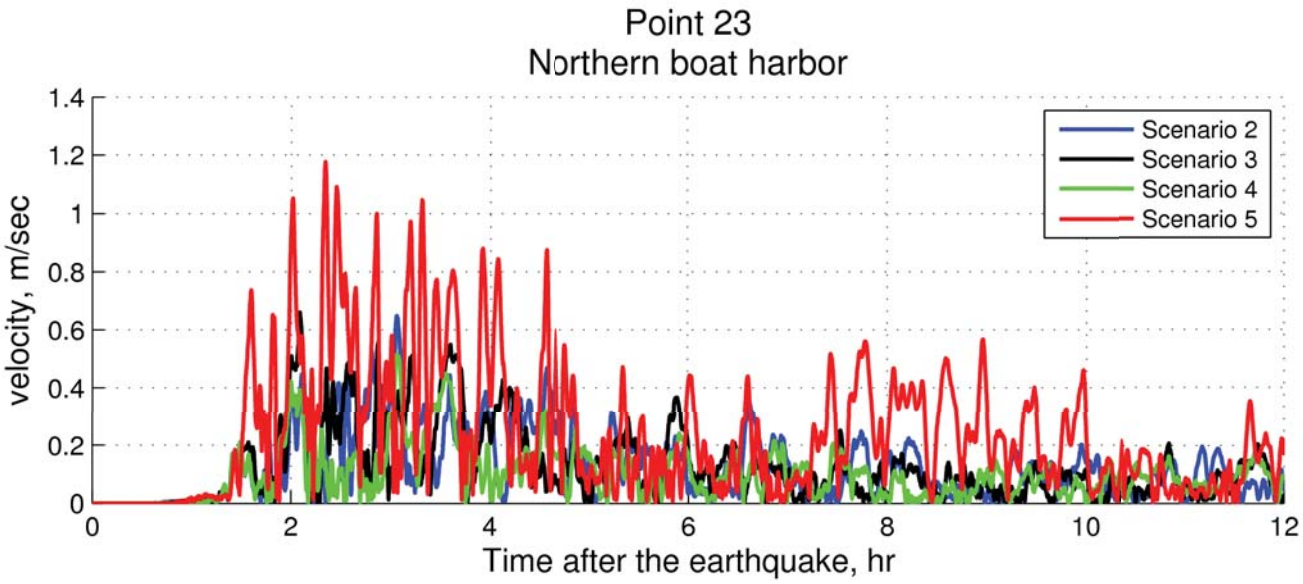
Point 23
Northern boat harbor
velocity, m/sec
Time after the earthquake, hr
Scenario 2
Scenario 3
Scenario 4
Scenario 5

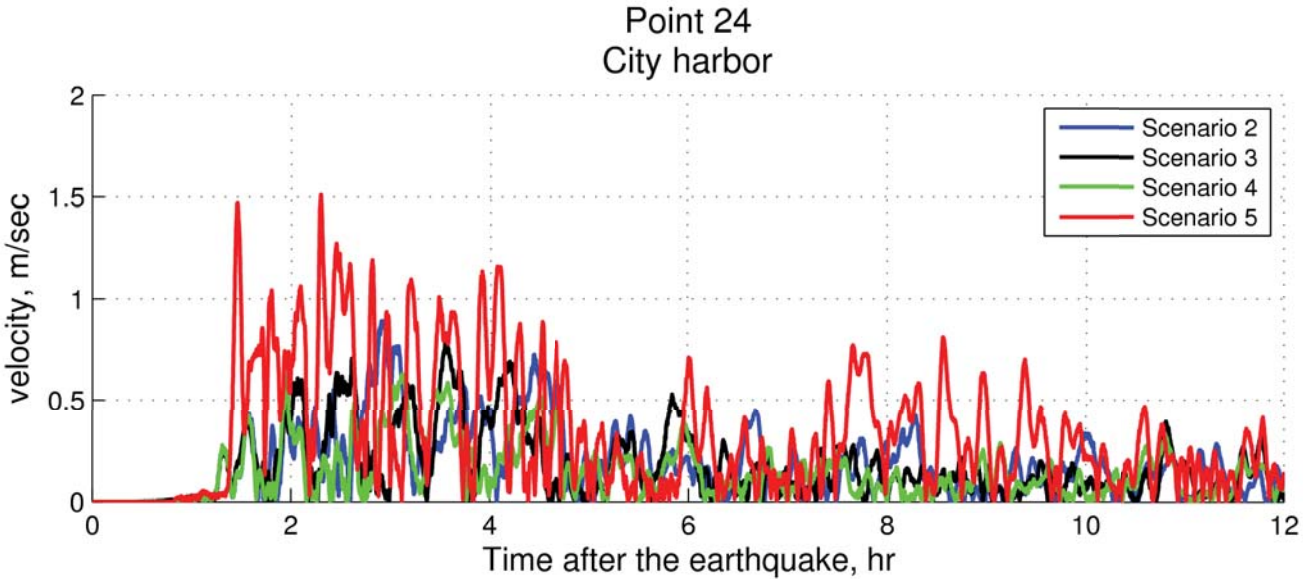
Point 24
City harbor
velocity, m/sec
Time after the earthquake, hr
Scenario 2
Scenario 3
Scenario 4
Scenario 5

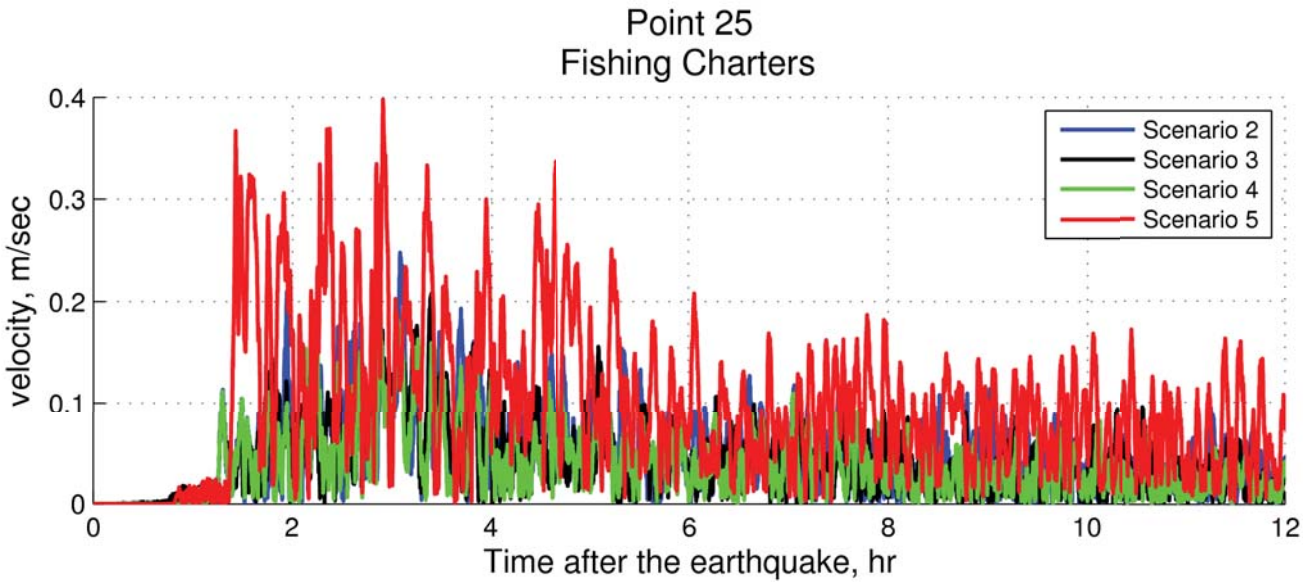
Point 25
Fishing Charters
velocity, m/sec
Time after the earthquake, hr
Scenario 2
Scenario 3
Scenario 4
Scenario 5
0
0.1
0.2
0.3
0.4
0
2
4
6
8
10
12

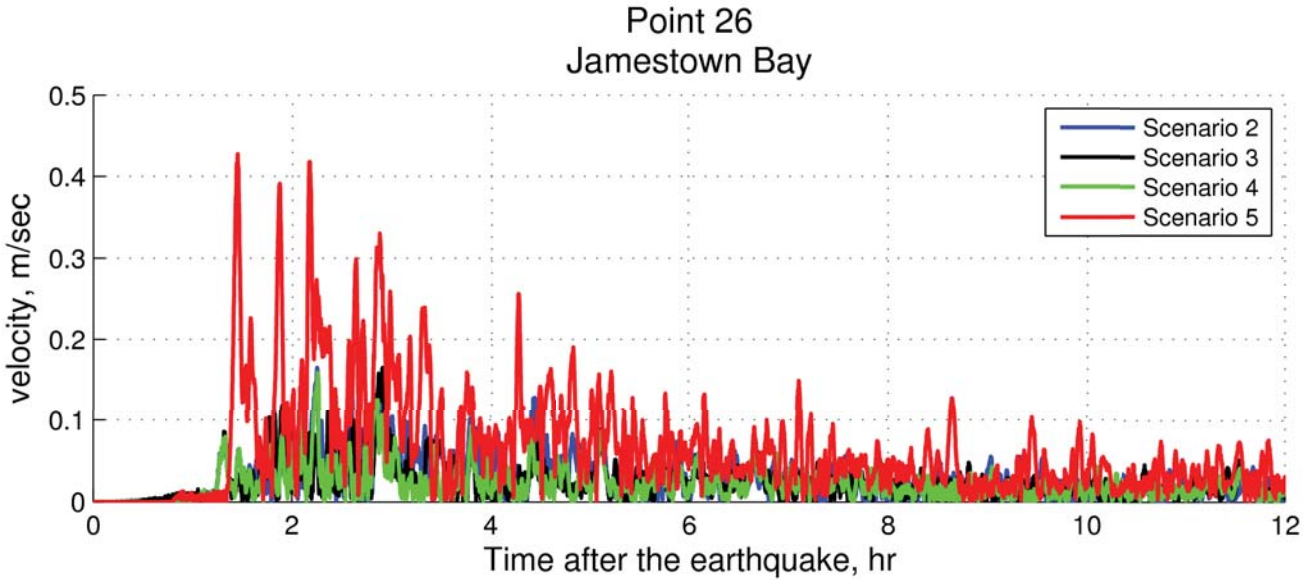
Point 26
Jamestown Bay
velocity, m/sec
Time after the earthquake, hr
Scenario 2
Scenario 3
Scenario 4
Scenario 5
0
0.1
0.2
0.3
0.4
0.5
0
2
4
6
8
10
12

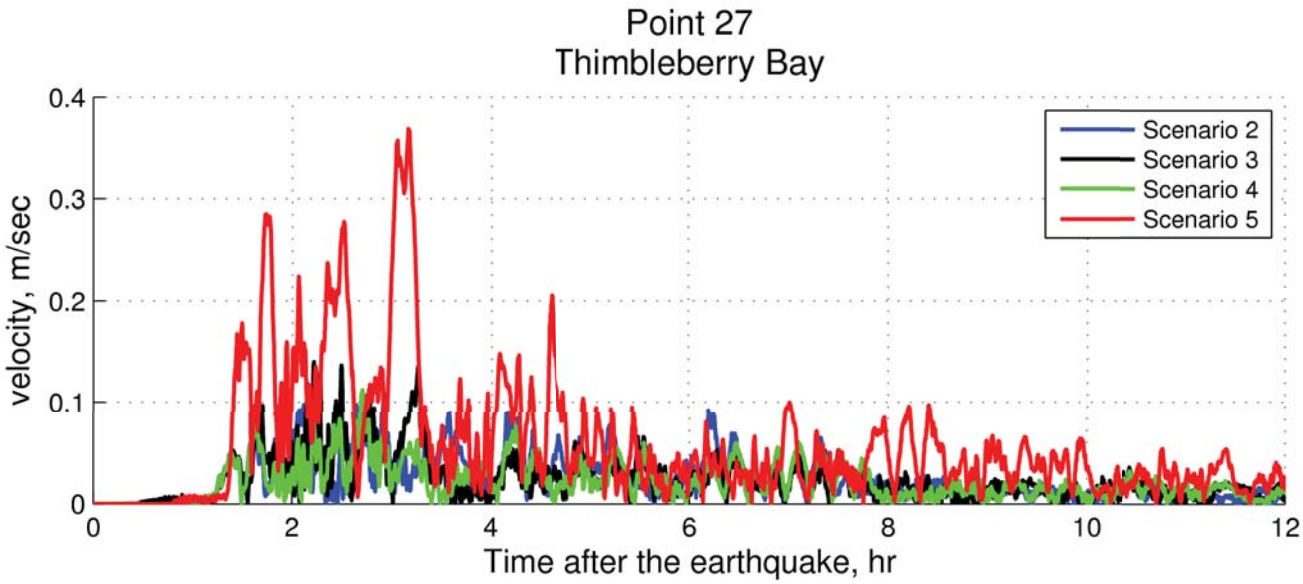
Point 27
Thimbleberry Bay
velocity, m/sec
Time after the earthquake, hr
Scenario 2
Scenario 3
Scenario 4
Scenario 5
0
0.1
0.2
0.3
0.4
0
2
4
6
8
10
12

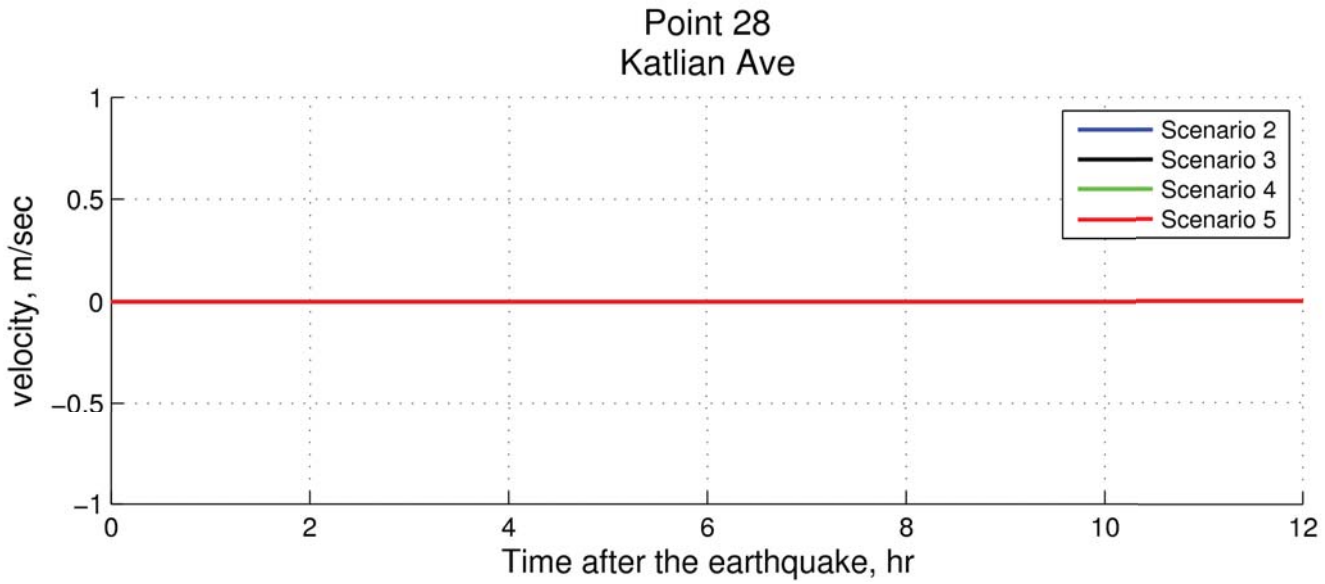
Point 28
Katlian Ave
velocity, m/sec
Time after the earthquake, hr
Scenario 2
Scenario 3
Scenario 4
Scenario 5

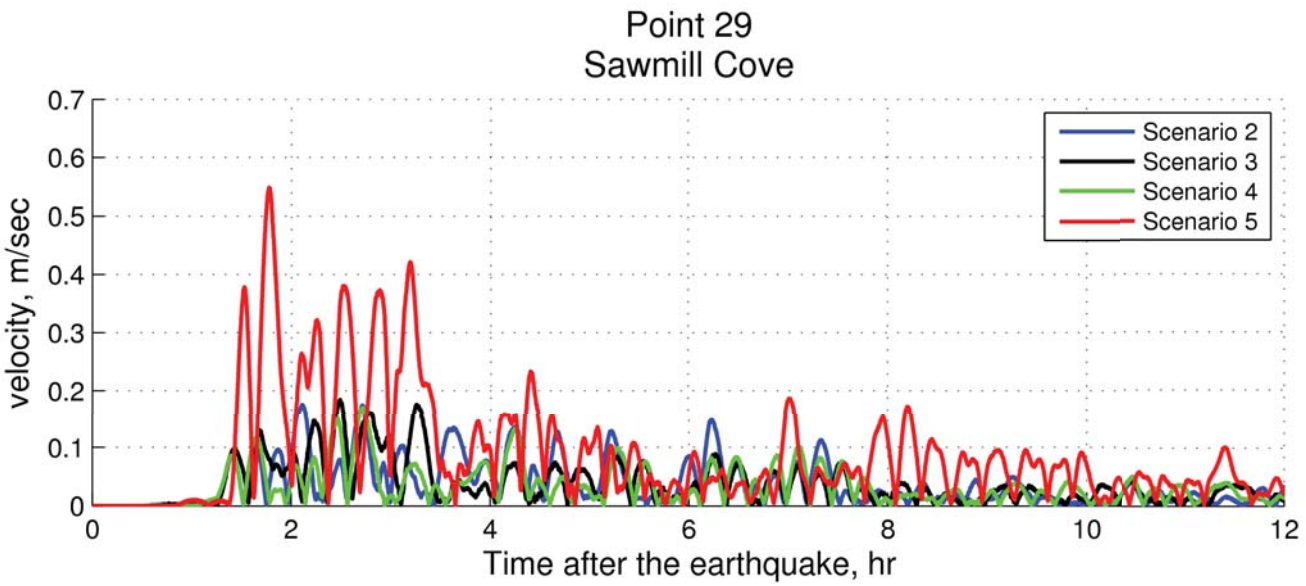
Point 29
Sawmill Cove
velocity, m/sec
Time after the earthquake, hr
Scenario 2
Scenario 3
Scenario 4
Scenario 5

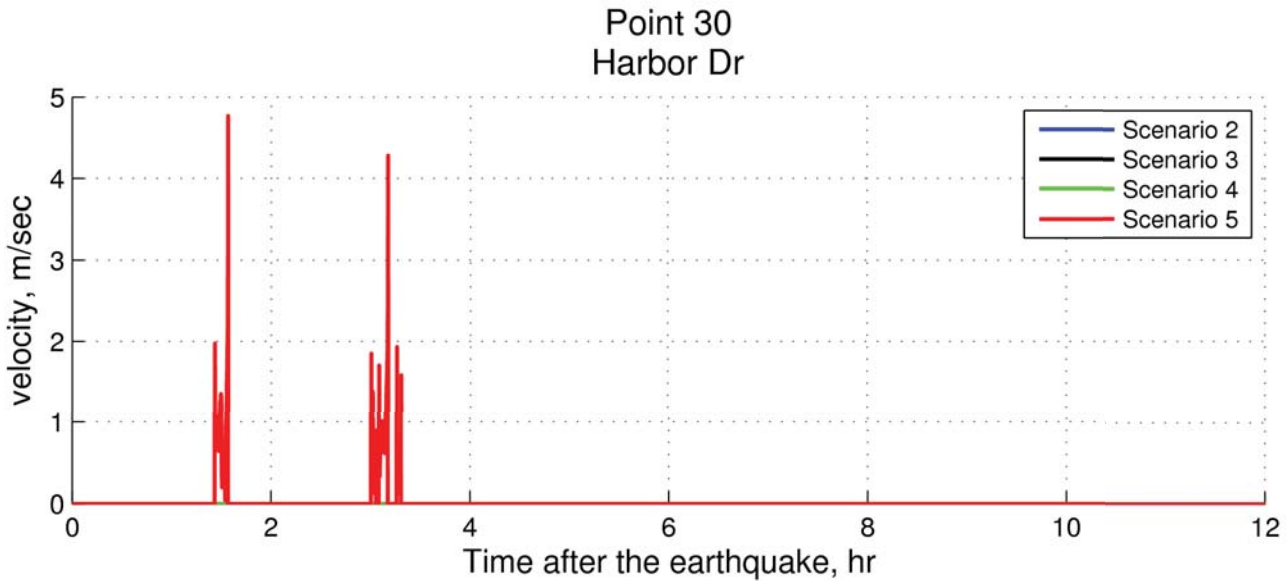
Point 30
Harbor Dr
velocity, m/sec
Time after the earthquake, hr
Scenario 2
Scenario 3
Scenario 4
Scenario 5

APPENDIX A-3
TIME-SERIES PLOTS OF WATER LEVEL AND VELOCITY AT SELECTED LOCATIONS FOR SCENARIOS 6–9

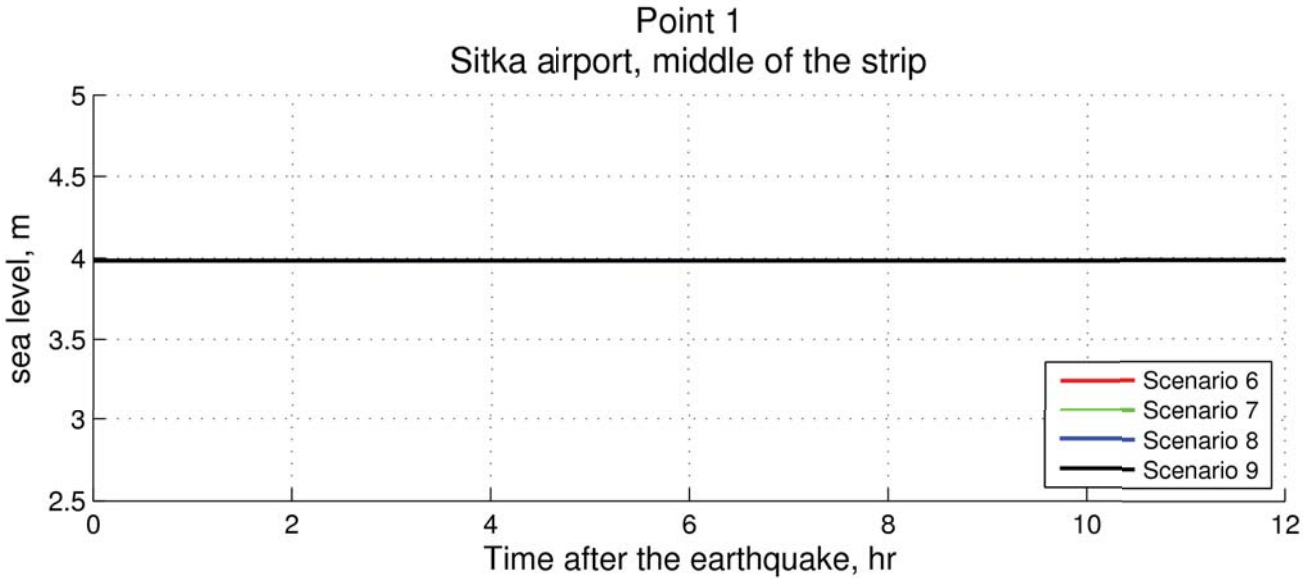

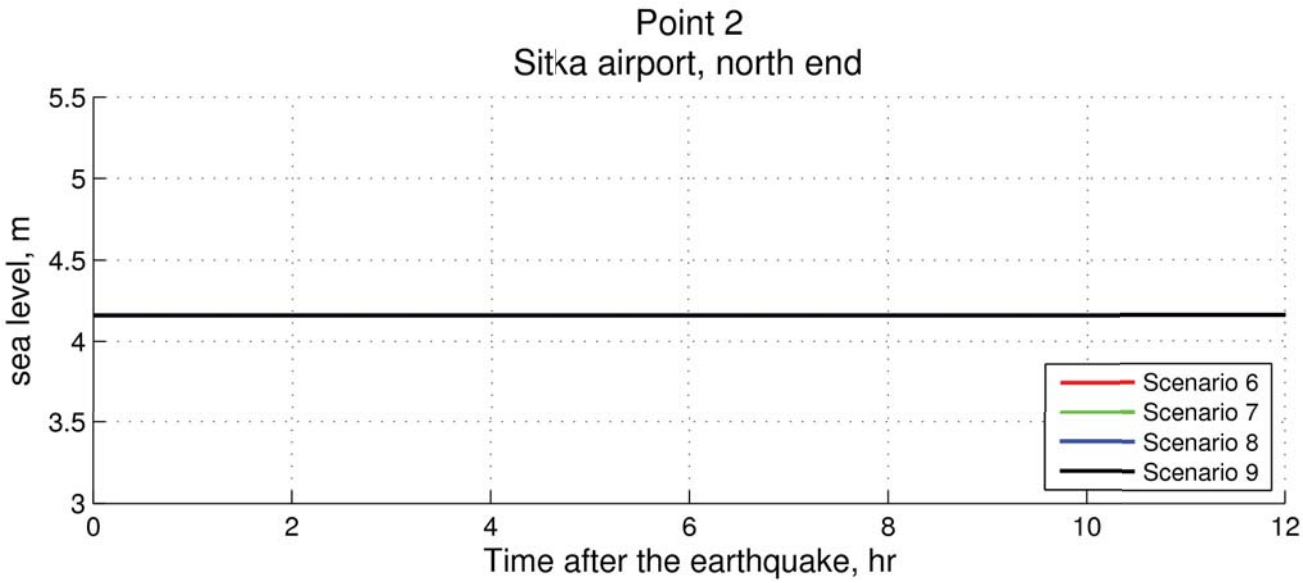

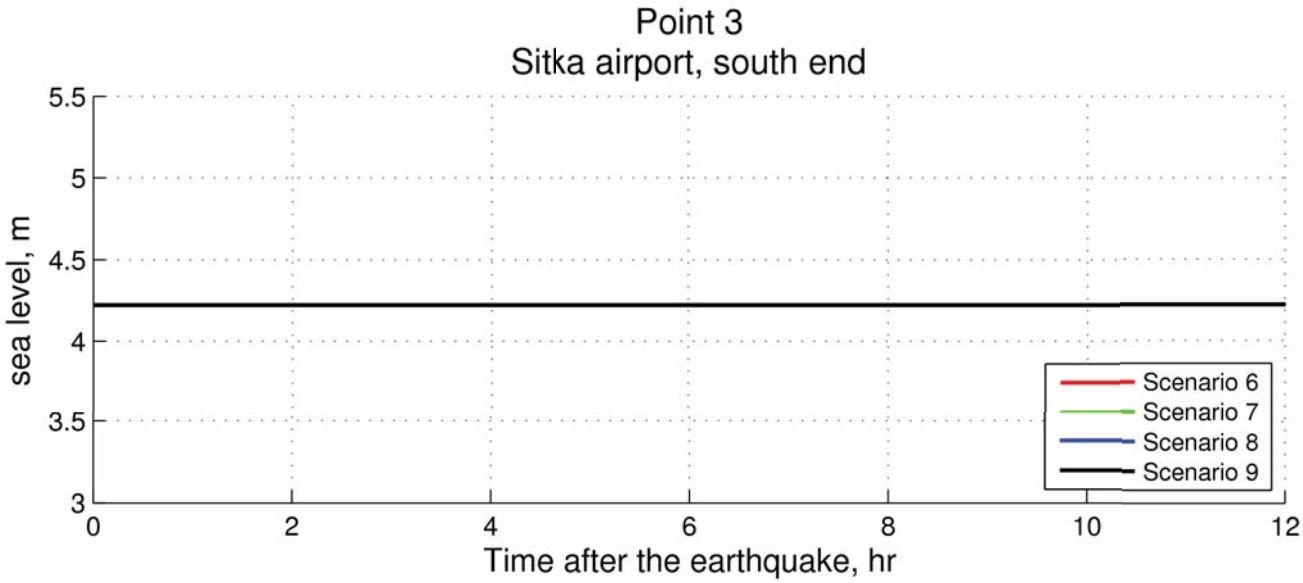

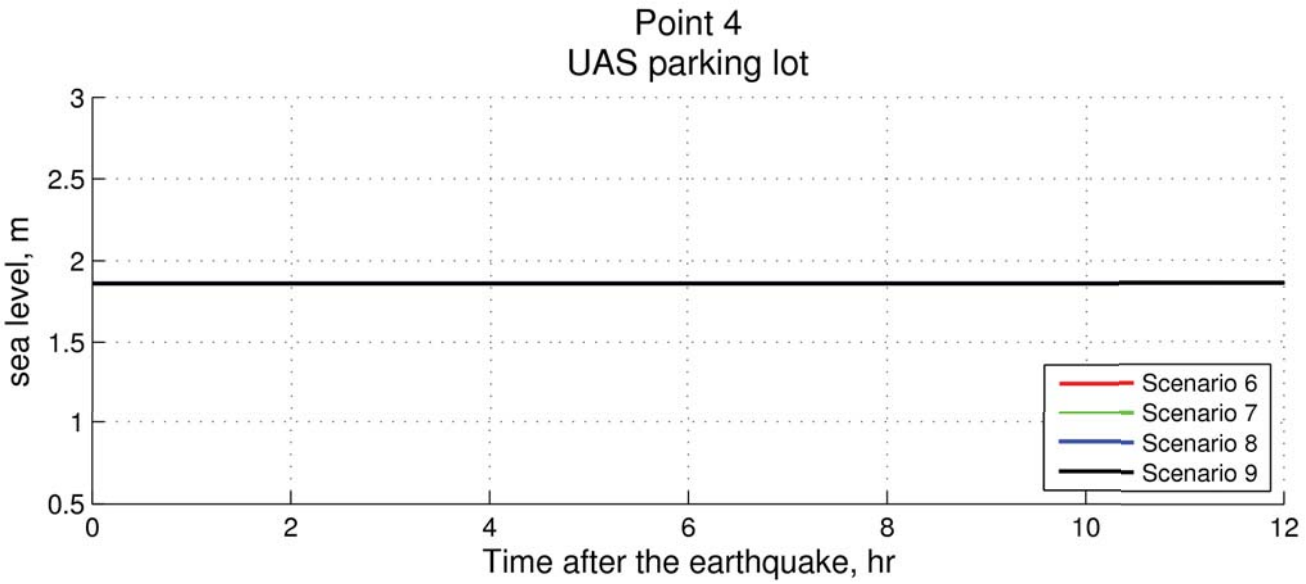
Point 4
UAS parking lot
sea level, m
Time after the earthquake, hr
Scenario 6
Scenario 7
Scenario 8
Scenario 9

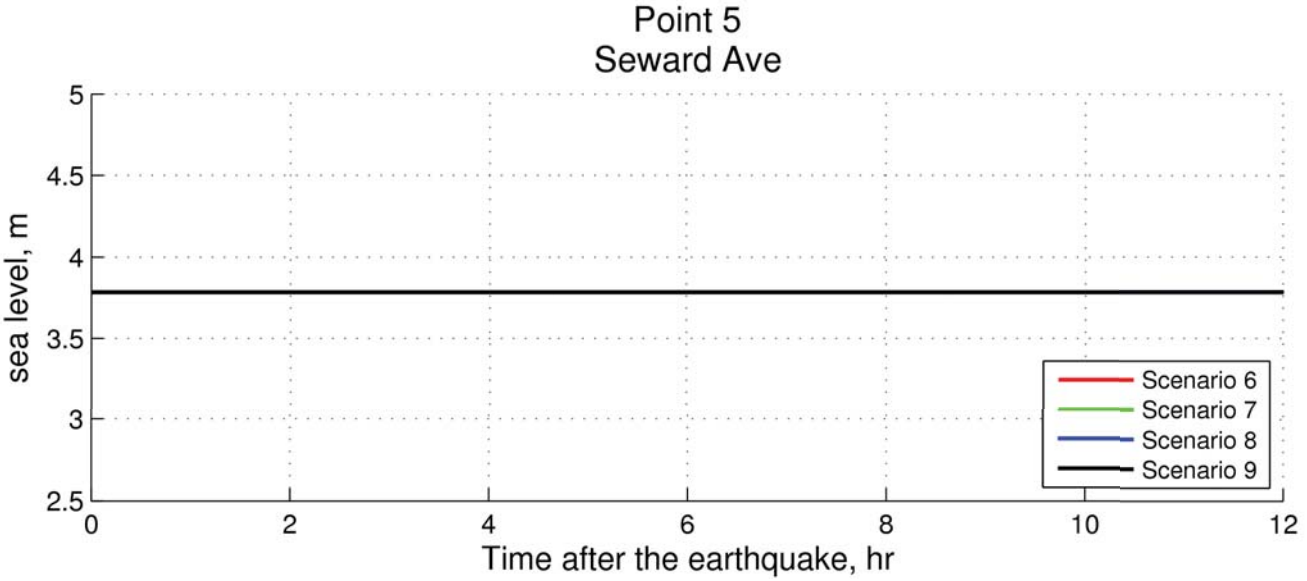
Point 5
Seward Ave
sea level, m
Time after the earthquake, hr
Scenario 6
Scenario 7
Scenario 8
Scenario 9

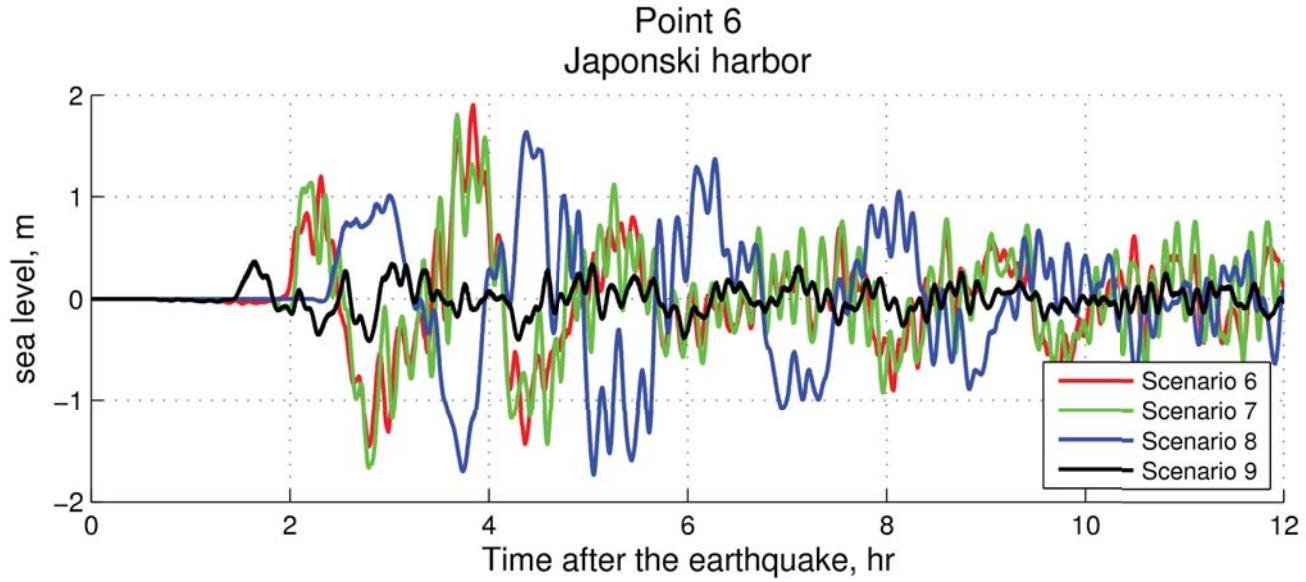
Point 6
Japonski harbor
sea level, m
Time after the earthquake, hr
Scenario 6
Scenario 7
Scenario 8
Scenario 9

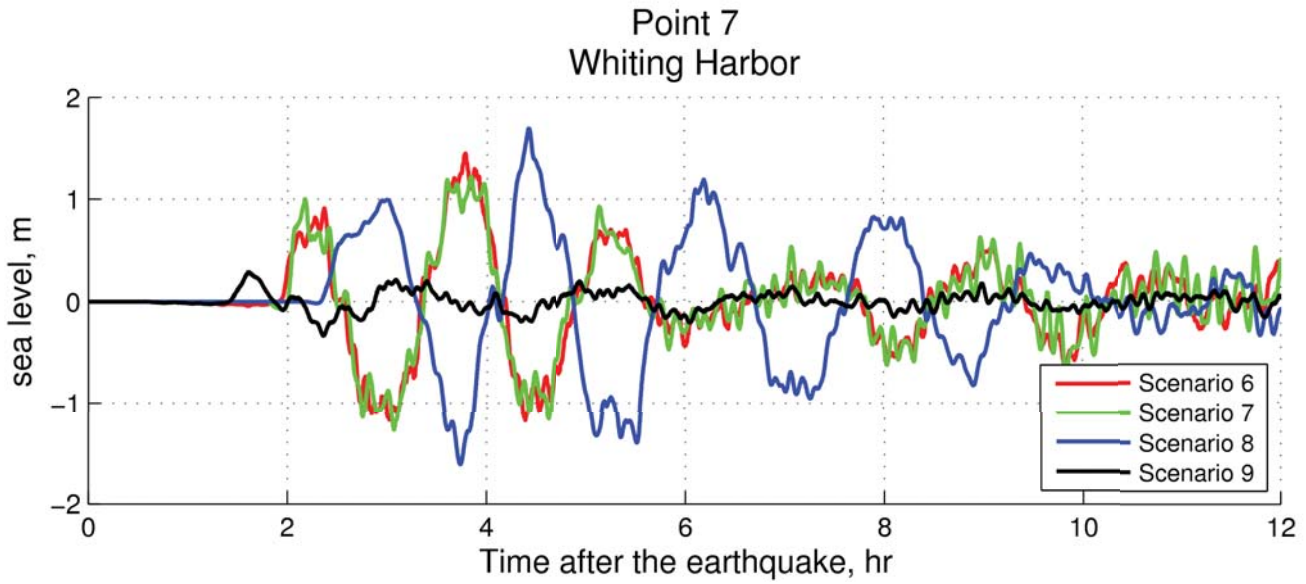
Point 7
Whiting Harbor
sea level, m
Time after the earthquake, hr
Scenario 6
Scenario 7
Scenario 8
Scenario 9

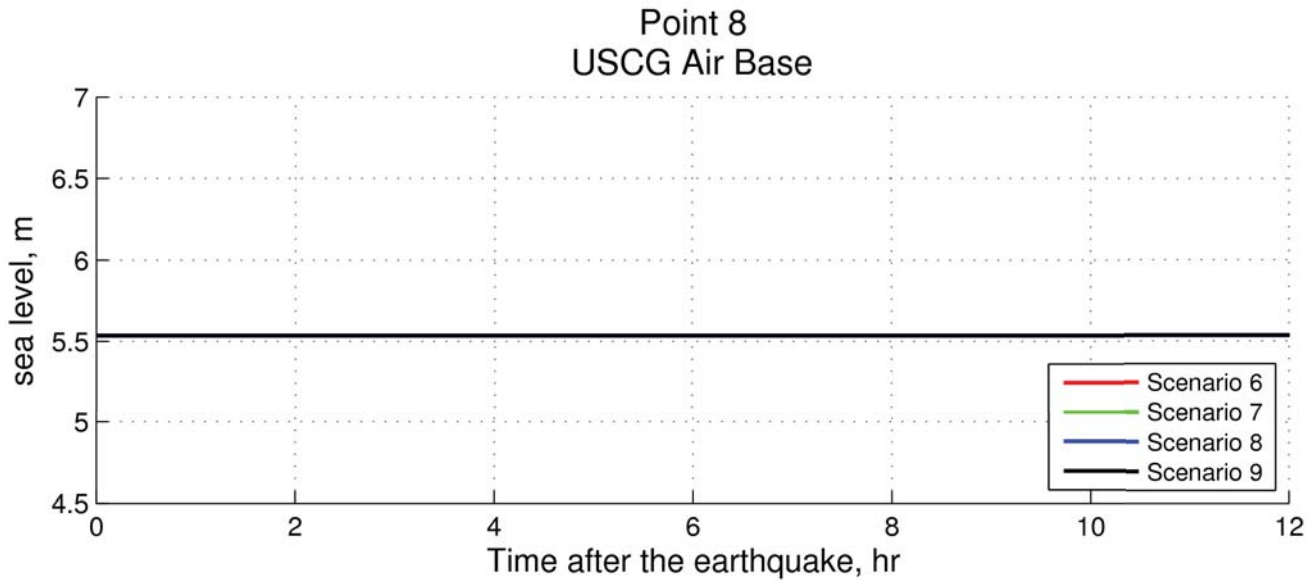
Point 8
USCG Air Base
sea level, m
Time after the earthquake, hr
Scenario 6
Scenario 7
Scenario 8
Scenario 9

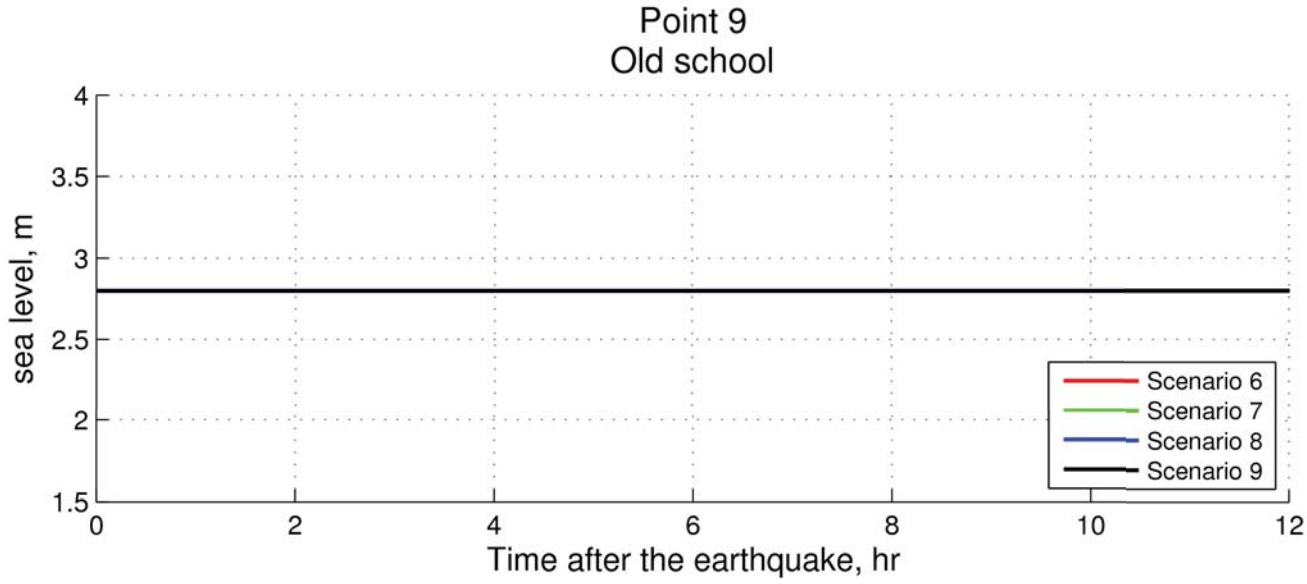
Point 9
Old school
sea level, m
Time after the earthquake, hr
Scenario 6
Scenario 7
Scenario 8
Scenario 9

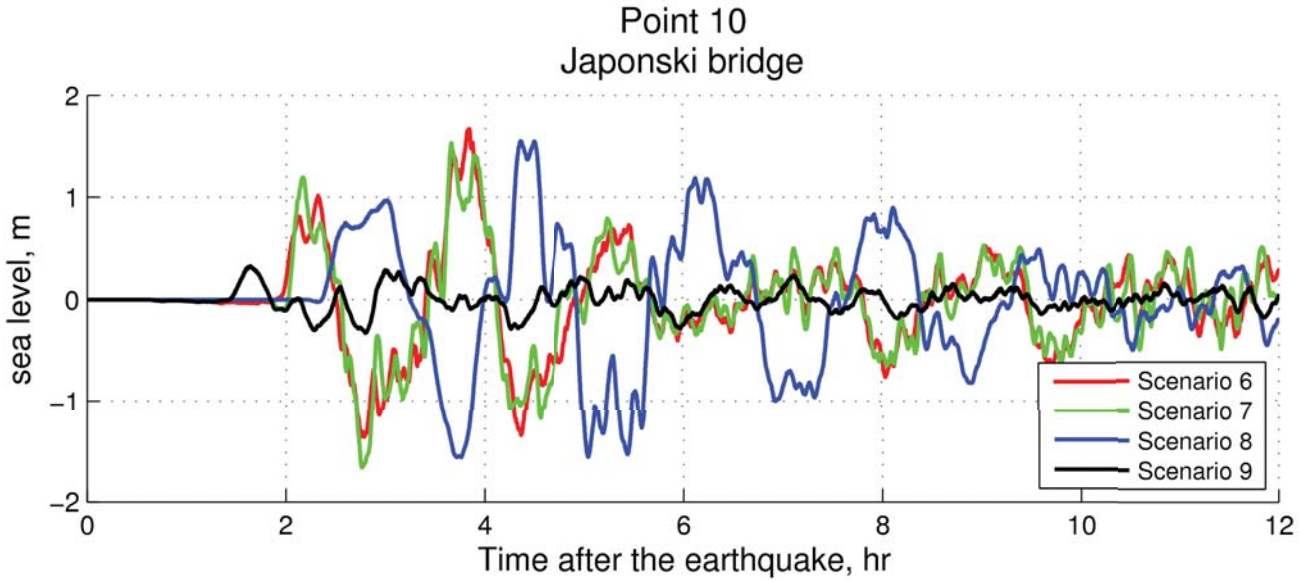
Point 10
Japonski bridge
sea level, m
Time after the earthquake, hr
Scenario 6
Scenario 7
Scenario 8
Scenario 9

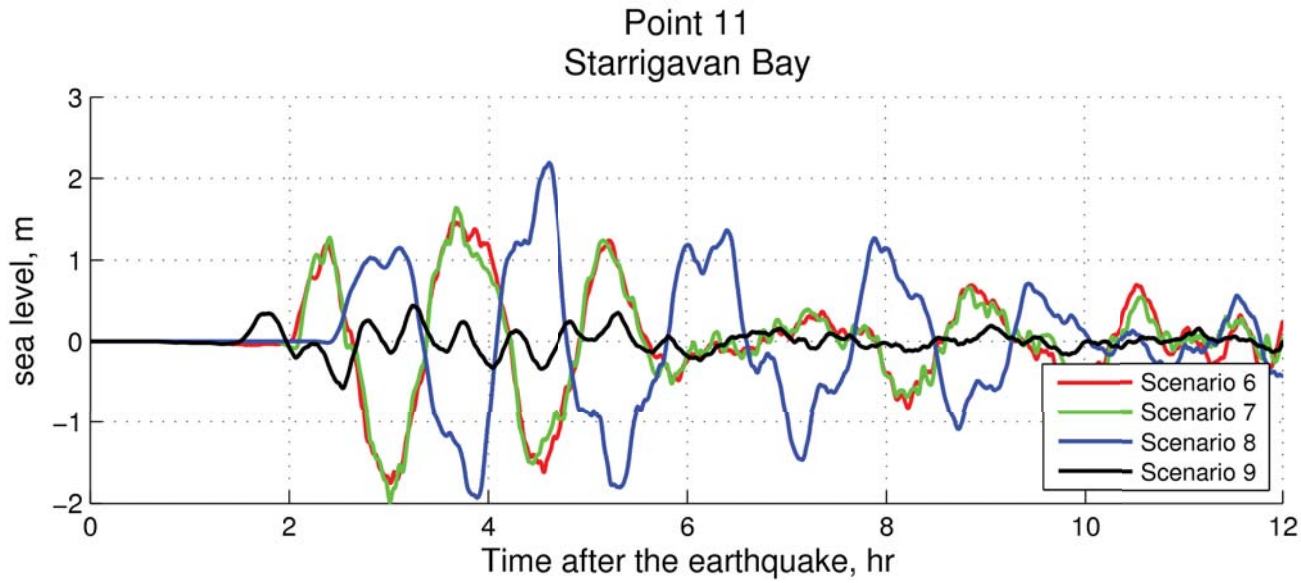
Point 11
Starrigavan Bay
sea level, m
Time after the earthquake, hr
Scenario 6
Scenario 7
Scenario 8
Scenario 9

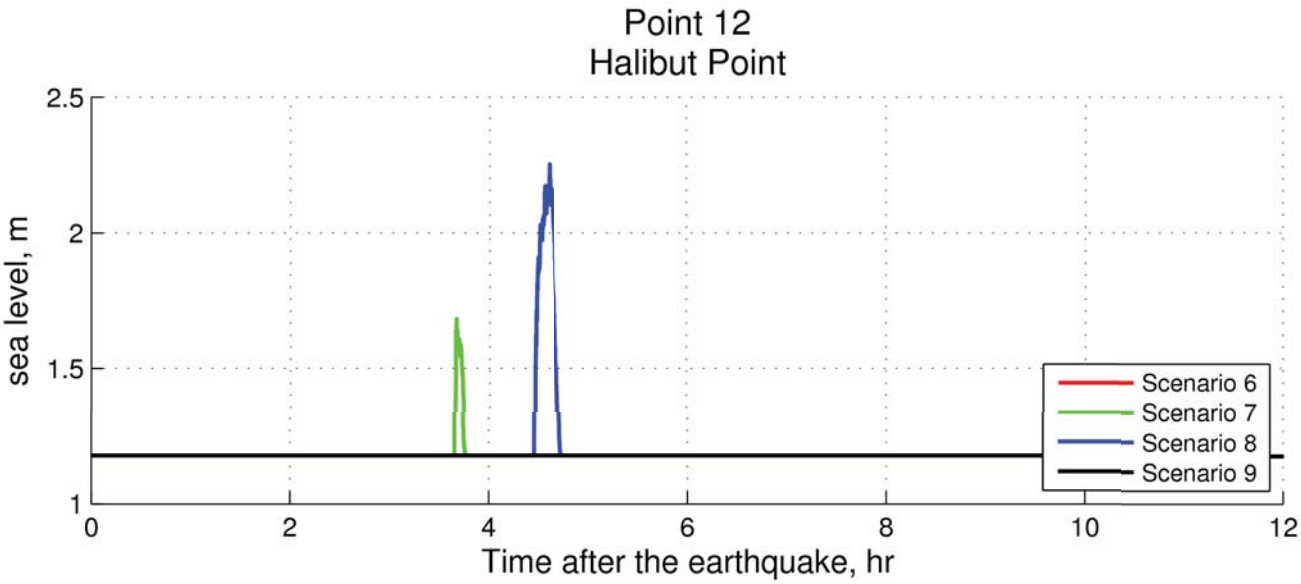
Point 12
Halibut Point
sea level, m
Time after the earthquake, hr
Scenario 6
Scenario 7
Scenario 8
Scenario 9

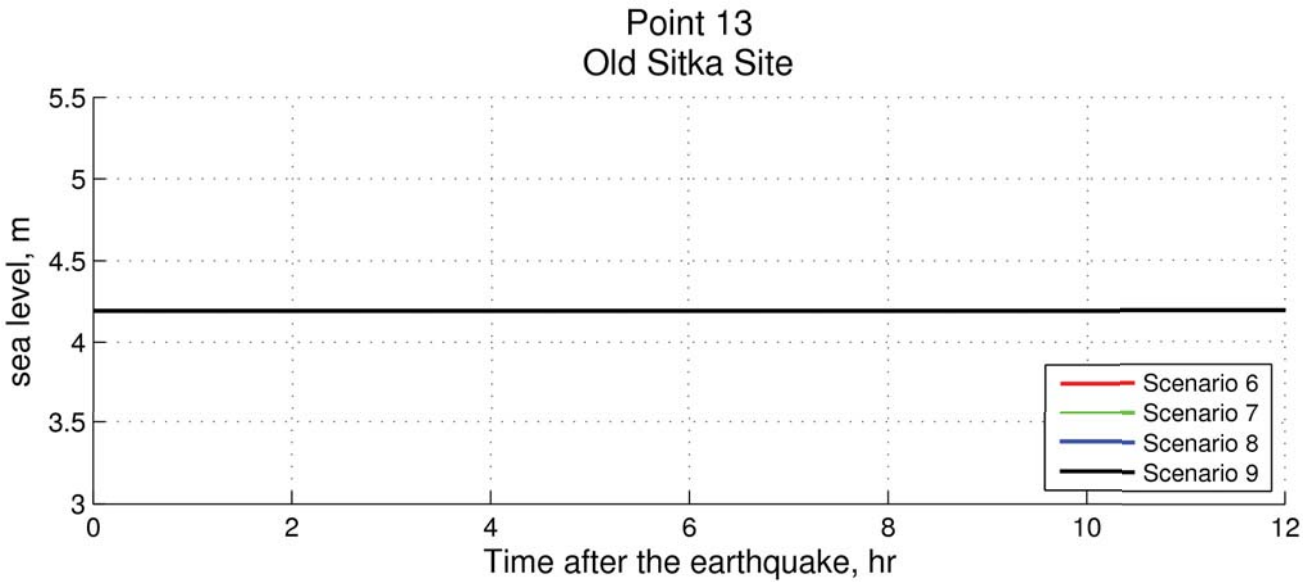
Point 13
Old Sitka Site
sea level, m
5.5
5
4.5
4
3.5
3
0
2
4
6
8
10
12
Time after the earthquake, hr
Scenario 6
Scenario 7
Scenario 8
Scenario 9

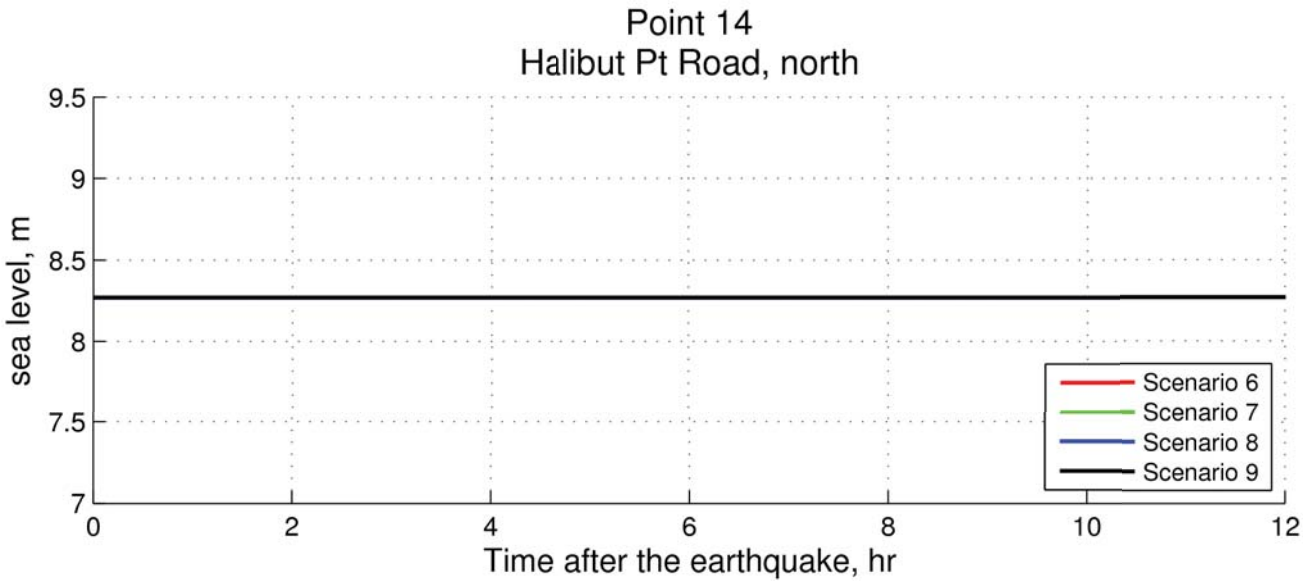
Point 14
Halibut Pt Road, north
sea level, m
9.5
9
8.5
8
7.5
7
0
2
4
6
8
10
12
Time after the earthquake, hr
Scenario 6
Scenario 7
Scenario 8
Scenario 9

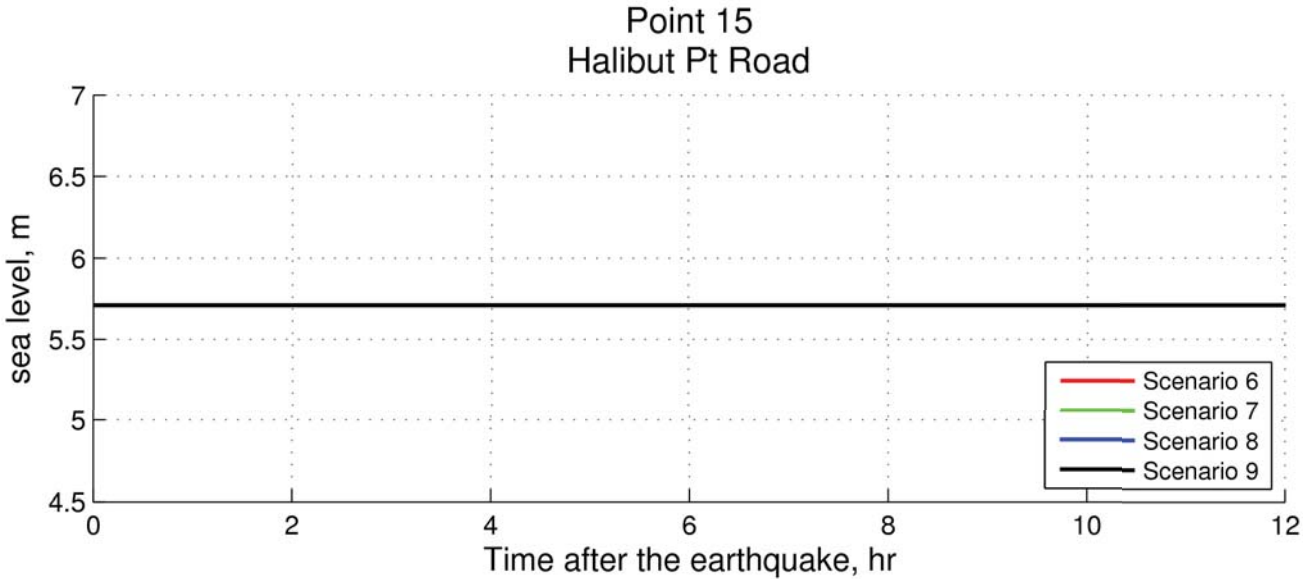
Point 15
Halibut Pt Road
sea level, m
7
6.5
6
5.5
5
4.5
0
2
4
6
8
10
12
Time after the earthquake, hr
Scenario 6
Scenario 7
Scenario 8
Scenario 9

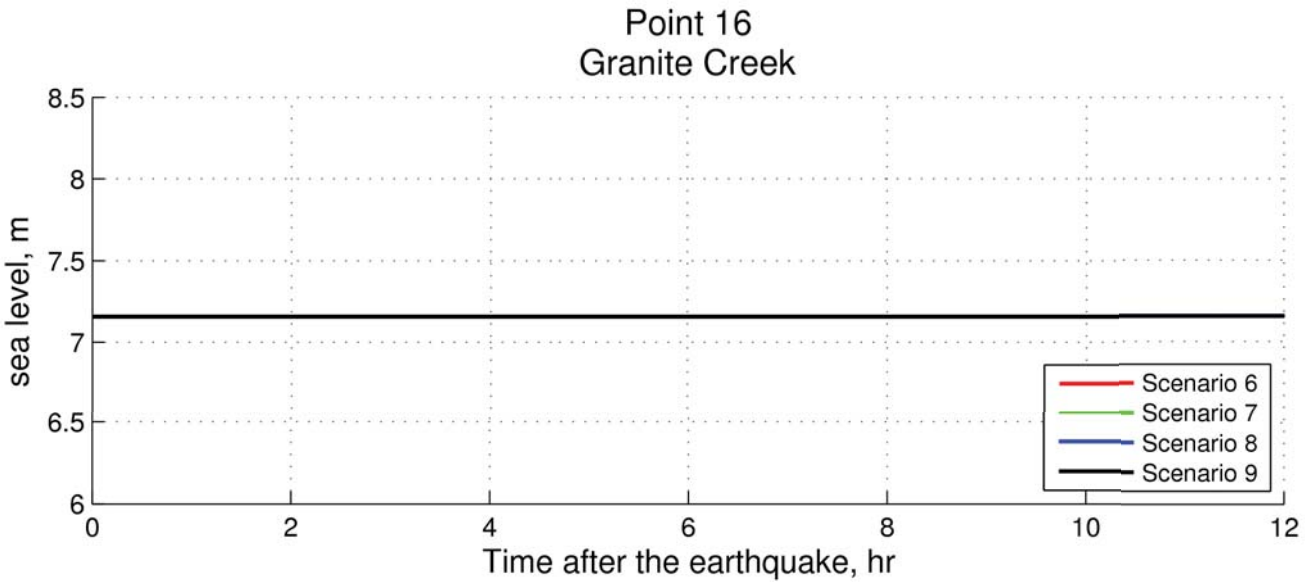
Point 16
Granite Creek
sea level, m
8.5
8
7.5
7
6.5
6
0
2
4
6
8
10
12
Time after the earthquake, hr
Scenario 6
Scenario 7
Scenario 8
Scenario 9

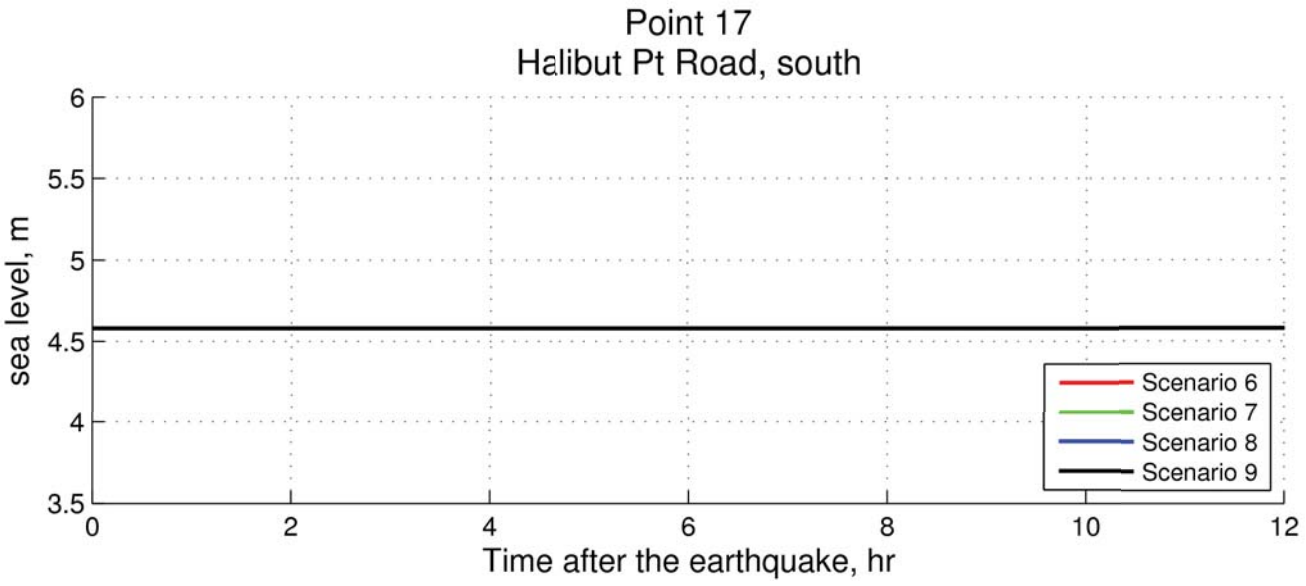
Point 17
Halibut Pt Road, south
sea level, m
6
5.5
5
4.5
4
3.5
0
2
4
6
8
10
12
Time after the earthquake, hr
Scenario 6
Scenario 7
Scenario 8
Scenario 9

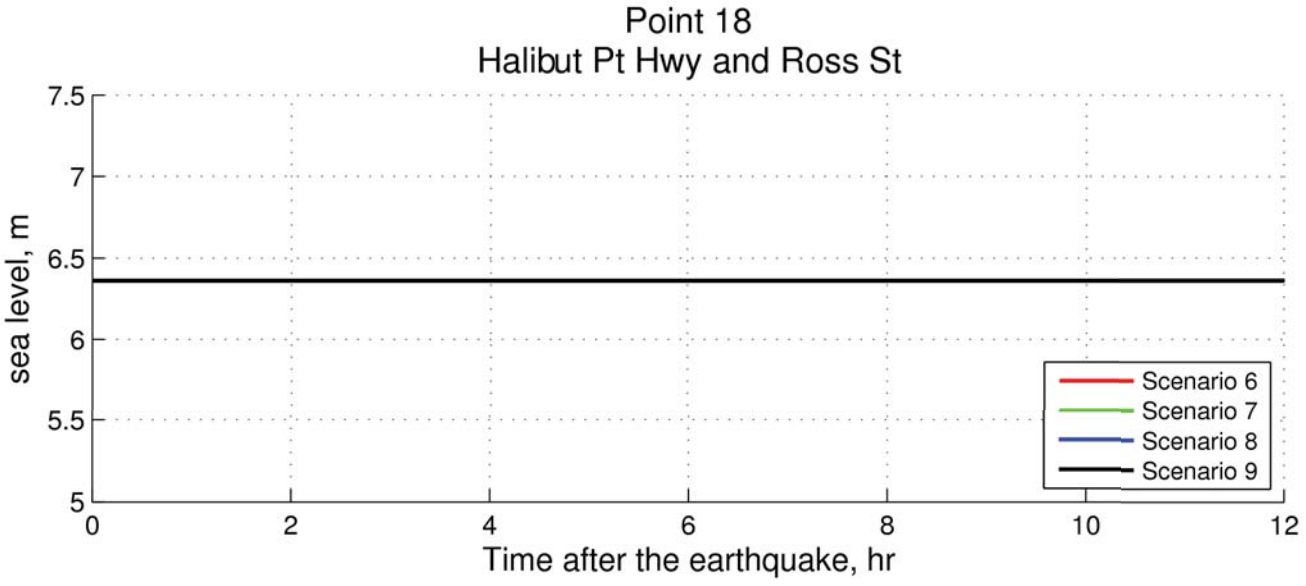
Point 18
Halibut Pt Hwy and Ross St
sea level, m
7.5
7
6.5
6
5.5
5
0
2
4
6
8
10
12
Time after the earthquake, hr
Scenario 6
Scenario 7
Scenario 8
Scenario 9

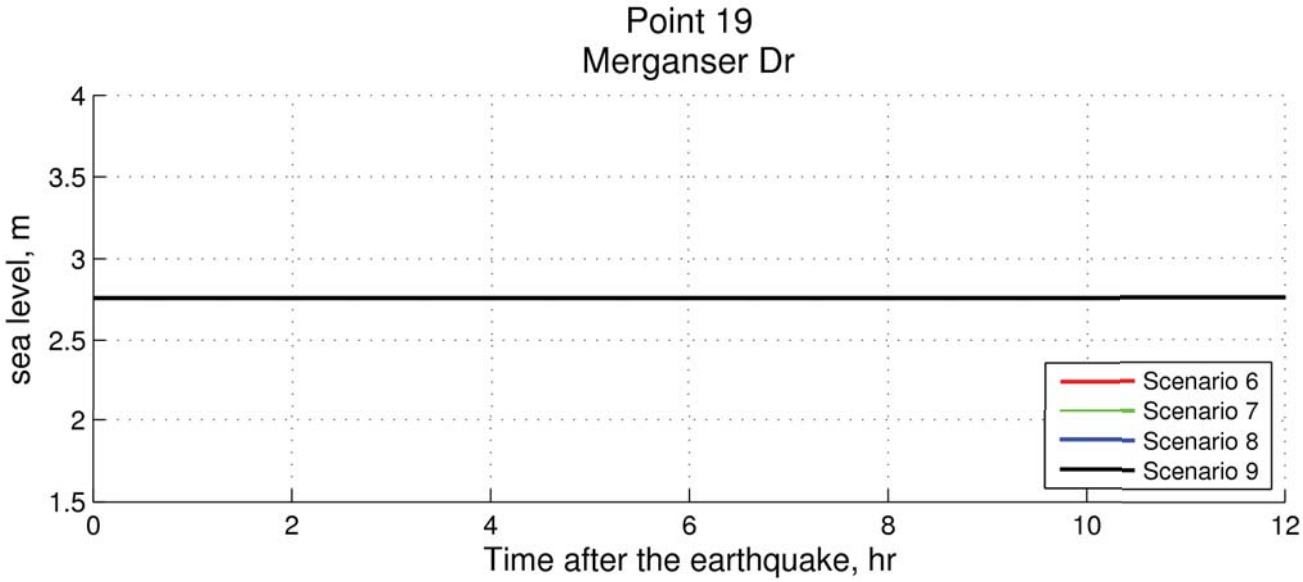
Point 19
Merganser Dr
sea level, m
Time after the earthquake, hr
Scenario 6
Scenario 7
Scenario 8
Scenario 9

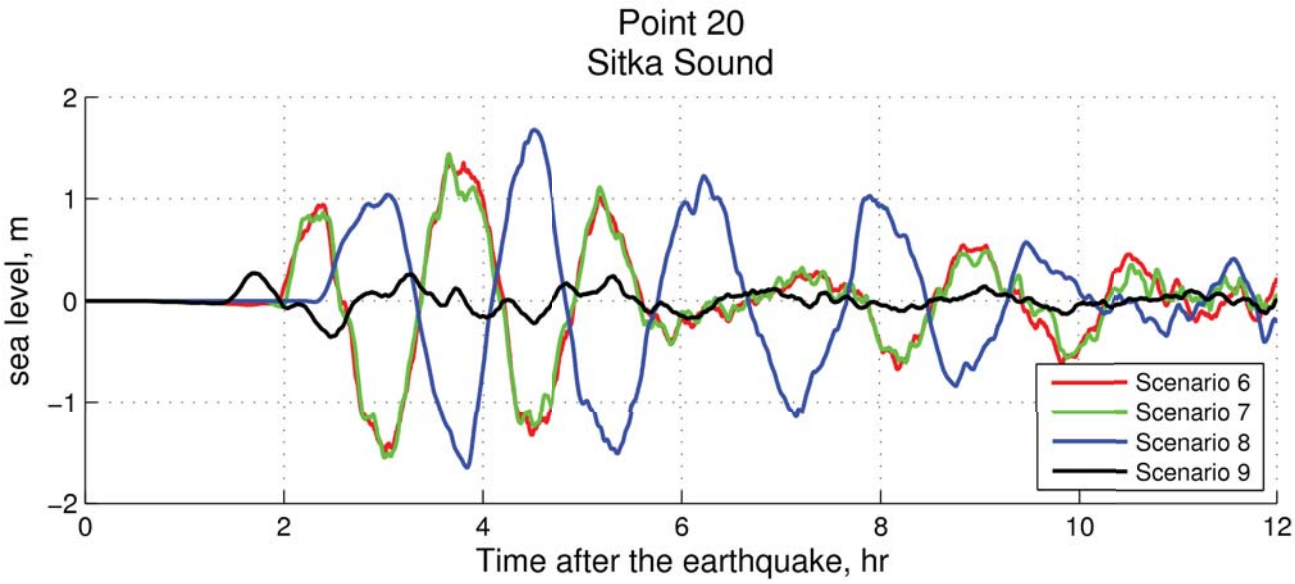
Point 20
Sitka Sound
sea level, m
Time after the earthquake, hr
Scenario 6
Scenario 7
Scenario 8
Scenario 9

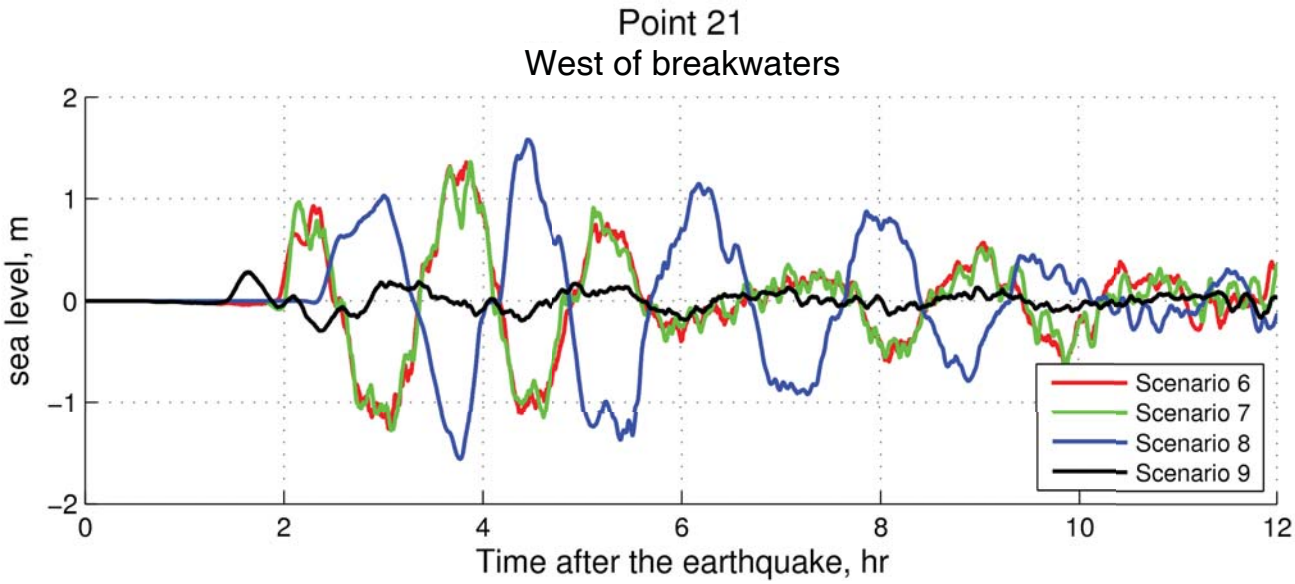
Point 21
West of breakwaters
sea level, m
Time after the earthquake, hr
Scenario 6
Scenario 7
Scenario 8
Scenario 9

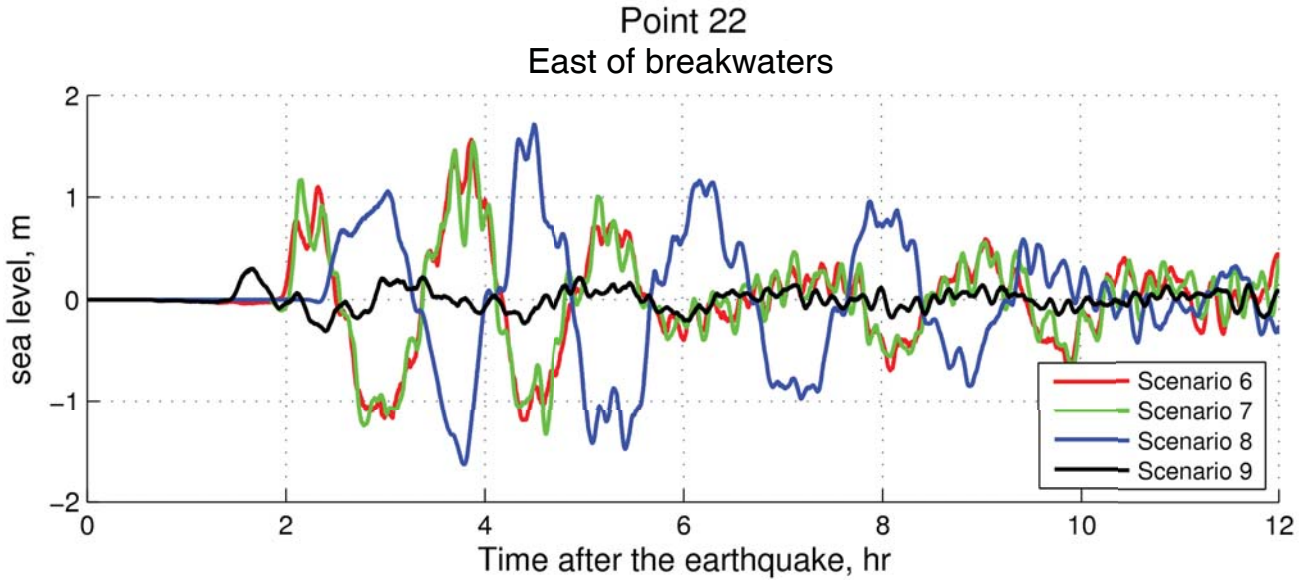
Point 22
East of breakwaters
sea level, m
Time after the earthquake, hr
Scenario 6
Scenario 7
Scenario 8
Scenario 9

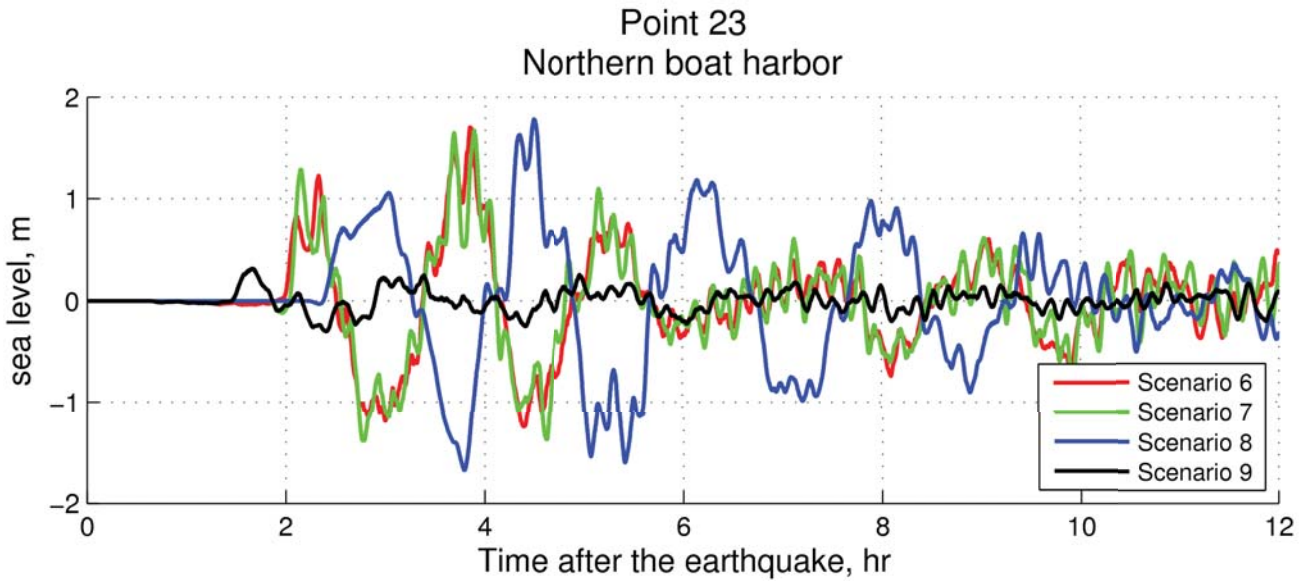
Point 23
Northern boat harbor
sea level, m
Time after the earthquake, hr
Scenario 6
Scenario 7
Scenario 8
Scenario 9

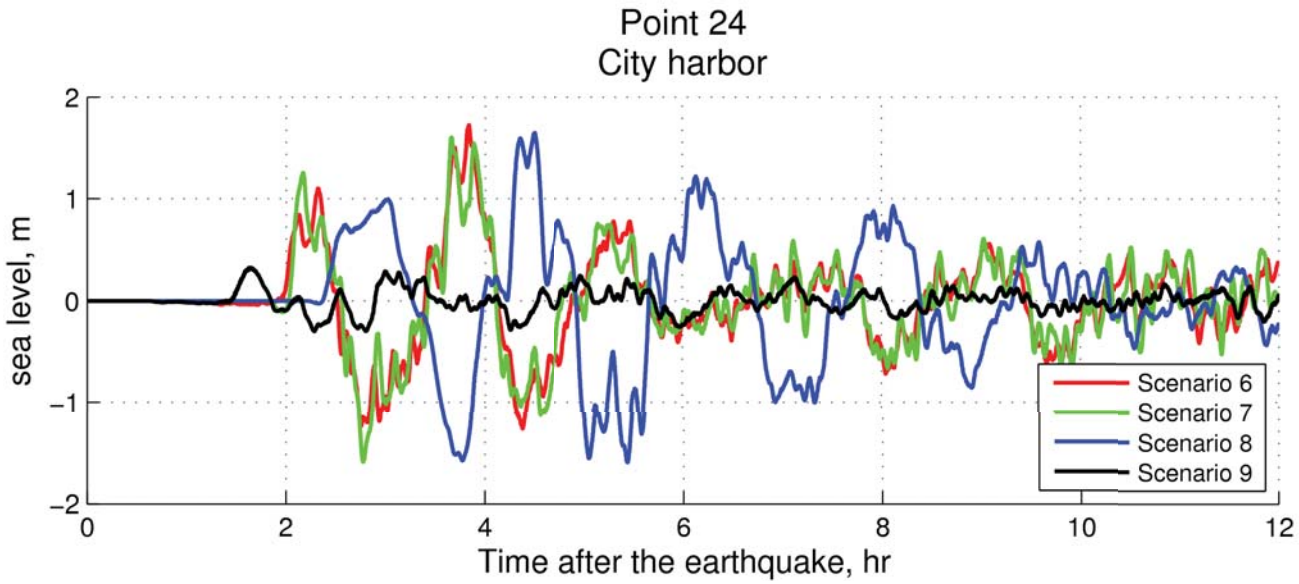
Point 24
City harbor
sea level, m
Time after the earthquake, hr
Scenario 6
Scenario 7
Scenario 8
Scenario 9

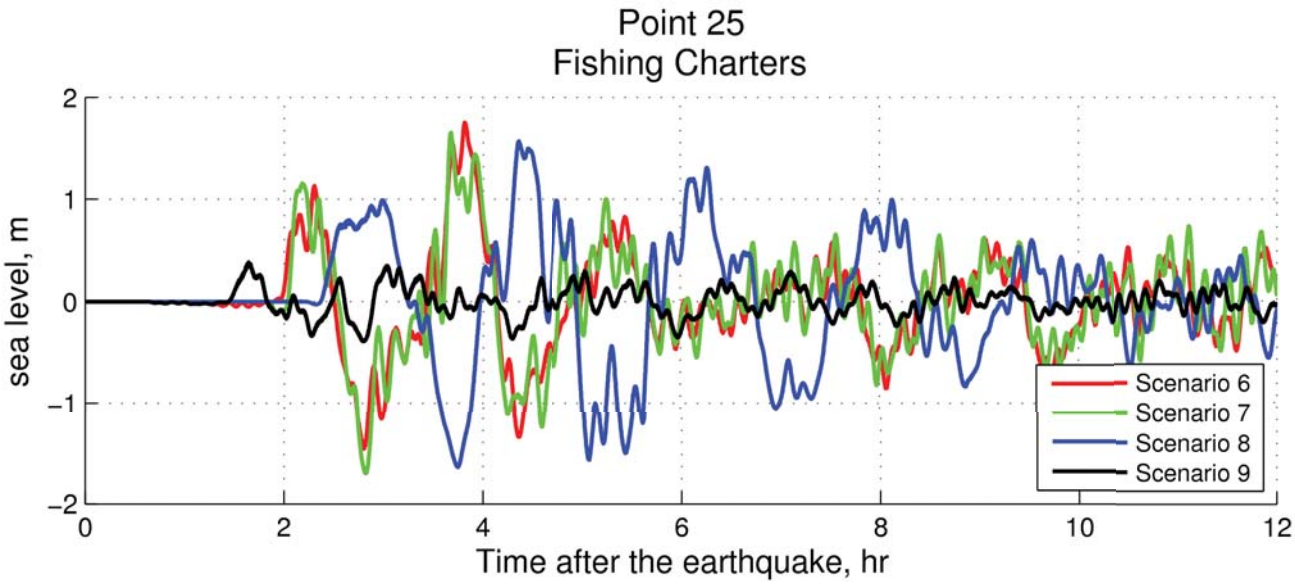
Point 25
Fishing Charters
sea level, m
Time after the earthquake, hr
Scenario 6
Scenario 7
Scenario 8
Scenario 9

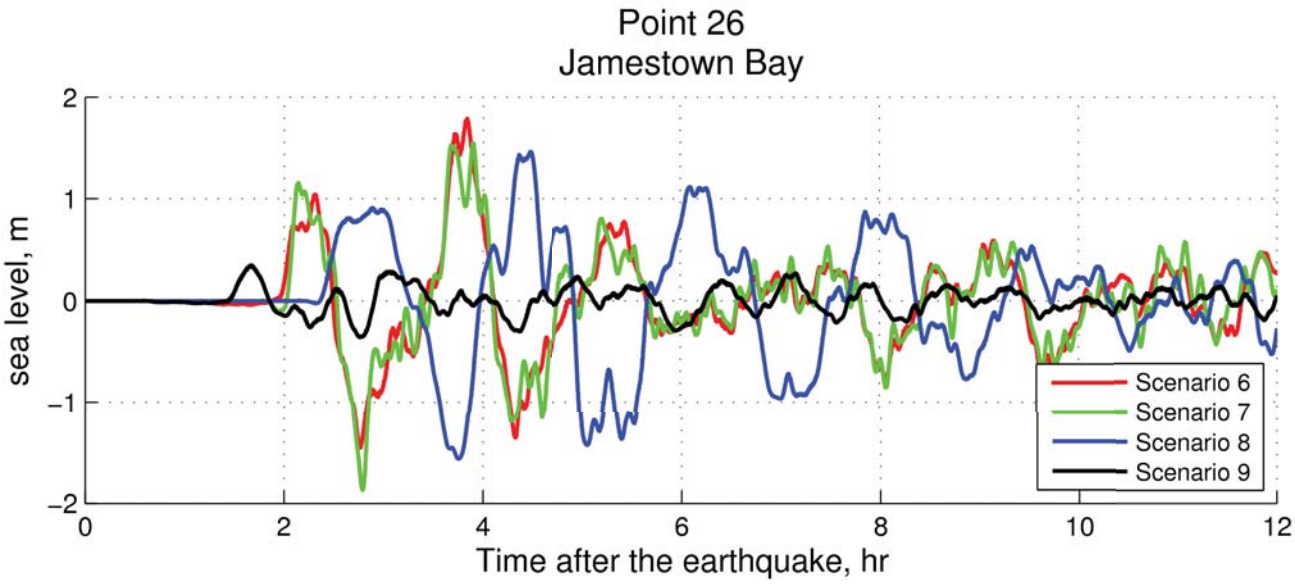
Point 26
Jamestown Bay
sea level, m
Time after the earthquake, hr
Scenario 6
Scenario 7
Scenario 8
Scenario 9

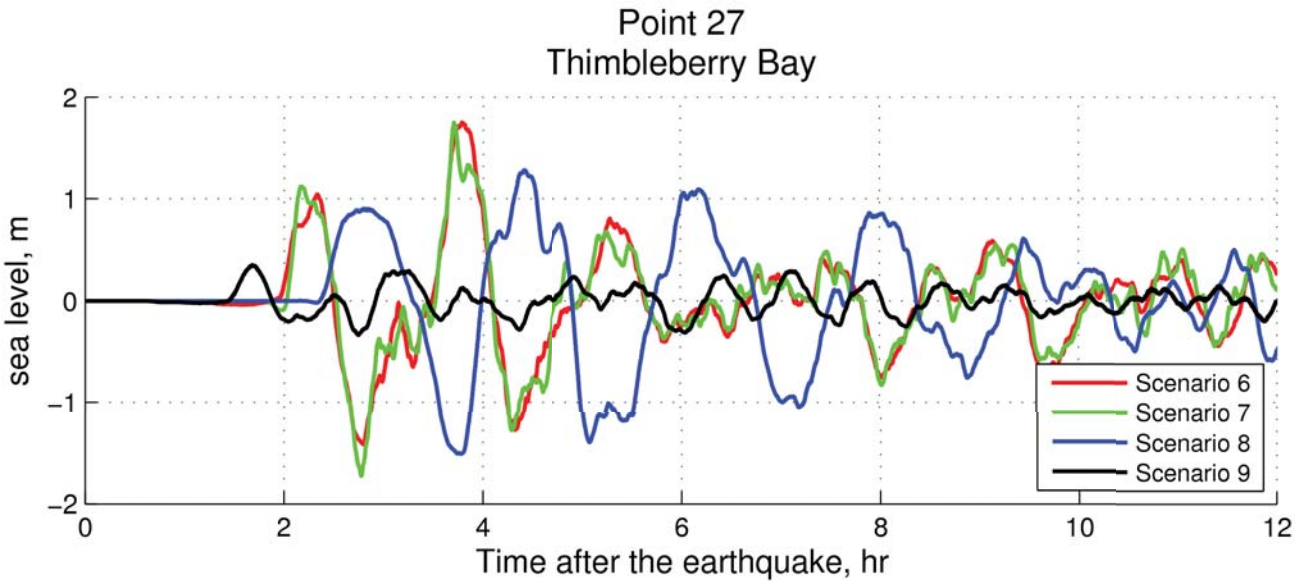
Point 27
Thimbleberry Bay
sea level, m
Time after the earthquake, hr
Scenario 6
Scenario 7
Scenario 8
Scenario 9

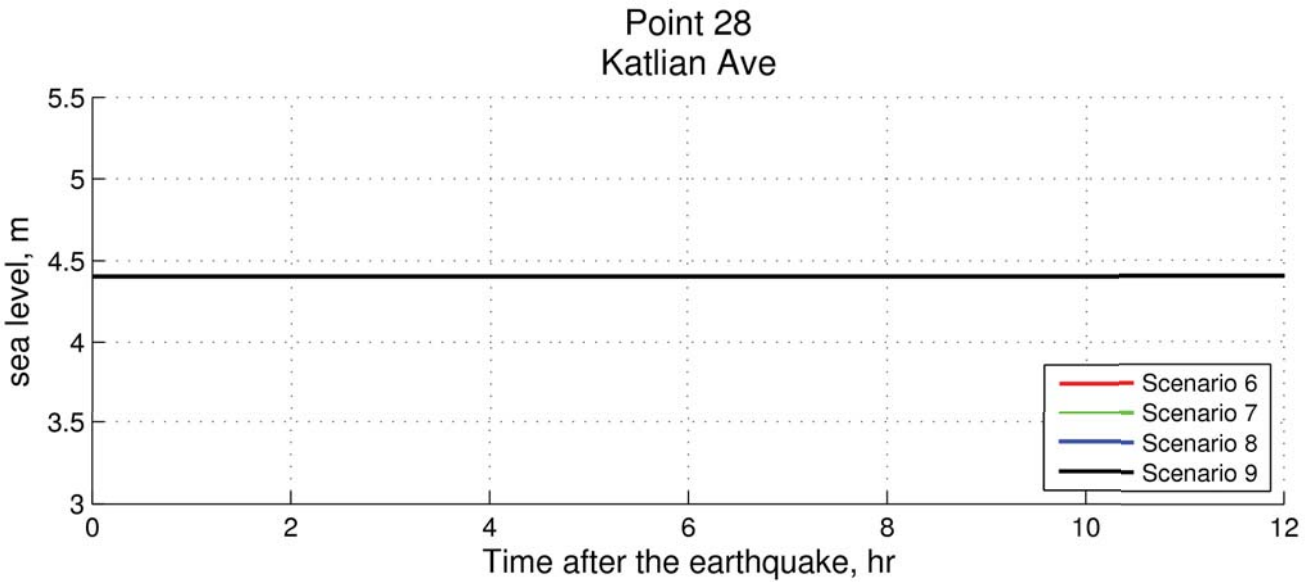
Point 28
Katlian Ave
sea level, m
Time after the earthquake, hr
Scenario 6
Scenario 7
Scenario 8
Scenario 9

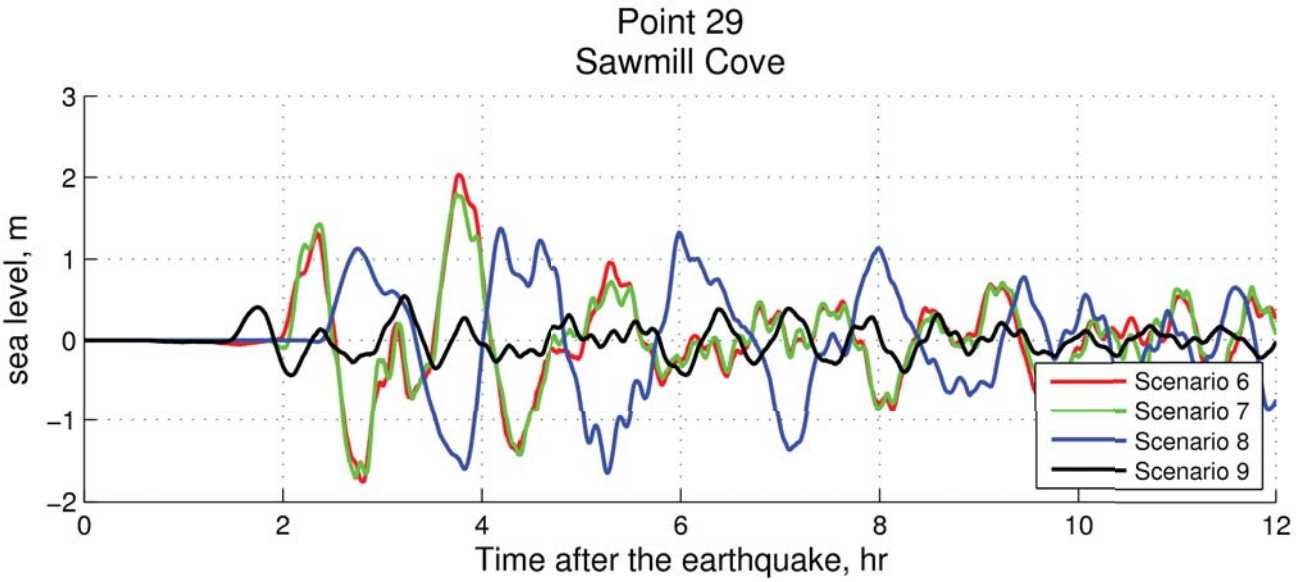
Point 29
Sawmill Cove
sea level, m
Time after the earthquake, hr
Scenario 6
Scenario 7
Scenario 8
Scenario 9

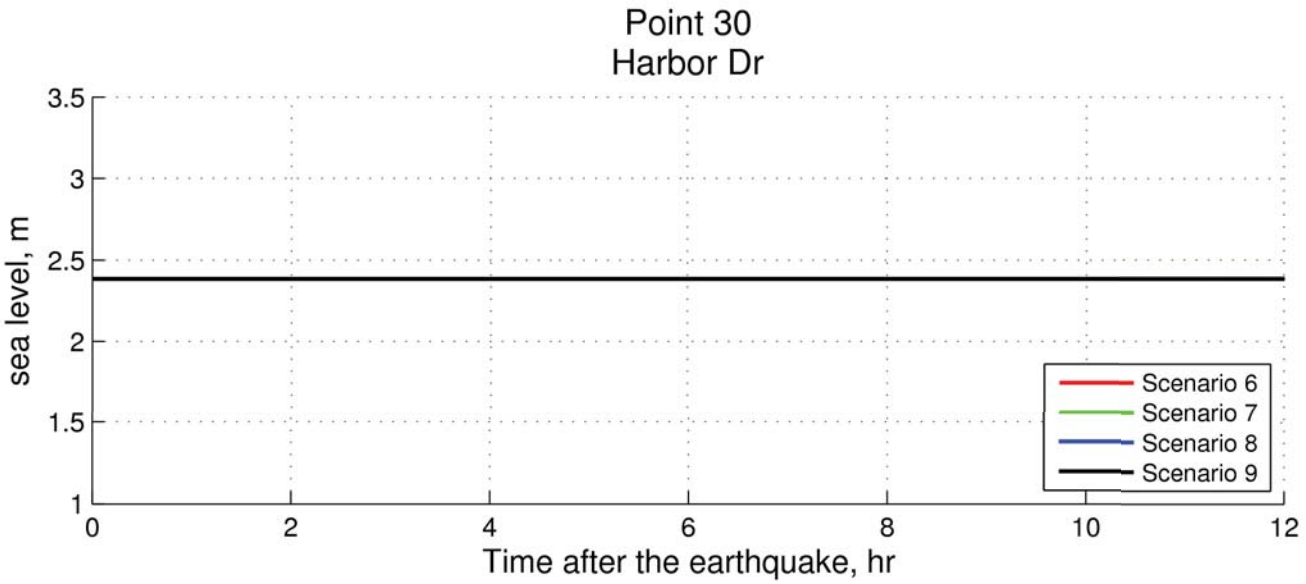
Point 30
Harbor Dr
sea level, m
Time after the earthquake, hr
Scenario 6
Scenario 7
Scenario 8
Scenario 9

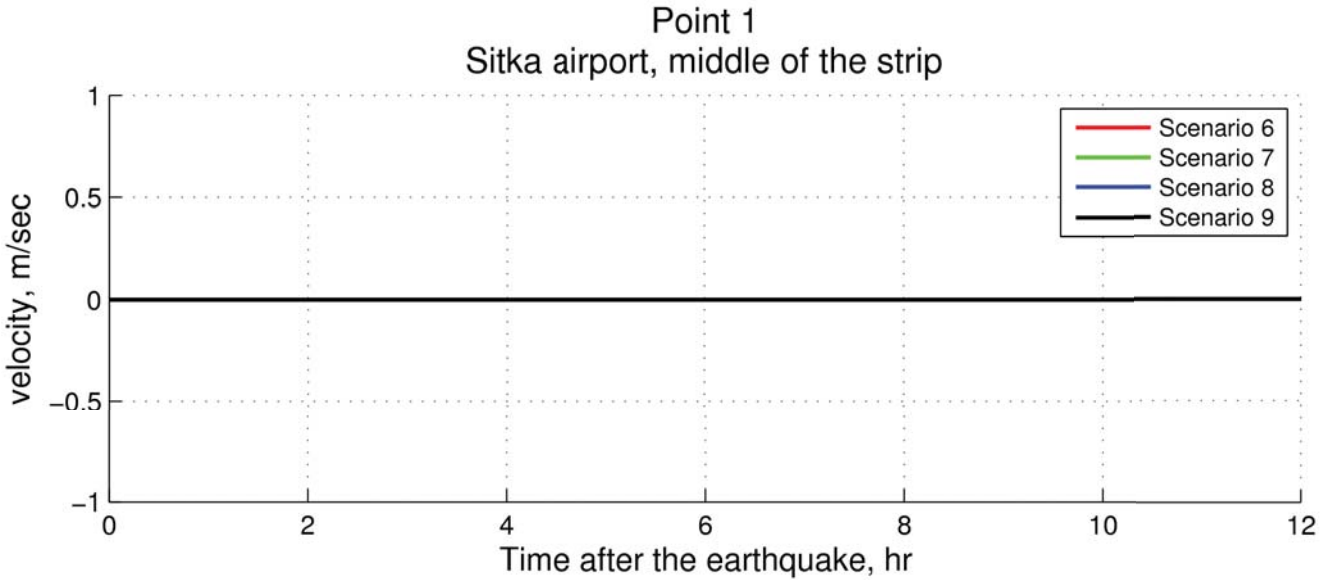
Point 1
Sitka airport, middle of the strip
velocity, m/sec
Time after the earthquake, hr
Scenario 6
Scenario 7
Scenario 8
Scenario 9
1
0.5
0
−0.5
−1
0
2
4
6
8
10
12

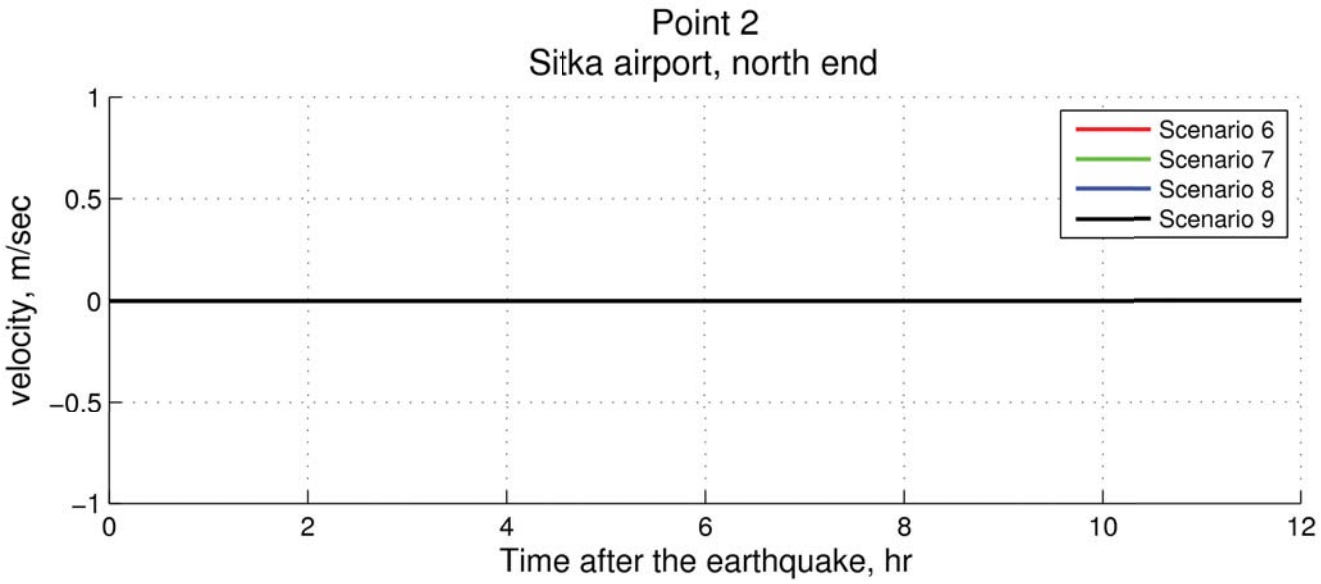
Point 2
Sitka airport, north end
velocity, m/sec
Time after the earthquake, hr
Scenario 6
Scenario 7
Scenario 8
Scenario 9
1
0.5
0
−0.5
−1
0
2
4
6
8
10
12

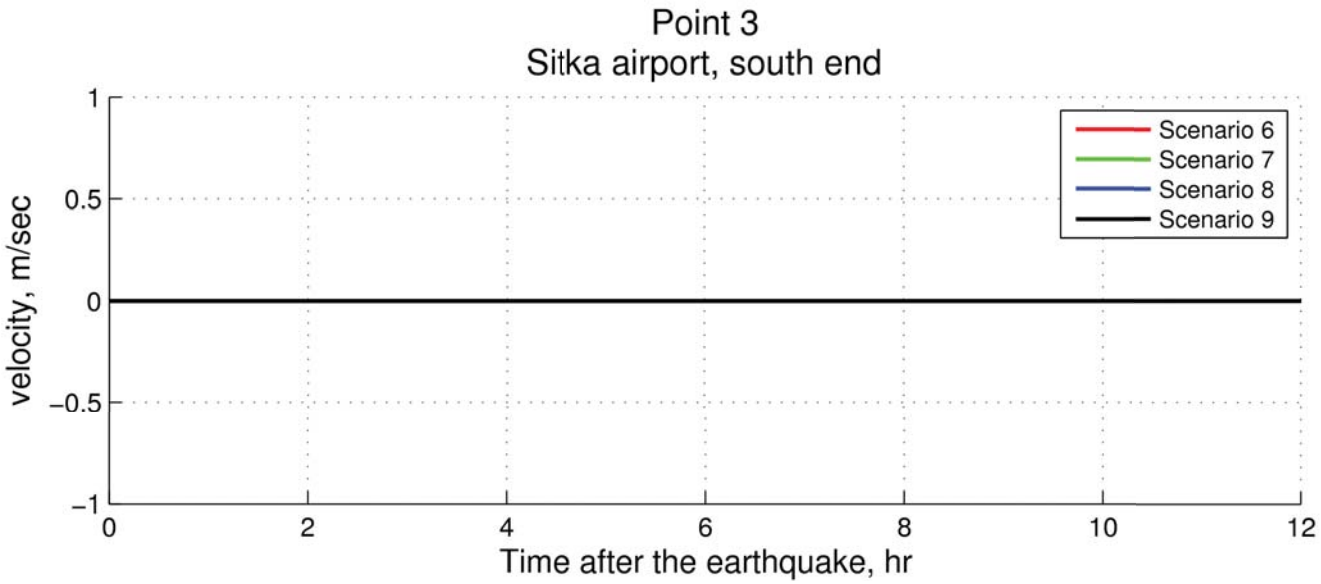
Point 3
Sitka airport, south end
velocity, m/sec
Time after the earthquake, hr
Scenario 6
Scenario 7
Scenario 8
Scenario 9
1
0.5
0
−0.5
−1
0
2
4
6
8
10
12

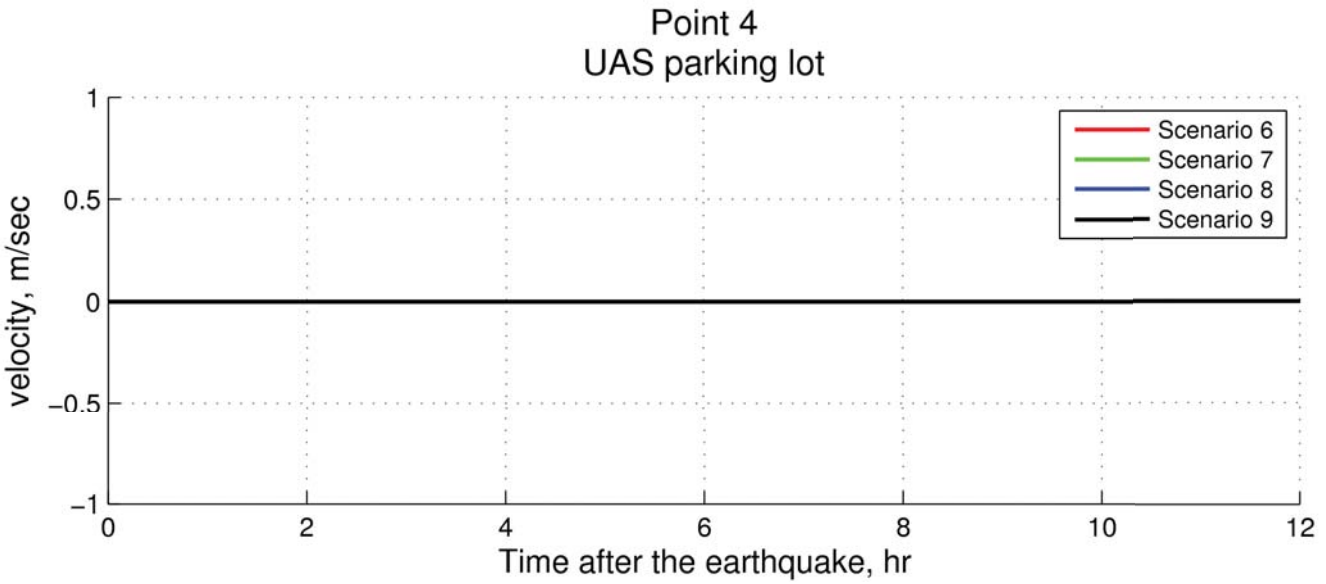
Point 4
UAS parking lot
Scenario 6
Scenario 7
Scenario 8
Scenario 9
velocity, m/sec
Time after the earthquake, hr

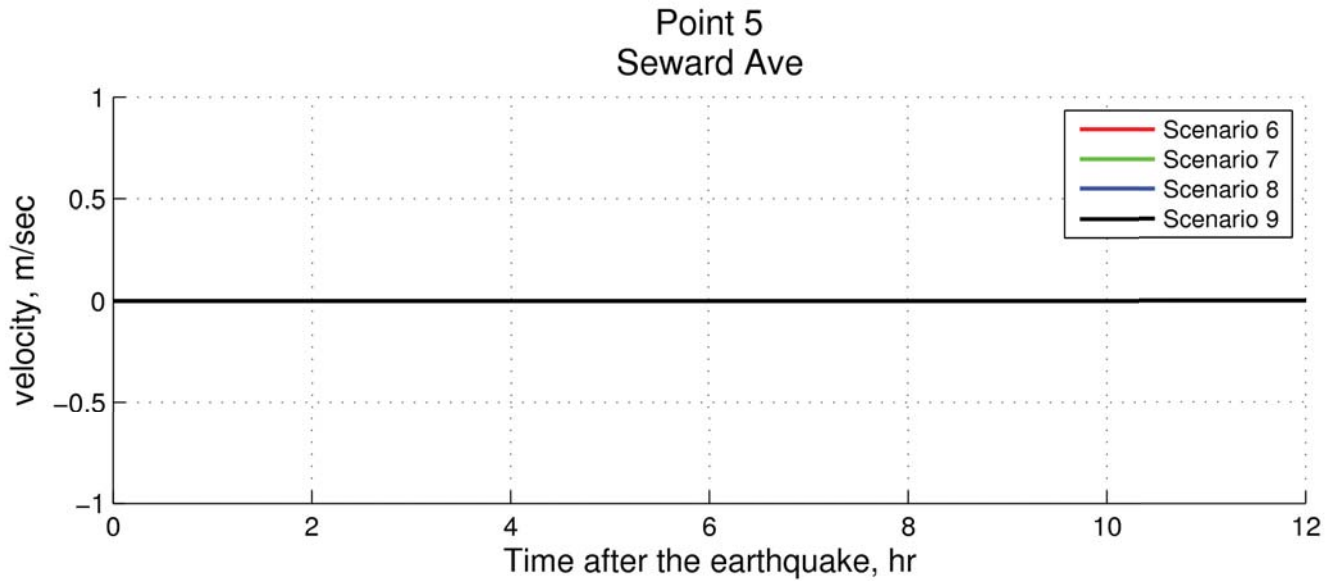
Point 5
Seward Ave
Scenario 6
Scenario 7
Scenario 8
Scenario 9
velocity, m/sec
Time after the earthquake, hr

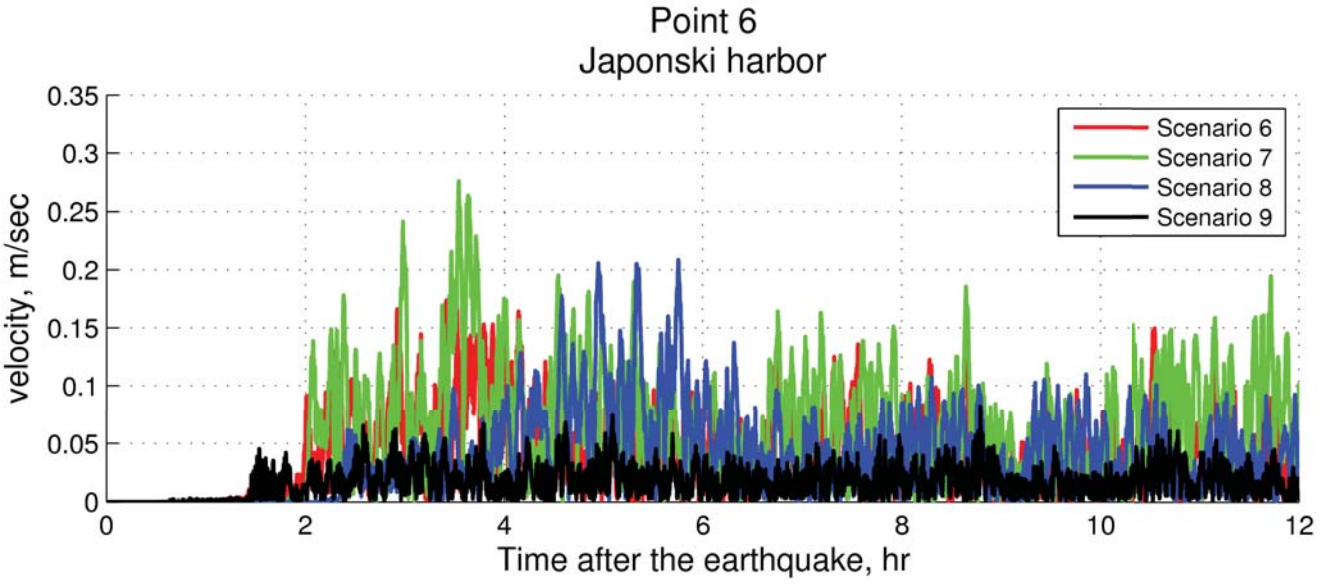
Point 6
Japonski harbor
Scenario 6
Scenario 7
Scenario 8
Scenario 9
velocity, m/sec
Time after the earthquake, hr

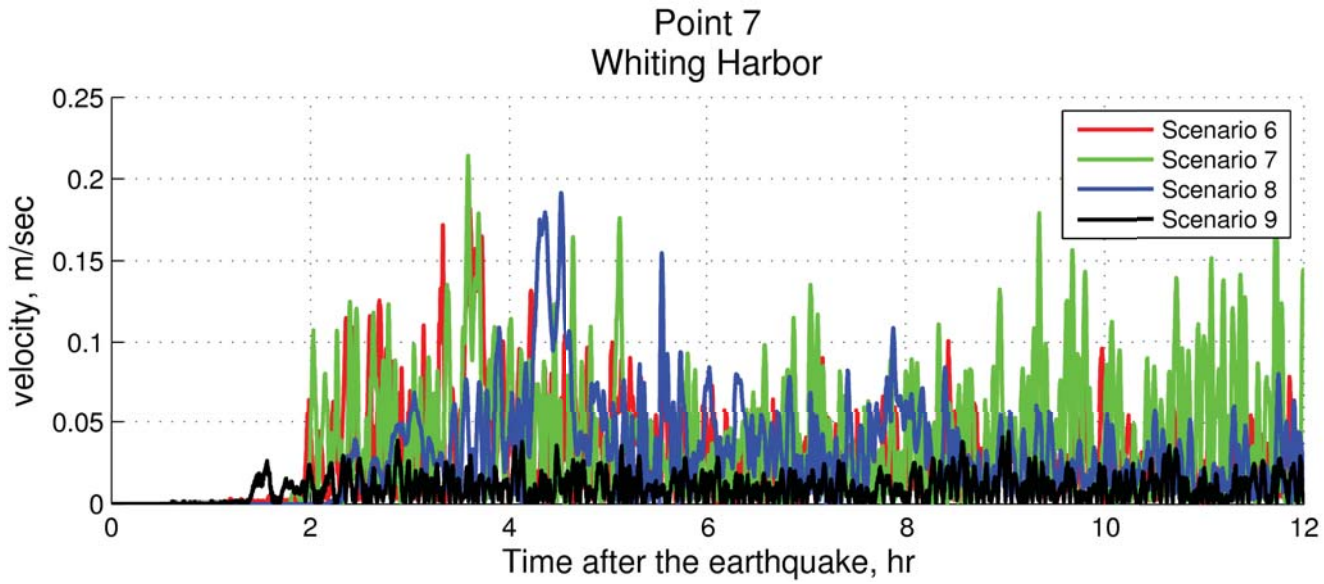
Point 7
Whiting Harbor
velocity, m/sec
Time after the earthquake, hr
Scenario 6
Scenario 7
Scenario 8
Scenario 9
0.25
0.2
0.15
0.1
0.05
0
0
2
4
6
8
10
12

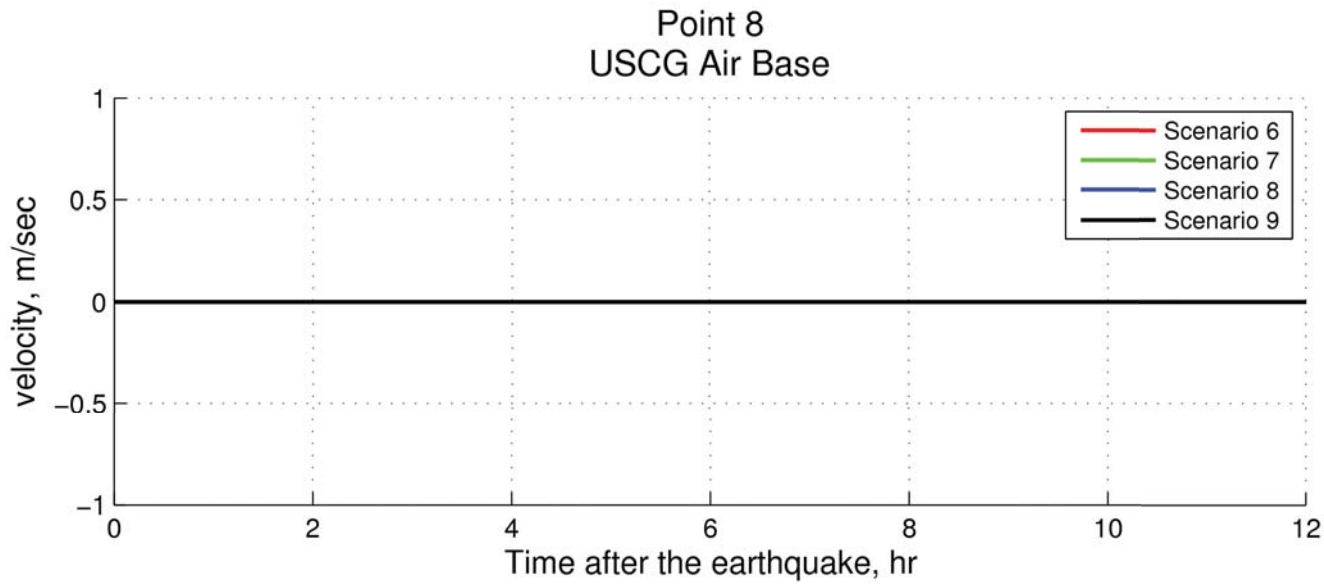
Point 8
USCG Air Base
velocity, m/sec
Time after the earthquake, hr
Scenario 6
Scenario 7
Scenario 8
Scenario 9
1
0.5
0
−0.5
−1
0
2
4
6
8
10
12

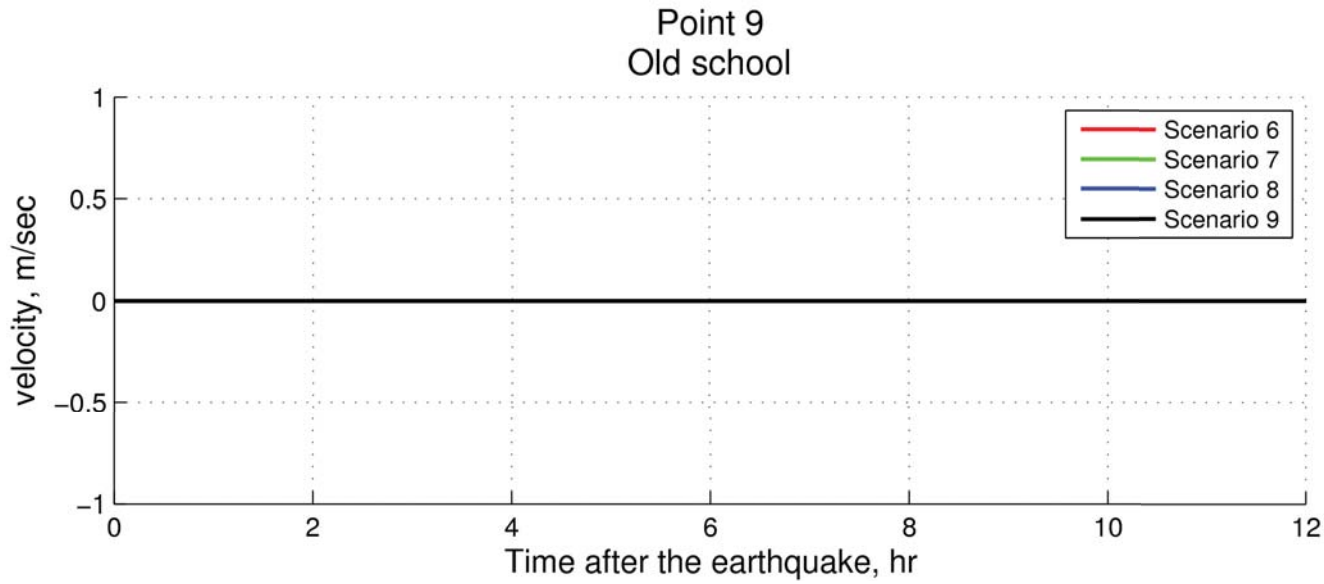
Point 9
Old school
velocity, m/sec
Time after the earthquake, hr
Scenario 6
Scenario 7
Scenario 8
Scenario 9
1
0.5
0
−0.5
−1
0
2
4
6
8
10
12

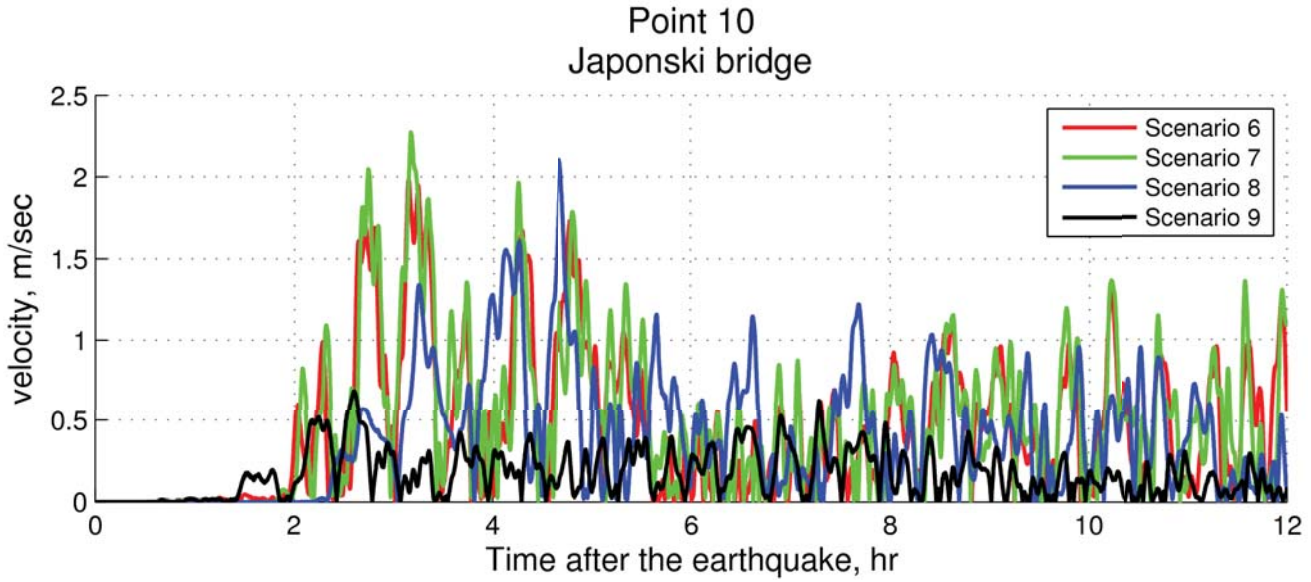
Point 10
Japonski bridge
velocity, m/sec
Time after the earthquake, hr
Scenario 6
Scenario 7
Scenario 8
Scenario 9

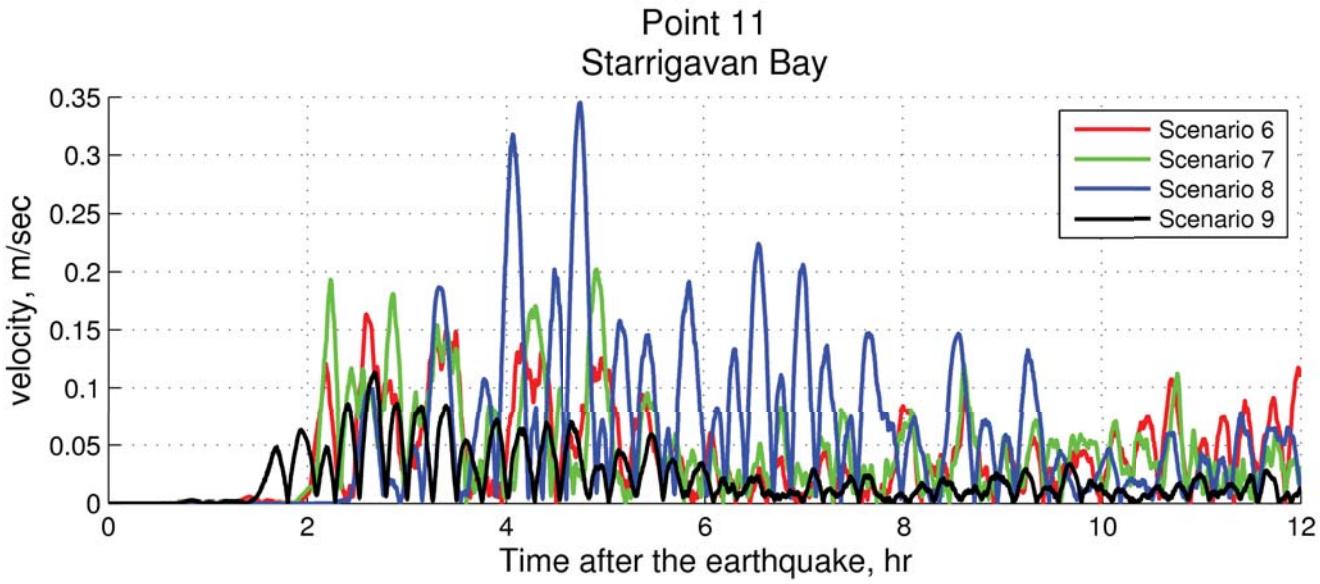
Point 11
Starrigavan Bay
velocity, m/sec
Time after the earthquake, hr
Scenario 6
Scenario 7
Scenario 8
Scenario 9

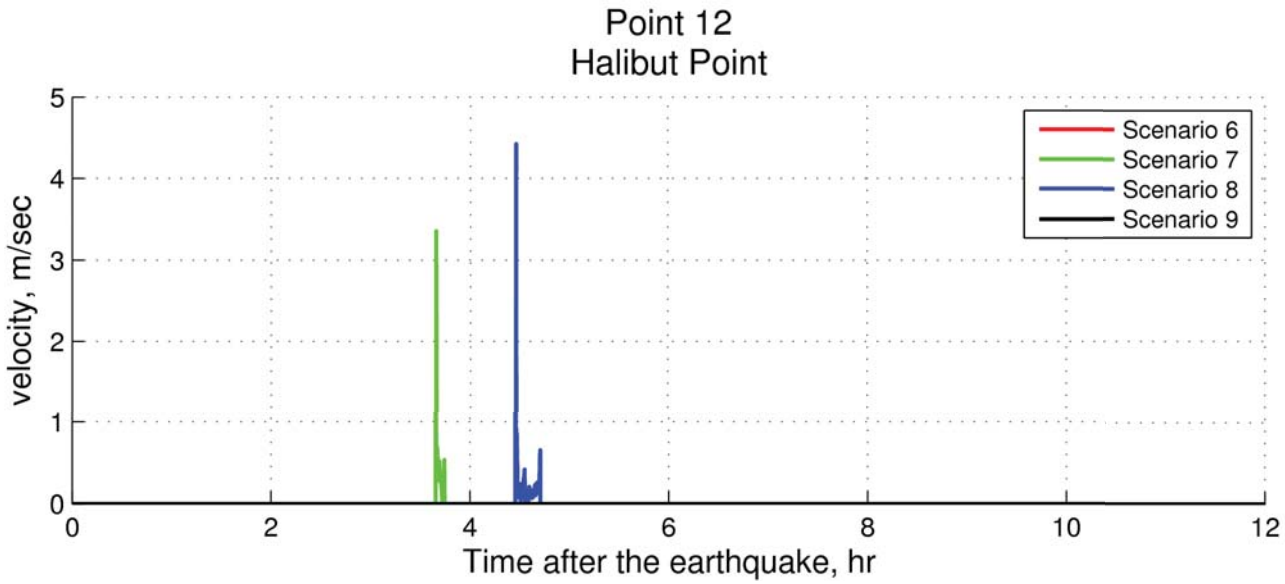
Point 12
Halibut Point
velocity, m/sec
Time after the earthquake, hr
Scenario 6
Scenario 7
Scenario 8
Scenario 9

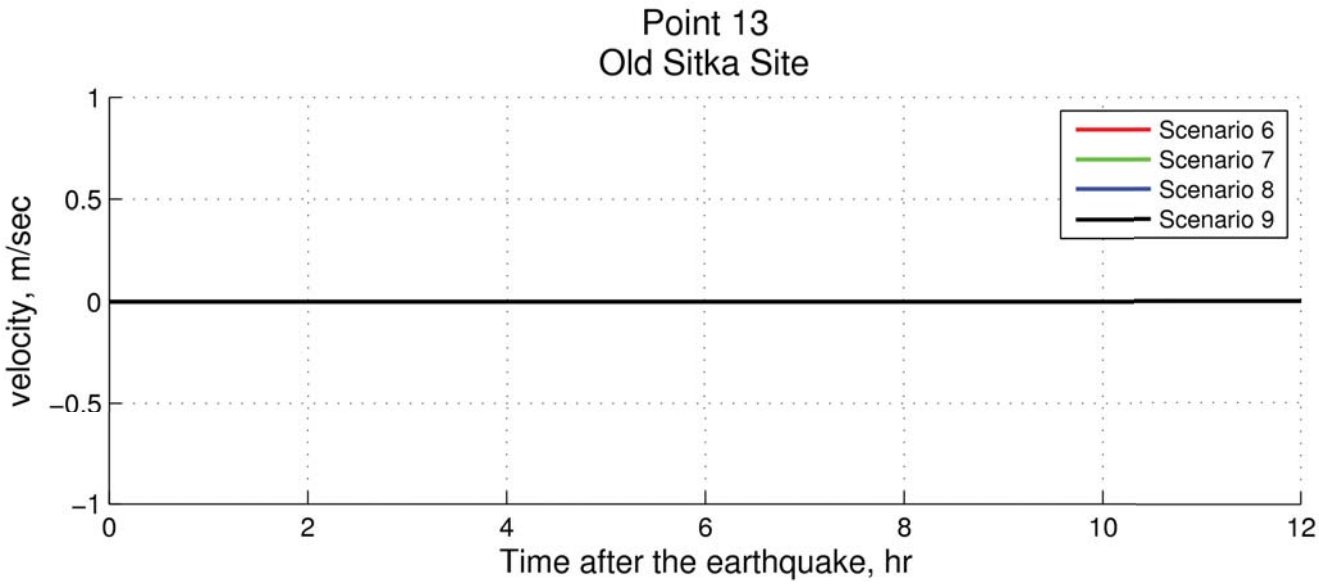
Point 13
Old Sitka Site
velocity, m/sec
Time after the earthquake, hr
Scenario 6
Scenario 7
Scenario 8
Scenario 9
1
0.5
0
−0.5
−1
0
2
4
6
8
10
12

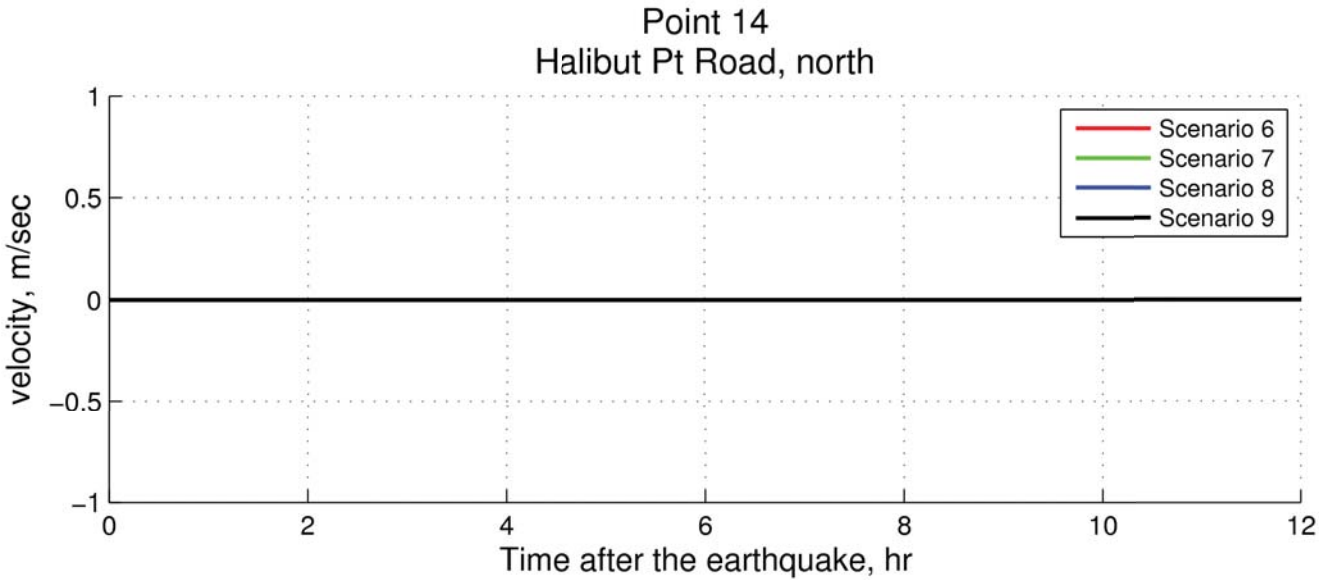
Point 14
Halibut Pt Road, north
velocity, m/sec
Time after the earthquake, hr
Scenario 6
Scenario 7
Scenario 8
Scenario 9
1
0.5
0
−0.5
−1
0
2
4
6
8
10
12

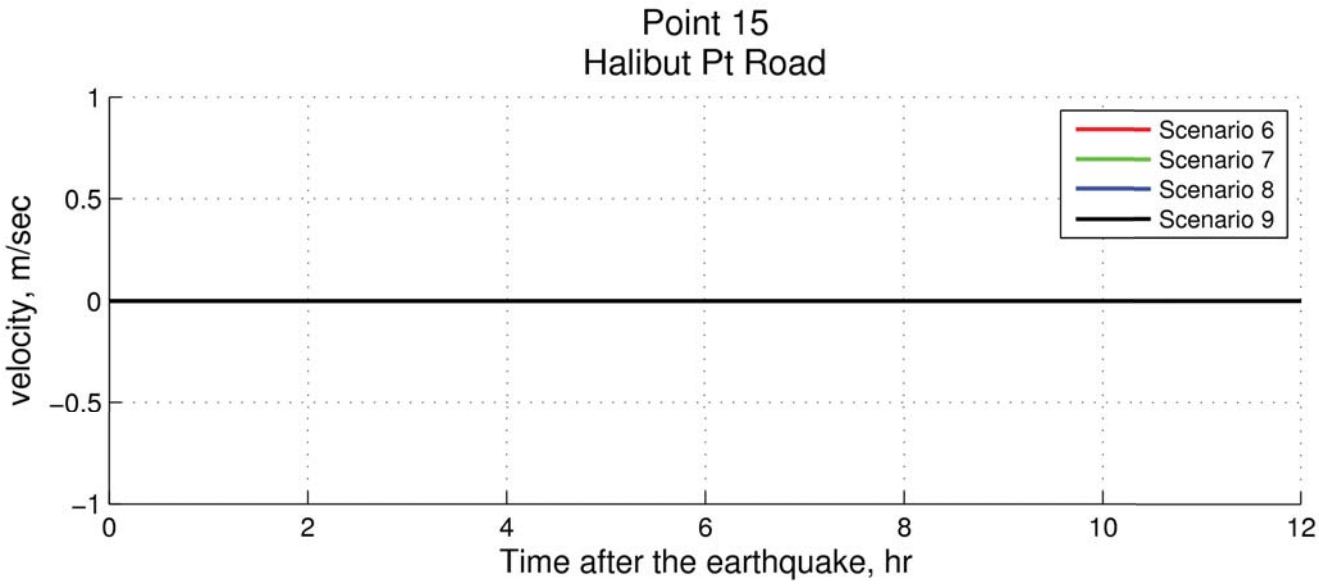
Point 15
Halibut Pt Road
velocity, m/sec
Time after the earthquake, hr
Scenario 6
Scenario 7
Scenario 8
Scenario 9
1
0.5
0
−0.5
−1
0
2
4
6
8
10
12

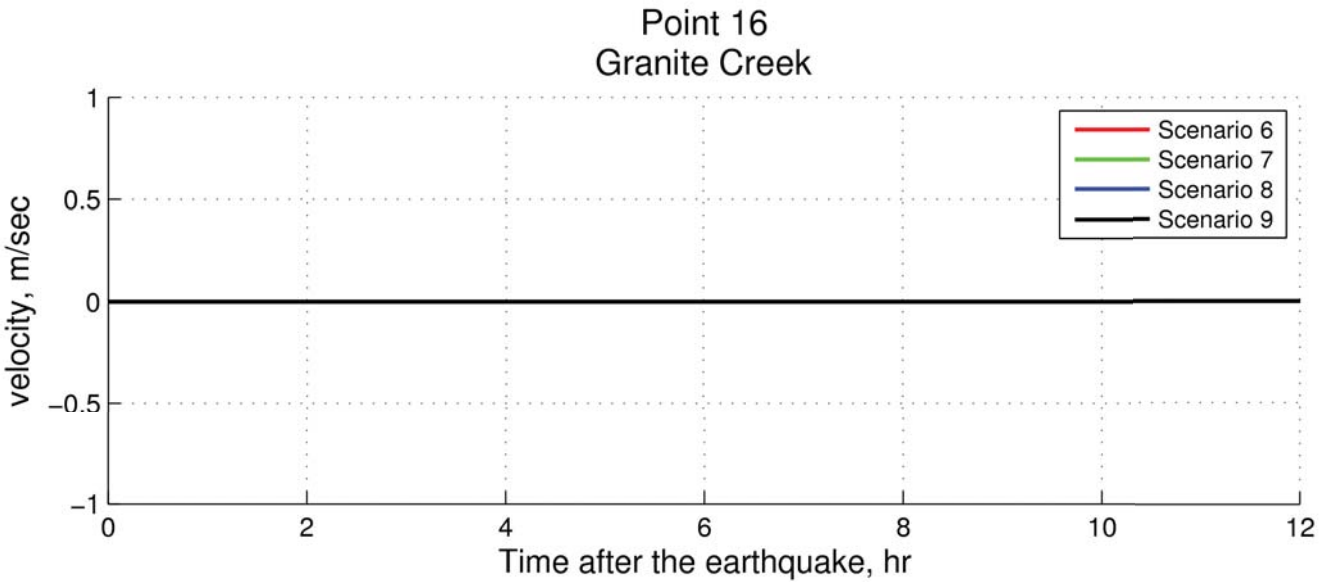
Point 16
Granite Creek
Scenario 6
Scenario 7
Scenario 8
Scenario 9
velocity, m/sec
1
0.5
0
−0.5
−1
0
2
4
6
8
10
12
Time after the earthquake, hr

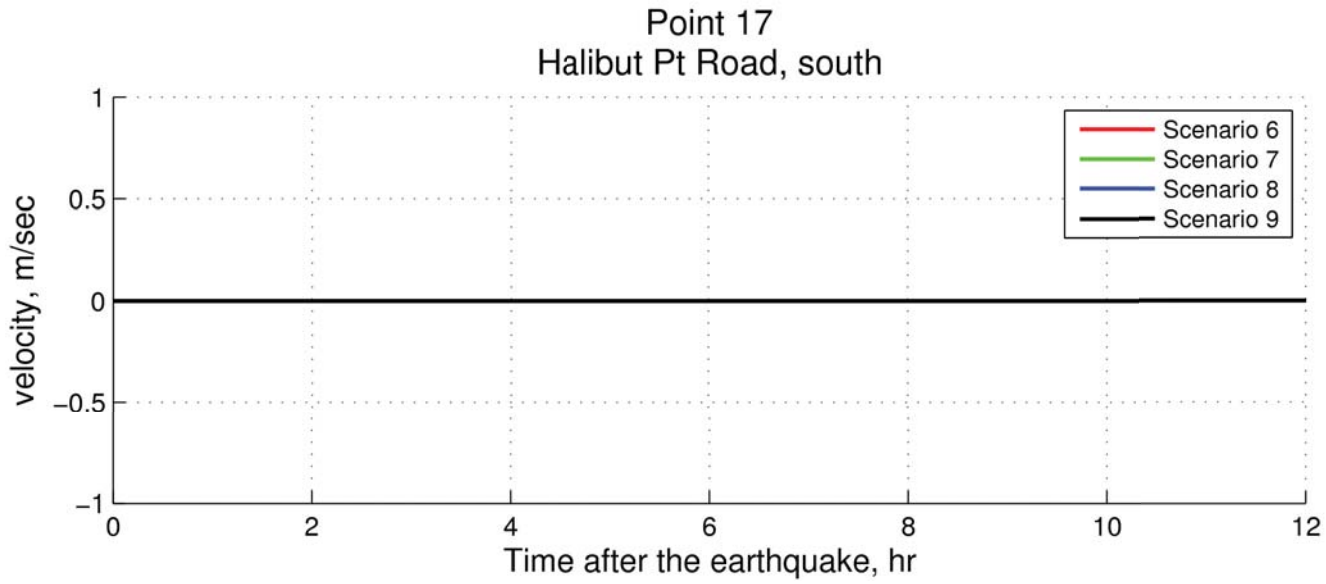
Point 17
Halibut Pt Road, south
Scenario 6
Scenario 7
Scenario 8
Scenario 9
velocity, m/sec
1
0.5
0
−0.5
−1
0
2
4
6
8
10
12
Time after the earthquake, hr

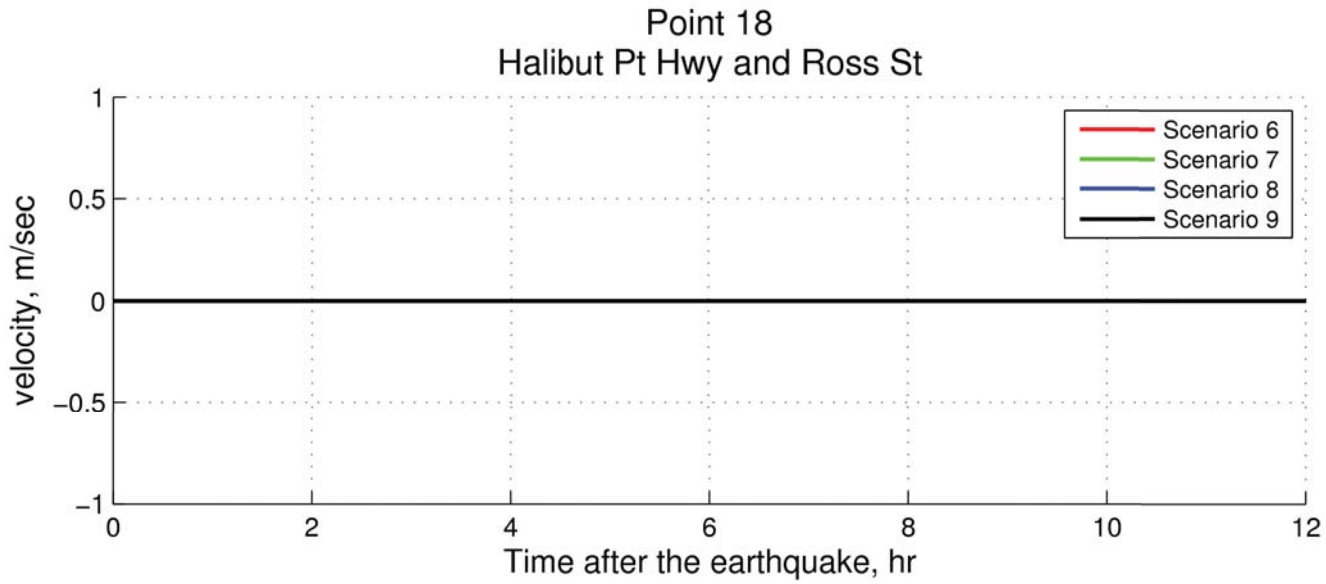
Point 18
Halibut Pt Hwy and Ross St
Scenario 6
Scenario 7
Scenario 8
Scenario 9
velocity, m/sec
1
0.5
0
−0.5
−1
0
2
4
6
8
10
12
Time after the earthquake, hr

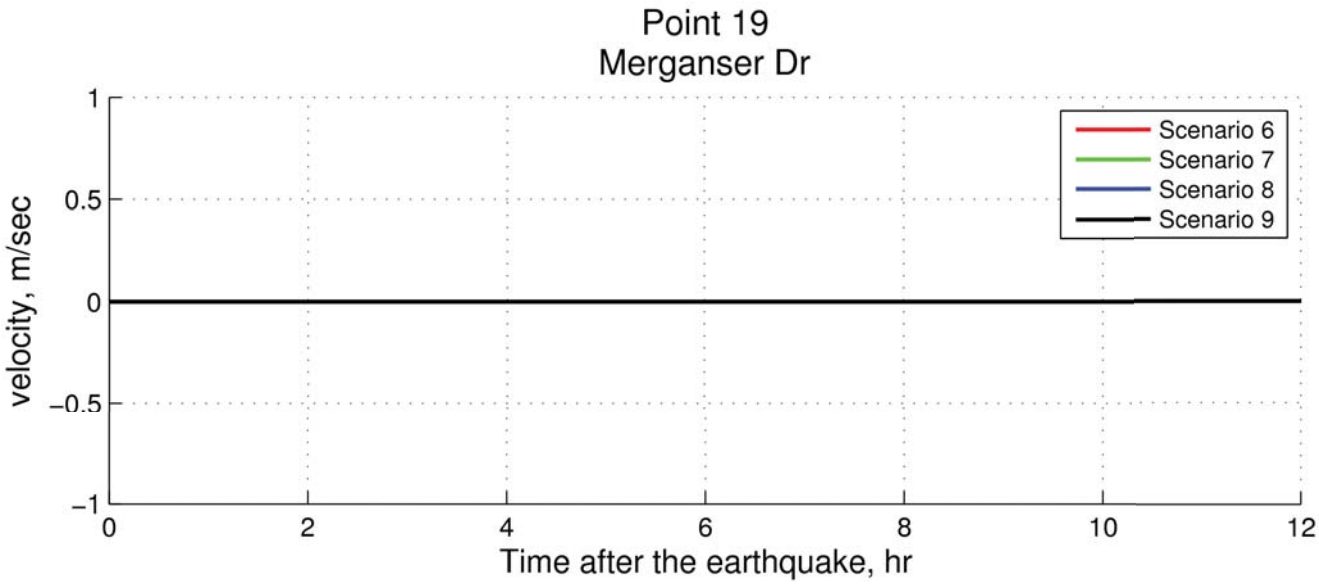
Point 19
Merganser Dr
Scenario 6
Scenario 7
Scenario 8
Scenario 9
velocity, m/sec
1
0.5
0
−0.5
−1
0
2
4
6
8
10
12
Time after the earthquake, hr

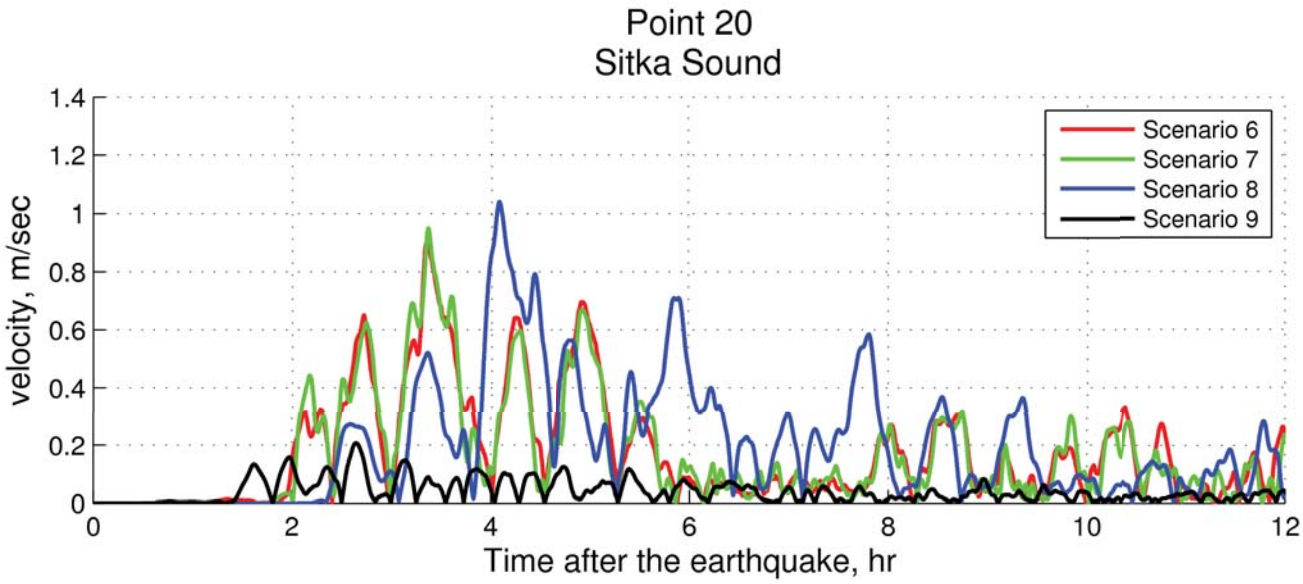
Point 20
Sitka Sound
Scenario 6
Scenario 7
Scenario 8
Scenario 9
velocity, m/sec
1.4
1.2
1
0.8
0.6
0.4
0.2
0
0
2
4
6
8
10
12
Time after the earthquake, hr

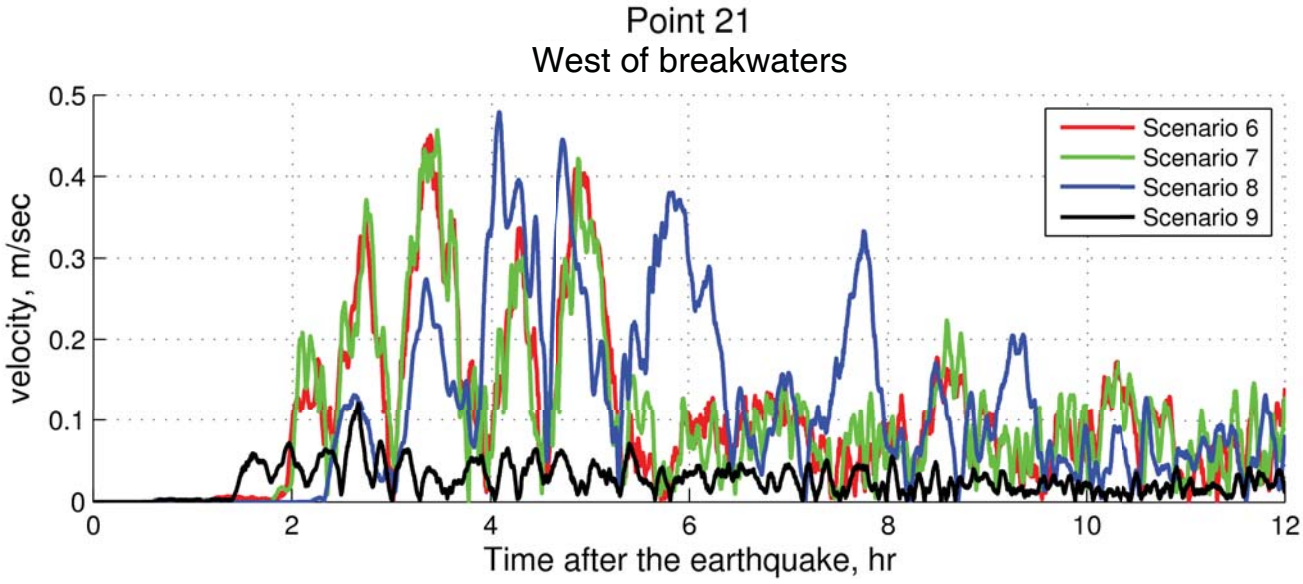
Point 21
West of breakwaters
Scenario 6
Scenario 7
Scenario 8
Scenario 9
velocity, m/sec
0.5
0.4
0.3
0.2
0.1
0
0
2
4
6
8
10
12
Time after the earthquake, hr

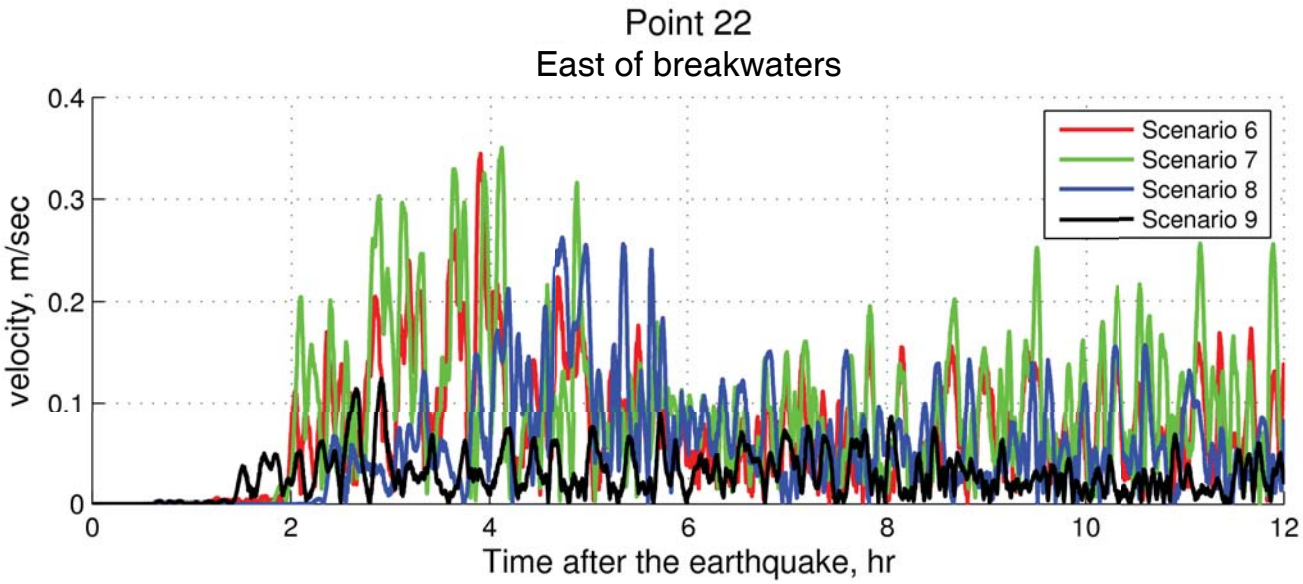
Point 22
East of breakwaters
velocity, m/sec
Time after the earthquake, hr
Scenario 6
Scenario 7
Scenario 8
Scenario 9

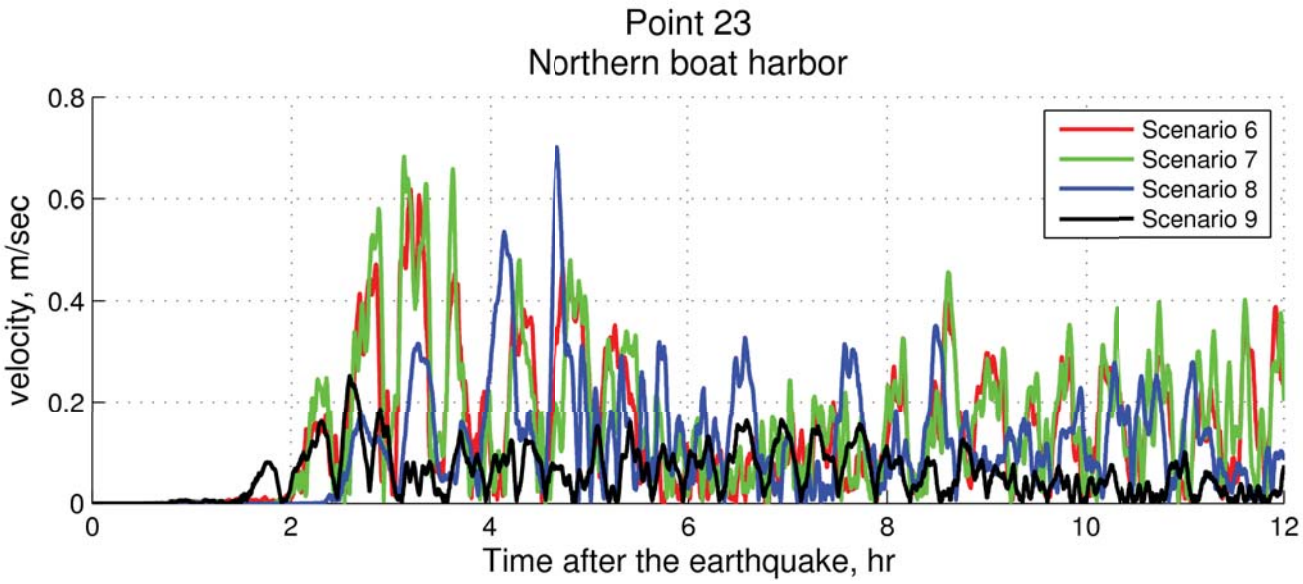
Point 23
Northern boat harbor
velocity, m/sec
Time after the earthquake, hr
Scenario 6
Scenario 7
Scenario 8
Scenario 9

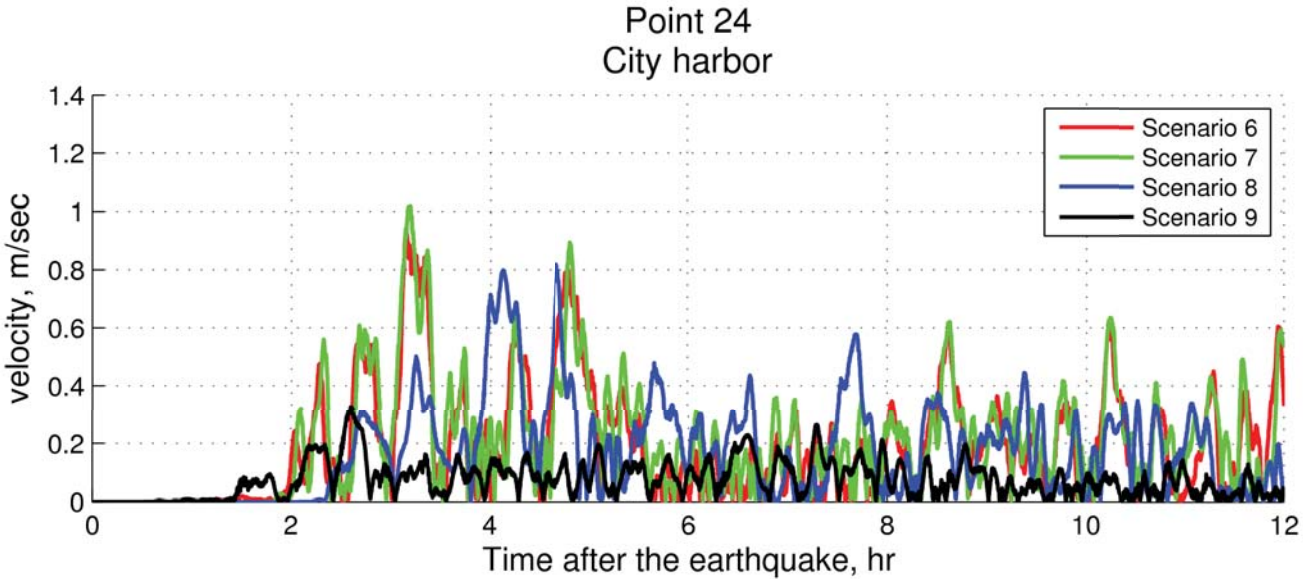
Point 24
City harbor
velocity, m/sec
Time after the earthquake, hr
Scenario 6
Scenario 7
Scenario 8
Scenario 9

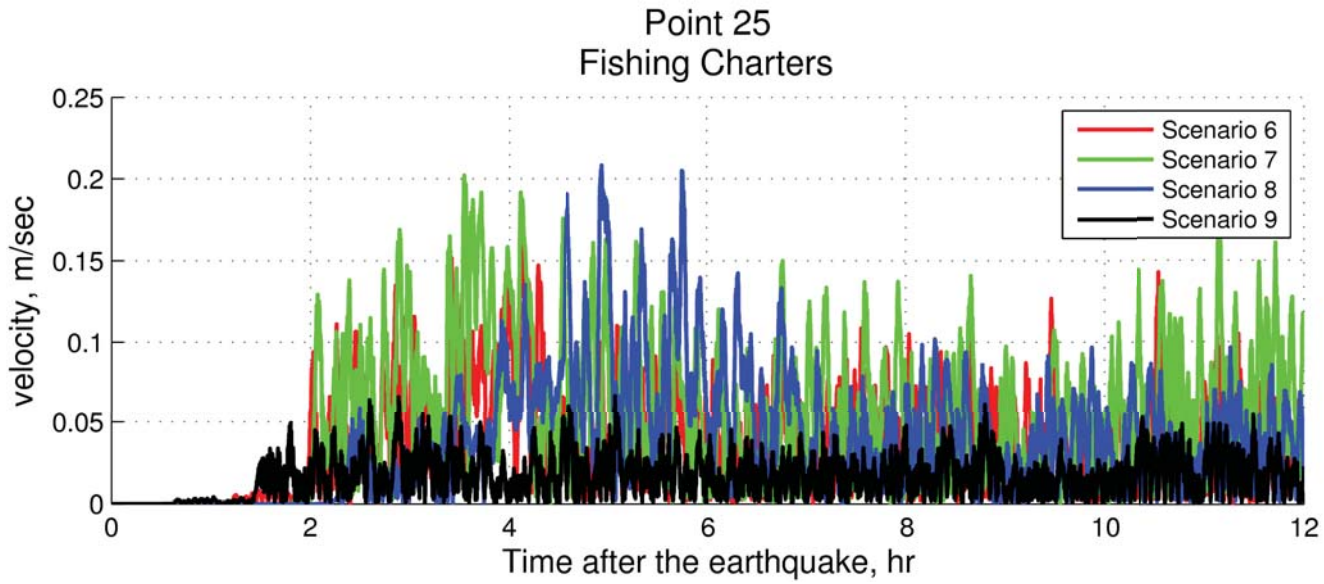
Point 25
Fishing Charters
velocity, m/sec
Time after the earthquake, hr
Scenario 6
Scenario 7
Scenario 8
Scenario 9
0.25
0.2
0.15
0.1
0.05
0
0
2
4
6
8
10
12

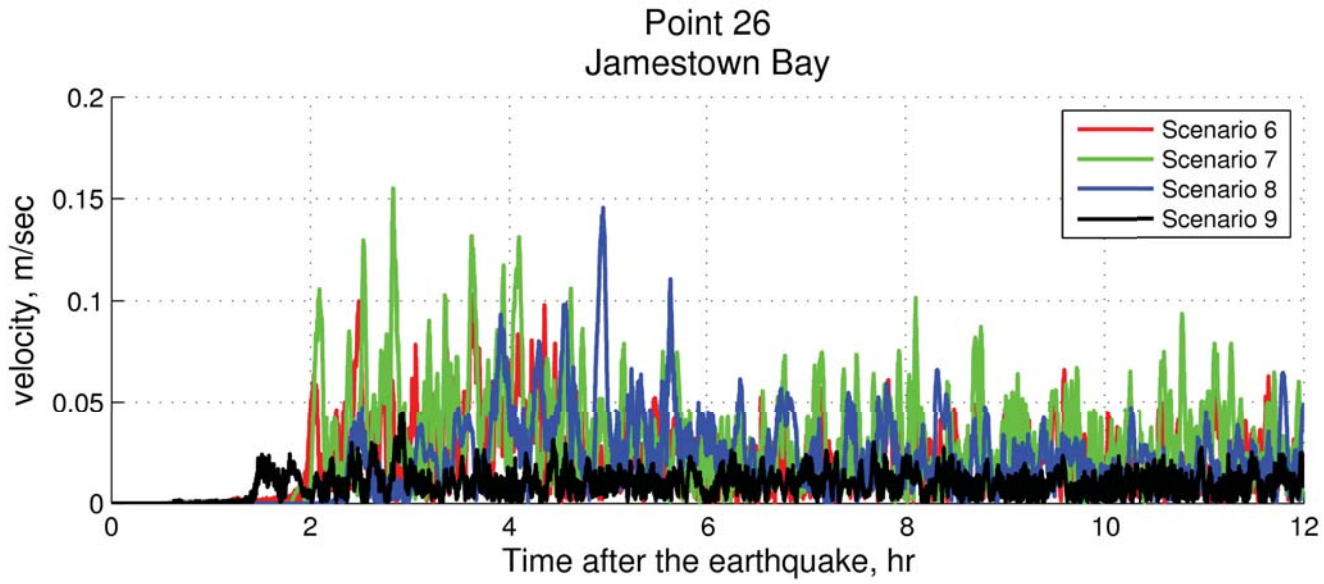
Point 26
Jamestown Bay
velocity, m/sec
Time after the earthquake, hr
Scenario 6
Scenario 7
Scenario 8
Scenario 9
0.2
0.15
0.1
0.05
0
0
2
4
6
8
10
12

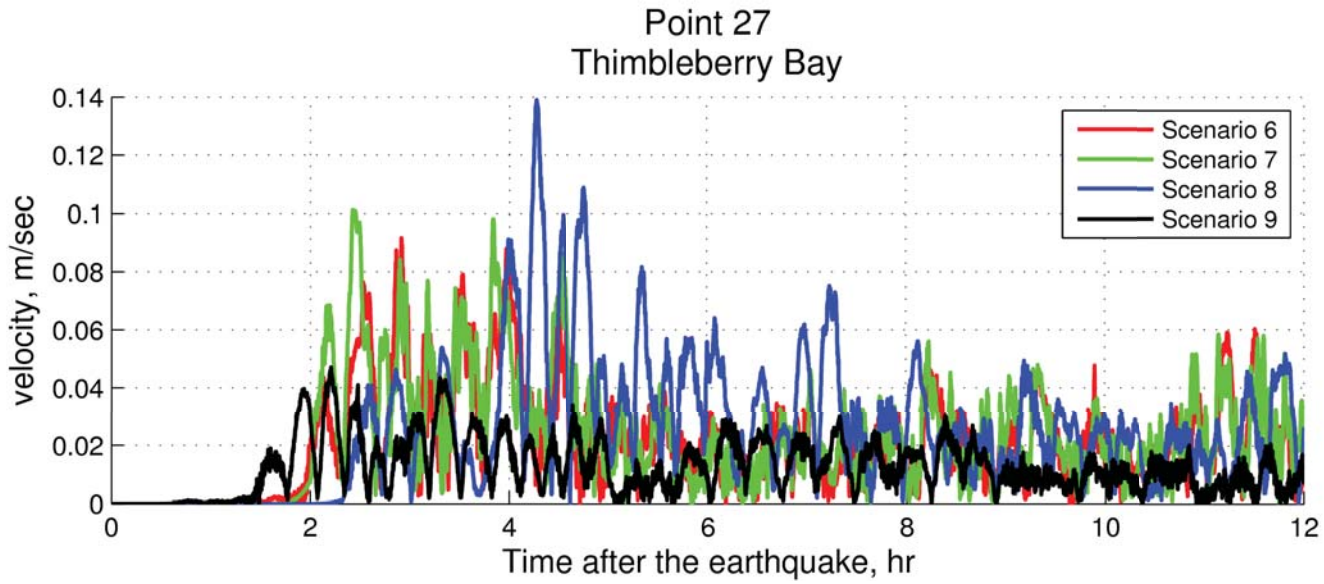
Point 27
Thimbleberry Bay
velocity, m/sec
Time after the earthquake, hr
Scenario 6
Scenario 7
Scenario 8
Scenario 9
0.14
0.12
0.1
0.08
0.06
0.04
0.02
0
0
2
4
6
8
10
12

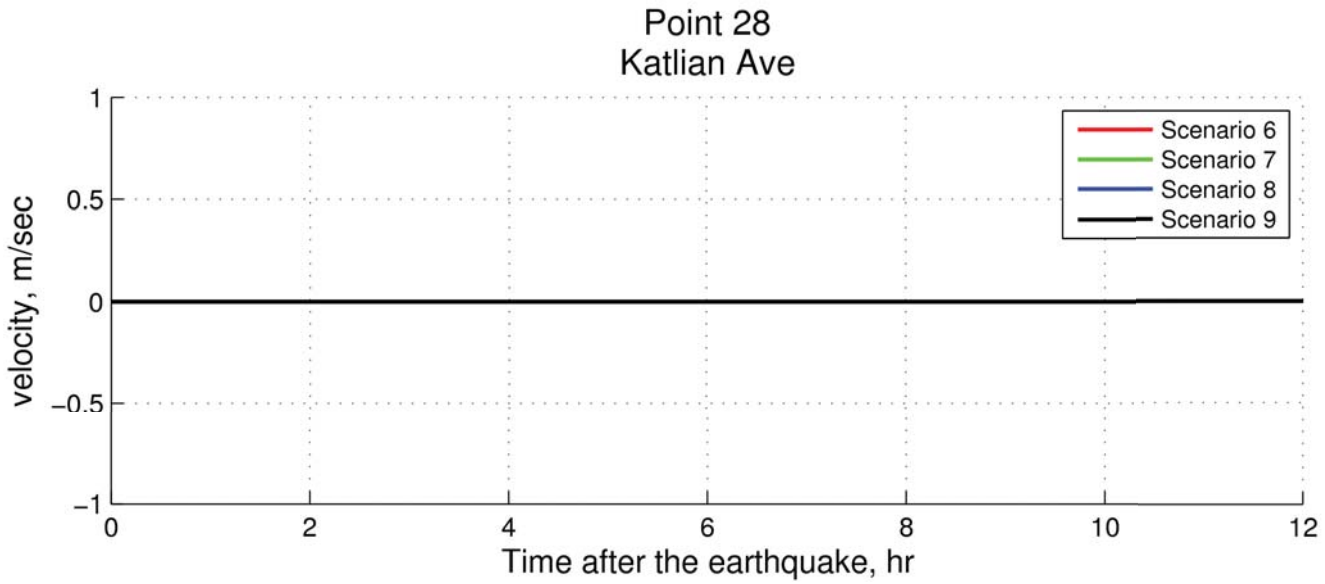
Point 28
Katlian Ave
Scenario 6
Scenario 7
Scenario 8
Scenario 9
velocity, m/sec
Time after the earthquake, hr

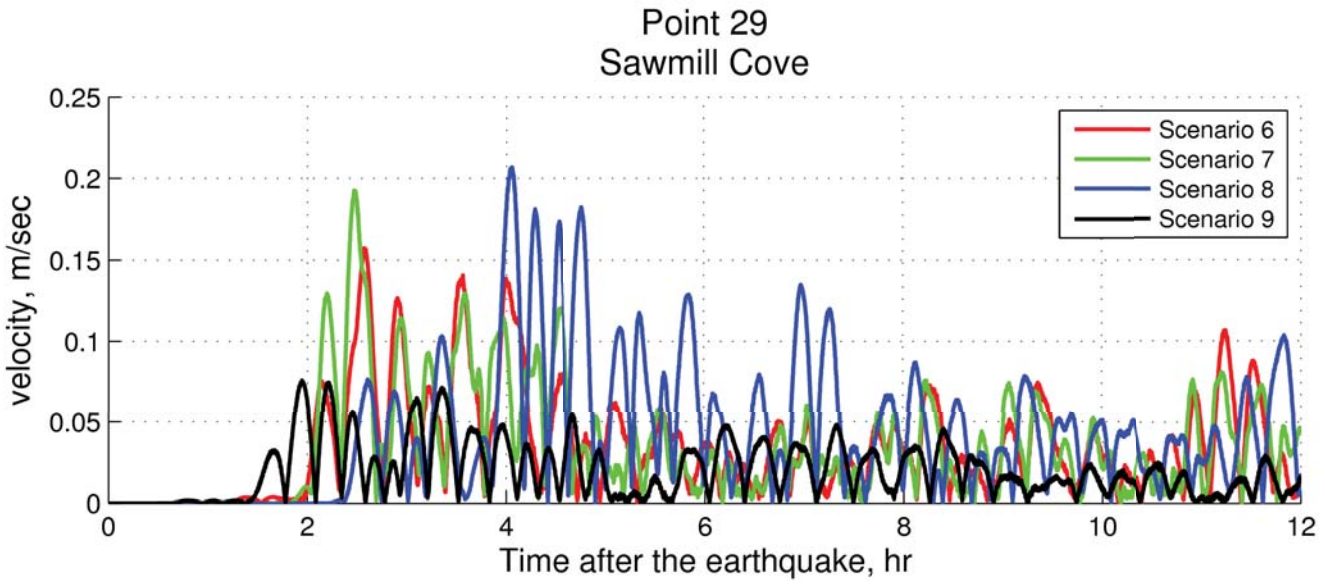
Point 29
Sawmill Cove
Scenario 6
Scenario 7
Scenario 8
Scenario 9
velocity, m/sec
Time after the earthquake, hr

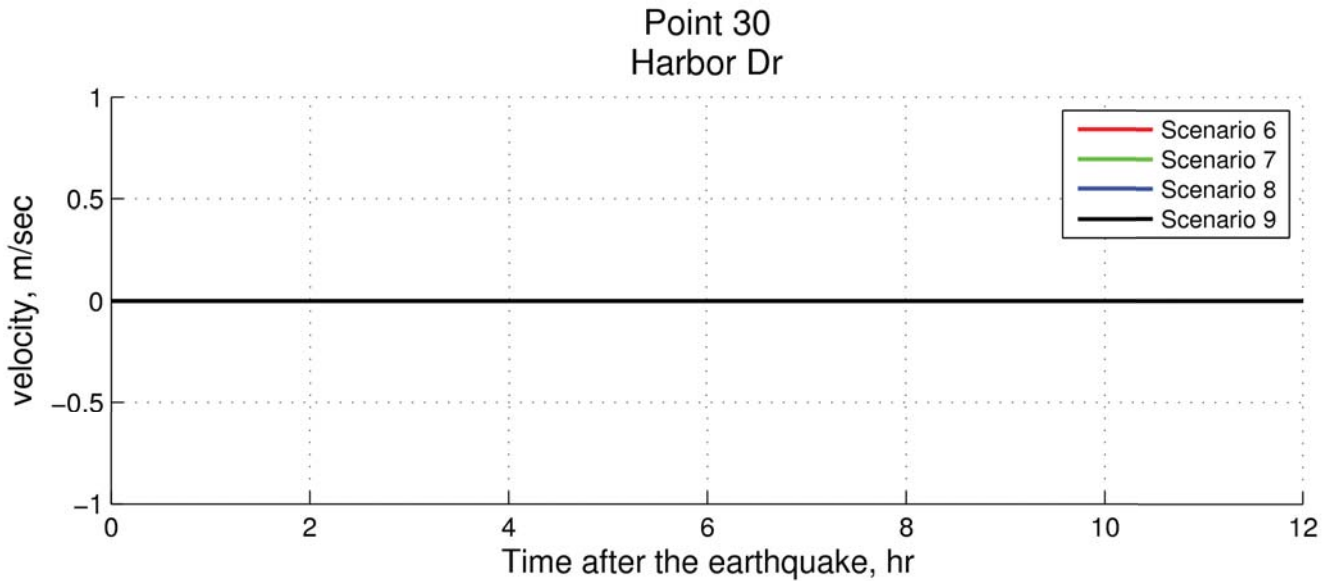
Point 30
Harbor Dr
Scenario 6
Scenario 7
Scenario 8
Scenario 9
velocity, m/sec
Time after the earthquake, hr